DTU Mechanical Engineering
Department of Mechanical Engineering

Surface engineering of Fe-C coatings

Jacob Obitsø Nielsen

PhD Thesis

Preface

This doctoral thesis is submitted in partial fulfilment of the requirements for obtaining the degree of PhD at the Department of Mechanical Engineering at the Technical University of Denmark (DTU). The project was funded by OCAS NV - ArcelorMittal Global R&D Gent (Belgium), a. h. nichro Haardchrom (Denmark) and Fast Track - Societal Partnership (Denmark), funded by the Innovation Fund Denmark (IFD), as well as the Department of Mechanical Engineering, Section of Materials and Surface Engineering at DTU, during the period 1. January 2017 to 4. April 2020. The project was supervised by Assoc. Prof. Karen Pantleon and (during the first year) Prof. Per Møller from the Department of Mechanical Engineering, Section of Materials and Surface Engineering, at DTU.

Jacob Obitsø Nielsen
Kongens Lyngby, Denmark, 4. April 2020

Declaration

I declare that, if not explicitly stated, none of the presented work in this doctoral thesis has been submitted in support of an application for another degree of this or any other university. I further declare that the presented work is my own work and that I have correctly acknowledged work of others.

Abstract

This doctoral thesis presents research work on the Fe-C coatings, which were electrochemically deposited using an iron(II)sulfate based electrolyte with citric acid as the additive and obtained a high microhardness around 800 HV that increased to about 1300 HV by dedicated annealing. Electrodeposited iron-carbon coatings are a promising wear protective alternative to hard chrome coatings, because they allow environmental friendly deposition of a coating with promising mechanical properties. The organic additives in the electrolyte are adsorbed in the coating during deposition and improve the mechanical properties by refining the microstructure.

Fe-C coatings with the same internal structure have been reproducibly deposited independently of the coatings thickness and the applied metallic substrate. A simple method is proposed specially adapted to estimate the adhesion between the Fe-C coating and a substrate after different pre-treatments. The influence of the operation conditions on the resulting material properties of the Fe-C coating has been systematically investigated and suggestions for the optimal operation conditions for long-term large-scale operation are provided in detail, which are required for the next step towards testing and implementation of the Fe-C coatings in industry.

The internal structure of the as-deposited Fe-C coating has been investigated, both at room temperature and during annealing, by advanced methods of materials characterization applying thermal analysis, microscopic and diffraction-based in-situ and ex-situ methods. The results essentially contribute to the understanding of the growth characteristics, co-deposition of light elements and the phase formation during electrodeposition of the Fe-C coatings. The main cause of the high hardness of the as-deposited Fe-C coating is interplay between the nanocrystalline microstructure and the coherent or semi-coherent precipitates inside the ferrite grains.

The characterization of an “organic compound” based on thermal analysis improved the understanding of the nature of the high amount of co-deposited carbon, oxygen and hydrogen within the as-deposited microstructure. The temperature induced evolution of the co-deposited elements has been studied ex-situ and in-situ and is discussed in relation to dedicated post deposition surface engineering to improve the properties of the coating even further.

The results essentially contribute to understanding of the internal structure of the electrodeposited Fe-C coatings and described the recommended operation conditions for a long-term large-scale production, which are needed to be considered as a sustainable alternative to hard coatings.

Resumé

Denne PhD-afhandling præsenterer forskningsresultaterne af arbejdet med Fe-C belægninger, som er elektrokemisk deponeret under anvendelse af en jern(II)sulfat baseret elektrolyt med citronsyre som additiv. Fe-C belægningen opnåede en høj mikrohårdhed på omkring 800 HV, som steg til ca. 1300 HV ved dedikeret varmebehandling. De elektrokemisk deponeret jern-kulstof belægninger er et lovende slidbeskyttende alternativ til hårdkrom belægninger, fordi de benytter en miljøvenlig proces til at producere belægninger med lovende mekaniske egenskaber. De organiske additiver i elektrolytten indfældes i belægningen og forbedrer de mekaniske egenskaber ved at raffinere mikrostrukturen.

Fe-C belægninger er reproducerbart deponeret med den samme indre struktur uafhængigt af belægningstykkelsen og det anvendte metalliske underlag. En simpel metode er præsentret der er specielt tilpasset til at estimere vedhæftningen mellem Fe-C belægningen og et underlag der er blevet forbehandlet ved brug af forskellige metoder. Driftsbetingelsernes indflydelse på de resulterende materialegenskaber af Fe-C belægningen er undersøgt systematisk, og der gives detaljerede forslag til de optimale driftsbetingelser for langvarig drift i stor skala, som er nødvendige for det næste trin med testning og implementering af Fe-C belægninger i industrien.

Den indre struktur af Fe-C belægningen er blevet undersøgt, både ved stuetemperatur og under varmebehandling, ved brug af avancerede materialekarakteriserings metoder i form af termisk analyse, mikroskopi og diffraktionsbaseret in-situ og ex-situ metoder. Resultaterne bidrager væsentligt til forståelsen af vækstegenskaber, indfældningen af lette elementer og fasedannelsen under deponeringen af Fe-C belægningerne. Hovedårsagen til den høje hårdhed af Fe-C belægningen er samspillet mellem den nanokrystallinske mikrostruktur og de kohærente eller semi-kohærente fase inde i ferrit kornene.

Karakteriseringen af en "organisk forbindelse" baseret på termisk analyse har forbedret forståelsen af den høje mængde indfældet kulstof, oxygen og hydrogen i den indre struktur. Udviklingen af de indfældet lette elementer er blevet undersøgt ved ex-situ og in-situ varmebehandling og diskuteres i relation til at benytte en dedikeret efterbehandling til forbedre belægningens egenskaber yderligere.

Resultaterne bidrager væsentligt til forståelsen af den indre struktur af de elektrokemiske deponeret Fe-C belægninger og beskriver de anbefalede driftsbetingelser for en langvarig produktion i stor skala, som er nødvendige for at blive betragtet som et bæredygtigt alternativ til hårde belægninger.

Acknowledgements

I would like to express my genuine gratitude to my main supervisor Assoc. Prof. Karen Pantleon for her guidance, encouragement, and attention to details in every part of the project. Her profound knowledge and curiosity for understanding all aspects of the project have been a source of inspiration and a driving force for setting up advanced complementary investigates that could lead to justification of our interpretations. She has provided me with attention and support when it was required and her problem-solving approach has formed me professionally and for that, I am truly grateful.

I am grateful for the support and opportunity provided by my co-supervisor Prof. Per Møller that saw the prospect in this project and invited the relevant project partners to participate. His active participation for the entire duration of the project was truly missed, but all that I hope for is he continue his recovery.

I would like to thank our project partners OCAS NV, ArcelorMittal Global R&D Gent, a. h. nichro Haardchrom and Fast Track - Societal Partnership for the financial support and for sharing their expertise during the project. I in particular want show appreciation for Carsten Jørgensen, Kristian Løkkegaard, Ansbert de Cleene, Dr. Joost de Strycker, Dr. Lars Pleth Nielsen, and Kasper Bondo for aiding the project in different manners.

The project has been assisted by a number of external experts and I would especially like to show my appreciation to Prof. Christoph Genzel, Dr. Manuela Klaus, Dr. Daniel Apel, and Dr. Matthias Meixner for their assistance during my beamtimes at the synchrotron facility HZB-BESSY II at the EDDI beamline. I am thankful for the theoretical and practical lessons given by Prof. Jakob Birkedal Wagner (CEN, DTU) on the subject on transmission electron microscopy. I am also grateful for the opportunity to perform an atom probe tomography analysis assisted by Dr. Frédéric Danoix at Normandie University.

I would like to recognize the support that I have received from my colleagues at the Section of Materials and Surface Engineering. I in particular want to acknowledge Flemming Bjerg Grumsen for his genuine interest in the project and sharing his theoretical and practical knowledge on crystallography, X-ray diffraction, and electron microscopy. I am grateful for Prof. Wolfgang Pantleons involvement in the investigation of the thermal stability and aiding with his expertise in numerical modeling. I would like to recognize Assoc. Prof. Thomas Lundin Christiansen for his contribution to the thermal analysis. Dr. Matteo Villa and Dr. Frank Niessen have been great company for social and professional discussions during the beamtimes at EDDI and in between. I appreciate the support from Peter Westermann for keeping the Galvano Laboratory a joyful place to work. I am thankful for the open door policy practiced by Prof. Marcel Somers where I always knew I could ask for counsel. Steffen Munch is acknowledge for his expertise and support in the metallographic laboratory along with Niklas Gammeltoft-Hansen. Jan Frank Pedersen and Lars Pedersen are acknowledge for their support in the workshop and Gitte Salomon for administrative support. Dr. Ömer Kücükyildiz have been a true friend and sparring partner. I have enjoyed each day at the office in the company of great material science engineers that have kept enthusiasm high. Five of them that finalized their projects before my deadline and the five that are still producing fascinating results.

Finally, I would thank my family for their support and I would especially like to thank my future wife that have tolerantly taking care of me during the project and uncomplainingly taken care of our newborn son Niels during the troublesome nights and the days that required long office hours.

List of published articles and conference contributions

Peer-reviewed articles

1. J.O. Nielsen, P. Møller, K. Pantleon, Electrodeposition of Iron with Co-deposition of Carbon: On the Nature of Nanocrystalline Fe-C Coatings, Metall. Mater. Trans. A. 50A (2019) 3785–3793.
2. J.O. Nielsen, K. Pantleon, Evolution of hard Fe–C electrodeposits with temperature, Surf. Eng. (2019), in press. Published online in October 2019.

Conferences contribution

1. Oral presentation, NASF SUR/FIN, Cleveland, Ohio, USA, 5. June 2018
2. Oral presentation, Junior Euromat, Budapest, Hungary, 10. July 2018
3. Poster presentation, Scandem, Lyngby, Denmark, 25. July 2018
4. Oral presentation, TMS, San Antonio, USA, 11. March 2019
5. Oral presentation, TMS, San Antonio, USA, 13. March 2019

List of articles under review

1. J.O. Nielsen, T.L. Christiansen, K. Pantleon, In-situ analysis of the thermal evolution of electrodeposited Fe-C coatings, submitted to Acta Materialia in December 2019, under review in revised version since March 2020.

List of abbreviations and symbols

Chemical elements symbols, chemical formulas, product/company names and SI-units are not included in this list

β_G	Gaussian contribution for the physical peak broadening
β_L	Lorentz contribution for the physical peak broadening
ε	Strain
η	Total overpotential
η_L	Lorentz factor
Θ	Diffraction angle
λ	Wavelength
σ_{RS}	Residual stress
φ	Sample rotation around surface normal during X-ray diffraction
Φ	Heating rate
ψ	Sample rotation around azimuth during X-ray diffraction
ψ_0^{hkl}	Strain free direction for a specific lattice plane
APT	Atom probe tomography
BF	Bright-field
BSE	Backscattered electrons
c	Speed of light
d	Thickness of the coating
d_0	Strain free lattice spacing
d_{hkl}	Lattice spacing
D	Crystallite size
DC	Direct current
DF	Dark-field
DI	Deionized
DTA	Differential thermal analysis
E	Activation energy
E_{hkl}	Lattice specific photon energy
EBSD	Electron backscatter diffraction
EDD	Energy-dispersive diffraction
EDS	Energy-dispersive spectroscopy
EELS	Electron energy-loss spectroscopy
F	Faradays constant
FIB	Focused-ion-beam
FWHM	Full-width-half-maximum
G	Gibbs free energy
GDOES	Glow discharge optical emission spectroscopy
h	Planck’s constant
I	Electric current
ICDD	International center for diffraction data
J	Current density
LOM	Light optical microscope
m	Mass
M	Molar mass

MS	Mass spectrometer
ODF	Orientation distribution function
pK_a	Acids dissociation constant
PDF	Powder diffraction file
R	Gas constant
ROI	Region-of-interest
SAED	Selected area electron diffraction
SE	Secondary electrons
SEM	Scanning electron microscope
t	Time
T	Temperature
TEM	Transmission electron microscope
TGA	Thermogravimetry analysis
TKD	Transmission Kikuchi diffraction
XEC	X-ray elastic constants
XPS	X-ray photoelectron spectroscopy
XRD	X-ray diffraction
z	Number of electrons

Table of Content

1 Introduction

The degradation of materials during mechanical loading, like for example for bearings, is one of the key issues that surface engineering attempts to solve. Electrochemical deposition as a rather efficient, industrially feasible and widely applied process provides a huge potential for numerous engineering applications. Although not being one of the most traditional materials synthesized by electrochemical deposition, the deposition of iron-based coatings is a promising alternative to bulk steel components requiring extensive surface treatments for strengthening, and will allow the changeover to more environmental friendly coatings compared to the presently predominant hard chrome coatings that from 2017 require authorization to be used for a specific purpose.

REACH (Registration, Evaluation, Authorization and Restriction of Chemicals Regulation) is the regulation of the European Union, adopted to improve the protection of human health and the environment from the risks that can be posed by chemicals. Substances of very high concern will gradually be identified in the ECHA 'candidate list' and finally included in annex XIV of the REACH Regulation. The chemical used to electrodeposit hard chrome coatings is chromium trioxide (CrO_3), which has been marked with the properties of concern of being carcinogenic and mutagenic, and is suspected to be toxic to reproduction, skin sensitizing and respiratory sensitizing. The imposed risk by chromium trioxide to both the environment and the people handling this chemical represents a threat and it was therefore included in the COMMISSION REGULATION (EU) No 348/2013 of 17 April 2013, with the description "*Chromium trioxide meets the criteria for classification as carcinogenic (category 1A) and mutagenic (category 1B) in accordance with Regulation (EC) No 1272/2008 and therefore meets the criteria for inclusion in Annex XIV…"*. When substances are listed in the annex, they cannot be marketed or used after a specified date (the so-called 'sunset date'), unless permission is given.

The application date for transitional arrangements when using chromium trioxide was the 21. March 2016 and the sunset date was the 21. September 2017, meaning that a company using chromium trioxide in its production must find a supplier who has received an authorization to use chromium trioxide. Otherwise, the company had to stop its production in September 2017. The rules underlying the authorization shall be respected, meaning that a company cannot buy chromium trioxide from a supplier for a specific purpose and then use the chemical for another. The risk to multiple sectors of industry is that their supplier does not receive the authorization to produce hard chrome coatings, and they will lack the possibility of protecting expensive components from wear and corrosion with a well-known coating that has been tested and used for years.

The Danish Working Environment Authority released a press message on the 4. February 2020, that the thresholds limit for chrome(VI) will be lowered from 0.005 mg/m^3 to 0.001 mg/m^3 on the 1. June 2020 and they will evaluate after four years whether the limit should be reduced further to 0.00025 mg/m^3. It is currently not fully clear how this will affect the cost of operation for the Danish hard chrome industry. Therefore, it is necessary to investigate alternative surface treatments based on environmental friendly chemicals that could be possible candidates to replace hard chrome in all aspects or within smaller fragments of the marked that hard chrome coatings are covering. At present, an all-round alternative has not been found yet.

This thesis will pay special attention to an electrodeposited Fe-C coating developed by a Japanese group decade ago and provide solutions to the challenges that are related to the long-term operation of the deposition process for industrial applications. The thesis furthermore aims at understanding the internal structure and associated properties of the Fe-C coatings in relation to both the deposition process and post-deposition annealing. The devotion to this coating is based upon its simple electrolyte consisting of in-expensive non-toxic chemicals with high abundance and the ability to produce a thick coating with a hardness similar to that of traditional hardened steel. A limitation of the Fe-C coating compared to hard chrome coatings is the lack of corrosion resistance, as the Fe-C coating cannot produce a stable passivating film in humid or aqueous environments. However, this is not a matter of concern for applications in lubricating atmosphere, where the material is protected from corrosion by other means.

Based on the present knowledge from literature, which is limited as the Fe-C coatings have been used mainly by the Japanese group and only recently experienced some revival, the thesis further develops the electrochemical deposition process of the Fe-C coatings and reveals the ideal operation conditions that ensure a high deposition rate, current efficiency and the ability to reproducibly deposit coatings with a homogenous appearance and predictable properties. This also includes the deposition on different substrates and a systematic study of appropriate pre-treatments of the substrate surface.

As the understanding of the internal structure of the Fe-C coatings is crucial for industrial applications, but widely lacking or inconsistent in literature, the thesis systematically investigates both as-deposited coatings and coatings after dedicated post-deposition annealing. To this end, complementary methods of materials characterization are applied with the particular focus on the in-situ annealing analysis of the evolving microstructure as a function of time and temperature. The revealed chemical composition, phase constitution and microstructure are related to the microhardness, as an important parameter for the performance of Fe-C coatings under mechanical loading and wear attack. The adhesion between the Fe-C coating and the substrate is an essential parameter for a wear resistant coating and a simple method without the need of specific instrumentation is suggested and tested to reproducibly estimate the adhesion towards any potential substrate.

Based on the obtained results from systematic electrodeposition on laboratory scale, the thesis includes suggestions for up-scaling the process for industrial large-scale deposition, which opens up for the next step towards testing and implementation of the Fe-C coatings in industry.

2 Literature review

The literature review is authored to acknowledge relevant research and to highlight what has previously been published on the subject of electrodeposited iron-based coatings.

The literature review should provide the reader with the required background knowledge to understand the experimental starting point and reasoning for the investigation of certain aspects in the present thesis about either the operational conditions or material characteristics that have not yet been fully understood and are discussed differently in literature.

A short introduction of the general concept of electrodeposition and the influence of the operation conditions on the resulting microstructure of the deposit will be given prior to the review on iron-based deposition to clarify certain terminology. The theoretical and practical application of the fundamentals of electrochemical deposition will be based on textbooks on the subject and Rene Winand's work on electrocrystallization [1–3].

2.1 Electrochemical deposition

Electrodeposition is a widely used process for both scientific and industrial purposes of depositing metals on a workpiece to change the surface properties with respect to, for example, wear resistance, corrosion resistance, decorative appearance or solderability. The quote from Rene Winand "*There is no true "theory" of electrocrystallization*" [2] can be bleak for the theoretician but encourage the experimentalist. Although, the work presented in this thesis will be experimental, it is required to understand the several factors that interact with the charge transport in the electrolyte and influence the deposition, and, thus, the resulting properties of the coated surfaces.

2.1.1 The electrochemical cell

It is important to introduce the main components used in electrodeposition before expanding on the theoretical presentation of the separate elements linked to the nucleation and growth of the metal structure.

A main component for electrochemical deposition is the electrolyte. The electrolyte is the medium in which the reduced metal ions are dissolved and it can be based on aqueous, organic and fused salts. This work will only include the aqueous electrolyte. The aqueous electrolyte is produced by mixing a soluble metallic salt with water. The reduction of the dissolved metal ions in the electrolyte at the surface of a workpiece requires an electron source as shown by the half cell reaction in Equation (1).

$$\mathrm{Me}^{z+} + z\mathrm{e}^- \rightarrow \mathrm{Me} \quad (1)$$

The types of electron source for the reduction of the metal ions can be divided into two categories: electrodeposition and electroless deposition. An external power supply provides the electrons in electrodeposition. A reducing agent in the electrolyte acts as the electron source in electroless deposition. This work will only include electrodeposition and the principle of a typical setup of an electrochemical cell is shown in Figure 1. The electrochemical cell consists of the aqueous electrolyte with dissolved metal ions (M^{z+}) and some electrodes. The external amplifier supplies a direct current (DC) through the wires connected to the electrodes, which are partially submerged in the electron conductive electrolyte. The electrodes will either be positively or negatively charged and are labeled anode (+) and cathode (-), respectively. The anode functions as the electron source through the simplified half cell reaction for a sacrificial anode as shown in Equation (2).

$$\mathrm{Me} \rightarrow \mathrm{Me}^{z+} + z\mathrm{e}^- \quad (2)$$

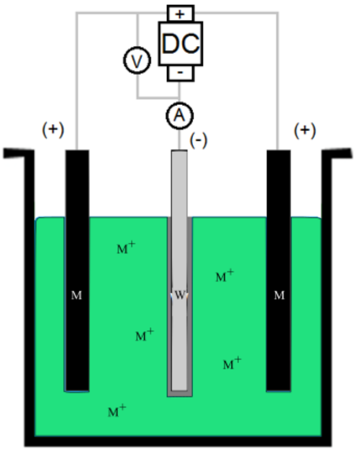

Figure 1: Illustration of the electrochemical cell.

2.1.2 The equilibrium electrode potential

The equilibrium within the electrochemical cell is shortly described with the absence of an external voltage or electric current to define the influence of the operation conditions prior to deposition.

The half-cell reactions described in Equation (1) and (2) will run simultaneously on the electrode/electrolyte interface until there is no net transformation of matter. A net charge between the electrode and the electrolyte will develop if the potential of the system promotes one of the half-cell reactions. A negative charge on the electrode will attract positively charged ions from the solution and repel the negatively charged ones. The charged interface between the electrode and the electrolyte is called the double layer [1,3].

The equilibrium potential is achieved when the reduction (Eq 1) is proceeding at the same rate as the oxidation (Eq 2). The concentration dependence of the equilibrium electrode potential ($E_{\text{equilibrium}}$) at the interface between the metallic electrodes and the electrolyte of a certain ionic concentration can be expressed by the Nernst equation as shown in Equation (3).

$$E_{\text{equilibrium}} = \mathrm{E}^0 + \frac{R \cdot T}{z \cdot F} \cdot \ln\left(\frac{Ox}{Red}\right) \tag{3}$$

where E^0 is the standard electrode potential, R is the gas constant, T is the electrolyte temperature, z is the number of electrons in the half cell reaction, F is Faradays number and Ox/Red is the ratio of oxidized to reduced elements.

The standard electrode potential for iron (Fe^{2+}) is -0.44 V in an aqueous solution having a pH-value of 7, a temperature of 25 °C and a Fe^{2+} concentration of 10^{-6} mol/L [4].

The Pourbaix diagram is used to illustate the thermodynamically stable phases of an aqueous electrochemical system as a function of the eqilibrium potential and the pH-value; the example for iron is shown in Figure 2.

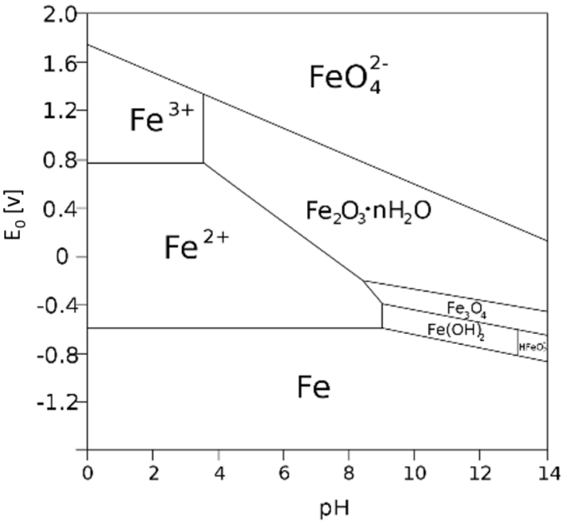

Figure 2: Pourbaix diagram for iron at 50 °C [5].

2.1.3 Mechanism of electrodeposition

The introduction of an external electric current on the electrodes will change their potential and depending on the charge they will function as anode (+) or cathode (-).

The overpotential (η) is described as the difference between the equilibrium electrode potential and the potential of the same electrode in the presence of an external current (E(I)) [1].

$$\eta = \mathrm{E(I)} - E_{\text{equilibrium}} \tag{4}$$

The total overpotential is a complex parameter that can be separated into the terms: charge transfer overpotential (η_a), diffusion overpotential (η_d), reaction overpotential (η_r) and crystallization overpotential (η_k).

$$\eta = \eta_a + \eta_d + \eta_r + \eta_k \tag{5}$$

- The charge transfer overpotential is defined by the rate of a charge (Me^+ or e^-), which is transferred across the double layer.
- The diffusion overpotential is defined by the rate of diffusion of ions involved in the overall partial electrode reactions.
- The reaction overpotential is defined by the partial chemical reaction rate.
- The crystallization overpotential is defined at the atomic level, thus, which atoms are either incorporated into the growing film on the cathode or removed from the electrodes.

The transfer of an electron across the double layer is normally not the limiting factor in electrodeposition and the charge transfer overpotential can be overcome by adjusting the applied voltage [5].

The concentration profile as a function of the distance (δ) from the cathode/electrolyte interface is illustrated in Figure 3.

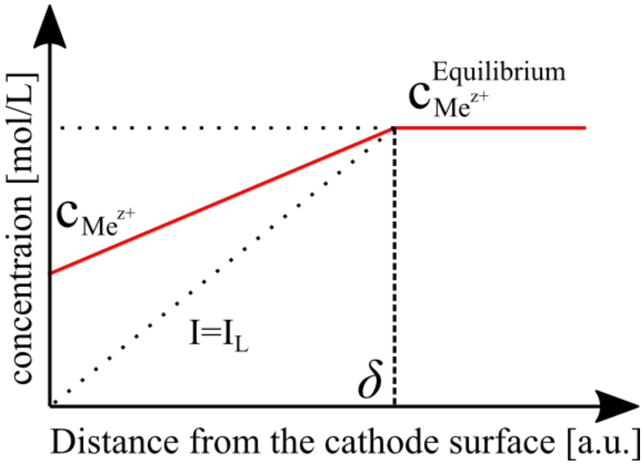

Figure 3: Illustration of the concentration profile near the interface between the cathode and electrolyte, Figure from [1]. $c_{Me^{z+}}^{Equilibrium}$ *is the equilibrium concentration when no current is applied,* $c_{Me^{z+}}$ *is the concentration of reacting substances at the cathode/electrolyte interface,* I_L *is the limiting current and* δ *is the distance of the diffusion zone from the cathode surface.*

The cathode/electrolyte interface will be depleted for reacting substances when the limiting current is applied and the deposition will be interrupted without a continuous diffusion of new metal ions towards the cathode/electrolyte interface. The limiting current should be avoided since it can lead to hydrogen and hydroxide development by the partial reaction as described in Equation (6).

$$2H_2O + 2e^- \rightarrow H_2(g) + 2OH^- \tag{6}$$

The formation of OH^- will locally increase the pH-value in the diffusion zone and can influence the deposition. There are several methods to avoid the concentration overpotential as a limiting factor like, increasing the metal ion concentration in the electrolyte, applying a lower current density, increasing the electrolyte temperature (increases ion diffusion, but also reaction rate) or applying stirring/agitation to the electrolyte.

The crystallization overpotential is difficult to investigate as it is necessary to take into account the local distributions of current densities, the concentration of reacting substances at the electrode/electrolyte interface and the inhibition intensity at the electrode [2]. The term inhibition relates to the presence of substances (molecules, atoms or ions) different from the reacting substances that hinder the cathodic process [2,6].

There are four main contributions for inhibition of the cathodic process [2].

1. A negative catalyst of a reaction that limits the crystallization overvoltage.
2. A simultaneous reduction of an inhibitor that decreases the resulting current density of the reacting substances and can lead to contamination of the deposit by decomposition of residues of the inhibitor species.
3. A change in the metallographic or crystallographic structure of the growing coating.
4. A change in the different types of overpotential as described above.

2.1.4 Nucleation in electrocrystallization

The experimental difficulties of evaluating the individual contributions to the total overpotential are evident and using the total overpotential as a single parameter disregards the correlation to the observed phase constitution of the deposit [2].

A detailed diagram showing the morphology of the deposits as a function of two parameters was established by Rene Winand and is shown in Figure 4 [2]. The morphologies of the deposit are divided into five main growth types:

1. Basis-oriented reproduction type (BR), being a lateral growth producing large crystals
2. Field-oriented isolated crystal type (FI), being whisker, dendrites or powder deposits
3. Twinning intermediate type (Z), being an intermediate morphology between the basis-oriented reproduction and the field oriented texture type
4. Field oriented texture type (FT), being a large number of elongated crystals perpendicular to the substrate
5. Unoriented dispersion type (UD), being a large number of small grains forming a coherent deposit

The first operation parameter ($J/\mathrm{c}_{\mathrm{Me}^{z+}}^{\mathrm{Equilibrium}}$) is the ratio between the applied current density (J) and the equilibrium metal ion concentration ($\mathrm{c}_{\mathrm{Me}^{z+}}^{\mathrm{Equilibrium}}$) in the electrolyte and the second operation parameter is the inhibition intensity. No deposition will occur when both parameters are low as a lack of local current density. A general trend is that increasing one of the parameters will result in an increased nucleation rate, which consequently decreases the average grain size. Increasing both parameters simultaneously will result in hydrogen evolution at the cathode surface.

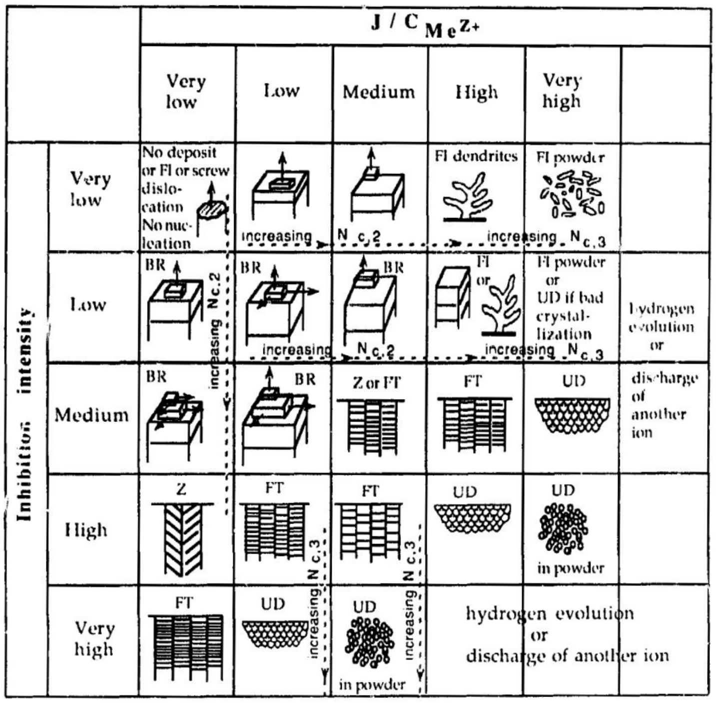

Figure 4: Detailed diagram of the possible types of polycrystalline electrodeposits as a function of current density/ion concentration and inhibition intensity. Figure from [2].

The benefit of the diagram shown in Figure 4 is that the total overpotential can be estimated based on the morphology of the deposit and the operation conditions can be adjusted to obtain the specific material properties, which are demanded for a certain application.

2.1.5 Current efficiency

The current efficiency of the system is important to estimate as it can reveal if a partial reaction is proceeding during deposition and is consuming electrons that otherwise would have contributed to the desired growth of the deposit by reducing the preferred metal ion. The current efficiency can be calculated by dividing the mass gain of the deposited sample with the theoretical mass gain that is possible using the specific operation conditions. The theoretical mass gain can be calculated according to Faraday's first law in Equation (7) [1].

$$m = \frac{I \cdot t \cdot M}{z \cdot F} \tag{7}$$

where m is the theoretical mass gain, I is the applied current, t is the deposition time, and M is the molar mass.

The thickness of the coating can also be used to estimate the current efficiency as the theoretical mass calculated by Equation (7) can be converted to the deposits thickness using the density of the metal being deposited and the surface area of the cathode. The current efficiency measured using the thickness of the deposit assumes that the current is homogenously distributed on the cathode surface, which is rarely the case.

2.1.6 Metal classes, inhibitors and additives

In general, the electrodeposition of different metals can be considered in three groups according to [2];

- Normal metals (Zn, Ag…) having a low melting point, low charge transfer overpotential, low surface tension, high hydrogen overvoltage and show a low tendency to adsorb inhibitors.
- Intermediate metals (Au, Cu…) having a moderate melting point, medium charge transfer overpotential and show a medium tendency to adsorb inhibitors.
- Inert metals (Fe, Ni, Cr…) having a high melting point and a high charge transfer overpotential, a high surface tension, a low hydrogen overvoltage and show a strong tendency to adsorb inhibitors.

The regular types of inhibitors that deliberately can be applied to the electrolyte can be separated into inorganic cations and anions. The cations (Na^+, K^+, Ca^{2+}…) are not dischargeable at the cathode and have a small effect. The anions (Cl^-, SO_4^{2-}, BF_4^-) can influence the charge of the double layer and affect the charge transfer overpotential. It has been observed that the inert metals can form adsorbed layers of metallic hydroxides (MeOH), which provide inhibition even in the absence of added inhibitors in the electrolyte [2].

Organic additives are also commonly added to an electrolyte. They fulfil multiple purposes and have various effects as grain refinement, levelling of the surface or reduction of internal stress in the coating [5]. The influence of the organic additives depends strongly on their affinity to water and whether they are adsorbed on the cathode.

- The organic additive will act as a strong inhibitor if it has no affinity to water and is strongly adsorbed at the cathode.
- The organic additive will give a small inhibition and acts as an activation agent if it is adsorbed at the cathode and has affinity to water.
- The organic additive will act as an activation agent if it is not adsorbed at the cathode and has affinity to water.
- The organic additive will have no effect if it is not adsorbed at the cathode and has no affinity to water.

Summary

The fundamentals of electrochemical deposition have been briefly described above and could be elaborated in more detail. The quote from Rene Winand "*There is no true "theory" of electrocrystallization*" seems to be accurate, but that does not mean that there is a lack of theory or understanding of each factor that accumulates to the electrochemical deposition of a metal. It is not the intention of the thesis to thoroughly investigate the influence of the various operation parameters on the individual overpotentials in the interface between the electrodes and the electrolyte, but to apply the practical understanding of the correlated effects detailed in Figure 4.

2.2 Electrochemical deposition of iron

The iron based electrodeposition has been conducted from countless variants of electrolytes normally based on either (1) an iron-sulfate bath, (2) an iron-chloride bath or (3) a mixture of iron-sulfate and iron-chloride baths [7,8]. The list of specific additives in the electrolyte containing both organic and inorganic salts is endless and the addition may improve the properties of the deposit and/or the operation conditions. The first method for electrodeposition of iron-based materials was reported over a century ago and has later been used for multiple purposes as purification of iron, wear protection, renovation of worn components or simply for a scientific interest. A historical review is well described in "The Metal – Iron" from 1935 by H.E Cleaves and J.G. Thompson and will be shortly summarized below [7].

The first reported preparation of iron by electrodeposition was in 1831 by Becquerel and was investigated for decades for a scientific curiosity [9]. In 1858 Garniers had patented a process for preparing electrotypes based on iron deposited on copper and later in 1869 the Russian Mint prepared bank notes printed using electrolytic iron electrotypes by a process developed by Klein [10,11].

A series of papers was published by Watt in 1887-1888 and listed 44 different electrolytes for the deposition of iron with the addition of both organic and inorganic salts [12]. Watt recommended the addition of a small dose of citric acid or tartaric acid for electrodeposition of iron and later Vie suggested that the formation of basic precipitates could be prevented by the addition of citric acid and sulfuric acid to the electrolyte [13].

The effect of the operation conditions for the electrodeposition of iron was published by Lee already in 1909 [14] and a brief summary of the results showed that:

- The hydrogen content and current efficiency increase as a function of temperature.
- The deposition rate and hydrogen content increase as a function of current density.
- The current efficiency and hydrogen content decrease as a function of acidity.
- The hardness of the deposit increase as a function of acidity and current density.
- The increase in hardness was associated with a reduction of the crystallite size.

A more recent description of the state of electrodeposition of iron and iron alloys is given in chapter 11 in Modern Electroplating by M. Izaki [8], who also authors multiple publications on Fe-C coatings based on an iron-sulfate electrolyte with the addition of citric acid and ascorbic acid [8,15–21]. The mentioned chapter in the book also includes a brief historic review of iron deposition and purposes, along with multiple bath compositions for both pure iron deposition and iron alloy deposition for specific functions. However, as is described very clearly by Izaki *"a significant problem with iron and iron alloy plating that has limited its* *usage to specialized or high-volume applications is that, despite usually lower costs for anodes and solutions, the expenditure for capital equipment and maintenance may be higher for an iron plating bath than for other more commonly used plating baths. Special high-temperature or corrosion-resistant equipment may be required to heat, agitate, filter, or ventilate the iron plating bath. Also, unless used regularly, the solution will oxidize gradually. The time and effort required to restore the electrolyte to an operable condition may outweigh the economic benefit of depositing a lower cost metal."* [8].

As described by M. Izaki, the use of iron in the oxidation state Fe^{2+} is desired as the presence of Fe^{3+} even in small amounts in the electrolyte will lower the current efficiency and cause the deposit to be brittle, stressed and pitted [8]. However, it is difficult to suppress the formation of Fe^{3+} completely as it is thermodynamically favorable for Fe^{2+} to oxidize to Fe^{3+} in the presence of air. The management of the operation conditions will be discussed in detail along with the partial reactions proceeding during the iron deposition in Section 8.3 to investigate how an iron-based system could function when the process is intended to be up-scaled for industrial use.

2.3 Electrochemical deposition of iron-carbon

The present review will only pay attention to the deposition of iron-carbon coatings from an iron-sulfate electrolyte with the addition of organic acids that function as complexing agent, carbon source and buffer. The Fe-C coatings are based upon its simple electrolyte consisting of non-toxic chemicals widely available and the ability to produce a thick coating with a hardness around 800 HV. The iron-carbon system was developed by Izaki et al. [15] and has been investigated by several authors to understand the various process parameter's influence on the resulting properties [17,22–25]. However, the effect of a single process parameter is difficult to evaluate because of the synergetic effect of the whole deposition conditions.

In the literature review below, the operation conditions of the system such as electrolyte composition, temperature, pH-value and current density are provided for the individual presented results to be able to consider the correlated effects.

The review will be divided into subsections. The first subsection will describe the current understanding of the materials properties of the Fe-C coatings and the different interpretation of some characteristics. The second subsection will describe the influence of the individual operation conditions on the resulting materials properties.

2.3.1 Material characterization of iron-carbon coatings

The material characterization of the Fe-C deposits will address the characteristics of the coating such as the appearance, grain size, morphology, chemical composition, co-deposited phases and temperature stability in order to interpret the mechanical properties and how to improve these. The presented results will be sorted such that only results from the coatings that have a prospect of being applied in operation will be taken into account. The results of the review will afterwards be interpreted and differences in the assessments of similar results will be explained.

2.3.1.1 Appearance, microstructure and morphology

The macroscopic appearance of the Fe-C coating is described as smooth dark-grey and mirror-bright [17,19,21]. The microstructure is fine-grained and cannot be resolved using a light optical microscope (LOM). The nanocrystalline microstructure consists of needle-like grains elongated along the growth direction as shown in Figure 5 [17,18,24,25]. The nanocrystalline grains are observed throughout the deposits without a considerable change over the film thickness for the Fe-C coatings. The average grain sizes are about 20 nm in the short axis and have an aspect ratio of approximately two to three [25].

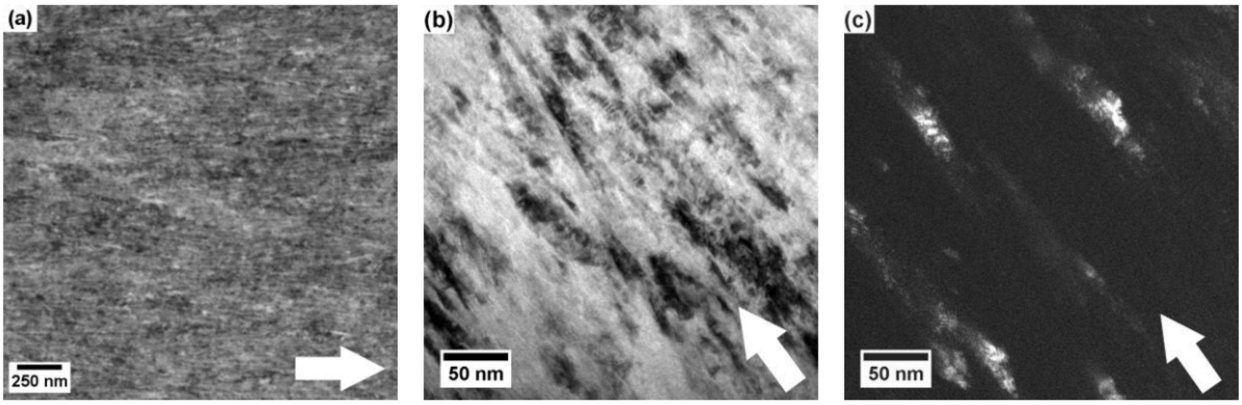

Figure 5: (a) Scanning electron microscopy micrograph of the microstructure of an as-deposited Fe-C coating in cross section using the backscatter-electron detector. Electrolyte composition of $FeSO_4$, tri-sodium citrate, ascorbic acid, sodium sulfate, temperature of 50 °C, pH-value of 4.2 and current density of 3 A/dm^2; Transmission electron microscopy micrographs using (b) Bright-field and (c) dark-field of an as-deposited Fe-C coating in cross-section. Electrolyte composition of $FeSO_4$, tri-sodium citrate, ascorbic acid, sodium sulfate, temperature of 65 °C, pH-value of 4.2 and current density of 5 A/dm^2. The white arrows indicate the growth direction. Figure from [25].

2.3.1.2 Chemical composition

The chemical composition of the Fe-C coating has been investigated using different techniques as X-ray photoelectron spectroscopy (XPS), evolved-gas-analysis, mass spectrometry (MS) and shows that the Fe-C coating consists of iron and the light elements hydrogen, carbon and oxygen are being co-deposited during deposition [17,24–26]. The content of each co-deposited element in the coating differs depending on the operation conditions applied during deposition as will be discussed in Section 2.3.2 and causes a large variation in the published results. Further, a quantified measurement of only either one or two of the three co-deposited light elements is usually included in a publication and hinders a thorough analysis and comparison.

The average carbon content is measured to be around 0.6 to 1.2 wt% [17,21,24–26]. The oxygen content is measured around 0.5 to 1.2 wt% [17] and the hydrogen content is measured to 0.01 to 0.08 at% or 0.0015 to 0.014 wt% [24]. The maximum solubility of the carbon, oxygen and hydrogen in ferrite (α-Fe), assuming binary alloys, can be found in the ASM handbook of alloy phase diagrams and is presented below to put these values into perspective.

- The solubility of carbon in ferrite is 0.021 wt%
- The solubility of oxygen in ferrite is ≈ 0 wt%
- The solubility of hydrogen in ferrite is 0.00025 wt%

The measured content of all the light elements exceeds their solubility in ferrite by a significant amount and the review related to the co-deposition, chemical nature and position of the elements in the microstructure will be continued below and in the following sections.

The incorporation of hydrogen is undesirable in hard materials as it increases the risk of failure through hydrogen embrittlement. Annealing the material at low temperature is strongly recommended to desorb the incorporated hydrogen before the deposit is put into operation. The desorption of the hydrogen at low temperature assumes that the hydrogen is trapped at the conventional sites within the microstructure being grain boundaries, dislocations or microvoids

[27]. The desorption of hydrogen from the Fe-C deposit has been measured in-situ to proceed from the expected trapping site (≈100 °C), and also at temperatures higher than predicted (360 °C) [24]. The high temperature desorption has resulted in the interpretation that hydrogen is also co-deposited in the form of vacancy–carbon–hydrogen clusters [24].

The chemical state of the deposited elements iron, carbon and oxygen has been investigated by XPS as shown in Figure 6 [17,18,26]. The results revealed that the peak for metallic Fe has a shoulder to higher binding energies that can be assigned to the presence of FeO and FeOOH. The peaks from oxygen originate from Fe_2O_3 and FeO. The carbon spectrum showed peaks that can be attributed to carboxyl groups, hydrocarbons or graphite and carbides.

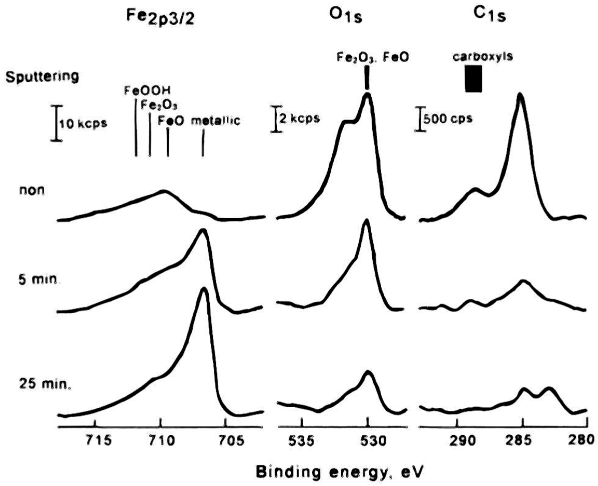

Figure 6: XPS spectrum of $Fe2_{p3/2}$, $O1_{1s}$ and $C1_s$ regions of a coating with 0.56 wt% carbon. Electrolyte composition of $FeSO_4$ and succinic acid, current density of 1.0 A/dm^2, pH-value of 2.4 to 3.6 and temperature of 50 °C. Figure from [17].

2.3.1.3 Phase analysis

X-ray diffraction (XRD) phase analysis of the as-deposited Fe-C coatings has been applied to investigate, which phases form during deposition [16–19,21,23–26,28].

The peak positions of ferrite α-110, α-200 and α-211 are indicated in Figure 7 [18] and there are no peaks related to oxides, carbides or austenite in the diffraction patterns. According to [18,19,21], the breadths of the diffraction peaks are increased with increasing carbon content in the deposit and a slight asymmetry was said to be measured with reference to the enlargements of the α-200 and α-211 peak profile. The asymmetry and breadth of α-200 and α-211 was suggested to be an effect of an elongation of the c-axis in the ferrite bcc unit cell converting it to a bct. The c/a ratio was estimated to 1.005 for a Fe-C coating having a carbon content of 1.0 wt% [16–18]. This elongation of the c-axis is said to point towards a martensitic or tempered martensite microstructure [18,19,21,23,26,28,29]. The presented figures and data related to the interpretation of the α-Fe peaks profile [18,19,21], do not allow the reader to make a judgement of analysis that supports the presented results. The enlargements of the α-200 and α-211 shown in Figure 7 show that the peaks are broad but do not allow the reader to conclude on the peaks symmetry. The interpretation that the breadth of the α-Fe peak is solely related to peak splitting is ambiguous and would require a comprehensive description of the peak fitting procedure. Further, a XRD pattern of freshly quenched iron-based martensitic microstructure having a carbon content of 1.0 wt% (comparable to the one in Fe-C coatings) would however measure two separate peaks with a certain distance and the c/a ratio would be 1.098 [30]. A XRD pattern of tempered iron-based martensitic microstructure having a carbon content around 1.0 wt% would have a lower c/a ratio along with diffraction peaks related to either η/ε-Fe_2C or θ-Fe_3C depending on its tempering stage [31,32].

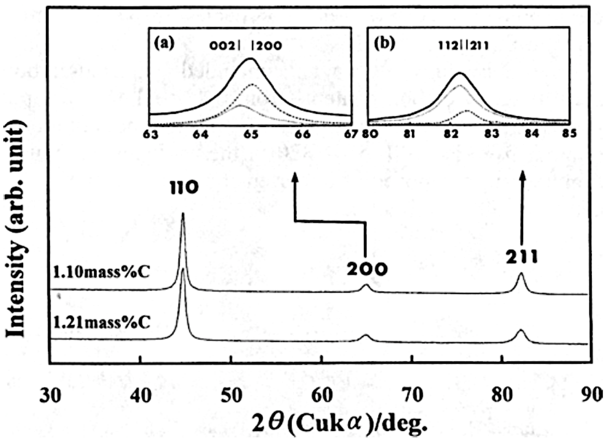

Figure 7: X-ray diffraction pattern of coatings with the indicated carbon content. Electrolyte composition of $FeSO_4$, citric acid and ascorbic acid, temperature of 50 ℃, pH-value is not provided and a current density of 2 and 3 A/dm^2. Figure from [18].

The as-deposited microstructure of the Fe-C coating having broad α-Fe peaks, also with a stated slight asymmetry, was measured along with a single additional peak of low intensity positioned at lower diffraction angles compared to the α-110, but not being ferrite as shown in Figure 8 [25,26]. The thermal evolution of the Fe-C coating as shown in Figure 8 will be discussed in Section 2.3.1.4. The phase identification of the additional peak in the as-deposited coating was based on the position of that single peak, the carbon content of nearly 1 wt% and the c/a ratio of 1.005 [18] for the peaks related to α-Fe and was suggested as ε-Fe_2C by Haseeb et al. [26]. However, a distinguishing between the two similar types of transition carbides (ε-Fe_2C and η-Fe_2C) is not possible as both have a diffraction plane matching the d-spacing related to the position of the additional peak [33]. The state of the Fe-C coatings was suggested as tempered martensite based on the presence of the suggested transition carbide and the c/a ratio measured for the peaks related to α-Fe [26]. However, the presented figure and data related to the interpretation of the α-Fe peak profiles [26], does not allow the reader to make a judgement of analysis that supports the presented results. The peak overlap with the copper substrate for the α-110 (cf. Figure 8) requires a detailed description of how the overlapping peaks are fitted separately and how the asymmetry is determined. A XRD phase identification requires at least three diffraction peak from the same phase to be unambiguous. The declaration in [26] that the microstructure of the Fe-C coatings is tempered martensite, based on the carbon content and an inadequate phase identification of η/ε-Fe_2C is problematic and does not take into account the presence of oxygen or hydrogen.

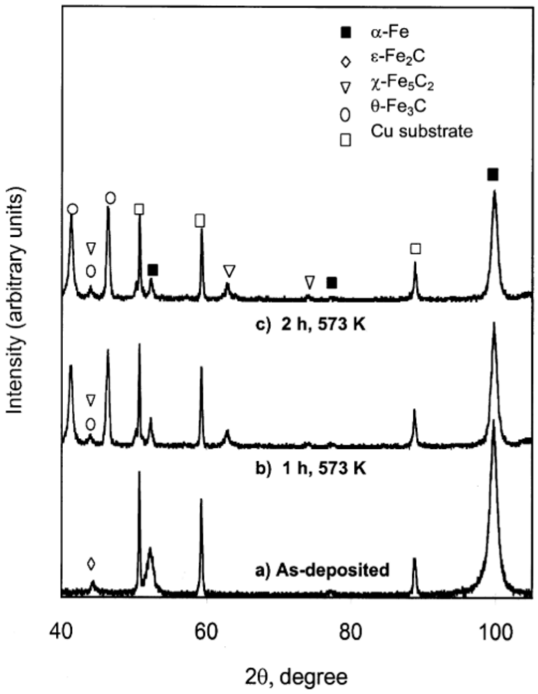

Figure 8: X-ray diffraction pattern of Fe-C coating with a carbon content of 0.96 wt%: a) as- deposited, b) tempered at 300 °C for 1 hour, and c) tempered at 300 °C for 2 hour. Electrolyte composition of $FeSO_4$, citric acid and ascorbic acid, temperature of 50 °C, pH-value is 2.5 and a current density of 2 A/dm^2. Figure from [26].

2.3.1.4 Thermal stability

The reason for exposing a deposit to elevated temperatures under controlled condition can be either to stabilize the microstructure and ensure that it does not evolve during operation conditions and/or to investigate its evolution through phase transformations and grain growth. The thermal evolution of the Fe-C coatings has been investigated in-situ and ex-situ using different techniques as XRD and differential scanning calorimetry (DSC) [16,24–26,29].

The thermal evolution of a Fe-C coating was investigated ex-situ using XRD phase analysis with the resulting diffraction patterns shown in Figure 8 and revealed that additional peaks developed during heating and these were suggested to match different carbides. After exposure to a temperature of 300 °C for 1 or 2 hours [26], the carbides χ-Fe_5C_2 and θ-Fe_3C were suggested to have formed from ε-Fe_2C, which Haseeb et al. state to be present in the as-deposited coating [26]. The suggested phase transformation of the meta-stable ε-Fe_2C to χ-Fe_5C_2 and finally θ-Fe_3C is what can be expected at elevated temperature for these carbides in steels [33]. However, the presence of oxygen was measured by XPS in the Fe-C coating [26], but the identification of oxides was not included in the phase analysis although matches would be possible. In the same study, the Fe-C coating was also investigated in-situ using DSC and the results are shown in Figure 9 for the first and second thermal cycle to 900 °C of the same sample [26]. There are two events measured around 100 °C and 360 °C on the first thermal cycle. The first exothermic peak was suggested as the formation for ε-Fe_2C and the second exothermic peak was related to the transformation of ε-Fe_2C into θ-Fe_3C. There were no further transformations recorded in the second heating cycle. Alternatively to the interpretation in [26], the two thermal events presented in Figure 9 match the temperature range of the low temperature (≈ 100 °C) and high temperature (≈ 360 °C) desorption of hydrogen measured by Fukumuro et al. [24], as described in Section 2.3.1.2. The desorption of hydrogen was not taken into account by Haseeb et al. [26] when evaluating the first or second exothermic peaks as their instrumental setup did not include a MS. The overall evaluation by Haseeb et al. [26] of the microstructure of the Fe-C coatings solely concerns iron and carbon, although their XPS measurements reveal the presence of oxygen by an asymmetric peak, which, as they suggest, indicates the presence of a hydroxide [26].

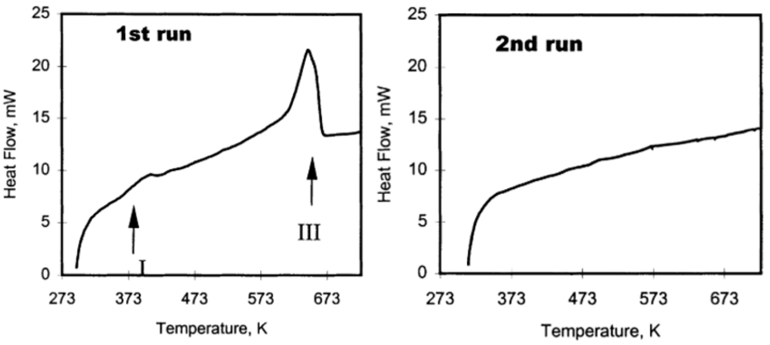

Figure 9: DSC curves of Fe-C coating with 0.96 wt% carbon annealed using a heating rate of 10 K/min in Ar atmosphere. (a) First cycle on as-deposited sample. (b) Second cycle. Electrolyte composition of $FeSO_4$, *citric acid and ascorbic acid, temperature of 50 °C, pH-value is 2.5 and a current density of 2* A/dm^2. *Figure from* [26].

A more recent study by Müller et al. [25], investigated the increase in hardness and the microstructure evolution as a function of annealing temperatures as shown in Figure 10 and Figure 11. The as-deposited microstructure of the Fe-C coating was measured as ferrite having a bcc crystal lattice and the additional peak, not being ferrite, is measured at a lower diffraction angle compared to α-110. The strong crystallographic texture of the as-deposited Fe-C coating complicated the phase analysis and no phase identification was proposed by Müller et al. for the additional peak [25]. The Fe-C coating exhibits a strong fiber texture with a <211> fiber axis in growth direction, according to a full texture measurement. The experimental details for the full texture measurement are not provided by Müller et al. nor are the measured pole figures or inverse pole figure.

The microstructure evolution for the isothermally annealed deposit showed that peaks related to magnetite (Fe_3O_4) were measured for an annealing temperature of 300 °C and cementite (Fe_3C) precipitates when the temperature was increased to 400 °C (see Figure 10) [25]. The annealings were performed for 1 hour under a pressure of about 10^{-5} mbar in a vacuum tube furnace to avoid oxidation with the atmosphere.

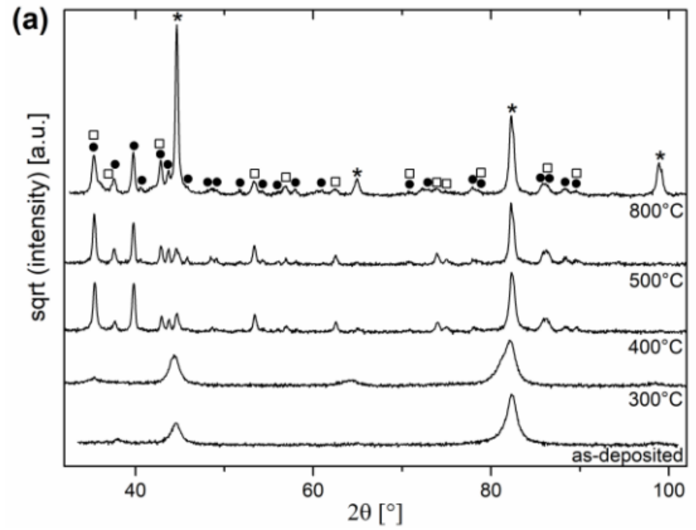

*Figure 10: X-ray diffraction patterns of coating with 1.0 wt% carbon before and after isothermal annealing for 1 hour at the indicated temperatures. Bragg peaks of ferrite, cementite, and magnetite are indicated with *, ●, and □ respectively. Electrolyte composition:*$FeSO_4$, *tri-sodium citrate and ascorbic acid, sodium sulfate, temperature of 65 °C, pH-value of 4.2 and current density of 5* A/dm^2. *Figure from* [25].

The hardness of the as-deposited coating was measured around 550-650 HV0.5 and was suggested as a result of the nanocrystalline grain size [25]. The hardness increased to a maximum of more than 800 HV0.5 for all samples when exposed to an annealing temperature of 400 °C. The hardness was found to remain above 500 HV0.5 when the samples were annealed at a temperature of 600 °C [25]. The formation of second-phase carbides and oxides with a significantly higher hardness compared to the iron matrix relates to the observed hardness increase at low annealing temperatures, whereas temperature dependent grain growth may cause the reported hardness decrease when the temperature is increased to above 400 °C [25].

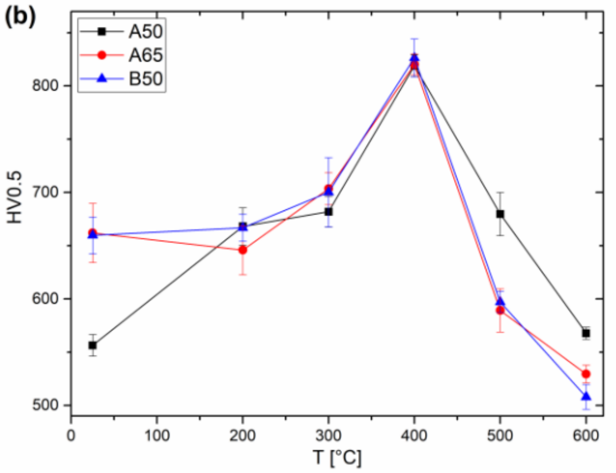

Figure 11: Hardness of Fe-C coatings annealed for 1 hour at the indicated temperatures. Electrolyte composition of A65: $FeSO_4$, tri-sodium citrate, ascorbic acid, sodium sulfate, temperature of 65 °C, pH-value of 4.2 and current density of 5 A/dm^2. Electrolyte composition of A50: $FeSO_4$, tri-sodium citrate, ascorbic acid, sodium sulfate, temperature of 50 °C, pH-value of 4.2 and current density of 3 A/dm^2. Electrolyte composition of B50: $FeSO_4$, citric acid, ascorbic acid, temperature of 50 °C, pH-value of 2.5 and current density of 3 A/dm^2. Figure from [25].

2.3.1.5 Assessment of results from literature

There is an agreement between the results that the microstructure of the Fe-C coating is nanocrystalline with elongated grains having their long axis parallel with the growth direction. The intensity of the individual XRD peaks of α-Fe suggest that the crystallographic texture can vary between coatings deposited under different operation conditions, but a strong fiber texture is common for the results.

The chemical composition of the Fe-C coating revealed iron, hydrogen, carbon and oxygen in quantities above the solubility in α-Fe. Different phases have been suggested based on the application of different methods: The XPS measurements found the phases FeO, FeOOH, Fe_2O_3, carboxyl groups, hydrocarbons, graphite and a peak assigned to carbides, but the presence of these phases has not at all or not clearly been identified in the XRD patterns. All XRD analysis has been performed using symmetric diffraction geometry without tilting the sample around the azimuth angle. A strong preferred crystallographic orientation of ferrite developed during the growth of the deposit and, assuming a preferred orientation for the additional phase (not being ferrite) or even an orientation relation to ferrite, the applied diffraction conditions may not have been appropriate yet for complete phase analysis. The formation of metallic hydroxides (MeOH) during deposition is likely for inert metals as iron [2], but these phases may exist within the microstructure with too low volume fraction for being detected by XRD. The major phase in as-deposited Fe-C coatings has been measured using XRD, but broad peaks with an apparent slight asymmetry resulted in different interpretations of the phase as either ferrite [24,25] or as martensite [17–19,22,23]. The microstructure being ferrite would require, assuming thermodynamic equilibrium, the carbon and oxygen to exist as precipitates within the microstructure. A second phase is measured by XRD as a single additional peak, but an identification based on that single peak is questionable. The identification of either an oxide or carbide would explain the nature of one of the elements, but not the other. The microstructure being martensite would predict the position of the carbon, but the measured carbon content would predict a much larger c/a ratio compared to what is measured. The arguments supporting and opposing either a martensitic or a ferritic microstructure are further discussed in detail in the published articles shown in Section 6.1.1.

The few available results on in-situ thermal analysis interpret the two events at 100 °C and 360 °C as either the third and fifth stages in the tempering of martensite [26] or the desorption of hydrogen adsorbed from electrolysis and the decomposition of vacancy–carbon–hydrogen clusters [24]. These single results are hard to cross-link with the other ex-situ studies to get a consistent view on the Fe-C coatings evolution at elevated temperatures. The formation of both magnetite and cementite during annealing supports the presence of both carbon and oxygen, but the ex-situ annealing measurements conceal the formation mechanisms of these phases. The formation of second-phase carbides and oxides resulted in a significant increase in hardness and offers a huge potential for surface engineering by post-deposition treatment. However, the grain growth at elevated temperature shall be taken into account, as it will result in a decrease in hardness.

The few literature studies and the differently deposited Fe-C coatings certainly cannot provide a full picture and do not allow for a conclusion on the phases present in the microstructure based on the present knowledge. A systematic and more comprehensive analysis is required to cross-link the published results and enable a holistic interpretation of the as-deposited microstructure and the resulting mechanical properties along with their evolution at elevated temperatures.

2.3.2 Influence of the operation conditions on iron-carbon based coatings

The as-deposited Fe-C coating is a result of the combined influence of the multiple operation conditions that intentionally can be adjusted prior to deposition as the current density, ion concentration, agitation, temperature, pH-value, additive and substrate. The direct comparison between the presented results is entangled as the individual studies investigating the influence of the same operation condition are performed with the remaining operation conditions being unalike. This section will first address the understanding of the influence of each of the operation conditions that has been varied. The influence of each of the operation conditions will then be discussed along with the differences between published results and what could have caused these variations. An assessment will be given on what still needs to be investigated to improve the understanding of the effect of the operation conditions on the resulting Fe-C coating.

2.3.2.1 Additives

The influence of the additive on the resulting microstructure and appearance of the Fe-C coatings has been studied with several types of carboxylic acids [17,19,22].

The effect of the type of additive on the coatings' hardness and elemental composition was examined using 12 different organic acids with the aim to find the optimal carbon source to obtain the highest hardness [17]. The carbon content in the deposit increased as a function of the alkyl chain length of the dicarboxylic acid added to the electrolyte as shown in Figure 12a. A similar trend of the increasing carbon content is seen as a function of the alkyl chain length for the monocarboxylic acid, with the exception of butyric acid. The oxygen contents also increased in the deposits from the baths containing an acid with a longer alkyl chain as shown in Figure 12b. The hardness of the deposits changed with the carbon and oxygen content, having a maximum hardness of 850 HV with a carbon content of 0.56 wt% and an oxygen content of around 1.5 wt% [17].

The Fe-C coatings deposited using citric acid being a tricarboxylic acid showed a similar appearance as l-malic acid being black and bright [19]. The carbon content of the deposit was increased from 0.6 to 1wt% and the current efficiency was slightly reduced from 90 to 83 %

for the deposits using l-malic acid or citric acid as additive, respectively [19]. The difference in hardness between deposits is not stated in the publication [19].

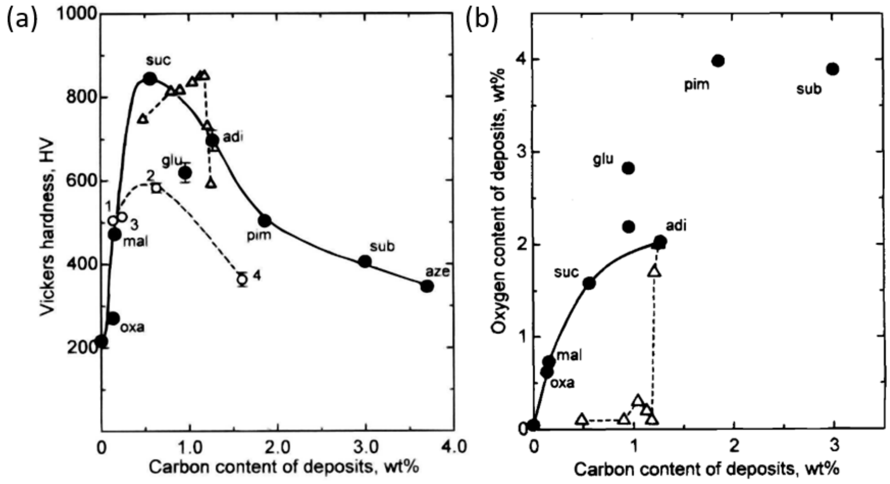

Figure 12: (a) The hardness as a function of the carbon content. (b) The oxygen content and carbon content of the deposits from electrolyte using different additive. (●) Deposits from electrolyte of $FeSO_4$ and with or without dicarboxylic acids with a current density of 1 A/dm^2, temperature of 50 °C and pH-value between 2.4 to 3.6. Additives: oxa = oxalic acid; mal = malic acid; suc = succinic acid, glu = glutaric acid; adi = adipic acid; pim = pimelic acid; sub = suberic acid; aze = acelaic acid. (○) Deposits from the bath with monocarboxylic acids obtained at 1.0 A/dm^2. Carbon source: (1) acetic acid; (2) propanic acid; (3) butanoic acid; (4) n-valeric acid. (Δ) Deposits from an electrolyte with citric acid and L-ascorbic as carbon sources with various current densities. Error bars represent the 95 % confidence limit. Figures from [17].

The influence of the additives citric acid and/or l-ascorbic acid in different amounts and different ratio on the resulting deposit was investigated [22]. The Fe-C coatings deposited with l-ascorbic were brittle and flaked off the substrate after deposition as a results of a high carbon concentration around 2.5 wt%. The Fe-C coatings deposited using citric acid had lower surface roughness and adhered to the substrate and the carbon content amount to around 0.9 wt%. The Fe-C coatings deposited using both l-ascorbic acid and citric acid had a similar appearance as the deposits from a bath containing only citric acid, a carbon content around 1.2 wt% and a hardness measured around 780 HV.

2.3.2.2 Concentration and ratio between $FeSO_4$ and citric acid

The appearance and hardness of the deposits has been examined for a range of current densities using a standard Hull cell and applying different electrolyte compositions where the concentration and ratio between $FeSO_4$ and citric acid were varied [21]. The deposits from the electrolytes with a low $FeSO_4$ concentration looked burnt in the high current density end of the Hull cell and no deposition was obtained in the low current density end. From the electrolyte with high $FeSO_4$ concentration and a low citric acid concentration, the deposits became grey and mirror-bright over the whole area of the cathode. The hardness of the deposit was measured around 700 HV. Deposition from the electrolyte with high $FeSO_4$ concentration and a high citric acid concentration revealed a grey and dull appearance with interference colors seen at low current densities. The uniformity of the coating was improved by adding NaCl to the electrolyte, but Na_2SO_4 did not affect the appearance of the deposit [21]. The addition on NaCl to the electrolyte did not influence the resulting hardness of the coating.

2.3.2.3 Current density

The effect of current density on the elemental composition and the hardness of the Fe-C coating has been examined in multiple articles [18,21–23,25] and representative results are shown in Figure 13 and Figure 14. The carbon content increases when the current density is increased as shown in Figure 13 [18]. The oxygen content is negligible when a low current density is applied, but a rapid increase is measured when the current density is increased to above 5 A/dm^2. The hardness of the coating is around 750-800 HV and increases due to the correlated effect that a higher current density increases the carbon content. The hardness drops when the increase in current density causes oxygen to be co-deposited.

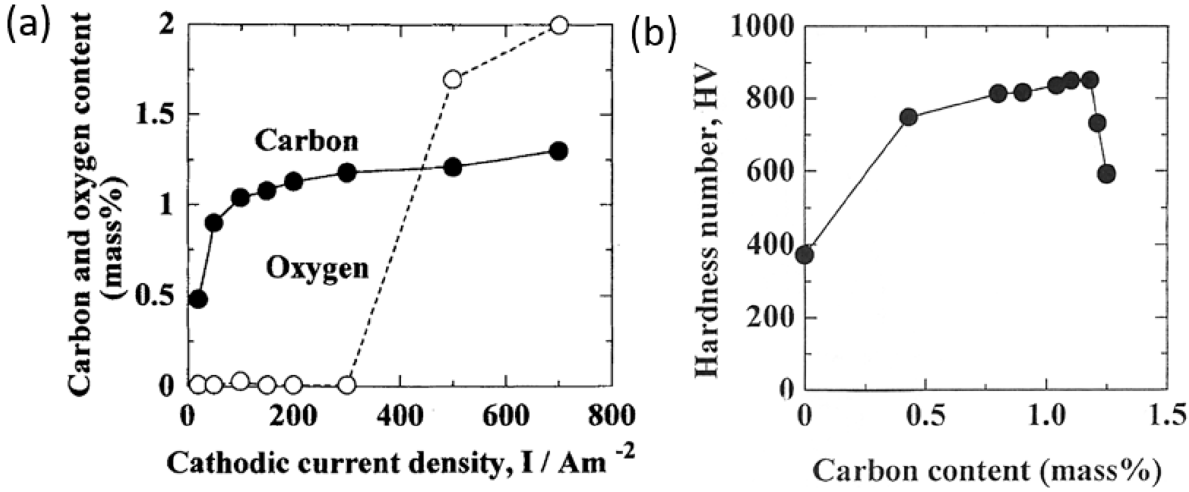

Figure 13: (a) Carbon and oxygen content in a Fe-C coating as a function of the applied current density. (b) The relationship between the hardness and the carbon content of the data presented in (a). Electrolyte composition FeSO$_4$, citric acid and L-Ascorbic acid, temperature of 50 °C, pH-value is not provided. Figures from [18].

The current efficiency of the system is lowest when using a low current density as shown in Figure 14 [23]. The current efficiency will either be independent of the certain current density or has a maximum followed by a decrease above a certain current density. The hardness of the deposit is lowest when a low current density is applied. The hardness will be independent of the current density above a certain current density.

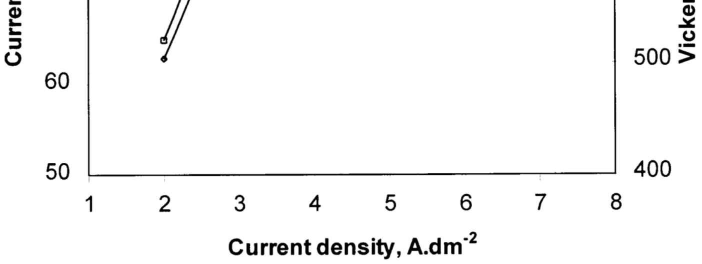

Figure 14: Current efficiency and hardness as a function of the applied current density. Electrolyte composition FeSO$_4$ and either succinic acid or asparainic acid, temperature 55 °C and pH-value of 2.5-2.6. (a) current efficiency - asparainic acid; (b) current efficiency - succinic acid; (c) hardness - asparainic acid; (d) hardness – succinic acid. Figure from [23].

2.3.2.4 Temperature of the electrolyte

The current efficiency of the system and the hardness of the deposit has been examined as a function of the electrolyte temperature and the result is shown in Figure 15 [23].

The current efficiency is either constant at the lower electrolyte temperatures followed by a decrease when the temperature is increased or it has an optimum condition at a specific temperature. The hardness of the deposit decreases when the electrolyte temperature is increased.

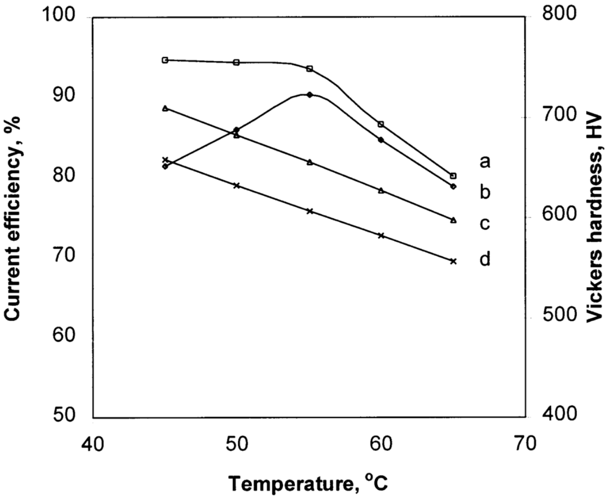

Figure 15: Current efficiency and hardness as a function of the electrolyte temperature. Electrolyte composition of $FeSO_4$ and either succinic acid or asparaginic acid, current density of 3.5 A/dm² and pH-value of 2.5-2.6. (a) current efficient – asparainic acid; (b) current efficient - succinic acid; (c) hardness - asparainic acid; (d) hardness - succinic acid. Figure from [23].

2.3.2.5 pH-value of the electrolyte

The current efficiency of the system, carbon content and hardness of the deposits have been examined in regard to the pH-value of the electrolyte and the results are shown in Figure 16 and Figure 17 [17,23].

The current efficiency of the system is lowest for the most acidic electrolyte. The current efficiency will either continue to increase, have an optimum or become independent when increasing the pH-value of the electrolyte. The maximum current efficiency of 100 % is nearly achieved for two of the systems having the least acidic conditions. The hardness of the deposit is either independent of the pH-value or increases when the pH-value is increased. The carbon content decreases when the pH-value of the electrolyte is increased.

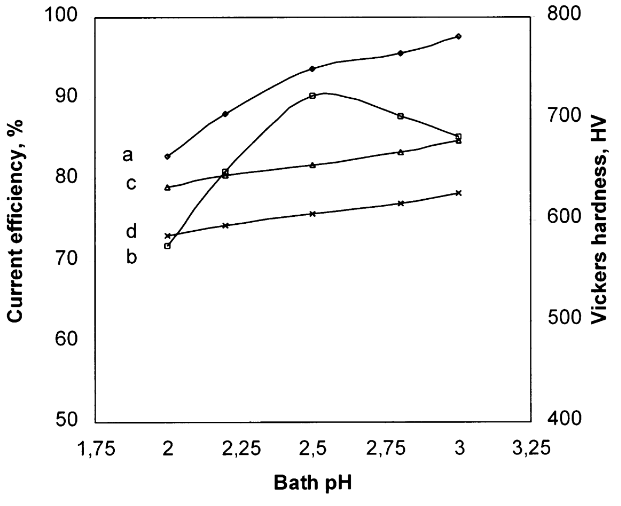

Figure 16: Current efficiency and hardness as a function of the pH-value of the applied electrolyte. The electrolyte composition of $FeSO_4$ and either succinic acid or asparaginic acid, current density of 3.5 A/dm², temperature of 55 °C. (a) current efficient - asparainic acid; (b) current efficient - succinic acid; (c) hardness - asparainic acid; (d) hardness - succinic acid. Figure from [23]

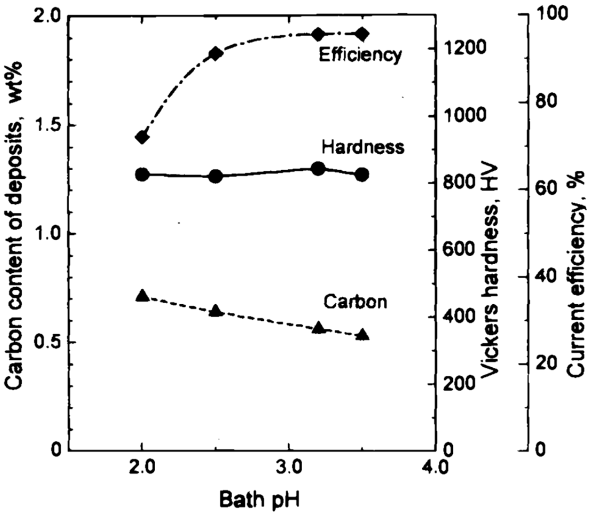

Figure 17: Carbon content, hardness and current efficiency as a function of the pH-value of the applied electrolyte. The electrolyte composition of $FeSO_4$ and succinic acid, current density of 1.0 A/dm^2, temperature of 50 °C. Figure from [17].

2.3.2.6 Assessment of results from literature

When the carboxylic acid is added to the electrolyte, it functions as a buffer, complexing agent and carbon source. The influence of the alkyl chain length and the number of carboxylic groups on the carboxylic acid showed that the carbon content increases when one of the factors is increased [17]. The oxygen content was only investigated using dicarboxylic acids and showed an increase in oxygen content when the alkyl chain length was increased. The hardness of the deposit has an optimum depending on the length of alkyl chain length, which is suggested to be correlated to an optimum carbon content of the system around 0.6 to 1.2 wt%. A higher hardness is obtained using dicarboxylic acid compared to monocarboxylic acid independent of the carbon content. The deposits became brittle and did not adhere to the substrate when using l-ascorbic acid as an additive, due to the amount of carbon being co-deposited being around 2.5 wt% [22]. The use of a tricarboxylic acid (citric acid) provided a similar appearance as the dicarboxylic acid (l-malic acid) and a higher carbon content around 1 wt% [19]. The publication [19] does not provide the difference in hardness between the deposits, but the carbon content of 1 wt% obtained using citric acid is within the optimum content proposed by [17]. The hardness of deposits using citric acid from other sources provide an average hardness around 700 HV [21]. The deposits from a bath containing both citric acid and l-ascorbic acid increased the carbon content to 1.2 wt% [17,22] compared to the 1 wt% carbon obtained from the bath containing citric acid [22]. The hardness of the deposit from the bath using both citric acid and l-ascorbic acid also provided a hardness of 780 HV [17,22] as the carbon content is within the optimum content [17]. The co-deposition mechanism for the additive was not investigated and the difference in the chemical structure of the additive and their influence on the deposits' appearance and hardness does not allow describing a relationship and proposing an ideal chemical composition. However, the function of the additive goes beyond its influence on the resulting material properties of the deposit, and requires it to act as a complexing agent to prevent the development of solid precipitates in the electrolyte and to act as a buffer to lower the changes in the electrolytes pH-value during deposition. The complexity of maintaining an electrolyte in its optimum operation conditions is significantly increased when more than one additive is added, as the concentration and ratio need to be stable during deposition.

The ratio between the concentration of iron-sulfate and citric acid showed that applying a low concentration of iron-sulfate results in deposits that appeared burnt [21]. The burnt appearance is normally related to the depletion of metallic ions at the cathode/electrolyte interface when the limiting current is exceeded and the increase in the iron-sulfate concentration also resolved the issue and a bright appearance was re-established. The increase in the citric acid concentration caused the appearance to become dull and resulted in no deposition at low current densities [21]. It is not stated in [21] whether the increase in citric acid resulted in an increase in the carbon content to outside the optimum conditions or caused its action as an inhibitor. Independent of its role, it has shown that the influence of the citric acid concentration on the deposit is significant and requires a systematic analysis.

The carbon and oxygen content will increase when the current density is increased [18,23]. The current efficiency will either have an optimum efficiency at a specific current density or be increased when the current density is increased [18,23] and this dependence is related to the specific additive used during deposition. The average grain size of the deposit will normally be decreased when the current density is increased and using a low current density is also shown to lower the hardness of the deposits. The hardness is also shown to have an optimum when the current density is varied, which seems correlated to the carbon and oxygen content being co-deposited.

The pH-value of the electrolyte influences the current efficiency of the system and using a pH-value below 2.5 will lower the current efficiency [17,23]. A lower pH-value can lead to cathodic hydrogen evolution as a partial reaction, which will decrease the current efficiency as the electrons are used to convert H^+ to hydrogen gas. The carbon content will decrease when the pH-value is increased [17,23]. The complex forming ability between the iron ion and the carboxylic acid depends on the acids dissociation constant (pK_a) and the pH-value of the electrolyte. The monoprotic acids, like propanic acid, will gain its H^+ below a certain pH-value related to its pK_a value and alter the conjugate base (COO^-) complex ability with the iron ion (Fe^{z+}). A polyprotic acid, like citric acid, will have more dissociation constants (pK_{a1}, pK_{a2} and pK_{a3}) which relate to the pH-values and the individual acid group loses their H^+. The decrease in the carbon content could be related to a change in the complex ability between the additive and the iron ions as a result of the additives' pK_a value and the electrolytes' pH-value. The hardness will either increase or be independent of an increase in the pH-value depending on the additive [23]. In this regard, the hardness was shown not to be influenced by the decrease in carbon content. In addition to the carbon content, the oxygen content, the crystallite size and the microstrain could also have an equally significant contribution to the hardness of the coatings.

The temperature of the electrolyte will influence the current efficiency and either have an optimum efficiency at a specific temperature or the efficiency will be decreased when the temperature is increased [23]. This dependence is related to the use of different additives. The hardness will decrease when the temperature of the electrolyte is increased, as the temperature of the electrolyte influences the diffusion and reaction overpotentials and will lead to larger crystallite sizes.

The few publications investigating the differently deposited Fe-C coatings do not allow concluding on the influence of the individual process parameters on the resulting coating. The resulting properties of the coating originate from the combined influence of the several adjustable operation conditions and a systematic analysis is required to better understand the effect on the as-deposited coating.

3 Scope of the project

Fe-C coatings with a hardness of nearly 800 HV have been successfully deposited from an electrolyte consisting of carboxylic acid and iron(II)sulfate. The deposition of Fe-C coatings occurred from a non-toxic electrolyte and with a higher current efficiency compared to the electrochemical deposition of hard chrome, but the higher hardness and corrosion resistance of hard chrome cannot be fully coped with the Fe-C coatings. Apart from the general feasibility of the process, neither the influence of the operation conditions on the resulting internal structure of the iron-based coatings nor the origin of the high hardness have been fully understood yet in literature. This is addressed in the thesis.

The interplay between different process parameters (pH-value, chemical composition of the electrolyte and the current density) affects the chemical and crystallographic nature of the Fe-C coatings and, thus, determines their properties and performance. The current understanding, based on prior publications, of the influence of the operation conditions on the resulting Fe-C coating is incomplete. The individual studies investigating the influence of a single operation condition used different settings for the remaining operation conditions, which hinders a direct comparison. Systematic studies are required for understanding the individual and synergetic influences for final optimization of the quality of the deposited coatings. This must and will take into account the stability of both the electrolyte and the resulting internal structure of the deposited coatings, not only for straightforward laboratory synthesis, but also when upscaling to a real industrial process. The deposition of samples was carried out in-house with a dedicated experimental plan to avoid batch variations and to ensure a traceability between the deposited coatings and the results obtained by advanced methods of characterization. This hands-on routine from deposition to characterization required additional time, but ensured that error-prone data could be accessed in relation to the specific operation conditions.

The typical nanocrystalline microstructure of electrodeposits requires high-resolution electron microscopy, which was applied and supplemented with diffraction analysis using X-ray and synchrotron radiation. The concentration of co-deposited light elements and the associated nature of their incorporation into the coating is important for understanding the growing microstructure and its stability as a crucial factor for obtaining reproducible coatings. However, quantitative detection of the concentration of light elements originating from the deposition process showed to be not straightforward, despite several attempts by advanced chemical element analysis. The nature of the co-deposited light elements is not completely understood and their position within the microstructure is discussed. In-situ thermogravimetric measurements coupled with mass spectroscopy and in combination with diffraction results revealed that the light elements precipitate as either oxides or carbides when the deposit is annealed, which results in a significant increase in the hardness of the deposit. Understanding the thermal evolution of these phases both supported the understanding of the as-deposited nature of the light elements and by itself is important for the final applications, which require stable coatings with predictable properties. The use of complementary methods for characterizing the internal structure of the coatings is an important part of the thesis and considered the key for understanding the growth characteristics, which finally allows engineering of surfaces.

The single additional diffraction peak, which is consistently measured with XRD in literature and in the present work but not being ferrite, is called the “nameless peak” referring to the not yet identified “nameless phase” in the as-deposited Fe-C coatings. The identification of this “nameless phase” is attempted by means of complementary methods and its significance for the high as-deposited hardness is discussed.

As a prerequisite for reproducible large-scale deposition of high quality coatings, the PhD project aims to the

1) systematic investigations and optimization of relevant operation conditions with particular focus on the chemical composition and long-term chemical stability of the applied electrolyte,
2) thorough investigation of the internal structure and occurring phase transformations of the deposited Fe-C coatings applying thermal analysis, microscopy and diffraction-based in-situ and ex-situ methods of materials characterization,
3) understanding of the relation between the operation conditions, the resulting microstructure and the mechanical properties.

4 Deposition and methods of materials characterization and testing

4.1 Experimental setup for electrochemical deposition

4.1.1 Management of the operating conditions

The chemical composition of the Fe-C electrolyte is relatively simple having iron-sulfate as the metallic salt providing the metal ions to the electrolyte and citric acid functioning as carbon source, buffer and complexing agent. The complexity of the process requires maintaining the electrolyte within the optimal conditions during deposition and when the bath is not used for deposition. This is delicate and requires a method to suppress the formation of Fe^{3+}, controlling the pH-value and maintaining a stable Fe^{2+} concentration. Further, the process needs to be able to be operational and stable for a longer period of time as a prerequisite for reproducible large-scale deposition of high quality coatings. Many of the challenges for electrodeposition of Fe-C deposits and their origin are described in the section below along with suggestions for handling these challenges. For suggestions on how to manage the operation conditions for large-scale operation, it is referred to Section 8.3.

4.1.1.1 Suppressing the oxidation of Fe^{2+} to Fe^{3+}

The oxidation state for iron Fe^{2+} (green) and Fe^{3+} (yellow) influences the color of the electrolyte and can be used as a guide to estimate if oxidation has been severe and whether a reduction of the electrolyte should be carried out prior to electrodeposition. The visual appearance of the Fe-C electrolyte shall be clear and green, free from any yellow tint. The presence of Fe^{3+} in the electrolyte is undesirable, but it is challenging to suppress in the presence of air as shown in Equation (8).

$$O_2(g) + 4Fe^{2+} + 6H_2O \rightleftharpoons 4FeOOH + 8H^+,\ \Delta G = -167\ \text{kJ}^{1} \qquad (8)$$

From Equation (8) it can also be seen that a way to suppress the oxidation is to increase the acidity of the electrolyte as this will increase the amount of H^+ in the solution and limit the reaction rate. Increasing the acidity of the electrolyte, will cause iron in its metallic state to be dissolved according to Equation (9) and will increase the pH-value as H^+ is consumed and increase the Fe^{2+} concentration in the electrolyte.

$$Fe + 2H^+ \rightleftharpoons Fe^{2+} + H_2(g),\ \Delta G = -91\ \text{kJ} \qquad (9)$$

An efficient method to suppress the amount of Fe^{3+} or reduce the electrolyte is to have a piece of iron with a large surface area somewhere in the electrolyte. This is a benefit due to the occurring reduction of Fe^{3+} to Fe^{2+}, but will increase the total iron ion concentration in the electrolyte according to Equation (10).

$$Fe + 2Fe^{3+} \rightleftharpoons 3Fe^{2+},\ \Delta G = -20\ \text{kJ} \qquad (10)$$

To verify the chemical reactions described in Equation (8), (9) and (10), which are proceeding without external influence, a series of different electrolytes was mixed and their development

---

[1] The changes of the Gibbs free energy (ΔG) for all chemical equation in this section has been calculated using the software HSC Chemistry 5.11.

was followed over a period of 12 days as shown in Figure 18. The lid was opened periodically on bottle nr. 4 and 5 to measure the pH-value during the 12 days and providing the electrolyte with a limited access to air compared to free access to air for the remaining electrolytes. The change in the visual appearance of different electrolytes is shown in Figure 18 and shows the difference between the as-mixed iron-sulfate based electrolytes with and without additives and after a period of 12 days without being used for deposition. The initial pH-value of the electrolytes was adjusted to 2.5 using diluted sulfuric acid and no significant variation was measured over the period of 12 days with the exception of the electrolyte containing iron wool (nr. 6 in Figure 18).

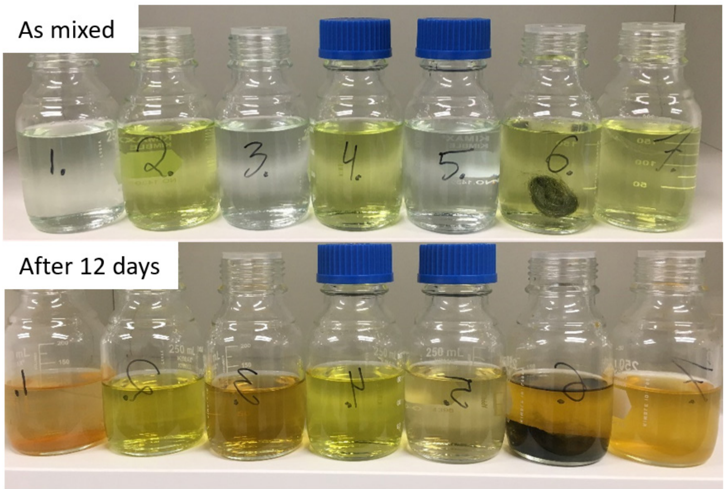

Figure 18: Picture of evolution of Fe-C electrolytes with and without additive over a period of time. A lid what introduced to the bottles marked with 4 and 5 to limits the access of air. The content of the electrolyte corresponds to: (1) iron-sulfate (2) iron-sulfate and citric acid (3) iron-sulfate, citric acid and ascorbic acid (4) iron-sulfate and citric acid (5) iron-sulfate, citric acid and ascorbic acid (6) iron-sulfate, citric acid and iron wool (7) iron-sulfate, citric acid and tri-sodium citrate. Figure from [34][2].

The beneficial effect of citric acid as a complexing agent that prevents solid precipitates and reduces oxidation (Eq 8) of the electrolyte is clear when comparing bottle 1 and 2 (Figure 18). The addition of the anti-oxidation agent ascorbic acid should reduce the oxidation rate, but did not appear to have a positive effect. The limited access to air did reduce oxidation, but did not prevent it completely. The addition of iron wool must be accompanied by the addition of sulfuric acid, as the pH-value increased (Eq 9) and resulted in the development of solid precipitates. The combination of citric acid and tri-sodium citrate resulted in solid precipitates in the electrolyte.

The reduction capability of Equation (10) could not be verified using the experimental setup described above as the pH-value was not adjusted over the period of time. Instead, an oxidized electrolyte was used to confirm the reduction of Fe^{3+} to Fe^{2+} by adding iron to the electrolyte (Eq (10)) in the form of iron wool as shown in Figure 19. The oxidized electrolyte (yellow) with a high concentration of Fe^{3+} is floating on top of a reduced electrolyte (green) as the iron wool is only in contact with that volume of the electrolyte and no stirring was applied. The pH-value of the oxidized electrolyte was measured to 2.0 and the pH-value of the reduced electrolyte was measured to 3.5. The results show that the reaction described in the Equations (9) and (10) is active and the citric acid complex with Fe^{2+} is heavier than its complex with Fe^{3+}.

---

[2] The results in [34] are based on the authors own work when affiliated to a. h. nichro Haardchrom prior to the PhD project.

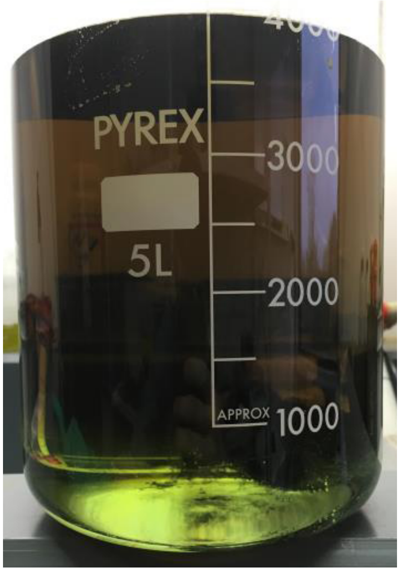

Figure 19: An oxidized Fe-C electrolyte were iron wool has been added and reduced the part of the electrolyte being in contact with the iron wool. Figure from [34].

The benefits of adding citric acid to the electrolyte is very clear as it prevents solid precipitates and lowers the oxidation rate. Introducing the anti-oxidant ascorbic acid does not improve the stability of the electrolyte in regards to suppressing oxidation and is not recommended. The reduction of an oxidized electrolyte by adding iron in its metallic state is a simple method to restore the electrolyte to operation conditions and will suppress oxidation. The iron is only required in the surface of the electrolyte as this is where the electrolyte has access to oxygen and the lighter citric acid complex with Fe^{3+} will float towards the surface. The pH-value of the electrolyte is required to be maintained by a separate process as the introduction of iron in its metallic state will consume H^+ ions and solid precipitates will develop at increased pH-values as predicted by the Pourbaix diagram shown in Figure 2.

4.1.1.2 Iron-sulfate or iron-chloride based electrolytes

The two most common types of electrolytes are iron-sulfate based and iron-chloride based. The present work continues the development of sulfate-based electrolytes, as the harsh environment of the chloride-based electrolyte will cause pitting corrosion of the iron anode when the bath is not used for deposition as shown in Figure 20. The iron anode will also be dissolved in an acidic sulfate-based electrolyte as described in Equation (9) but without pitting corrosion. The difference between a Fe-C coating deposited from an iron-sulfate based electrolyte and an iron-chloride based electrolyte with the otherwise similar operation conditions will be discussed in Section 6.2.1.

Figure 20: Iron anodes submerged for 68 hour in an iron-chloride based electrolyte. Figure from [34]

4.1.1.3 Regulating the pH-value

The citric acid acts as a buffer to reduce the changes in the pH-value during deposition. However, the pH-value is influenced by the partial reactions proceeding during deposition, which strongly depend on the type of anode used in the setup. The main types of anodes that can be deployed in electroplating are the sacrificial anode and the inert anode and they behave different in the electrolyte as described below.

Sacrificial anode

The sacrificial anode is a metallic workpiece of high purity of the same material as the main metallic ion in the electrolyte. The anode will be dissolved during deposition and maintain the metallic ion concentration in the electrolyte if the current efficiency of the whole system is 100 %. The electric current in the electrolyte is generated from the anode reaction shown for the example of an iron anode in Equation (11).

$$\mathrm{Fe} \rightleftharpoons \mathrm{Fe}^{2+} + 2\mathrm{e}^{-}\ , \Delta G = 91\ \mathrm{kJ} \tag{11}$$

The benefit of the sacrificial anode is that it is a relatively cheap investment and metallic ions are supplied continually during operation. An increase in the concentration of metallic ions in the electrolyte will occur if the cathodic current efficiency is below 100 %. The concentration of metallic ions in the electrolyte can be reduced by diluting the electrolyte with water.

The sacrificial iron anode will be dissolved in the acidic electrolyte and suppress the oxidation while the system is not used for deposition following Equation (9) and (10), respectively. The increased pH-value (Eq. (9)) of the electrolyte results in the formation of solid precipitates as shown with the example of iron wool in Figure 18, bottle 6. The system requires a continuous addition of sulfuric acid to maintain the pH-value within the operation condition and to prevent solid precipitates to develop.

The sacrificial anode needs to be changed periodically, as it dissolves when submerged in the electrolyte. This will change the geometry of the anode and can alter the current field lines from the anode towards the cathode in the electrolyte. The change in current field lines can result in variations in the deposits between batches. The use of a sacrificial anode increases the operation cost of the system, because new anodes need to be acquired and installed periodically.

Inert anode

The inert anode is a metal that does not dissolve during deposition. The electrons are supplied from the inert anode by electrolysis of water as described in Equation (12).

$$2\mathrm{H_2O} \rightleftharpoons \mathrm{O_2(g)} + 4\mathrm{H}^{+} + 4\mathrm{e}^{-}\ , \Delta G = 483\ \mathrm{kJ} \tag{12}$$

The benefit of the inert anode is that it will maintain its geometry during operation.

The disadvantages of the inert anode is that the electrolysis of water will produce O_2 as shown in Equation (12) and rapidly oxidize Fe^{2+} to Fe^{3+} through Equation (8). The result of a 20 min deposition using an inert lead anode can be seen in Figure 21. The electrolysis of water will also produce an excess of H^+, which will lower the pH-value of the electrolyte.

Figure 21: Electroplating of Fe-C coating after 20 min using an inert lead anode. Figure from [34]

The oxidation of Fe^{2+} to Fe^{3+} can be reduced by using a Nafion membrane as a proton conductor around the inert anode as shown in Figure 22. The investment for these anodes is significantly higher compared to sacrificial and inert anodes, as they normally consist of titanium coated with a noble metal and are custom made for a specific purpose/workpiece. The electrolysis of water will still produce an excess of H^+, which will lower the pH-value of the electrolyte. The addition of a base to the electrolyte is not recommended to increase the pH-value. Solid precipitates will develop locally when the alkaline solution is introduced as a salt or liquid due to the rapid local increase in the pH-value. The precipitates will be dissolved after a period of time when stirring is applied and the overall pH-value is within the requested operation conditions.

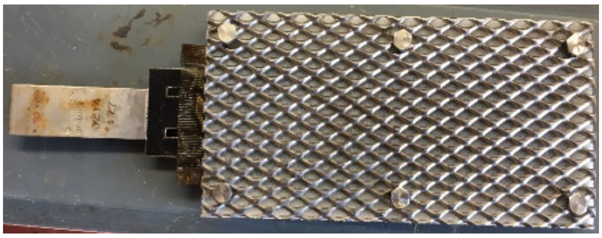

Figure 22: Inert anode with a nafion membrane. Figure from [34].

4.1.1.4 Experimental setup for laboratory deposition

The chemical reactions as described above reveal that several setups are possible with different benefits and disadvantages. The setup as shown in Figure 23 has been applied to produce the samples examined during the PhD project. The setup uses a sacrificial IF steel anode and manual logging and adjustments of the pH-value was required during deposition. The sacrificial anode was selected as it increases the pH-value during deposition and 10 vol% sulfuric acid was used for the adjustment of the pH-value, compared to the inert anode that would lower the pH-value during deposition and require a base to adjust the pH-value. The temperature was controlled by a thermocouple connected to the heating plate below. The current was controlled by a DC amplifier (not shown in the image), which was connected to the anode and cathode by the red and black wire, respectively. This setup has the advantages of being scalable in regards to the total volume of the electrolyte between 1 and 10 L.

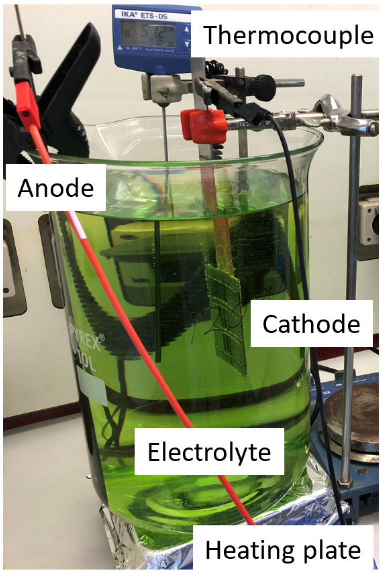

Figure 23: Experimental setup for Fe-C deposition using a sacrificial iron anode as applied for the present work.

The infrequent deposition of samples and the low cost of the chemicals permitted for a new electrolyte to be mixed when needed and it was usually disposed after deposition. This renewal of the electrolyte reduced the risk of depositing samples from an oxidized electrolyte or from an electrolyte being outside the required chemical composition.

4.1.1.5 Operation conditions

The operation conditions that have been varied for electrodeposition of the Fe-C coatings are shown in Table 1. The effect of the substrate and the coatings thickness on the material properties will be discussed in Section 6.1.1. The chemical composition of the electrolyte and the applied current density will be discussed in Section 6.2.1. The influence of the pH-value on the resulting microstructure and the current efficiency will be discussed in Section 6.3.1.

Table 1: Operation conditions for electrodeposition of Fe-C coatings.

Operation conditions	
Temperature	50 °C
$FeSO_4 \cdot 7H_2O$	Varied from 40 to 120 g/L
$C_6H_8O_7 \cdot H_2O$	Varied from 1.2 to 3.6 g/L
pH-value	Varied from 2 to 3.7
Current density	Varied from 3.0 to 4.0 A/dm^2
Anode	IF steel

Preparing the bath for deposition was done following the procedure below.

- A beaker is 80% filled with deionized (DI) water and the thermal couple is set to (50 °C) and stirring by a magnet is applied.
- The chemicals are measured precisely and citric acid is added to the DI water in the beaker.
- The iron-sulfate is added to the solution when the temperature is between 40-50 °C.
- DI water is added to reach the required volume.
- The iron anode is submerged into the electrolyte to prevent the oxidation.
- The pH-value of the electrolyte is measured when the temperature reached 50 °C.
- The pH-value is adjusted using diluted sulfuric acid if the pH-value is out of range (2.5-2.8).
- The pre-treatment of the sample is started when the electrolyte is in operating conditions.

The method of pre-treatment of the substrate prior to deposition is strongly dependent on the substrate material and the general procedure is given below:

- Anodic degreasing was done for 60 s at 5V.
- The sample was rinsed in water a few times.
- Activation of the substrate was carried out as discussed in Section 6.4.1
- The sample was rinsed in water a few times.

4.1.2 Co-deposition of additional elements and surface engineering

The co-deposition of additional elements can have different purposes as to increase the corrosion resistance by co-deposition of an element being less noble than iron or to increase the hardness by solid solution strengthening. However, operating an electrolyte for alloy deposition is complicated and requires a system that is continually controlled such that the chemical composition of the electrolyte is stable and can produce a coating having the desired ratio between elements. The complexity of developing a stable electrodeposition alloying system made the investigation of co-deposition of different additional elements, as described below, a proof-of-concept with suggestions on how to continue the development if desired.

4.1.2.1 Co-deposition of boron

The addition of boric acid to the electrolyte was done in order to investigate its buffer capacity and its ability to be co-deposited in order to increase the hardness of the deposit further by introducing an additional light element. The solubility of boron in ferrite is 0 wt% at room temperature [35]. The operation condition for the deposition is shown in Table 2.

Table 2: Operation conditions for Fe-C-B coating

Operation conditions	
Temperature	50 °C
Composition	80 g/L $FeSO_4 \cdot 7H_2O$ 8 g/L H_3BO_3 1.2 g/L $C_6H_8O_7 \cdot H_2O$
pH-value	2.5-2.6
Current density	3.5 A/dm^2

The boric acid had no significant influence on the stability of the pH-value during operation and the appearance of the deposit with boric acid added to the electrolyte was similar to the deposit without the addition of boric acid. It was possible to deposit an adherent coating, but the chemical analysis using glow discharge optical emission spectroscopy did not measure a signal from boron and may suggest that the element has not been co-deposited. The hardness of the coating was measured with a value of 650 HV, which is lower compared to the Fe-C coatings deposited from an electrolyte without boric acid. The microstructure of the coating deposited using boric acid was investigated using XRD phase analysis. The diffraction pattern of the coatings deposited under the same operations condition of the Fe-C coating with the exception of boric acid was similar in terms of peak intensity and peak profile.

The addition of boric acid will impact the environment-friendly aspect of Fe-C coatings as boron is covered in the hazard statement H360 “May damage fertility or the unborn child”.

It is not recommended to investigate the addition of boric acid to the electrolyte to improve the materials properties of the coating, as a reduction of hardness of the coating was measured although there was no indication that boron was co-deposited.

4.1.2.2 Co-deposition of manganese

The addition of manganese in the coating should improve the corrosion resistance of the coating in alkaline solutions by the development of a stable passivating oxide layer [36]. Manganese is less noble than iron and will act as anodic protection [36]. The solubility of manganese in ferrite is 3 wt% at room temperature [35]. The current density and pH-value of the system was varied during several experiments, before the values summarized in Table 3 produced a coating with an acceptable uniform appearance.

Table 3: Operation conditions for Fe-C-Mn coating

Operation conditions	
Temperature	50 °C
Composition	40 g/L $FeSO_4 \cdot 7H_2O$ 40 g/L $MnSO_4 \cdot H_2O$ 1.2 g/L $C_6H_8O_7 \cdot H_2O$
pH-value	2.5
Current density	3.0 A/dm^2

The appearance of the deposit is dark-grey and mirror bright. The chemical analysis using glow discharge optical emission spectroscopy measured a signal from manganese in the deposit, but could not quantify the elemental content. The microstructure and hardness of the coating have not been investigated.

The addition of manganese sulfate to the electrolyte can be used to co-deposit manganese and still produce an acceptable uniform appearance. The addition of manganese sulfate impact the environment-friendly aspect of coatings as manganese is included in the hazard statement H373 “Causes damage to organs through prolonged or repeated exposure” and H411 “Toxic to aquatic life with long lasting effects”.

It is only recommended to investigate the addition of manganese sulfate to the electrolyte if the coating is required to withstand alkaline environments.

4.1.2.3 Co-deposition of tungsten

The addition of tungsten in the coating will improve the corrosion resistance in acidic solutions by the development of a stable passivating oxide layer [36]. Tungsten is less noble than iron and will act as anodic protection [36]. The solubility of tungsten in ferrite is 0 wt% at room temperature [35]. The operation conditions for the deposition can be seen in Table 4.

Table 4: Operation conditions for Fe-C-W coating

Operation conditions	
Temperature	50 °C
Composition	80 g/L $FeSO_4 \cdot 7H_2O$ 3 g/L $Na_2WO_4 \cdot 2H_2O$ 11.3 g/L $C_6H_8O_7 \cdot H_2O$
Current density	3.0 A/dm^2

The appearance of the deposit is dark-grey and mirror bright after deposition and a blue appearance developed after the deposit has been exposed to air for some time. The chemical analysis using glow discharge optical emission spectroscopy measured a signal from tungsten in the deposit, but could not quantify the elemental content. The microstructure and hardness of the coating have not been investigated.

The addition of sodium tungstate dihydrate to the electrolyte can be used to co-deposit tungsten and still produce a good appearance. The addition does not affect the environment-friendly aspect of coatings.

It could be of interest to further investigate the addition of tungsten to the electrolyte.

4.1.2.4 Surface engineering with zinc

The deposition of a zinc coating on top of a Fe-C coating is expected to improve the corrosion resistance by anodic protection as zinc is less noble compared to iron [36], but would not produce a stable passivation layer. The zinc layer will be rapidly removed in case of wear due to its low hardness. Annealing the deposits would enable diffusion between the zinc and iron and could produce an alloy surface layer. The durability of the alloy surface layer would be increased if a similar hardness of the Fe-C would be achieved. The operation conditions for the zinc deposition can be seen in Table 5. The Fe-C coating having a zinc layer was annealed at 300 °C for up to 48 hour for diffusion to occur. The solubility of zinc in ferrite is 3 wt% at 300 °C [35].

Table 5: Operation conditions for bright zinc plating.

Operation conditions	
Temperature	20 °C
Composition	55 g/L $ZnSO_4 \cdot 7H_2O$ 150 g/L NaCl
Current density	3 A/dm^2
pH-value	5

The zinc layer had delaminated on several locations after the annealing. The delamination of the zinc layer refers to low adhesion, which may relate to the higher thermal expansion coefficient for zinc compared to iron. The diffusion zone was investigated using EDS mapping and showed that diffusion had occurred only at a few sites.

It is not recommended to continue the work as a uniform diffusion zone between iron and zinc could not be established during annealing.

4.1.3 Substrates and sample geometries

The electrochemical deposition process simply requires a conductive substrate connected to the power supply in order to reduce the metallic ions upon and the deposit will grow as a function of time. The sample geometry is very important for specific methods of materials characterization and the ability to produce a coating on a thin or thick substrate can have different benefits and in some cases it would be best to completely avoid having a substrate when investigating the deposited coating. A brief introduction of some of the cathode designs developed and applied during the thesis and their intended experimental purpose will be presented below along with some samples that required a more advanced deposition setup compared to Figure 23. The grey and mirror-bright appearance of the Fe-C coating makes it difficult to capture the coatings characteristics using a standard camera. The reflection of light on the coatings surface will in some cases make the coating appear dark-grey or completely black. The reader should not put too much emphasis on this.

A cathode design that can produce multiple samples in a single deposition is very practical as it ensures that all samples are deposited simultaneously, thus, at the same pH-value, temperature, and chemical composition. The cathode design depends on the required size of the samples and the substrate material. The illustration of a general cathode design for deposition under identical conditions in one and the same run, thus, producing several samples on different substrates, is shown in Figure 24a. One actual example of a cathode designed to investigate the influence of the substrate material is shown in Figure 24b were brass and steel were deposited under the same conditions.

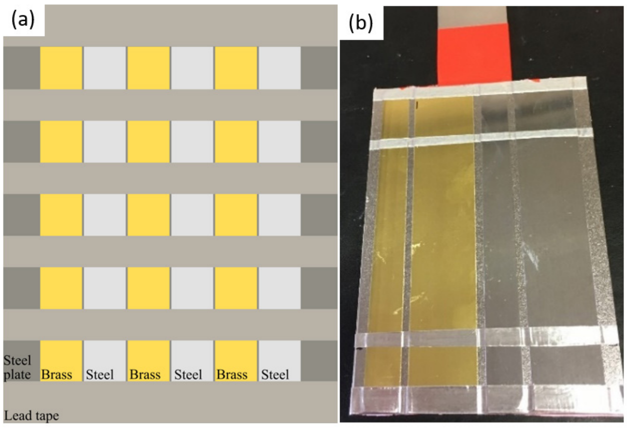

Figure 24: (a) Illustration of general cathode design for deposition of Fe-C coatings under identical conditions on steel and brass strips attached on a steel plate using lead tape. (b) One example of a cathode design used for deposition under identical conditions of Fe-C coating on different substrates being brass and steel.

The use of hardened spring steel was found to have low adhesion towards the Fe-C coatings and was used to produce free-standing Fe-C coatings by easily removing the coating from the substrate. For better support of the thin hardened spring steel strips, they were attached to a steel plate using lead tape as shown in Figure 24a and Figure 25a. The pattern of the lead-tape ensured that the deposit from the area closest to the center could be collected and investigated separately from the deposit close to the edge. The homogeneity of the deposit could be evaluated using the cathode design in Figure 25a. The free-standing coating as shown in Figure 25b was primarily used for thermal analysis as the substrate would not influence the measurement.

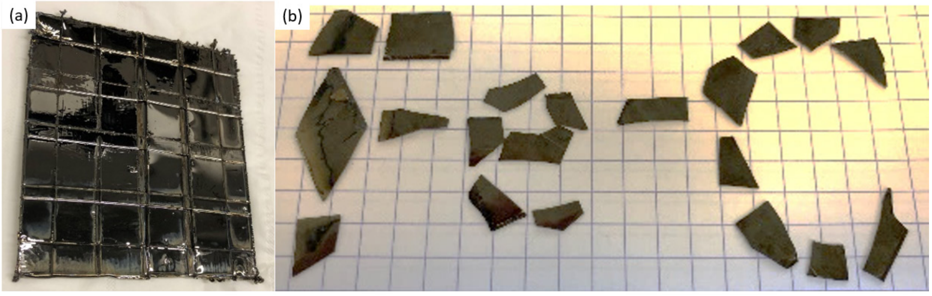

Figure 25: (a) A cathode design after Fe-C deposition with hardened spring steel attached on a steel plate using lead tape and (b) pieces of free-standing Fe-C coating (as mosaic for illustration), used for thermal analysis by in-situ DTA/TGA-MS, in-situ EDD phase analysis during heating or measurement of the carbon content by LECO.

The lead-tape was also found to have low adhesion towards the Fe-C coatings and was used to produce free-standing Fe-C coatings by easily removing the coating from the substrate. For obtaining dedicated samples for TEM analysis, the lead-tape was attached to a steel plate for support as shown in Figure 26a and Figure 26b, before and after deposition, respectively. The resulting free-standing Fe-C coatings have the geometry of a 3 mm disc and are shown in Figure 26c, which were intended to be used as TEM samples (after electropolishing) as they would fit into the standard TEM sample holder.

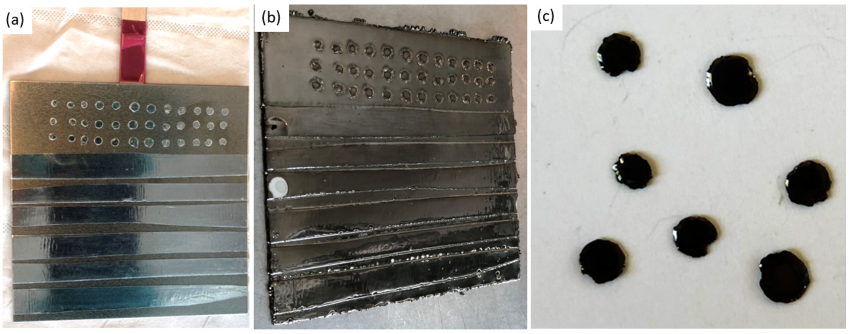

Figure 26: (a) Cathode disc prior to deposition, consisting of lead-tape attached to a steel plate both in strips and as 3 mm. (b) Cathode shown in (a) disc after deposition. (c) Free-standing 3mm disc of Fe-C coating intended as TEM samples after electropolishing.

For the deposition of dedicated samples in the form of discs and cylinders of different dimensions as shown in Figure 27, rotation of the cathode was applied to ensure a uniform thickness and to remove hydrogen bubbles developed during deposition on the surface.

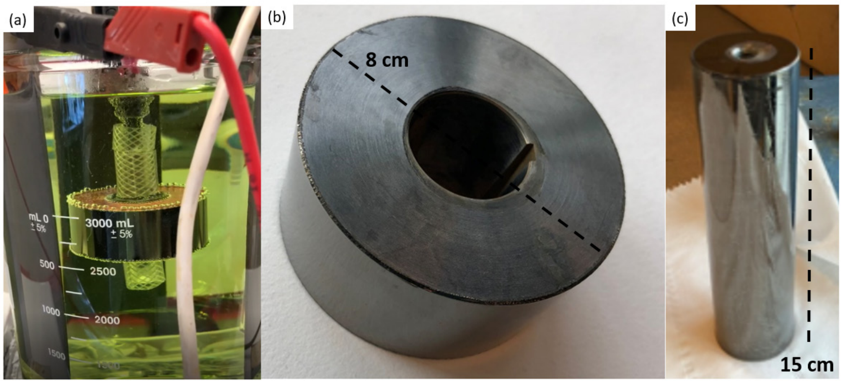

Figure 27: (a) Setup for deposition of a disc used in wear test, with rotation applied to ensure a homogenous thickness and to remove hydrogen bubbles, (b) disc for wear test plated with Fe-C coating and (c) cylinder plated for wear test.

The size of some samples required a larger setup for plating compared to the one shown in Figure 23 and a PVC pipe was introduced as shown in Figure 28a. The temperature was controlled by a heating element in the top of the electrolyte. However, a thermal gradient from the top to the bottom caused severe troubles during the first depositions. The introduction of stirring removed the gradient and a uniform coating was plated on the steel pipes as shown in Figure 28b.

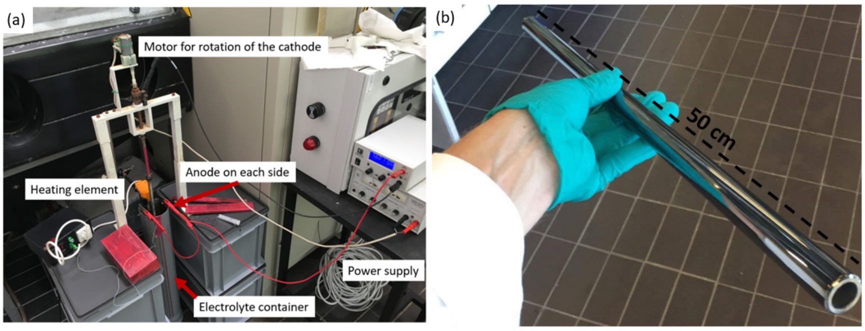

Figure 28: (a) Electrodeposition setup for plating steel pipes applying rotation of the cathode and (b) steel pipe plated with the Fe- C coating.

4.2 X-ray diffraction

In this section, the general principle of XRD will be given, as the technique is the primary tool for the phase analysis, line profile analysis, texture analysis, and residual stress analysis. The general theory of each method of characterization will be presented along with the experimental setup and sample preparation. The conventional method using a lab scale diffractometer and a beam with a fixed wavelength for the angle-dispersive diffraction mode will be covered and extended to energy-dispersive synchrotron diffraction using a white beam.

4.2.1 Phase analysis

X-rays are electromagnetic waves with a much shorter wavelength (λ) compared to visible light. Two waves travelling in the same direction and interacting with a crystalline material can either reinforce (constructive interference) or cancel each other (destructive interference) depending on their individual phase. The periodic arrangement of atoms causes constructive interference of the scattered X-rays at specific angles (Θ) predicted by Bragg's law as shown in Equation (13),

$$\lambda = 2d_{hkl} \cdot sin(\Theta) \tag{13}$$

where d_{hkl} is the lattice spacing between crystallographic planes.

The lattice spacings are characteristic for specific materials and are one parameter that can be investigated from a recorded XRD pattern, although it contains much more information about the material than the lattice spacing alone. The information contained within a diffraction peak and how it can be applied for further analysis is described below:

- The peak position can be used for phase analysis and to determine the macro stresses (Section 4.2.4)
- The peak width/shape can be used to determine the crystallite size and microstrain using the line profile analysis (Section 4.2.2).
- The peak intensity can be used for phase analysis and crystallographic texture analysis (Section 4.2.3).

4.2.2 Line profile analysis

The crystallite size and microstrain of a phase can be obtained by analyzing the broadening of peaks in the diffraction pattern. The integral breadth ($\beta_{measured}$) of the peak can be calculated from the full width half maximum (FWHM) and the Lorentz factor (η_L) obtained by peak fitting using the pseudo-Voigt function (Section 4.2.6) [37] as shown in Equation (14)[3].

$$\beta_{measured} = \frac{\eta_L \cdot \pi \cdot FWHM}{2} + \frac{(1-\eta_L)}{2} \cdot \sqrt{\frac{\pi}{\ln(2)}} \cdot FWHM \tag{14}$$

However, there are two main contributions to the measured breadth of a peak [37] being the instrumental broadening ($\beta_{Instrumental}$) and the physical broadening ($\beta_{physical}$) as shown in Equation (15).

$$\beta_{measured} = \beta_{instrumental} + \beta_{physical} \tag{15}$$

---

[3] The FWHM obtained from the pseudo-Voigt fitting is used, which does not distinguish between the Gaussian and Lorentzian part of the profile.

It is only the physical broadening that is of interest for the determination of the crystallite size (strictly speaking: the size of coherently diffracting domains) and microstrain and therefore the instrumental broadening needs to be determined from a reference sample and subtracted from the measured broadening. The resulting physical broadening, in terms of the integral breadth, of the pseudo-Voigt function consists of the contributions from the Lorentz (β_L) and Gaussian (β_G) functions as shown in Equation (16) [37].

$$\beta_{physical} = \eta_L \cdot \beta_L + (1 - \eta_L) \cdot \beta_G \tag{16}$$

The two methods for line-profile analysis that can be applied are the single line method and the Williamson-Hall plot, respectively [38,39].

4.2.2.1 Williamson-Hall

A Williamson-Hall plot consist of the values $\beta_{physical} \cdot \cos(\Theta) \cdot \lambda^{-1}$ plotted as a function of $2 \cdot \sin(\Theta) \cdot \lambda^{-1}$. The calculation of the measured integral breadth for a pseudo-Voigt function was given in Equation (14). The points in the Williamson-Hall plot are used for a linear regression, from which the crystallite size can be determined from the reciprocal value of the intercept with the y-axis and the microstrain can be determined from the slope of the fit. The Williamson-Hall plot requires multiple peaks from the same phase to obtain a good fit.

4.2.2.2 Single-line method

Scientifically justified assumptions that the peak broadening due to small crystallite sizes results in a Lorentzian peak profile and the peak broadening due to microstrain results in a Gaussian peak profile [40], are used for the single-line method of line profile analysis. The single-line method [39] can be used to determine the crystallite size (D) and microstrain (ε) from a single peak using Equation (17) and (18), respectively.

$$D = \frac{\lambda}{\beta_L \cdot \cos(\Theta)} \tag{17}$$

$$\varepsilon = \frac{\beta_G}{4 \cdot \tan(\Theta)} \tag{18}$$

4.2.3 Texture analysis

The crystallographic orientation of crystallites within the materials can be random or of preferred orientation. Only the grains being orientated with a crystalline plane that satisfies Bragg's law are measured by XRD. The diffraction pattern measured using a symmetric beam path and without tilting the sample is different for a polycrystalline material consisting of grains of random orientation, a polycrystalline material with a strong texture (grains have a preferred orientation within the material) and a single crystal. The diffraction pattern for a single crystal and the textured material will only include a single or a limited number of the (according to the extinction rules) allowed diffraction peaks. The diffraction pattern for the polycrystalline material consisting of grains of random orientation will consist of all allowed diffraction peaks with a specific intensity relation dependent on the multiplicity of the diffraction plane.

4.2.4 Residual stress analysis

4.2.4.1 $\sin^2\psi$ method

The $\sin^2\psi$ method determines the macrostresses within a material from the lattice strain measured for the same lattice plane in different azimuth angles. [37,41]. The $\sin^2\psi$ method is suitable for polycrystalline materials with a random crystallographic orientation and a homogeneous biaxial stress state. The method requires that the principal strains are translated to principal stresses with the help of the hkl-dependent X-ray elastic constants (XEC) s_1^{hkl} and $1/2s_2^{hkl}$. The lattice strain for a specific lattice plane ($\varepsilon_{\varphi\psi}^{hkl}$) oriented in a certain direction related to the angles φ and ψ corresponds to Equation (19). The strain free lattice spacing (d_0) either can be determined from a reference material, which is free of macrostresses, or from the measurement of the sample at its strain-free direction according to Equation (21).

$$\varepsilon_{\varphi\psi}^{hkl} = \frac{d_{\varphi\psi}^{hkl} - d_0}{d_0} \tag{19}$$

The lattice strain is measured for several azimuth angles from 0 to 90° and each value is plotted as a function of $\sin^2\psi$ and assuming a biaxial rotational symmetric stress state, the linear relation should hold as shown in Equation (20).

$$\varepsilon_{\varphi\psi}^{hkl} = \frac{1}{2}s_2^{hkl} \cdot \sigma_{\parallel} \cdot sin^2(\psi) + 2 \cdot s_1^{hkl} \cdot \sigma_{\parallel} \tag{20}$$

When plotted as a function of $\sin^2\psi$, the macrostresses can be determined from the slope of the linear fit or from the intercept with the y-axis. An increasing slope will be measured when tensile stresses are acting parallel with the surface and a decreasing slope will show compressive stresses acting parallel with the surface.

The strain free direction $\sin^2\psi_0^{hkl}$ where $\varepsilon_{\varphi\psi}^{hkl} = 0$ can be determined for a material by rewriting Equation (20) and is shown in Equation (21).

$$sin^2(\psi_0^{hkl}) = \frac{-2s_1^{hkl}}{\frac{1}{2}s_2^{hkl}} \tag{21}$$

A measurement in the strain free direction for a peak provides the lattice spacing without the influence of a macrostrain and can be used to determine the size of the unit cell.

The XEC's for ferrite according to the Eshelby-Kröner model have been used and can be found in Table 3 of [37]. The value of s_1^{hkl} and $1/2s_2^{hkl}$ and their corresponding strain free directions (ψ_0^{hkl}) are shown for ferrite in Table 6.

Table 6: XEC's for specific lattice planes for ferrite and their strain free direction.

hkl	110	200	211	220	310	222	321
s_1	-1.24	-1.88	-1.24	-1.24	-1.65	-1.02	-1.24
$1/2s_2$	5.70	7.63	5.70	5.70	6.94	5.06	5.70
ψ_0 [°]	41.16	44.59	41.16	41.16	43.57	39.42	41.16

4.2.4.2 Crystallite group method

The crystallite group method was developed to analysis the macrostresses within a textured material [42]. The crystallite group method uses only the measured lattice strain from the grains of main crystallographic orientation. The lattice strain of a certain lattice plane is measured at the specific azimuth angles from 0 to 90° related to the main crystallographic orientation and each value is plotted as a function of $\sin^2\psi$. The macrostresses can be determined from the slope of the linear fit or from the intercept with the y-axis.

The angle between lattice planes for a cubic system can be calculated using Equation (22).

$$\cos\phi = \frac{h_1 h_2 + k_1 k_2 + l_1 l_2}{\sqrt{(h_1^2 + l_1^2 + l_1^2)(h_2^2 + l_2^2 + l_2^2)}} \qquad (22)$$

4.2.5 Conventional angle-dispersive X-ray diffraction

A Bruker AXS D8 Discover X-ray diffractometer equipped with an Eulerian cradle and operated with Cr-K_α radiation was used for qualitative phase analysis, line profile analysis and quantitative crystallographic texture analysis. A Göbel mirror was used to obtain a high intense, parallel beam for phase analysis and line profile analysis and limits the error caused by sample displacement. The setup can be seen in Figure 29. The calculated penetration depth (i.e. the depth from where 63% of the diffracted beam comes from) in iron corresponds to a maximum of about 6 µm within the measured range of diffraction angles up to the possible 160 °2Θ. The Eulerian cradle enabled the rotation of the sample around the sample surface normal (φ) and an azimuth angle (ψ) being the inclination angle between diffraction vector and sample surface normal.

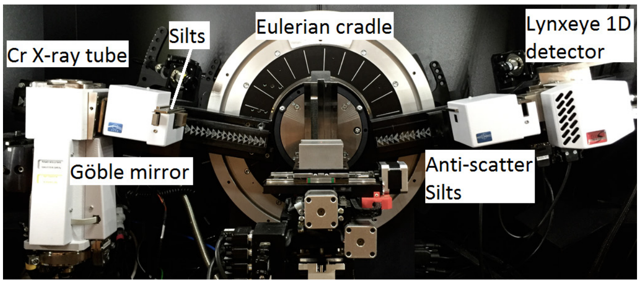

Figure 29: Picture of the X-ray diffraction setup used for phase analysis and line-profile analysis.

4.2.6 Energy-dispersive synchrotron diffraction

Energy-dispersive diffraction (EDD) was performed in-situ and ex-situ at the synchrotron facility BESSY II at the EDDI beamline. In EDD, a white X-ray beam with a continuous photon energy spectrum is used at a fixed diffraction angle 2Θ. The diffraction occurs for the planar lattice spacing d_{hkl} at a photon energy E_{hkl} as shown in Equation (23) [43],

$$E_{hkl} = \frac{h\,c}{2\sin\Theta} \cdot \frac{1}{d_{hkl}} \qquad (23)$$

where h is Planck’s constant and c is the speed of light.

The schematic layout of the beamline components can be seen in Figure 30. The energy spectrum is recorded by a germanium detector and a complete diffraction spectrum with a multitude of diffraction lines, E_{hkl}, is recorded simultaneously under fixed geometrical conditions. The sample is positioned on an Eulerian cradle that allowed for rotation of the sample to acquire diffraction spectra with an azimuth angle up to 75°. The phase analysis needs to take into account that diffraction peaks also contain the fluorescence lines from elements within the materials and escape peaks from the detector in addition to the Bragg peaks from the sample [44]. The fluorescence lines for all elements can be found in [45]. The escape peaks are measured at a distance of -9.876 keV and -10.983 keV from Bragg reflections of high intensity.

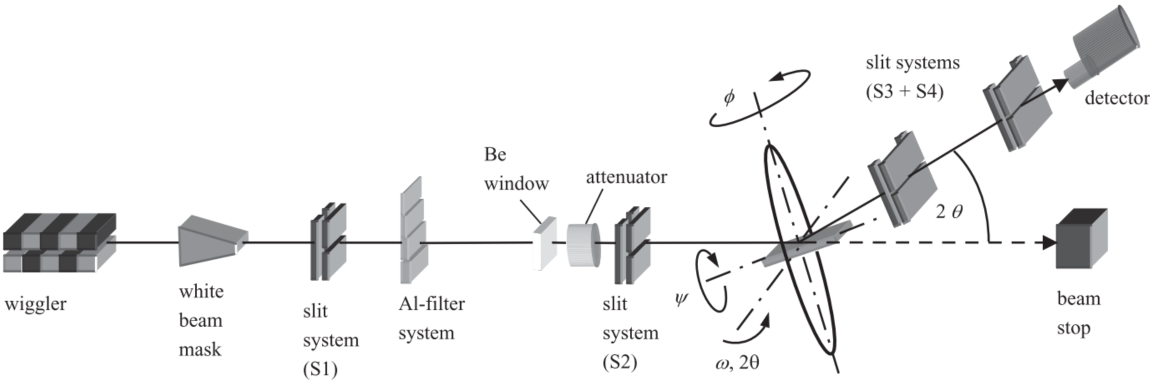

Figure 30: Schematic layout of the main beamline components. Figure from [43].

The opening of the slit system S2 was adjusted to achieve a high flux when the experimental setup did not include rotation or inclination of the sample or for the depth resolved phase analysis. The diffraction angle of 2Θ was adjusted to match the experimental purpose and a small angle was used to increase the distance between the peaks with the consequence of losing the higher order peaks. The low diffraction angle setup (2Θ = 8°) was used to investigate the development and thermal evolution of the oxides and carbides during in-situ annealing. A diffraction angle setup with (2Θ > 8°, up to a maximum of 26°) was used to investigate the higher order reflection from the ferrite peaks for selected measurements.

Owing to the different photon energies, the structural information contained in each diffraction line at the energy E_{hkl} has to be assigned to different average information depths [43]. For the applied symmetric diffraction geometry and a diffraction angle of 2Θ = 8°, which remains fixed during the measurement, the 211 reflection of iron corresponds to an information depth of about 67 µm.

In addition to the abovementioned measurements in reflection geometry, selected samples have been measured in transmission. The high beam flux at the EDDI beamline and the low beam divergence enable the application of a narrow slit system (S1 and S2 in Figure 30) for the incoming beam to define a small gauge volume having a height around 10 µm [37]. The small gauge volume allows for depth revolved phase analysis for the Fe-C coating measured in transmission.

Alternatively, to the EDDI beamline at the synchrotron facility, a laboratory EDD diffractometer was used for selected samples, which were measured after shut down of the dedicated beamline at BESSY.

4.2.7 In-situ annealing

The synchrotron EDD has the advantages of a high flux that allows for short recording times with good counting statistic and it measures a complete diffraction pattern at a fixed diffraction angle 2Θ. This enables in-situ annealing measurements that can detect phase evolutions with a high resolution in regards to time and/or temperature. The in-situ annealing experiments were performed in an Anton Paar DHS 1100 Domed Hot Stage under continuous flow of inert argon gas at a constant pressure of 1.4 bar. Both isochronal and isothermal annealing experiments were carried out. The sample was clamped onto the heating stage to avoid lifting or bending at elevated temperatures as shown in Figure 31. Scrap iron was placed inside the heating chamber to avoid oxidation of the Fe-C coating. The temperature was measured with a Pt-Pt10Rh thermocouple fixed to the stage.

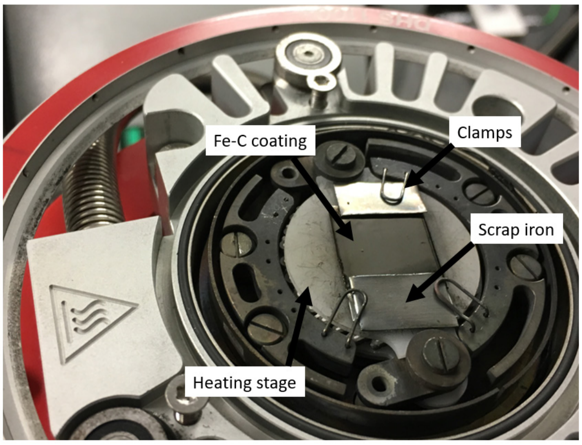

Figure 31: The Anton Paar DHS 1100 heating dome stage with a Fe-C sample clamped to the stage.

4.2.8 Experimental setups and data analysis

4.2.8.1 Peak fitting for conventional XRD

The commercial software Topas 2.1 was used to fit the diffraction peaks using a pseudo-Voigt function, which is a super position of a Lorentz and Gauss function. The fitting procedure takes into account the contribution from the $K_{\alpha 1}$ and the $K_{\alpha 2}$ components of the applied X-rays and corrects for instrumental background. The following parameters are obtained for each fitted peak:

- The 2Θ peak position.
- The integrated intensity.
- The full-width-half-maximum.
- The Lorentz factor (contribution of Lorentz and Gauss profiles)

A quartz standard sample was used to correct the possible offset of the measured peak positions.

4.2.8.2 Peak fitting for energy-dispersive diffraction

The data analysis of the EDD spectra was done using a Matlab-routine provided by the beamline scientists at the EDDI-beamline at BESSY II. The Matlab-procedure ensures that the spectra are corrected for ring-current, wiggler spectrum, and absorption. A peak fitting procedure is included that uses the pseudo-Voigt function and provides the relevant peak parameters as described above for further analysis. A gold reference standard was used for calibration of the energy offset.

4.2.8.3 Phase analysis

The qualitative phase analysis was carried out on the as-deposited Fe-C coatings and ex-situ annealed Fe-C coatings to investigate the phases present in the microstructure using both conventional XRD and EDD. A symmetric beam path was applied. For selected samples, as an attempt to improve the phase analysis, the azimuth angle of the sample was varied to change the diffraction conditions and to allow the detection of phases with a specific crystallographic orientation. The measured phases in the Fe-C coating are identified according to a match with a reference powder diffraction file (PDF) by the International Centre for Diffraction Data (ICDD).

4.2.8.4 Line profile analysis

The line profile analysis has been conducted using conventional XRD and EDD. Independent of the method of characterization, a LaB_6 powder reference sample was measured to correct for the instrumental peak broadening. The diffraction patterns for LaB_6 were measured using the same experimental setups that were applied for the measurement of the Fe-C coatings. The integral breadth of the LaB_6 peak that was closest to the 2Θ peak position of the sample peak being analyzed was used for correcting of the instrumental broadening. The individual integral breadth of the Gaussian and Lorentz contributions corresponding to the physical broadening of the pseudo-Voigt function and the Lorentz factor using the equations and the required empirical coefficients described in Appendix 1 of chapter 5 in [46].

The strong texture and limited number of peaks for the Fe-C coating measured using Cr-K_α radiation prevented the Williamson-Hall plot from being applied for conventional XRD. Only, the α-110 peak could been analyzed by the single line method for conventional XRD, as the substantial peak broadening of α-211 exceeds the available measurement range.

The EDD spectra allowed the higher order peaks for ferrite to be used for line-profile analysis.

4.2.8.5 Texture analysis

The quantitative crystallographic texture analysis was performed using conventional XRD and measured the 110-, 200- and 211-pole figures of α-Fe applying sample rotations around the surface normal (φ, $0° \leq \varphi \leq 360°$, step size 5°) and sample tilts around the azimuth angle (ψ, $0° \leq \psi \leq 75°$, step size 5°). The measured intensities were corrected for background intensity, and a Fe-powder standard was used to correct for defocusing associated with tilting. The orientation distribution function (ODF) was calculated in MTEX using the zero-range method [47]. The maxima in the inverse pole figures in normal direction to the substrate were used to determine the fiber axis <uvw>, as ideal fiber textures apply for all Fe-C coatings.

4.2.8.6 Stress analysis

The as-deposited Fe-C coating has been measured at the azimuth angles from 0 to 75° in steps of 1° using EDD. Such fine tilt angles in steps of 1° are not required for the $\sin^2\psi$ method or the crystallite group method but allowed the measurement to be applied for other analysis as well. The sample was not rotated around φ as a rotational symmetric stress state is assumed. A gold standard was measured under similar conditions to calibrate each diffraction spectrum for energy offset.

The measured reflections for each spectra that could be reliable fitted were included in the $\sin^2\psi$ method, but the strong fiber texture of the Fe-C coating hindered the analysis of macrostresses.

The angles between lattice planes and the <311> orientation of ferrite are shown in Table 7 and only these hkl-specific peaks in the measured spectrum at the specific azimuth angles were included in the crystallite group method.

Table 7: Angle between different lattice planes and the <311> orientation of ferrite.

<hkl>	110	200	211	220	310	222	321
Azimuth angles [°]	31	25	10	31	17	31	14
	64	72	42	64	40	64	36
			60		56		50
			75		68		62
							71

The peaks that could not be fitted reliably, because of low intensity, were disregarded. It was not possible using the crystallite group method to perform a linear regression between the measured lattice strains as a function of $\sin^2\psi$ and the experiment was not further evaluated.

4.3 Microstructure investigation

In this section, the general principle of light optical and electron microscopy will be given followed by the advanced methods of characterization accessible on the electron microscopes, such as selected area electron diffraction (SAED), electron energy-loss spectroscopy (EELS) and energy-dispersive spectroscopy (EDS). In addition, experimental methods of sample preparation using the focused ion beam (FIB) installed on the dual beam scanning electron microscope are described.

4.3.1 Light optical microscopy

The LOM uses visible light and a system of lenses to magnify images of small objects. The best resolution of a common LOM is around 200 nm for a metallographically prepared sample [48]. The use of the Zeiss AXIO LOM was limited by the nanocrystalline microstructure of the Fe-C coating and is therefore used solely to measure:

- The thickness of the deposits, including the thickness homogeneity
- The diagonals of the Vickers hardness indentation
- The crack length in the coating/substrate interface induced by a dedicated Vickers indentation for adhesion testing

The samples were metallographically prepared as cross sections by either hand polishing, a Struers RotoPol or a Struers Abramin prior to the investigations. The preparation procedure varied depending on the experimental setup, but in general, the samples were cold embedded in epoxy for cross section analysis. The embedded samples were ground using a 220 SiC grinding paper until the whole area of the samples was affected. Thereafter were the samples ground for 3 min in steps using 500, 1000 and 4000 SiC papers. The samples were cleaned in an ultrasound bath with ethanol before they were polished for 3 min using 3 µm diamond paste on a Struers MOL plate and afterwards using 1 µm diamond paste on a NAP plate. Different etching solutions were used on the polished samples depending on the requirements of experimental characterization:

- OPS was used for final polishing and to reveal microstructure features
- Nital was used for revealing the microstructure features
- Murakami was used to investigate the precipitation of carbides

4.3.2 Scanning electron microscopy

The scanning electron microscope (SEM) produces images of a sample by scanning the surface with a focused beam of electrons. The high-energy electrons interact with the specimen in a pear-shaped interaction zone and produce secondary electrons (SE), backscattered electron (BSE) and characteristic X-rays that can be detected using different detectors installed in the microscope.

4.3.2.1 The microscopes

A FEI Helios EBS3 dual beam SEM was used for imaging using SE to investigate topographical features and the morphology of the microstructure on metallographically prepared cross sections. The gallium ion source installed on the FEI Helios EBS3 dual beam was mainly used for sample preparation and for sputtering of material required for the ring-core milling technique.

A FEI Nova NanoSEM 600 equipped with a Bruker e-FlashHD EBSD system was used for transmission Kikuchi diffraction (TKD).

4.3.2.2 Imaging

The SE was used to investigate the topography and microstructure of the Fe-C coating. It was a challenge to obtain sharp micrographs at high magnification of the microstructure as the average grain size of the Fe-C coating is close to the spatial resolution of the microscope.

The BSE was not applied, because the Fe-C coatings mainly consist of iron and the spatial resolution would not match the resolution required to investigate the position of the light elements.

4.3.2.3 Energy-dispersive spectroscopy

The use of the characteristic X-rays for chemical analysis was avoided because the investigation would have focused on the light elements carbon and oxygen. The FEI microscopes were not equipped with a cold-finger that could limit the carbon contamination produced by the electron beam on the surface of the sample. The carbon contamination would lead to an increased signal from carbon and provide an experimentally error that cannot be corrected afterwards.

4.3.2.4 Transmission Kikuchi diffraction

Electron backscatter diffraction (EBSD) is a technique to determine the crystallographic orientation of individual grains within a polycrystalline specimen and to identify separate crystalline phases [48]. The formation of TKD patterns by transmission through an electron transparent specimen in the SEM is a technique that improves the spatial resolution compared to EBSD and a spatial resolution around 15 nm can be obtained [49]. The electron transparent lamellae that were investigated by TKD provided only a few of the Kikuchi patterns of high quality that could be matched during an area scan. The TKD measurement was not continued further, as the requirement for the optimization of the experimental procedure for the present samples did not uphold the potential advantage of the technique. The investigated electron transparent lamellae covering both coating and substrate can be seen in Appendix 12.2.

4.3.2.5 Ring-core milling

The macrostresses of the Fe-C coating can be investigated on the surface using the FIB ring-core milling technique [50,51]. The ring-core-milling requires a stable microscope with no beam drift during the milling process. This was not achieved using the FEI Helios EBS3 dual beam SEM and the investigation was halted after a few unsuccessful attempts. The SEM micrograph and image correlation procedure of the ring-core milling investigation can be seen in Appendix 12.4.

4.3.3 Transmission electron microscopy

4.3.3.1 The microscopes and software

The transmission electron microscope (TEM) investigations were carried out using different microscopes depending on the specific investigation.

A Joel 3000F (300 keV) and a JEOL 2100 (200 keV) was mainly used for obtaining bright-field (BF) and dark-field (DF) micrographs and for SAED.

A Titan Analytical 80-300ST (300 keV) was used for high resolution BF and EELS.

The commercial available software DigitalMicrograph 3.21 and JEMS 4.56 were used for phase identification of SAED patterns and for crystallographic orientation determination. The SAED patterns were calibrated using a gold reference standard acquired with the same microscope settings.

4.3.3.2 Sample preparation

Electropolishing of the free-standing Fe-C coatings, which were directly deposited as a 3 mm disc as shown in Figure 26 was tried for subsequent TEM analysis, but the samples fractured when pressure was applied during clamping in the sample holder for the Struers TenuPol-5.

An electropolished electron transparent sample of an as-deposited Fe-C coating in cross section was prepared for TEM investigation. The electropolishing was initiated because it is more gentle (and free of artefacts) compared to FIB lift-out preparation. However, the electropolished Fe-C coating was severely oxidized by the electropolishing solution, which limited the use of this sample.

Instead, the electron transparent lamellas used in TKD, TEM, and atom probe tomography investigation were prepared using the FIB lift-out technique. The nanocrystalline Fe-C coating with columnar grains requires the production of two types of samples for a full investigation of the morphology of the nanocrystalline grains.

The samples were prepared in plane-view (parallel with the surface) where the electron beam is parallel with the growth direction of the coating, thus, along the length of the columnar grains. The plane-view samples have the benefit that the number of overlapping grains is reduced and the chemical investigation of the elements within the grain boundaries is less affected. The samples prepared in cross section are investigated with the electron beam being perpendicular to the long direction of the elongated columnar grains and the length and width of the grains can be investigated. The position of the region-of-interest (ROI) on the Fe-C coating determines the type of lamella that can be produced and different positions of the ROI along with the lamellas possible purposes is shown in Figure 32a. The spotted specimen stub for SEM as shown in Figure 32b, was used as a sample holder for FIB lift-outs procedure from the Fe-C coating cross section.

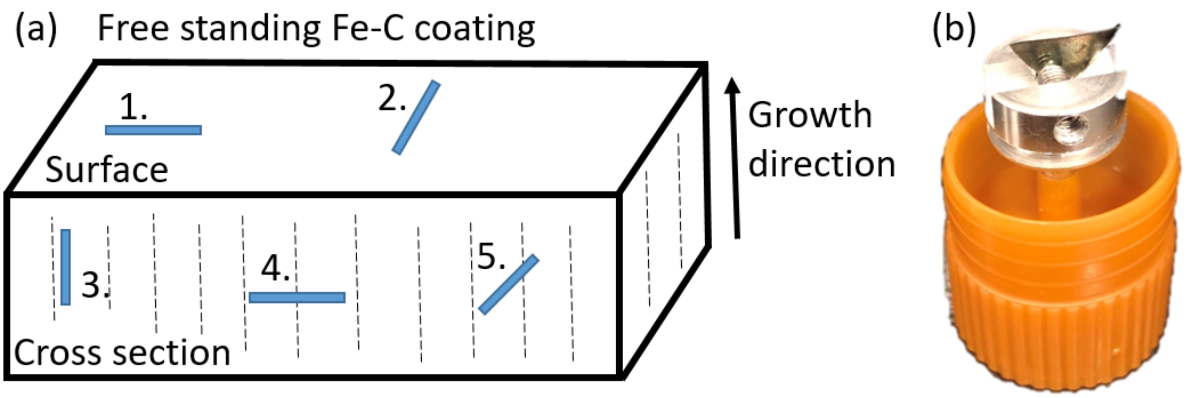

Figure 32: (a) Illustration of a free-standing Fe-C coating with different regions-of-interest (blue lines) marked for FIB lift-out and the resulting purpose of the lamellas; (1-3) TEM lamella prepared in cross section and apt needles with the grain boundaries being perpendicular to the direction of the needle, (4) TEM lamella prepared in plane view and (5) apt needles with the grain boundaries having a 45° angle compared to the direction of the needle. (b) SEM sample holder for sample preparation from the cross section of a free-standing coating.

An illustration of the FIB lift-out procedure is shown in Figure 33 and the following setting was used in each step:

1: Find a ROI and apply a protective platinum layer (1-2 µm) using an ion beam (30 kV, 0.26 nA)

2-3: Use the ion beam (30 kV, 9 nA) to sputter away material from both sides of the ROI, using regular cross section and parallel pattering.

4-5: Use the ion beam (30 kV, 0.9 nA) to clean each side of the ROI and thin the lamella to around 0.6-1 µm, using cleaning the cross section[4] on one side at a time.

6: Use the ion beam (30 kV, 0.9 nA) to perform an L-shaped undercut (sputter the lamella free in one side and at the bottom), using two rectangles and parallel patterning.

7: Weld the tip of the Omniprobe to the upper corner of the lamella with platinum deposition using the ion beam (30 kV, 26 pA)

8: Use the ion beam (30 kV, 0.9 nA) to free a lamella by sputtering the remaining side attached to the sample, using a rectangle patterning.

---

[4] The ion beam mills line by line of a rectangular area towards one side of the pattern

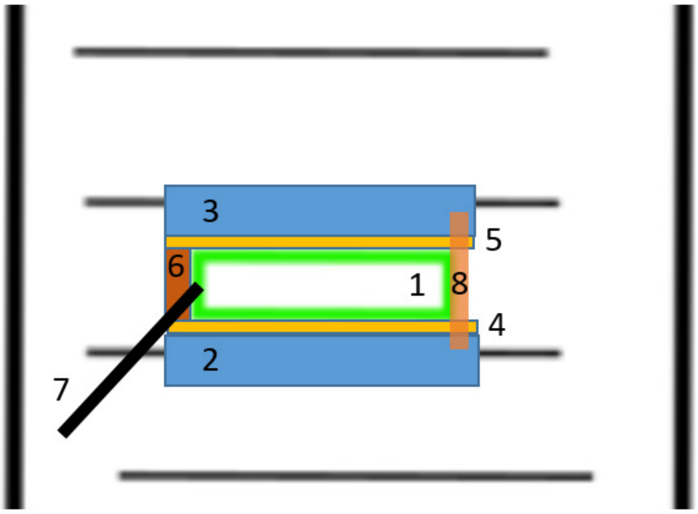

Figure 33: Illustration of the lift-out procedure for an electron transparent lamella. (1) Platinum deposition on region-of-interest, (2-3) rough FIB-milling, (4-5) FIB-cleaning, (6) FIB-undercut, (7) attach Omniprobe and (8) FIB-milling to free lamella.

The lamella attached to the Omniprobe was transported and welded by platinum deposition to a TEM 3 mm standard copper grid using the ion beam (30 kV, 26 pA) for TEM and TKD investigation. The lamella was thinned using the ion beam in order to become electron transparent using the following procedure.

9: Thin one side of the lamella using the ion beam (30 kV, 0.9 nA) and a cleaning cross section pattern. The sample is slightly over-tilted in order to remove material from the bottom first. The tilt angle is aligned to ensure the lamella is tilted so the top and bottom are intact during thinning.

10: Repeat 9. for the other side of the lamella

11: Thin the first side of the lamella using the ion beam (30 kV, 0.44 nA) and a cleaning cross section pattern. Use the electron beam to image the sample regularly and ensure the lamella is tilted so the top and bottom are intact during thinning.

12: Repeat 11. for the other side of the lamella

13: Repeat 11 with a lower current for the ion beam (30 kV, 90 pA)

14: Repeat 13 for the other side of the lamella.

The sample's final thickness depends on its intended use. A thickness of around 100 nm is suitable for electron diffraction experiments, but a thinner sample is required for high-resolution BF imaging and EELS.

When the lamella has been thinned to its intended thickness a low voltage cleaning step is done using the ion beam (5 kV, 26 pA) on both sides of the lamella.

4.3.3.3 Imaging

The primary beam of high-energy electrons interact with the specimen by different mechanisms that produce the contrast seen in the image. The electrons also generate characteristic X-rays during the interaction with the samples that can be detected using EDS. The contrast in the micrograph is generated by the mass-density, diffraction and/or phase contrast mechanisms [52]. The two types of imaging modes used were BF and DF.

4.3.3.4 Electron diffraction

The electron diffraction in a TEM specimen follows the same theory as for XRD, which is described in Section 4.2, and the Bragg equation relates the lattice spacing and scattering angle and the wavelength of the electrons. A selected area diffraction (SAD) aperture is used to limit the area of interest. Dependent on the crystallite size, different diffraction patterns can be measured as shown in Figure 34. The single spots will correspond to specific lattice planes in the phase having a large crystallite size or being single crystal. The distance from the center spot to the diffraction spot, can be converted to the corresponding lattice spacing within a phase and the angles between the spots can be used for phase identification and to determine the crystallographic orientation. A diffraction pattern from more than one grain consists of a number of patterns rotated around the center. For nanocrystalline materials, a small SAD aperture is important to identify each of the phases and the crystallographic orientations. In nanocrystalline materials, the diffraction pattern will appear like full circles, consisting of multiple single crystal diffraction patterns rotated around the center.

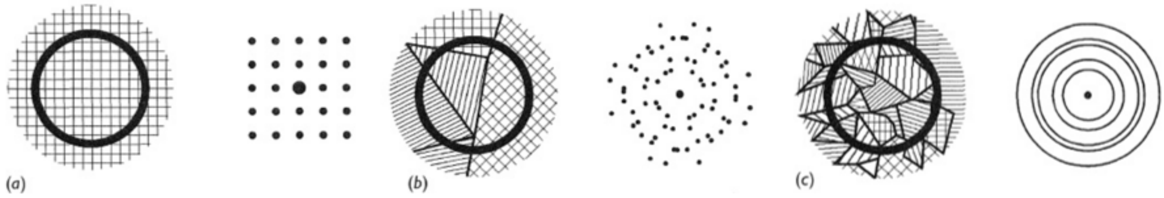

Figure 34: Types of diffraction patterns seen in TEM. (a) large crystallite or single crystals, (b) polycrystalline material with more grains in the ROI and (c) nanocrystalline material with multiple grain in the ROI. Figure from [1].

The presence of a strong texture in the measured Fe-C coating lead to an uneven distribution of diffraction spots along the rings, which would appear in a randomly oriented sample, so they become visible as arcs. Some of the different types of diffraction patterns that can be measured for a texture material are shown in Figure 35 [53].

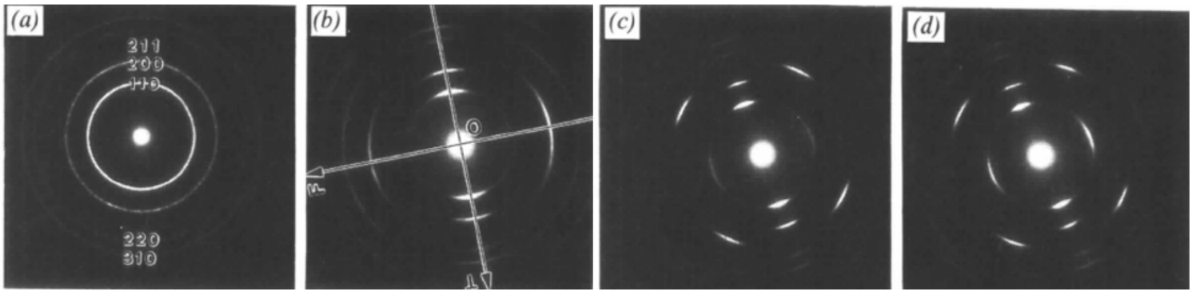

Figure 35: Types of diffraction patterns seen in TEM of a textured bcc. Cr film at (a) 0, (b) 21, (c) 38, and (d) 43° tilt. Figure from [53].

Also converged electron beam diffraction patterns and Kikuchi patterns were recorded to identify a phase and determine its crystallographic orientation. However, the nanocrystalline grain size of the Fe-C coating resulted in overlapping grains in the electron transparent lamellas and hindered the analysis.

The crystallites related to a diffraction spot can be visualized by using a small objective aperture in combination with tilting the primary electron beam. The objective aperture is positioned on the transmitted beam spot (center spot) and the primary electron beam is tilted until the diffraction spot of interest is centered in the aperture. The contrast of the DF image will consist of the electrons diffracted by the crystallites having that specific crystallographic orientation.

4.3.3.5 Chemical analysis

4.3.3.5.1 Energy-dispersive spectroscopy

EDS is possible in TEM and can be used to analyse the concentration of elements in a specimen. The analysis is an automated process done by software where different settings can be applied as mapping of an area or a point analysis. A cold finger is installed in the TEM to lower the carbon contamination on the sample produced by the high-energy electron beam. The quantified measurement of light elements is still however susceptible for this type of error and EDS measurements were not carried out due to the risk of over interpretation of untrustworthy data.

4.3.3.5.2 Electron energy-loss spectroscopy

The EELS measures how many electrons have lost an energy due to inelastic scattering [54]. The convergence of the electron beam has an effect on the spatial resolution of the analysis and elemental quantification can be obtained with nanometer precision. The spectrum can be roughly split into two different regions: the low-loss spectrum and the high-loss spectrum. The low-loss spectrum contains the zero-loss peak and the plasmon peaks, and will not be discussed in details. The main energy loss mechanism is ionization in the high-loss spectrum. Electrons belonging to localized orbitals are excited to unoccupied energy states above the Fermi level of the specimen. These energy loss is characteristic to the species present in the sample, and as such can be used to obtain accurate information about the chemistry of a sample. The EELS analysis was used to localize the position of carbon and oxygen in the nanocrystalline iron microstructure, by measuring an EELS spectrum across several grains. However, the measured carbon signal indicates a carbon contamination on the sample produced by the high-energy electron beam and the result is therefore only included in the Appendix 0. The characteristic energy loss for carbon, oxygen and iron is [54]:

- Carbon: 280-320 eV
- Oxygen: 500-550 eV
- Iron: 700-730 eV

4.4 Chemical Analysis

4.4.1 Glow discharge optical emission spectroscopy

The glow discharge optical emission spectroscopy (GDOES) measurements were performed for the depth resolved investigation of the chemical composition of the coatings. A Horiba GD profiler 2 was used for all measurements. The instrument was calibrated to quantify carbon and iron using several reference samples of low alloyed steel with different carbon content up to 1.3 wt%. Further elements than carbon could not be quantified and will be presented as the measured signal [V] for each elements.

The measurement technique is strongly dependent on the material examined and a series of measurements were performed on identical Fe-C coatings in order to find the optimum experimental parameters of power and pressure that would create a flat crater profile. Multiple samples of approximately 10 µm Fe-C coatings were deposited on a brass substrate in order to measure the interface between the coating and the substrate with a high precision. A series of measurements using different instrumental values of power and pressure were conducted and the crater profiles were investigated using an Alicona Infinite Focus microscope to create a 3D surface measurement as shown in Figure 36. The optimal setting for creating a homogeneous material removal in the bottom of the crater was obtained with a power of 1000 W and a pressure of 50 Pa, and these conditions have been used for all measurements reported in this thesis.

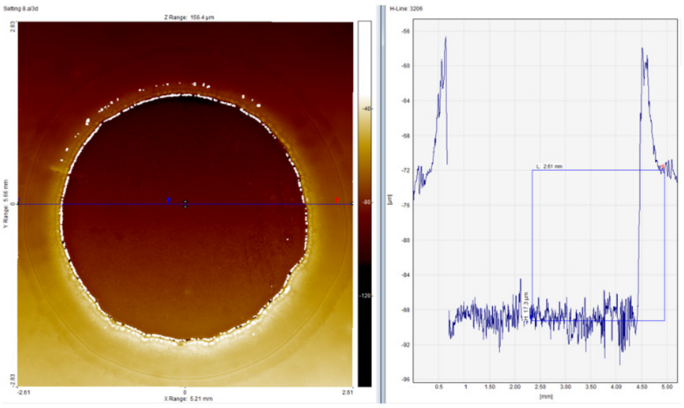

Figure 36: 3D surface map and crater profile of GDOES measurement using an power of 1000 W and a pressure of 50 Pa.

4.4.2 Evolved-gas-analysis

The carbon content in the Fe-C coatings was determined using a carbon analyzer LECO CS230, which measures the amount of CO_2 evolved by high-frequency induction heating of the sample in an O_2 atmosphere. The measurements were performed using an amount of 0.1 g of a free-standing Fe-C coating. The instrument was calibrated using multiple low alloy steel reference samples having a carbon content up to 3.41 wt%.

4.4.3 Atom probe tomography

The atom probe tomography (APT) uses a field evaporation of atoms to build a 3-dimensional reconstruction of the evaporated volume by analysis of the time of flight and the impact on a 2D detector of the individual ions [55]. APT investigations were carried out at CNRS, Normandie University in Rouen, France on a CAMECA LEAP 4000 HR atom probe. The APT samples were prepared by the FIB lift-out procedure and using the microloop method. However, the sample broke shortly after the measurement was initiated and therefore only a limited amount of data was obtained. The APT analysis and limited results are described in Appendix 12.1.

4.5 Thermal analysis

The thermal analysis was done in order to investigate the Fe-C coatings' thermal stability. It revealed the occurring phase transformations in-situ and correlates them with the desorption of co-deposited elements and associated mass changes.

4.5.1 Experimental setup

Simultaneous thermogravimetry (TGA) and differential thermal analysis (DTA) were performed in a Netzsch STA 449F3 coupled with a Netzsch QMS 403 Aëolos quadrupole MS. The setup enables the detection and identification of evolved gases in time correlation with enthalpy and mass changes. The MS is an analytical technique that measures the mass-to-charge ratio of ions and can identify the elements in the evolved gas. The in-situ isothermal and in-situ isochronal annealing experiments were performed both individually and in combination.

A free-standing Fe-C coating weighing about 250 mg was placed in an alumina crucible. The sample chamber was pumped to vacuum and flushed with argon three times prior to each measurement. Heating was carried out in an inert atmosphere created by flowing argon gas through the chamber, unless otherwise mentioned. The MS was set to measure the mass to charge ratio from 0 to 50 u, to ensure a rapid measuring frequency and good time correlation with the DTA and TGA signal. The sample was hold for 2 hours at 40 °C to ensure a stable and consistent environment before the first heating cycle and in between the sequential heating cycles. The commercial software NETZSCH Proteus thermal analysis 6.1.0 was used for data analysis. The identification of elements measured by the MS was based on the mass to charge ratio. For example, water (H_2O^+) and carbon dioxide (CO_2^+) will be measured at 18 and 44 u, respectively.

4.5.2 Isothermal analysis

The in-situ isothermal annealing was done to anneal a sample over a period of time at a fixed temperature and evaluate the desorbed gases and mass loss. The setup was also used as a furnace for producing samples used for ex-situ XRD phase analysis or hardness measurements on annealed coatings. The benefit of the Netzsch STA 449F3 is that the small sample chamber causes only an insignificant temperature gradient. Further, the temperature sequence can be programmed to ensure the same heating or cooling rate is used for different samples and the time at the holding temperature is exact.

4.5.3 Isochronal analysis

The in-situ isochronal annealing revealed the temperature of specific phase transformations and the enthalpy of transformations. An exothermal reaction will release energy and an endothermal reaction will consume energy. For example, the precipitation of carbides are measured as exothermal [56] and the phase transformation of ferrite to austenite is endothermal. The heating rate (Φ) was adjusted to fit the experimental purpose. A low heating rate will produce a smaller energy signal that is closer to the equilibrium temperature for the transformation and a high heating rate will produce a stronger signal but the phase transformations are shifted to higher temperatures. The coupling with MS provides the possibility to measure if the light elements are desorbed from the sample during the phase transformation and can help with the identification of a specific transformation.

A sample was subjected to two or three heating cycles using the same temperature range and heating rate for isochronal analysis. The first and second isochronal annealing were adjusted for instrumental background by using the second and third isochronal annealing, respectively.

4.5.4 Evaluation of activation energy

The in-situ isochronal annealing was performed using different heating rates to measure the change in temperature of a specific phase transformation and calculate its activation energy by means of the Kissinger analysis [57,58].

A phase transformation can be traced as a function of time and temperature. The temperature determines the atomic mobility and the time defines the duration of the process. The fraction of a phase transformed (*f*) from one state to another can be expressed using Equation (24).

$$f = \frac{(p(t) - p_0)}{(p_1 - p_0)}, \text{with } 0 \leq \text{f} \leq 1 \tag{24}$$

With $p(t)$ being the physical property of the material investigated at a specific time and p_0 and p_1 correspond to the initial and final state of the transformation, respectively.

The variable (*β)* is applied to describe the path of the transformation because the variables time and temperature are not suitable alone. The variable β is proportional to the temperature and time as shown in Equation (25) and (26), assuming the transformation mechanism is invariable in the temperature-time region [56].

Isothermal annealing

$$\beta = k(T)t \tag{25}$$

Isochronal annealing

$$\beta = \int k(T)dt \tag{26}$$

where $k(T)$ is the rate constant at a specific temperature. The rate constant for the isochronal annealing is time dependent whereas it is a fixed constant using the isothermal annealing. The Arrhenius equation is adopted for the rate constant as shown in Equation (27)

$$k = k_0 \cdot e^{\frac{-E}{RT}} \tag{27}$$

where k_0 is the pre-exponential factor and E is the activation energy.

The activation energy for an isothermal analysis can be obtained from the length of time between two fixed stages of transformation f_1 and f_2 measured at different temperatures as shown in Equation (28)

$$\ln(t_{f2}\text{-}t_{f1}) = \frac{E}{RT} - \ln(k_0) + \ln(\beta_{f2}\text{-}\beta_{f1}) \tag{28}$$

The activation energy was determined by plotting $\ln(t_{f2}-t_{f1})$ as a function of 1/T and using the slope of a linear regression between the points.

The activation energy for an isochronal analysis can be obtained with the approximation that allows the use of Equation (29), i.e. the temperature integral approximation and a constant heating rate is applied [57].

$$\beta = \frac{T^2 \cdot \mathrm{R} \cdot \mathrm{k}}{\Phi \cdot \mathrm{E}} \tag{29}$$

The activation energy can be determined from the temperature of a fixed stage in the transformation ($T_{f'}$) measured using different heating rates as shown in Equation (30)

$$\ln\left(\frac{T_{f'}^2}{\Phi}\right) = \frac{E}{R \cdot T_{f'}} + \ln\left(\frac{E}{\mathrm{R} \cdot k_0}\right) + \ln(\beta_{f'}) \tag{30}$$

The activation energy is determined by plotting $\ln(T^2_{f'}/\Phi)$ as a function of $1/T_{f'}$ and using the slope of a linear regression between the points. The values for $T_{f'}$ refer to the maxima of exothermic peaks, which were determined by fitting a Gaussian function to the background subtracted peaks.

4.5.5 Chemical analysis for oxygen and hydrogen

The amount of co-deposited hydrogen trapped at possible trapping sites (grain boundaries, dislocations and microvoids) was quantified using the mass loss measured by TGA after isothermal annealing at low temperature in an inert atmosphere.

The amount of oxygen was analyzed using a reducing H_2 atmosphere, high temperatures and a long duration, although the reduction of the developed oxides provided a challenge for the technique.

A detailed description of the experimental procedure and the results of the quantified amount of hydrogen trapped at grain boundaries, dislocations and/or microvoids and the reduction of the developed oxides at high temperature are provided in Section 7.2.2.

4.6 Mechanical testing

4.6.1 Microhardness measurements

A Future Tech Inc. FM700 and a Struers DuraScan microhardness tester with Vickers geometry were used to measure the microhardness of Fe-C coatings from their surface and from the metallographically prepared cross section. The microhardness measurement from the cross section was positioned in the middle of the coating and the load was varied for different samples to ensure that the distance from indent to the interface and surface was minimum 2.5 times the diagonal of the indent. The indent was positioned at least 3 times the diagonal of the indent away from one another. The microhardness depth profile on the cross section of the Fe-C coating was performed using the Struers DuraScan, where the position of each indent was programmed. Multiple rows were used to maintain the required distance between the individual indents and still provide a high resolution as shown in Figure 37.

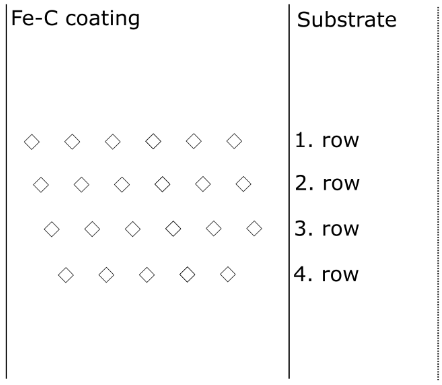

Figure 37: Illustration of microhardness depth profile.

4.6.2 Adhesion testing using the interface indentation test

The adhesion of the Fe-C coating was investigated by applying a microhardness Vickers indentation in the interface of the coating and the substrate, which was carried out for the example of deposition on a hardened Calmax steel. The load of the indentation was varied and the development of cracks in the interface from the indentation was investigated by LOM. As the method does not provide absolute values, but rather allows the comparison of different samples, it was applied to test the different pre-treatments of the substrate before deposition. The substrate was pre-treated prior to the deposition using different acids and varied treatment times, which is described in detail in Manuscript IV.

The samples were not embedded in epoxy in order to avoid having material surrounding the sample. A special sample holder was required to fix the samples during the metallographic preparation as shown in Figure 38a and to ensure a 90° angle between the cross section and the sides that were used to fix the sample during the indentation as shown in Figure 38b. The setup produced a plane parallel cross section that was required for the microhardness indentations.

The cross section of the samples were grinded and polished on a Struers Abramin following the metallographic preparation as described in Section 4.3.1.

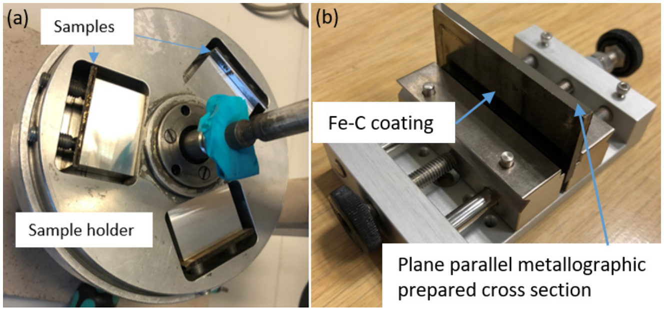

Figure 38: (a) Samples in the Struers Abramin sample holder for metallographic preparation of their cross section and (b) Fe-C coating deposited on hardened calmax steel with metallographic prepared cross section in the sample holder for interface indentation test.

The Future Tech Inc. FM700 was used for the microhardness indentations as the indent could be precisely positioned in the interface. The length of the cracks were determined by the LOM using a Struers DuraScan that allowed the samples to remain in the holder used for microhardness indentations during the capture of the micrograph of the cross section with the indent.

4.7 Deposit stress analyzer

The deposition of a relatively thin coating of 5 to 10 µm on a reference test strip can be used to evaluate the amount of stress that exist within the deposit. The setup of the commercial available deposit stress analyzer is comprised of a disposable metallic test strip and a measurement stand. The use of test strips of different metals can provide information about the substrate effect on the development of internal stresses. The test strip has two legs with one side of each leg being covered with a non-conductive film to avoid deposition. The test strip is placed on a test stand after it has been deposited and the distance that the test strip leg tips have spread is measured (U). The measured stresses are in compression if the deposited sides move towards each other and tensile if the deposited sides are away from each other. The example of a Fe-C coating deposited on a copper test strip with internal stresses measured as compressive is shown in Figure 39.

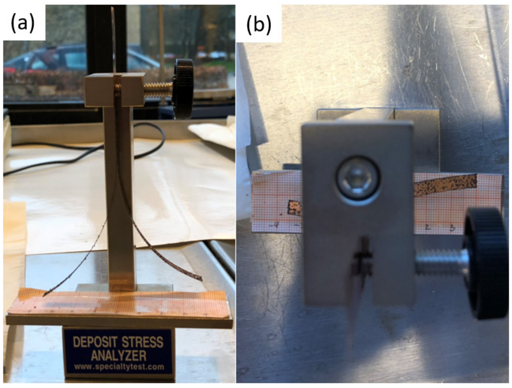

Figure 39: Deposit stress analyzer of Fe-C coating deposited on a copper test strip. (a) The leg of the test strip is shown to be separated. (b) The distance between the tips of legs can be measured and the deposited sides are towards each other revealing compressive stresses.

The thickness of coating (d) was determined by the weight gain of the test strip following deposition and using the density of the coating and the cathode surface area. The residual stresses in the deposit can be calculated using Equation (31).

$$\sigma_{RS} = U \cdot K \cdot R_E - 3d \tag{31}$$

where K is a calibration constant provided by the manufacture of the test strips and R_E is a correction factor for the difference in Young's modulus between the deposit and the substrate. The value of $K = 0.3771$ and $R_E = 1.2$ (for the Young's modulus of the Fe-C coating, 210 GPa was used and 175GPa for the copper test strip as provided by the supplier).

5 Summary of results

This Section provides a summary of the results, which in Chapter 6 and Chapter 7 are presented in form of manuscripts (either already published or planned for publication) and supplementary material. The summary is kept to a minimum and no references are given. For these, the reader is referred to the respective result chapters.

5.1 Manuscript I

Electrodeposition of iron with co-deposition of carbon – on the nature of nanocrystalline Fe-C coatings

The manuscript is addressed to the understanding of as-deposited coatings. The substrate-unbiased, thus only deposition dependent intrinsic growth, of the Fe-C coatings is investigated using amorphous substrates. The operation conditions during deposition are fixed with the exception of time, because the coating's evolution as a function of its thickness is of interest. The investigation is required as the growth type of the Fe-C coating is unknown and specific growth types can lead to a thickness-specific microstructure. The current efficiency influence on the coating thickness, and the resulting hardness, chemical composition, phase constitution, and crystallographic texture of the Fe-C coatings are analyzed.

The Fe-C coating is deposited as a nanocrystalline dense coating without cracks and the current efficiency of the deposition lowers for longer deposition. The carbon content is measured at 0.88 wt% and is homogenously distributed within the coating independent of the thickness. The Fe-C coating also includes hydrogen and oxygen, but their quantity could not be determined. The hardness of the coating is nearly 800 HV and independent of the thickness of the coating. The crystallite size and microstrain of α-110 are calculated by line profile analysis. The crystallographic texture of the coating consist of a strong <311> fiber texture. The strain-free lattice spacing of ferrite is measured and match that of carbon-free ferrite and reveal that the, often in literature proposed, terminology of "martensite" is not appropriate for the electrodeposited Fe-C coatings. Further peaks, certainly belonging to the same phase, are indicated in the measured XRD patterns, but of small intensities and all peaks are overlapping with the ferrite peaks expect one ("nameless peak"). The results suggest that an orientation relation exists between ferrite and the additional phase (in later manuscripts called the "nameless phase").

The initial investigations revealed a significant amount of results that were not included in the published manuscript. Among the results are the influence of the substrate on the resulting coating and stress measurements and these are instead provided in the supplementary material following the manuscript.

The results show that Fe-C coatings produced from the same operation conditions are comparable even when deposited in different thicknesses.

5.2 Manuscript II

Study of Fe-C coatings electrodeposited using specific operation conditions to control the mass transfer rate

The objective of the manuscript is the understanding of the effect of the operation conditions and the type of electrolyte on the resulting as-deposited state of the coatings. The operation conditions for electrodeposition of the Fe-C coatings are varied in order to investigate the optimal conditions in regard to the current efficiency and study the influence on the materials properties. The use of a sacrificial anode in an electrochemical deposition with a current efficient below 100% will increase the iron concentration as described in Section 4.1.1. The increased iron concentration can be countered by increasing the current density as a fixed ratio between these two parameters is expected to result in the same total overpotential according to the diagram of morphologies shown in Figure 4 of the thesis. The difference between a Fe-C coating deposited from the iron-sulfate and iron-chloride electrolyte with the same iron concentration and using otherwise identical operation conditions is also described in the manuscript. The current efficiency of the deposition process is measured along with the Fe-C coatings hardness, phase constitution, and carbon content. The applied cathode design allows the homogeneity of the Fe-C coating to be studied over the cathode surface area.

The XRD patterns for the Fe-C coating from the iron-chloride electrolyte measured the “nameless peak”, which conclude that this phase forms independent of the presence of sulphur. The material properties are identical for the ones for the investigated Fe-C coatings from an iron(II)sulfate based electrolyte, but the deposition rate and current efficiency are highest for the operation conditions using the highest iron sulfate concentration and current density.

The manuscript is followed by supplementary results from a design of experiment that varied the iron sulfate concentration, citric acid concentration and the current density to investigate these effects on the appearance of the Fe-C coating as the only material property being evaluated. The citric acid concentration strongly influences the appearance independent of the variation in current density and iron sulfate concentration.

The results show that it is possible to deposit Fe-C coatings with the same material properties over a wide range of iron sulfate concentration when the current density is managed accordantly.

5.3 Manuscript III

The influence of the electrolytes pH-value on the material properties of the electrodeposited Fe-C coating

In the present manuscript, the pH-value of the electrolyte is varied in order to investigate its influence on the resulting Fe-C coating. The pH-value of the electrolyte will change during deposition to higher or lower values depending on the applied type of anode as described in Section 4.1.1.3 and it is therefore essential to map the pH-region that is optimal for the deposition of the Fe-C coatings. The influence of the pH-value on the resulting coating was evaluated using the current efficiency of the process and the Fe-C coatings chemical composition, hardness, appearance, and phase constitution.

The analysis revealed that the current efficiency is lower when the pH-value of the electrolyte is below 2.5 compared to nearly 100 % for the samples deposited for 1 hour above this pH-value. The appearance of the coatings was similar for the depositions using a pH-value below 3.2 and the coatings deposited using a pH-value above 3.4 developed oxides on the surface shortly after deposition. The “nameless phase” was measured in the XRD patterns for the coatings deposited using a pH-value below 3.4 and the change in the measured intensity of the “nameless peak” as a result of the pH-value was discussed in relation to the measured changes in the peak profile for α-110. The carbon content of the coatings showed a maximum amount being co-deposited at a pH-value around 3.0. The trend in carbon content is discussed in relation to the complex ability between Fe^{2+} and citric acid as a function of the pH-value of the electrolyte. The hardness of the coating was independent of the pH-value used during deposition and the measured material and process variations as described above.

The experimental procedure using the same electrolyte for all depositions resulted in different carbon contents for samples deposited in the same pH-region. The difference could be estimated accurately by calculating the consumption of carbon in the electrolyte as a function of hours the electrolyte had been used for deposition. This result shows that it is possible to estimate the consumption of citric acid during deposition and it can be used as a method to calculate when citric acid is required to be replenished during longer operations using the same electrolyte.

The results shows that it is possible to deposit Fe-C coatings with the same hardness over a wide range of pH-values. However, the pH-value shall be maintained between 2.5 and 3.0 in order to produce a similar appearance, avoid the development of oxides, and have the highest current efficiency.

5.4 Manuscript IV

Screening of pre-treatments using the interface indentation test for optimizing the adhesion between the Fe-C coating and hardened tool steel

The influence of the pre-treatment applied to the substrate before deposition on the adhesion between the Fe-C coating and a hardened tool steel is investigated. To this end, a specific test method has been applied, which evaluates the response of the sample on a hardness indentation in the interface of the coating and substrate (interface indentation test). The adhesion between the deposit and the substrate is one of the most important properties for the restoration of a worn component and for a wear resistant coating, because any delamination of the deposit would result in failure during operation. The methods of characterizing the adhesion are destructive and often require special equipment for a reliable and reproducible test. The interface indentation test is a simple and reproducible method to evaluate the adhesion between the coating and a substrate by positioning a Vickers hardness indent directly in the interface of the coating and the substrate and evaluate the propagation of a likely crack.

A method to quantify the adhesion has been published by J. Lesage et al. that varies the load of the indentation and evaluate the change that is measured to the length of the developed crack in the interface. The large variation between measurements that are related to the interface indentation test complicates the evaluation proposed by J. Lesage et al. and an absolute value of adhesion is not required for many purposes.

A simpler method of estimating the work of adhesion using the interface indentation test is proposed in the present study. The method is specifically adapted for the screening of different pre-treatments and currently require that the same type of coating is deposited with the same thickness on the same type of substrate in order to compare the results. The method differs from the test proposed by J. Lesage as only a single load is applied. The equation used to estimate the work of adhesion is simplified due to material related inputs that can be considered as constants (same substrate, same thickness etc.). The method handles the large variation between measurements by using the statistics with the two-sample t-test to evaluate the confidence level when comparing the obtained results.

The present study has estimated the work of adhesion obtained between the Fe-C coating and hardened calmax steel that was pre-treated differently using the new proposed interface indentation test method. The result stated with a confidence above 95 % that two out of the five different pre-treatments produced a lower adhesion compared to the pre-treatment with the highest mean value measured.

The results of the present study outline the importance of choosing the correct pre-treatment for obtaining good adhesion and proposes how different pre-treatments can be benchmarked when a new substrate/coating combination is required.

5.5 Manuscript V

Evolution of hard Fe-C electrodeposits with temperature

In contrast to above introduced manuscripts, which were addressed to as-deposited coatings, the present one aims to understand the thermal stability of the Fe-C coatings. The thermal stability of the Fe-C coating is important to understand the as-deposited nature of the light elements and the effect of the temperature induced phase transformations. Isothermal annealing was carried out in furnaces at different temperatures over different times and the annealed coatings were subsequently (ex-situ) investigated by EDD and TEM. This was further supplemented with in-situ thermal analysis for thermo-gravimetric measurements, also coupled with MS during annealing. The complementary measurements revealed thermal decompositions and associated phase transformations, which supplement previous results and provide an interpretation of the internal structure of electrodeposited Fe-C coatings.

A phase transformation is uncovered by a mass loss and desorption of hydrogen around 250 °C that enable the development of both magnetite and cementite. The phase transformation at 250 °C is not related to the “nameless phase” or ferrite and this phase is in the later manuscripts called the “organic compound”. The thermal analysis also measured the phase transformation around 360 °C that has been published by Haseeb et al. and Fukumuro et al as described in Section 2.3.1, but the observed relation to the desorption of hydrogen does not support Haseeb’s et al. interpretation that this transformation is related to the transformation of ε/η-Fe_2C to Fe_3C. The complementary investigation of the thermal analysis and EDD indicated a correlation between a phase transformation measured in-situ by DTA around 360 °C and “nameless peak” measured ex-situ by EDD. However, the ex-situ isothermal annealing analysis did not allow concluding upon this. The TEM investigation supplements the diffraction results and confirms the presence of both magnetite and cementite after annealing. The hardness of the Fe-C coatings increased by annealing as a result of the precipitation of magnetite and cementite.

The manuscript is followed by supplementary results from hardness and EDD measurements of ex-situ annealed Fe-C coatings at different temperatures and for different times.

These, from a scientific point of view, highly relevant results on the role of co-deposited light elements during annealing are also important from an application point of view, because the high hardness of 800 HV for the as-deposited coatings further increases to around 1300 HV by annealing.

5.6 Manuscript VI

In-situ analysis of the thermal evolution of electrodeposited Fe-C coatings

The manuscript is a progression on the study of thermal stability studied on ex-situ annealed Fe-C coatings, but takes full advantage of a high flux at EDDI that enables in-situ annealing measurements to detect phase evolutions with a high temperature resolution. The thermal evolution of the as-deposited Fe-C coatings is followed by means of in-situ synchrotron diffraction analysis and in-situ thermal analysis using DTA/TGA coupled with MS. The in-situ isochronal annealing EDD analysis using a low heating rate revealed the as-deposited phases, along with the temperature induced phase transformations from room temperature to above the austenitization temperature. The applied complementary thermal analysis confirmed the specific temperatures of the occurring phase transformations using the same heating rate as the in-situ EDD analysis. The activation energy of the phase transformations measured by DTA were determined by applying different heating rates and examining the shift in the transformation temperature using an isochronal Kissinger analysis.

The in-situ isochronal annealing EDD measurement was experimentally challenging, as realignments of the sample were required due to changes in the samples height during the measurement at two specific temperatures. The complementary DTA/TGA coupled with MS revealed the role of hydrogen related to the changes in the samples height. The temperatures of the precipitation of magnetite and cementite were precisely determined by in-situ EDD along with the temperatures of the solid state phase transformations of magnetite to wüstite and ferrite to austenite. The “organic compound” was characterized solely by thermal analysis and its designation was selected as it consist of the same light elements that are being co-deposited from citric acid being carbon, oxygen and hydrogen. The desorption of hydrogen around 360 °C corresponds to the transformation of the “nameless phase” and that hydrogen is included in the “nameless phase” points towards a type of iron-hydroxide. The activation energy was determined for the desorption of hydrogen from electrolysis and for the phase transformations of the “organic compound” and the “nameless phase”.

The manuscript is supplemented by the thermal analysis that investigated the hydrogen and oxygen content in the Fe-C coating using the TGA and a reducing atmosphere and elevated temperatures. A specific in-situ isochronal annealing measurement is also included that reveal the extent of the change in sample height during the in-situ annealing analysis.

The role of all the light elements is emphasized, they define the as-deposited state of the Fe-C coatings and the thermal evolution. The results are necessary for optimized engineering of surfaces as they provide details on the alterations of the internal structure and associated properties of electrodeposited Fe-C coatings.

5.7 Manuscript VII

Interpretation of the evolution of microstrain and crystallite size for ferrite during annealing of nanocrystalline electrodeposited Fe-C coatings

The present manuscript reexamine the in-situ isochronal annealing EDD measurement using line profile analysis to evaluate the changes of crystallite size and microstrain on ferrite. The analysis also includes an in-situ isochronal annealing EDD measurement using a higher heating rate. The higher heating rate will shift the transformation temperature to a higher value depending on the activation energy. The use of two different heating rates allows to evaluate whether the occurrence of several observations at one and the same temperature, like phase transformations and the evolution of both microstrain and crystallite size in ferrite, occur consistently and correlated to each other or by coincidence. The different heating rates are expected to indicate a consistent temperature shift for any correlated transformation. The line profile analysis investigates the α-211 as this is the peak of highest intensity and reflects (almost) the preferred <311> orientation of as-deposited coatings. A TEM investigation of the as-deposited Fe-C coating and a Fe-C coating ex-situ annealed above the “nameless phase” transformation temperature supplements the in-situ annealing EDD analysis.

The analysis unfold the impact on the microstrain at separate temperatures as a result of the phase transformations of the “organic compound” and the “nameless phase”. The onset of grain growth for the <211>-oriented ferrite grains is measured at the temperature of the transformation of the “nameless phase”. The location and role of the “organic compound” and the “nameless phase” within the Fe-C coating are discussed based on the revealed evolution of the microstrain and crystallite size in ferrite. The TEM analysis did not identify the “nameless phase” in the SAED patterns, but the measured intensity for magnetite could be a transformation state of the “nameless phase” as Manuscript VI suggest that the “nameless phase” exist as an iron-hydroxide in the as-deposited coating.

The manuscript is supplemented with an evaluation procedure (work in progress), which converts the isochronal annealing experiments to isothermal annealing such that the grain coarsening for the Fe-C coating at a specific isothermal holding temperature can be predicted as a function of time. Furthermore, the results can then be compared with the measured ex-situ samples reported in Manuscript V.

The as-deposited position of the “nameless phase” and the “organic compound” inside the microstructure propose the origin of the high hardness of the as-deposited coatings in conjunction with the nanocrystalline grain size of ferrite.

6 Results regarding the as-deposited Fe-C coatings

6.1 The nature of the as-deposited Fe-C coating and the influence of the coatings thickness and the substrate

6.1.1 Manuscript I

Electrodeposition of iron with co-deposition of carbon – on the nature of nanocrystalline Fe-C coatings[5]

Jacob Obitsø Nielsen*, Per Møller, Karen Pantleon

Technical University of Denmark, Department of Mechanical Engineering, Produktionstorvet, building 425, DK – 2800 Kongens Lyngby, Denmark

*Corresponding author: jacobon@mek.dtu.dk

Abstract

Fe-C coatings were electrodeposited from an iron-sulfate electrolyte containing citric acid as a carbon source. Differently thick coatings were deposited onto amorphous substrates, which allows substrate-unbiased nucleation and thereby enables the study of the intrinsic growth of Fe-C coatings. The internal structure of the Fe-C coating was systematically investigated applying complementary methods of materials characterization using microscopy, spectroscopy, and X-ray diffraction analysis, which was further supplemented with microhardness measurements. For the measured high carbon concentration of more than 0.8 wt pct, the experimental results indicate the formation of Fe_2C carbides. Together with the nanocrystalline carbon-free ferrite grains with strong <311> fiber texture, the carbides provide a very high microhardness of almost 800 HV, as measured for the Fe-C coatings independent of the coating thickness. The results essentially contribute to understanding of the growth characteristics and phase formation during electrodeposition of the Fe-C coatings, which is needed for their industrial applications as hard coatings.

I. INTRODUCTION

Electrochemical deposition of iron from iron-sulfate baths was developed a century ago and implies the advantages of a cheap electrolyte, low operating temperature and low susceptibility to oxidation of the electrolyte [1]. Originally, electrodeposition of iron was mainly used for short-term restoration of worn or damaged surfaces of machine components [2,3], as for these applications, the ease of site-specific deposition and attractive mechanical properties of the coatings were of main interest. More recently, the intended co-deposition of other elements (e.g., tungsten, nickel, phosphorous and zinc) from advanced electrolytes inspired a revival of the original interest in iron-based coatings [4]. Of particular interest is the co-deposition of carbon and iron, and iron-carbon (Fe-C) coatings have been synthesized not only by electrochemical deposition [5-13], but also by physical vapor deposition [14-17]. Although different morphologies and structures of Fe-C coatings ranging from amorphous to crystalline and different carbon concentrations are reported for the various deposition processes, all Fe-C

---

[5] Published work: Metallurgical and Materials Transactions A, 50A (2019) 3785-3793. The format of the published article was adapted to the format of the doctoral thesis.

coatings possess very high hardness, being similar to the hardness of martensite in steels. Despite that similarity, the peculiarities of the growth of Fe-C coatings suggest essential differences to traditional hardening of steel and, hence, a different origin of microstructure and properties. Despite a general consistency in the literature regarding the good mechanical properties of Fe-C coatings, their growth characteristics and, in particular, the role of carbon in the coatings are aspects that not fully are understood yet. This, however, is essential for the promising application of Fe-C coatings as a novel type of hard and wear-resistant surfaces, which both enables straightforward repairing of worn surfaces by site-specific deposition and the large-scale deposition on components exposed to mechanical loading during operation.

Electrodeposited Fe-C coatings have a huge potential for surface engineering, including tailoring of the deposition parameters to optimize the growth characteristics and additional modifications during post-deposition treatments of the coatings. Understanding the correlation between the applied deposition conditions and the resulting microstructure is a prerequisite for the successful transfer of knowledge obtained on laboratory scale into a reliable, reproducible, large-scale production [18,19]. In addition to the type of electrolyte and the process parameters, like current density and temperature, both nucleation and growth of electrodeposits are further affected by the nature of the substrate, which influences the size, shape, crystallographic orientation of the grains, and consequently, resulting properties of the coatings. Previous studies dedicated to electrochemical deposition of Fe-C coatings refer to an iron-sulfate bath with the addition of a small amount of carbon-containing organic acids [5-13]. The type of such organic additives has been found to determine not only the possible amount of co-deposited carbon but also the macroscopic appearance as well as the topography, morphology, and associated properties of the Fe-C coatings [7,12,13]. In addition to the electrolyte composition, also the effect of the pH value, the deposition temperature and the applied cathode current density have been investigated [5-10,12].

The present work reports on systematic studies of Fe-C coatings, which were electrodeposited from an iron-sulfate electrolyte with citric acid as additive. To investigate the intrinsic growth characteristics of the coatings, electrodeposition was carried out onto amorphous nickel-phosphorous (Ni-P) substrates under identical process parameters. Only the deposition time was varied to result in Fe-C coatings with various thicknesses up to several tenths of micrometers. Based on thorough materials characterization of the as-deposited coatings with a focus on their internal structure and the corresponding microhardness, the incorporation of carbon in the coatings is discussed, also in relation to previously reported results from the literature. The present work is dedicated to the understanding of the as-deposited Fe-C coatings, which provides the basis for further surface engineering either by tailoring the deposition process or subjecting the as-deposited coatings to post-deposition treatments.

II. MATERIALS AND EXPERIMENTAL METHOD

A. Electrochemical Deposition

1. Substrate

Fe-C depositions were carried out on amorphous substrates, with the aim of investigating the effect of the electrolyte and the applied process parameters without any additional influence on the coating growth. The substrates have been obtained by pretreating low-carbon steel plates by electroless plating of a Ni-P film from the commercial electrolyte MacDermid Enthone VAND-ALOY 4100 containing 10 to 12 wt pct P. The resulting amorphous Ni-P film with a thickness of about 20 µm ensures substrate unbiased growth during subsequent electrodeposition of Fe-C coatings. Prior to Fe-C deposition, the Ni-P substrates were subjected to cathodic degreasing at 5 V for 2 minutes followed by 2 minutes of surface activation in commercial dry acid 629 SV from EngTech Scandinavia.

2. Deposition Parameters

The electrolyte was prepared from chemicals of analytical grade with a concentration of 0.143 mol/dm^3 iron(II) sulfate heptahydrate, 6.2 x 10^{-3} mol/dm^3 citric acid monohydrate, and deionized water. The 5 L of the electrolyte were freshly mixed for each sample to avoid any possible oxidation or aging of the electrolyte as an additional influence on the microstructure and properties of the Fe-C coatings. The electrolyte temperature amounted to 50 °C and mechanical stirring was applied during deposition. The pH value of the electrolyte was maintained between 2.5 and 2.8 during deposition using a 10 vol pct sulfuric acid solution. An interstitial free steel plate was used as an anode, and the Ni-P coated plates with dimensions of 5 x 5 cm were used as cathodes. One side of these substrate plates was covered with an electrolyte-resistant tape to ensure deposition only on the side toward the anode.

Electrodeposition of Fe-C coatings was carried out at a constant current density of 3.0 A/dm^2, which was applied for various deposition times between 30 and 300 minutes. The applied deposition parameters and the electrolyte composition have been optimized based on previous studies on electrodeposited Fe-C coatings [5–13]. The coatings were immediately after deposition rinsed in water, followed by rinsing in ethanol and then carefully dried to avoid oxidation. The samples were protected from any contact with oxidizing environments during storage. For subsequent microstructure analysis, the samples were cut such that only the center part with homogeneous coating thickness was investigated, thus, disregarding the possibly higher current density near the sample edges.

The designation of a sample indicates the thickness of the coating, e.g., Fe-C_30µm corresponds to a coating of 30 µm thickness deposited on the Ni-P substrate.

B. Materials Characterization

1. Chemical Analysis

The carbon content in the coatings was determined using a carbon analyzer LECO CS230, which measures the amount of CO_2 evolved by high-frequency induction heating of the sample in an O_2 atmosphere. The measurements were performed using an amount of 0.1 g of a Fe-C coating removed from the substrate.

A depth profile of the chemical composition was obtained by means of glow discharge optical emission spectroscopy (GDOES) using a Horiba equipment GD profiler 2 with Quantum XP software. The instrumental settings and procedure were established based on investigations of the crater profile using surface roughness measurements by 3D coordinate measurements with an Alicona InfiniteFocus. The GDOES measurements were calibrated with multiple low-alloy steel standards having different carbon contents up to 1.3 wt pct. The content of hydrogen and oxygen is given as measured intensity because these elements have not been calibrated.

2. Microscopic Analysis

Microscopic analysis was carried out on cross sections of the samples. Before cross section preparation, the samples were coated with a 10 µm layer of nickel to protect the surface of the

Fe-C coatings. Samples were embedded in epoxy resin, which hardens at room temperature and avoids any risk of introducing artifacts to the as-deposited coatings. The cross sections were metallographically prepared and polished with OP-S for 3 minutes as a final preparation step. An Olympus GX41 light optical microscope (LOM) was used for the thickness measurements on cross sections. A FEI Quanta 200 ESEM scanning electron microscope (SEM) was used for investigations on the cross sections.

3. X-ray Diffraction Analysis

A Bruker AXS D8 Discover X-ray diffractometer equipped with an Eulerian cradle and operated with Cr-K_α radiation was used for qualitative phase analysis, line profile analysis, and quantitative crystallographic texture analysis. A Göbel mirror was used to obtain a high, intense parallel beam for phase analysis and line profile analysis, while a PolyCap optics was used to ensure a parallel beam for texture analysis along with a vanadium filter to avoid K_β-radiation. The calculated information depth in iron corresponds to a maximum of about 6 μm within the measured range of diffraction angles between 50 and 160 deg 2Θ.

X-ray diffraction (XRD) phase analysis was carried out applying a symmetric beam path. Samples were measured using a step size of 0.02 deg 2Θ and a measurement time of 20 seconds per step to ensure high resolution and good counting statistics. For qualitative phase analysis, the measured diffraction angles were corrected for any offset related to the alignment of the diffractometer using a LaB_6 reference sample.

XRD line profile analysis was carried out for the 110, 200, and 211 reflections of α-Fe. The measured diffraction patterns were fitted with a superposition of two linked pseudo-Voigt functions corresponding to the $K_{\alpha 1}$ and the $K_{\alpha 2}$ components of the applied X-rays. Only the fitting results for the K_{a1} component were used for interpretation. Fitting with the pseudo-Voigt function revealed the following parameters for further analysis: (1) the 2Θ peak position, (2) the full-width-half-maximum (FWHM), (3) the shape of the peak defined by the contribution of Gaussian and Lorentzian function to the peak profile, and (4) the integrated intensity of the measured peaks. The measured peak broadening was corrected for the effect of instrumental broadening applying a LaB_6 standard powder sample. The resulting physical peak broadening was expressed as integral breadths β, calculated from the FWHM and the profile shape, and subjected to the single line method for separating the simultaneous influences of the size of coherently diffracting domains (interpreted as the crystallite size) and lattice microstrain on peak broadening [20,21].

For quantitative crystallographic texture analysis by means of XRD, 110-, 200- and 211-pole figures of α-Fe were measured for all samples, applying sample rotations around the surface normal (azimuth angle φ, $0 \leq \varphi \leq 360$ deg, step size 5 deg) and sample tilts (pole angle ψ, $0 \leq \psi \leq 75$ deg, step size 5 deg). Measured intensities were corrected for background intensity, and a Fe-powder standard was used to correct for defocusing associated with tilting. For texture quantification, the orientation distribution function was calculated in MTEX using the zero-range method [22]. The maxima in the inverse pole figures in normal direction to the substrate were used to determine the fiber axis <uvw>, as ideal fiber textures apply for all Fe-C coatings. Inverse pole figures in directions within the plane of the coating revealed random rotations around the fiber axis. Accordingly, the corresponding orientation densities in the normal direction are a measure of the texture strength.

4. Microhardness Measurements

The microhardness was measured using a Future Tech Inc. FM700 microhardness tester with Vickers geometry, applying a load of 10 g. Measurements were performed both on the surface and on metallographically prepared cross sections. Microhardness measurements on the surfaces of all samples represent averages over 20 measurement positions, while results from measurements on the cross sections correspond to 10 indentations in the middle of the coating.

III. RESULTS

A. Microscopic Analysis of Fe-C Coatings

Microscope investigations of the cross sections indicate uniform coatings with homogeneous coating thicknesses, as shown in Figure 1 on the example of sample Fe-C_58µm. While the surface roughness of the original steel substrate is still maintained in the Ni-P substrate layer (cf. Figure 1(a), steel–Ni-P and Ni-P–Fe-C interfaces), a leveling effect occurs during the growth of the Fe-C coating resulting in a smooth surface (cf. Figure 1(a), interface Fe-C–Ni). The figure indicates that the surface roughness of the Fe-C coating considerably decreased already at a thickness of 16 µm and the surface fully leveled out for coating thicknesses of 30 µm and above. The cross sections also revealed that the microstructure is very fine grained and cannot even be resolved with SEM (cf. Figure 1(b)).

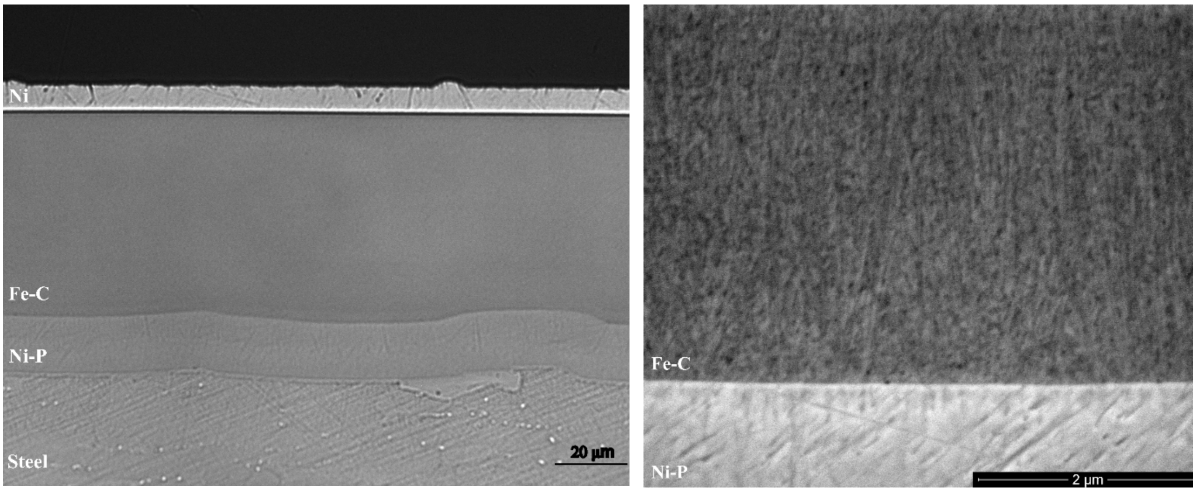

(a) (b)

Figure 1: Cross section of sample Fe-C_58µm. Ni-P corresponds to the amorphous substrate layer on top of steel, while a Ni film protects the surface of the Fe-C coating during metallographic preparation. a) LOM image, b) SEM image.

Although neither LOM nor SEM can resolve the very fine-grained microstructure of the Fe-C coatings, microscopy of the various cross sections revealed the thickness of the Fe-C coatings as a function of the applied deposition time, which allowed calculation of the deposition rate. The results shown in Table I indicate that the deposition rate is highest with 0.27 µm/min at the beginning of the deposition, thus, for the thinnest coatings and drops to 0.19 µm/min for the thickest coating of the present study.

B. Chemical Analysis

Chemical analysis applying the LECO system determined the carbon concentration to be 0.88 ± 0.02 wt pct, which represents an average value over the whole thickness of a coating. The presence of such a high carbon concentration is confirmed by GDOES, which further supplements with the depth distribution of relevant elements like carbon, oxygen, and hydrogen. In the depth profiles shown on the example of sample Fe-C_16µm in Figure 2, the first few micrometers should be disregarded as they relate to the running-in period during sputtering from the surface. The interface between the Fe-C coating and the substrate, seen as a drop in carbon, oxygen, and hydrogen concentrations, is obtained after a total time of about 160 seconds, which corresponds to a sputter depth of 22 µm. A homogenous distribution of carbon is measured across the coating thickness. In addition, significant intensities are measured for hydrogen and oxygen, which reveal that these elements are present in the coatings, although they cannot be quantified. The slightly decreasing content of hydrogen could be an artifact from the sputtering process and local heating of the measured region, which would result in a higher concentration in the beginning of the measurement when hydrogen may diffuse toward the surface.

Table I: Thickness measurements and calculated average deposition rate.

Deposition time [min]	Thickness [µm]	Average deposition rate [µm/min]
30	8	0.27
60	16	0.27
120	30	0.25
300	58	0.19

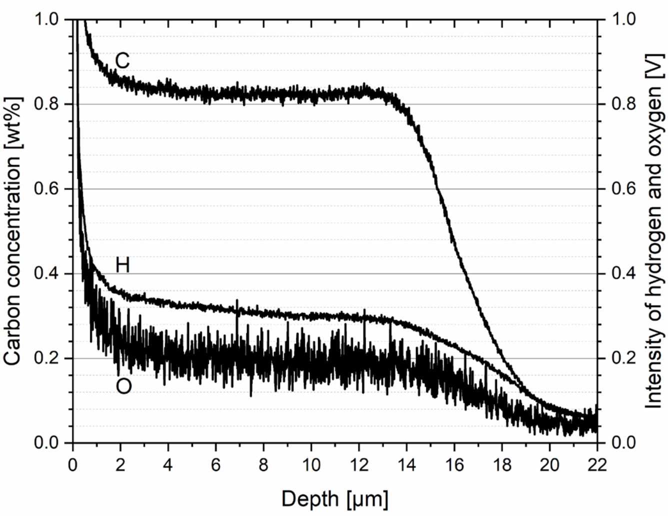

Figure 2: GDOES depth profile measured for the sample Fe-C_16µm. The concentration of carbon refers to the left y-axis, while measured intensities for hydrogen and oxygen refer to the right y-axis.

C. X-ray Diffraction Analysis

The XRD patterns of the Fe-C coatings are shown in Figure 3 and clearly reveal the presence of α-iron (JCPDS card 6-696). Depending on the coating thickness, the various reflections show different intensity ratios indicating slight changes of the preferred grain orientation with coating thickness. Also, independent of the thickness, further peaks in addition to the ones from the α-iron phase are observed for the measured samples at about 58.05 deg 2Θ, 137.59 deg 2Θ and 150.73 deg 2Θ (an additional peak at 126.5 deg 2Θ should be disregarded because it refers to the K_β radiation, which has not been filtered out). While the peak around 58.05 deg 2Θ is of highest intensity and free-standing, the other peaks are less distinct and hardly visible with only small intensity in the wide tails of the α-iron peaks (cf. inserts in Figure 3). Such weak and overlapping peaks considerably complicate straightforward phase analysis for the present Fe-C coatings. Thorough peak fitting was carried out, also for the overlapping and weak peaks, and the resulting d-spacings of all fitted peaks are shown in Table II. The table reveals that all peaks shift slightly toward larger d-values when the thickness of the coating increases from 8 μm to 30 μm, without remarkable further changes at 58 μm. Such changes of d-values suggest changes of residual stresses and/or chemical changes in the coatings. As that observed shift toward larger d-values with increasing thickness is most pronounced for the first two peaks (cf. Table II), another observation seems particularly interesting in this respect. Table II indicates a correlation between these two peaks, thus, the 110 reflection of α-iron and the peak of the yet unidentified phase having a d-spacing of about 0.236 nm: irrespective of the coating thickness, the ratio of the lattice spacing between both peaks remains constant with 1.163 ± 0.001.

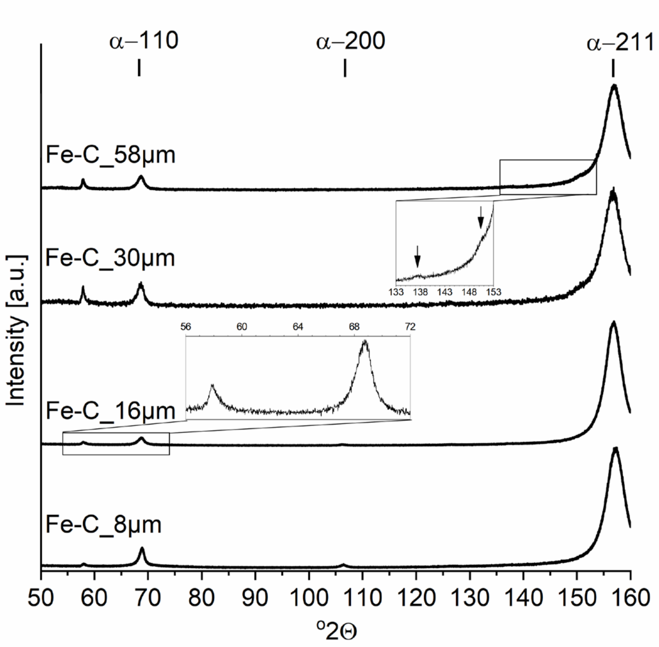

Figure 3: X-ray diffraction pattern of Fe-C coatings. (The maximum value of 160 °2Θ corresponds to the upper limit of the measurement range and, therefore, the broad α-211 cannot be recorded completely.)

Table II: d-spacing [nm] obtained from peak profile fitting of XRD patterns with diffraction angles °2Θ, as measured for Fe-C coatings (cf. Figure 3).

°2Θ	Phase	hkl	Fe-C_8μm	Fe-C_16μm	Fe-C_30μm	Fe-C_58μm
58.1			0.2360 nm	0.2361 nm	0.2366 nm	0.2364 nm
68.6	α-iron	110	0.2027 nm	0.2031 nm	0.2033 nm	0.2032 nm
106.2	α-iron	200	0.1430 nm	0.1431 nm		
137.6			0.1228 nm	0.1228 nm	0.1229 nm	0.1228 nm
150.7			0.1183 nm	0.1183 nm	0.1184 nm	0.1184 nm
156.7	α-iron	211	0.1168 nm	0.1169 nm	0.1169 nm	0.1169 nm

Similar challenges with phase identification, as encountered in the present work, have been reported in literature, but inconsistent conclusions on the crystalline phases in the Fe-C coatings indicate that the nature of growth and phase formation in such electrodeposits is still under discussion. While there is general agreement in the literature (and the present work) that the peaks of highest intensity in the measured diffraction patterns refer to an iron-rich phase, different explanations for the presence of carbon and the corresponding formation of carbon-containing phases have been reported [5-9,14,15,23]. The various hypotheses for the presence of carbon in the Fe-C coatings are discussed and verified for the present samples below (see Section IV).

All Fe-C coatings have in common that the 211 reflection of α-iron is of highest intensity in the Θ-2Θ scans, the 110 of α-iron is clearly visible, and the 200 reflection of α-iron is of very low intensity or fully absent. Comparing the measured intensity ratios with the JCPDS card of randomly oriented α-iron, the presence of a pronounced preferred orientation of grains in the Fe-C coating is obvious. For its quantification, crystallographic texture analysis by means of pole figure measurements has been carried out. For all Fe-C coatings, the pole figures revealed the presence of fiber textures with rotational symmetry of the measured intensity distributions as shown in Figure 4 on the example of sample Fe-C_16µm. For fiber textures, inverse pole figures in normal direction straightforwardly allow quantification of the fiber axis, which describes the preferred orientation in the growth direction of the coatings. All Fe-C coatings consist of a ⟨311⟩ fiber texture, as shown in Figure 5. The fiber axis ⟨uvw⟩ and the corresponding orientation densities in multiples of random distribution are summarized for all samples in Table III. Although the ⟨311⟩ fiber axis is rather strong for all coatings, slight changes of the texture strength are observed as a function of coating thickness: The strength of the ⟨311⟩ increases slightly with coating thickness.

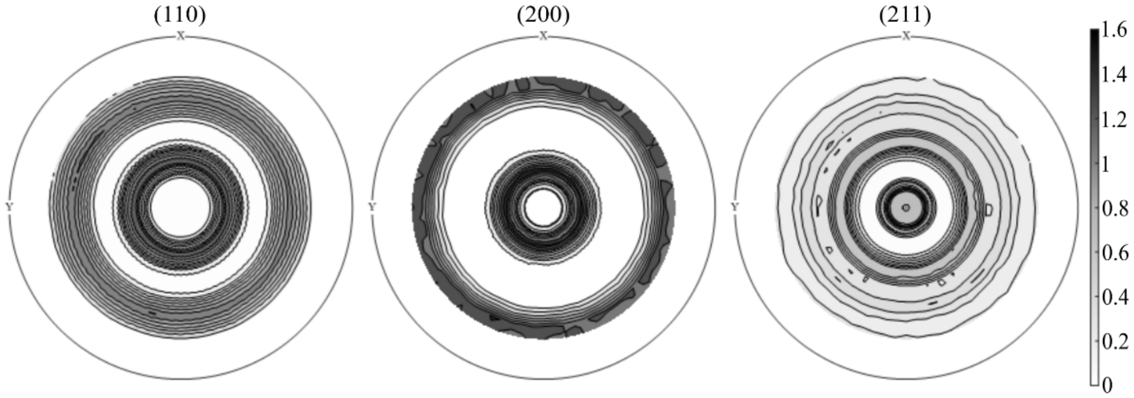

Figure 4: Pole figures of α-iron as measured by XRD for the sample Fe-C_16µm.

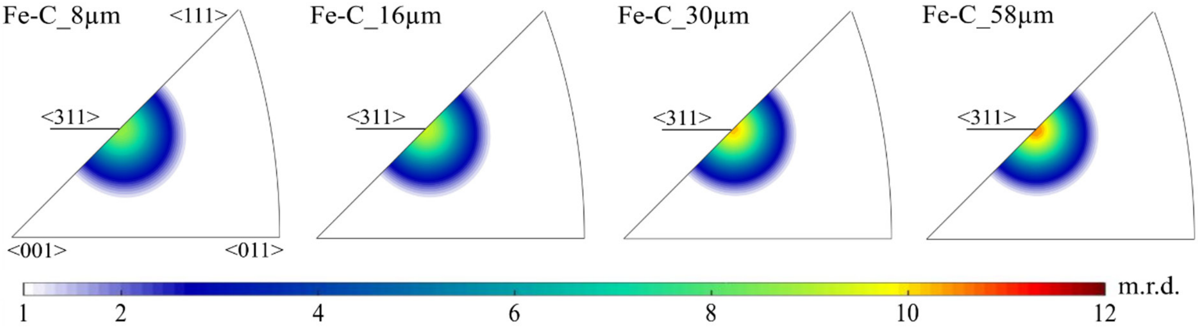

Figure 5: Inverse pole figures in growth direction obtained by XRD measurements.

It would be of interest to further analyze the ⟨311⟩ oriented grains as they represent the majority of grains in the Fe-C coatings, but as the 311 is a forbidden reflection for the bcc α-iron, it is not accessible from a Θ-2Θ scan. Instead, the 211 reflection (corresponding to grains deviating by about 10 deg from the real ⟨311⟩ preferred orientation) shows the highest intensity in the diffraction pattern, but it does not allow for accurate peak profile analysis. Due to substantial peak broadening, the 211 exceeds the available measurement range (only up to 160 deg 2Θ can be measured by conventional XRD); thus, it cannot be recorded completely, and weak peaks of a second phase overlap with the left tail at lower 2Θ of the 211 peak. Both hinders thorough peak profile analysis of the 211 peak, and therefore, only the 110 peak of α-iron has been used for quantification of both crystallite size and microstrain from the measured peak profiles. Accordingly, the corresponding results in Table IV do not represent the average over all grains of the Fe-C coatings, but instead they reflect data for ⟨110⟩-oriented grains only, which constitute a minority of all grains. The crystallite size of ⟨110⟩ grains is in the order of about 10 nm and does not change with coating thickness. The microstrain evolves with coating thickness, and shows a sudden change in the thickness range between 16 and 30 µm.

Table III: Crystallographic texture of Fe-C coatings with varying thickness.

Sample	Fiber axis ⟨uvw⟩	Strength [m.r.d.]
Fe-C_8µm	⟨311⟩	9.3
Fe-C_16µm	⟨311⟩	9.3
Fe-C_30µm	⟨311⟩	10.4
Fe-C_58µm	⟨311⟩	11.2

Table IV: Integral breadth β [°2Θ], corrected for any instrumental effects, and corresponding crystallite size D [nm] and microstrain ε [rms], as obtained from XRD profile analysis.

Sample	β [°2Θ]	D [nm]	$\varepsilon \cdot 10^{-3}$ [rms]
Fe-C_8µm	1.6195	9.8	0.37
Fe-C_16µm	1.9473	8.2	0.44
Fe-C_30µm	2.0360	8.7	3.50
Fe-C_58µm	2.0969	8.1	2.70

D. Microhardness

High microhardness values of almost 800 HV0.01 have been measured for all Fe-C coatings, almost independent of the coating thickness, as shown in Table V. Microhardness measurements on the cross sections verified the high microhardness of Fe-C coatings.

*Table V: Microhardness of Fe-C coatings measured from the surface and cross section of the coatings. *Cross sections with low coating thickness cannot be measured reliably.*

Sample	Surface - HV0.01	Cross section - HV0.01
Fe-C_8µm	775 ± 24	*
Fe-C_16 µm	780 ± 25	*
Fe-C_30 µm	780 ± 20	792 ± 16
Fe-C_58µm	775 ± 16	789 ± 14

IV. DISCUSSION

The chemical analysis revealed co-deposition of carbon with an average concentration of 0.88 ± 0.02 wt pct C and indicates that oxygen and hydrogen are present in the Fe-C coatings (cf. Figure 2). These elements certainly originate from the citric acid in the electrolyte, although hydrogen also might be caused by hydrogen evolution, which is a typical phenomenon occurring during electrodeposition. Despite intensive attempts applying various methods of dedicated high-resolution microscopy and element analysis, it remains challenging to quantify and locate the co-deposited hydrogen and oxygen in the coating, and this work will continue. The reducing nature of the interface between cathode and electrolyte is likely either to decompose citric acid into smaller fragments of a carboxylic form or to result in the incorporation of species in their elemental form in the microstructure of the Fe-C coatings. Then, they would likely react with iron, producing hydroxides, oxides, or carbides. In thermodynamic equilibrium, none of these elements (carbon, oxygen, hydrogen) is expected to be in solid solution in α-iron, which is unambiguously identified by XRD.

XRD also revealed that the microstructure of α-iron is nanocrystalline with crystallite sizes just below 10 nm for the <110>-oriented grains. Neither coarsening of the nanocrystalline grains as a function of coating thickness nor any growth selection from the interface toward the surface has been observed by XRD or SEM. Although the nanocrystalline nature of the coatings would allow segregation of elemental carbon (and oxygen and hydrogen) in the numerous grain boundaries, the present study does not allow for such a conclusion, and dedicated high-resolution microscopy with chemical analysis at grain boundaries is in progress. The present study, however, clearly indicates a second phase, in addition to α-iron, as revealed by the additional peaks shown in Figure 3 and quantified in Table II. Also, being of low intensity and partly overlapping with peaks of α-iron, which considerably complicates straightforward phase analysis, the origin of these additional peaks, having d-spacings of 0.2360 nm, 0.1228 nm, and 0.1183 nm, has to be discussed.

The co-deposited oxygen cannot solely explain these peaks, which do not match with Fe_2O_3 (hematite) or Fe_3O_4 (magnetite), and the presence of hydrogen does not refer to any phase related to these peaks without speculations. However, the location of carbon, which has been measured with a high concentration of more than 0.8 wt pct C in the as-deposited coatings, has not been explained yet. It also is not consistently reported in the literature, although similar experimental results have been obtained. The following possibilities can be discussed and will be related to the present results.

In early studies of Fe-C coatings [6-9], observations of peak asymmetries have been related to a supersaturation of the bcc α-Fe (ferrite) phase resulting in a tetragonal distortion of the iron lattice corresponding to the bct α'-Fe (martensite) phase. For the well-known formation of martensite in steel, the tetragonal distortion of the lattice originates from the preferred incorporation of carbon on octahedral interstitial lattice sites in the z-axes compared to the x- and y-axes, which for steels is a consequence of the diffusionless transformation from the fcc iron lattice (austenite) [24]. This explanation for tetragonal martensite and the corresponding peak asymmetry due to the presence of double reflections of 101 and 110 for α'-Fe, however, does not apply for the present electrodeposited samples, where there is no obvious reason for a preferred occupancy of interstitial sites with carbon along one particular direction only. Furthermore, the high concentration of carbon in the present samples would cause a remarkable peak splitting due to the high tetragonal distortion of the lattice. Such splitting of the iron peaks into two distinct peaks, which are apart from each other according to the lattice expansion/contraction in z- or x- and y-direction, has not been observed by XRD (cf. Figure 3). If, instead, carbon would be incorporated with equal probability on all interstitial sites, the strong supersaturation of the lattice would cause a remarkable peak shift in XRD. Large supersaturation of bcc α-Fe with carbon has been reported for vapor-deposited films (up to 5 wt pct) [14,15] and in steels after severe deformation [25], thus, for nonequilibrium states. Although electrodeposition often does not provide thermodynamic equilibrium and, thus, favors the formation of nonequilibrium phases, there is no experimental evidence for the present Fe-C coatings that carbon is in a supersaturated solid solution in the α-Fe phase. For determining the undisturbed lattice spacing even in the potential presence of stresses, XRD has been performed in the strain-free direction of the Fe-C coating (by tilting the sample around the azimuth angle of ψ_0 = 41.43 deg) and has revealed the lattice spacing of the (110) crystallographic planes with d_0 = 0.2026 nm, which agrees exactly with data for carbon-free α-Fe (JCPDS card 6-696) and rejects the possibility of any carbon-supersaturation of the α-Fe lattice. The high concentration of carbon is therefore likely to have caused precipitations, as discussed below.

Consistent with recent studies on Fe-C coatings [5,13,23] is the present observation of an additional peak corresponding to a lattice spacing of d = 0.2360 nm (cf. Figure 3 and Table II). Phase analysis has mainly to be based on that peak because it is the only one (in addition to the peaks of α-Fe) that is of high intensity and not overlapping with others. Further peaks corresponding to d-spacings of 0.1228 and 0.1183 nm indicating a second phase can support various hypotheses for phase identification. In the following, the presence of carbides is discussed.

For carbon-steels, Fe_2C carbides can exist as either hexagonal ε-Fe_2C (JCPDS card 36-1249) or orthorhombic η-Fe_2C (JCPDS card 37-999), both being transition carbides toward the formation of Fe_3C at higher temperatures [26-29]. Both ε-Fe_2C and η-Fe_2C are very similar to each other, and earlier in the literature [5], ε-Fe_2C was reported for Fe-C coatings. The actual lattice parameters of the transition carbides have been reported to be alloy specific [30] and can therefore vary slightly. The ε-Fe_2C carbide having lattice parameters of a = 0.2735 nm and c = 0.4339 nm [30] can explain the measured peaks corresponding to $d_{\varepsilon\text{-}100}$ = 0.2369 nm, $d_{\varepsilon\text{-}103}$ = 0.1234 nm, and $d_{\varepsilon\text{-}200}$ = 0.1184 nm. The η-Fe_2C carbide having lattice parameters of a = 0.4704 nm, b = 0.4318 nm, and c = 0.2830 nm can also explain the measured peaks according to $d_{\eta\text{-}011}$ = 0.2367 nm, $d_{\eta\text{-}230}$ = 0.1228 nm, and $d_{\eta\text{-}022}$ = 0.1183 nm. Even the slight peak asymmetry (see magnified insert in Figure 3) can be assigned to η-Fe_2C. Other carbides, like Fe_3C, Fe_5C_2, Fe_7C_3, cannot explain the observed results and certainly are not present in the as-deposited Fe-C coatings.

To test the suggestion of either ε-Fe_2C or η-Fe_2C carbides, XRD has been carried out under various sample tilts and rotations, but no additional reflections or higher intensities could be revealed. However, when tilting the sample about the angle ψ, the intensity of the 110 α-Fe lowers until the peak fully disappears at ψ = 12 deg and the intensity of the peak, corresponding to the d-spacing of 0.2360 nm, does the same, thus, the intensity changes of both peaks are correlated. This suggests a crystallographic orientation relation between α-Fe and ε-Fe_2C or η-Fe_2C, respectively. This is further supported by the observation of a correlated peak shift between 110 α-Fe and the supposed 100 ε-Fe_2C or 011 η-Fe_2C, which occurs independent of the coating thickness as mentioned above (cf. Table II). The low intensities of measured XRD peaks for carbides of ε-Fe_2C or η-Fe_2C suggest a low volume of carbides in the coating, and the rather broad peak(s) further indicate that the corresponding carbide phase is nanocrystalline and might be fine dispersed. In an attempt to locate these carbides, the embedded samples were re-polished and etched with Murakami etchant for a dedicated SEM investigation, but no carbon-rich phase could be resolved. In conclusion, despite the clear experimental evidence of a second phase and the strong suggestion that it is associated with the formation of Fe_2C carbides in the Fe-C coatings, its final identification requires further investigations.

Independent of the nature of the not-yet clearly identified carbide, which is present in the as-deposited Fe-C coatings in addition to α-Fe, the carbide phase is expected to contribute essentially to the high hardness of the coatings being in the order of that of martensitic steels. Both ε-Fe_2C and η-Fe_2C carbides are associated with excellent mechanical properties [31-34], but also the nanocrystallinity of ferrite grains and the detected additional elements of H and O, comprising the peculiar nature of electrodeposited coatings, contribute to the high hardness. Being metastable carbides, the thermal stability of ε-Fe_2C and η-Fe_2C is expected to be limited, which provides an additional possibility for further surface engineering by post-deposition treatments.

Already at fairly low coating thicknesses, the coating growth is fully dictated by the deposition process and reproducible coatings can be deposited reliably. Final applications of the Fe-C coatings utilizing their high hardness and related wear resistance, certainly aim at thick coatings and the observed changes of the deposition rate might become relevant. The observed lowering of the deposition rate after 120 minutes might be affected by several influences: changes of the chemical concentrations in the electrolyte during the longer deposition times, a passivation of the steel anode by a magnetite layer developed on its surface during deposition or an increase of the hydrogen evolution at the cathode surface. The lowered deposition rate and the substantial change in microstrain, which may be related to each other, had no apparent effect on the macroscopic appearance of the Fe-C coatings having a dark shiny color, as well as neither on their microstructure nor the resulting microhardness.

V. CONCLUSION

Fe-C coatings were electrochemically deposited from an iron-sulfate electrolyte with citric acid as an additive. The very high microhardness of the as-deposited coatings and their chemical composition containing 0.88 wt pct C suggest a similarity to martensitic steel, but such rushed terminology is not appropriate for the present Fe-C coatings. No tetragonal martensite has been detected; instead, the Fe-C coatings consist of carbon-free ferrite and a second phase of ε-Fe_2C or η-Fe_2C carbides. While these carbides are known to form during low-temperature tempering of as-quenched martensite, for the present Fe-C coatings, it cannot be concluded whether the carbides form directly during deposition or whether they result from an initial as-deposited phase with a high driving force for carbide precipitation during continued deposition. The Fe-C coatings are nanocrystalline and exhibit a strong fiber texture with a <311> fiber axis in growth direction. The chemical composition of the coatings, their microstructure, and the high microhardness of almost 800 HV have been observed to be independent of the coating thickness. This indicates the strong impact of the deposition conditions on the coating growth and offers the possibility for tailoring the microstructure and properties by further optimization of the electrodeposition process.

The homogeneous and reproducible deposition process, resulting in reliable Fe-C coatings independent of the applied coating thickness, allows for both the comparison of different coatings and the adaption of the thickness to a given purpose or application, which is important for industry. Furthermore, the obtained understanding of the incorporation of co-deposited carbon as fine carbides provide the essential prerequisite for a wide range of applications, where the ability to deposit thick coatings with high hardness is very attractive. Further properties, like adhesion, wear resistance, and corrosion resistance, as well as the coating's thermal stability, are currently being investigated. One of the most critical properties is the oxidation resistance of iron-based materials, but oxidation would only restrict the potential applications to lubricated surfaces and not be a general hindrance for technical applications.

ACKNOWLEDGMENTS

The authors gratefully acknowledge OCAS NV, ArcelorMittal Global R&D Gent (Belgium), a. h. nichro Haardchrom (Denmark), and Fast Track - Societal Partnership (Denmark), funded by the Innovation Fund Denmark (IFD), for financial support.

REFERENCES

[1] H.E. Cleaves, J.G. Thompson, *The Metal - Iron, Alloys of Iron Research Monograph Series,* McGraw-Hill Book Company, New York and London, 1935, pp. 5-17.

[2] A.E. Tashkin, *Russ. Eng. J.*, 1969, vol. 49, pp. 20-21.

[3] G.I. Morozov, V.I. Morozov, Met. Sci. Heat Treat., 1974, vol. 16, pp. 888-890.

[4] M. Schlesinger, M. Paunovic, M. Izaki, *Modern Electroplating*, 5th ed, John Wiley & Sons, Hoboken, New Jersey, 2010, pp. 309-326.

[5] A.S.M.A. Haseeb, Y. Hayashi, M. Masuda and M. Arita, Metall. Mater. Trans. B, 2002, vol. 33, pp. 921–927.

[6] Y. Fujiwara, M. Izaki, H. Enomoto, T. Nagayama, E. Yamauchi, A. Nakae, J. Appl. Electrochem., 1998, vol. 28, pp. 855–862.

[7] Y. Fujiwara, T. Nagayama, A. Nakae, M. Izaki, H. Enomoto and E. Yamauchi, J. Electrochem. Soc., 1996, vol. 143, pp. 2584–2590.

[8] A.S.M.A. Haseeb, M.Z. Huq, Met. Finish., 1997, vol 95, pp. 30–34.

[9] M. Izaki, T. Omi, Metall. Mater. Trans. A., 1996, vol. 27, pp. 483-486.

[10] N. Miyamoto, K. Yoshida, M. Matsuoka, J. Tamaki, J. Electrochem. Soc., 2004, vol. 151, pp. C645-C648.

[11] M. Izaki, N. Miyamoto, A. Nakae, T. Hasegawa, S. Watase, M. Chigane, Y. Fujiwara, M. Ishikawa, H. Enomoto, J. Electrochem. Soc., 2002, vol. 149, pp. C370-C374.

[12] M. Panayotova, Surf. Coat. Technol., 2000, vol. 124, pp. 266–271.

[13] T. Müller, J. Grimwood, A. Bachmaier, T. Schöberlm R. Pippan, Metals, 2018, vol. 8(5) 363

[14] S.D. Dahlgren, M.D. Merz, Metall. Mater. Trans., 1971, vol. 2, pp. 1753-1760.

[15] A. Weck, C.W. Sinclair, C.P. Scott, C. Maunder, J. Mater. Sci., 2002, vol. 47, pp. 6939-6947.

[16] I. Jouanny, V. Demange, J. Ghanbaja, E. Bauer-Gosse, J. Mater. Res., 2010, vol. 25, pp. 1859-1869.

[17] X. Zhao, R.J. Sanderson, L. MacEachern, R.A. Dunlap, Electrochimica Acta, 2015, vol. 170, pp. 16-24.

[18] R. Winand, Hydrometallurgy, 1992, vol. 29, pp. 567–598.

[19] M. Paunovic, M. Schlesinger, *Fundamentals of Electrochemical Deposition*, 2nd ed, John Wiley & Sons, Hoboken, New Jersey, 2006, pp. 113-137.

[20] J.I. Langford. J. Appl. Cryst., 1978, vol. 11, pp. 10–14.

[21] T.H. de Keijser, J.I. Langford, E.J. Mittemeijer, A.B.P. Vogels, J. Appl. Cryst., 1982, vol. 15, pp. 308–314.

[22] C. Esling, E. Bechler-Ferry, H.J. Bunge, J. Phys. Lettres, 1981, vol. 42, pp. 141–144.

[23] N. Miyamoto, S. Sakamoto, H. Tamura, M. Matsuoka, J. Tamaki, J. Electrochem. Soc., 2005, vol. 152, pp. C488-C492.

[24] D.A. Porter, K.E. Easterling, M.Y. Sherif, *Phase transformations in metals and alloys*, 2nd ed, Chapman & Hall, New York, NY, 2009, pp. 382-396.

[25] G.A. Nematollahi, B. Grabowski, D. Raabe, J. Neugebauer, Acta Metall., 2016, vol. 111, pp. 321-334.

[26] Y. Hirotsu, S. Nagakura, Acta Metall., 1972, vol. 20, pp. 645–655.

[27] H.L. Yakel, Int. Met. Rev., 1985, vol. 30, pp. 17-40.

[28] S.W. Thompson, Mater. Charact., 2015, vol. 106, pp. 452-462.

[29] S.W. Thompson, Metallogr. Microstruct. Anal., 2016, vol. 5, pp. 367-383.

[30] H.K.D.H. Bhadeshia, *Bainite in steels*, 3th ed, Maney Publishing, Hanover Walk, Leeds 2015, pp. 62.

[31] X.T. Deng, T.L. Fu, Z.D. Wang, R.D.K. Misra, G.D. Wang, Mater. Sci. Technol., 2016, vol. 32:4, pp. 320-327

[32] L. Hui, Z.Q. Chen, Z. Xie, C. Li, Stability, J. Supercond. Nov. Magn., 2018, vol. 31, pp. 353-364.

[33] X. Chong, Y. Jiang, J. Feng, J. Alloys Compd., 2018, vol. 745, pp. 196-211.

[34] A. Oila, C. Lung, S. Bull, J. Mater. Sci., 2014, vol. 49, pp. 2383-2390.

6.1.2 Supplementary material regarding the coatings thickness or the substrate

Nucleation and growth of electrodeposits is affected by the nature of the substrate, which can influence the size, shape and crystallographic orientation of grains and, consequently, also the resulting properties of the electrodeposits [2]. The present work reports on systematic studies of Fe-C coatings, which have been electrodeposited with various thicknesses on different substrates under identical process parameters apart from the deposition time. The operation conditions for electrodeposition of the Fe-C coatings are the same as described in Manuscript I.

6.1.2.1 The microhardness

The microhardness of the deposits was measured from the surface using the method described in Manuscript I. A high microhardness value of almost 800 HV0.01 has been measured for all Fe-C coatings, almost independent of the coating thickness and the type of substrate, as shown in Table 8. For a few samples, the surfaces have not been ideal for hardness indentations with low load due to micro-pits from slight oxidation (coatings with 30 µm on steel and 165 µm on brass); the corresponding less reliable hardness values are therefore marked in Table 8.

*Table 8: Microhardness of Fe-C coatings measured from the surface. *Surface topography of these samples affects the measured hardness.*

Thickness [µm]	Substrate	
	Steel	Brass
16	792 ± 15 HV0.01	805 ± 16 HV0.01
30	760* ± 17 HV0.01	-
58	797 ± 14 HV0.01	-
165	812 ± 15 HV0.01	765* ± 19 HV0.01

6.1.2.2 The crystallographic texture

The crystallographic texture of the deposits was quantified using the method described in Manuscript I. All Fe-C coatings consist of a ⟨311⟩ fiber texture, as shown in Figure 40. The fiber axis ⟨uvw⟩ and the corresponding orientation densities in multiples of random distribution are summarized for all samples in Table 9. The slight changes of the texture strength shown for Ni-P substrates as a function of coating thickness as described in Manuscript I is revealed neither for the steel substrate nor for the brass substrate.

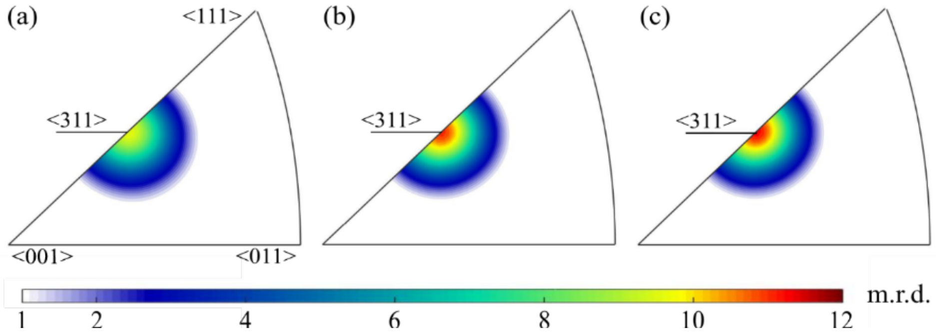

Figure 40. The inverse pole figure in growth direction obtained by XRD measurements for Fe-C coatings with a thickness of 16 µm on different substrates: (a) Ni-P, (b) steel and (c) brass.

Table 9: Crystallographic texture of Fe-C deposits with varying thickness and substrate. The values in the table represent the fiber axis in growth direction and the strength of the fiber axis [m.r.d.], respectively.

Thickness [µm]	Substrate	
	Steel	Brass
16	⟨311⟩ - 11.0	⟨311⟩ - 11.0
30	⟨311⟩ - 12.0	-
58	⟨311⟩ - 12.0	-
165	⟨311⟩ - 11.0	⟨311⟩ - 12.0

6.1.2.3 Deposit stress analyzer

As an alternative to XRD stress analysis, which for the strongly textured samples could not be applied reliably, the stress deposit analyzer was used to test the residual stresses in the coating after deposition as described in Section 4.7. The coatings were deposited in two different thicknesses and on two different metals such that the influence of thickness and substrate can be evaluated. The operation conditions were the same as described in Manuscript I but using a deposition time of 20 or 40 min. The thickness of the coating was confirmed using the mass gain of the test strips after deposition. The two test strips for each condition were deposited using the same electrolyte.

Results and discussion

The determined residual stresses in the Fe-C coating with different thickness and on different substrates are shown in Figure 41. The residual stresses in the Fe-C coating are compressive and below 200 MPa independent on the substrate and the thickness of the coating. The amount of compressive stresses are slightly higher on the copper substrate compared to the iron strips and is suggested as a result of the lattice mismatch between the copper substrate and Fe-C coating, although the determined stresses represent average values over the whole coating thickness and all present phases. A slight increase is seen in the mean value of compressive stresses for the thicker coatings, although the variations are close to the standard deviation.

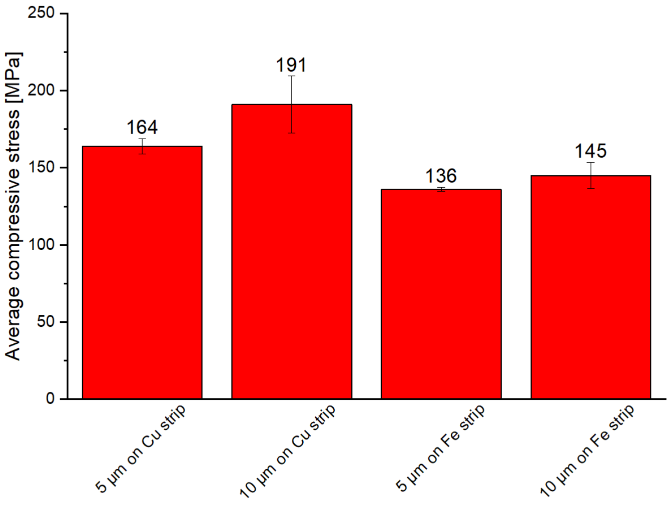

Figure 41: Deposition of Fe-C coating on copper and iron strips for testing of residual stresses.

6.1.3 Supplementary material regarding the nature of the as-deposited Fe-C coatings

Some of the investigations that have been conducted, but were not included as part of a manuscript, concern different aspects of the material properties of the as-deposited Fe-C coating and are included in this section. The investigated samples were deposited simultaneously using a cathode design as described in Section 4.1.3. The Fe-C coatings were deposited with a thickness of 360 µm on a steel and a brass substrate using the operation conditions described in Manuscript I with the deposition time being extended to 15 hours.

6.1.3.1 Energy-dispersive diffraction analysis

The samples were investigated using EDD at the EDDI beamline at the synchrotron facility BESSY II.

6.1.3.1.1 Phase analysis

All prior publications that have included XRD analysis have been performed without tilting the sample around the azimuth angle [16–19,21,23–26,28] and only a single additional diffraction peak (not being ferrite) has been measured using this experimental setup. This study was conducted to search for supplementary peak related to the phase (not being ferrite) by changing the diffraction conditions.

The EDD allowed the full spectrum being measured at a fixed diffraction angle as described in Section 4.2.6. The use of a low diffraction angle of $2\Theta = 8°$ ensured a good separation between the diffraction peaks. A symmetric beam path was applied and the sample was inclined around the azimuth angle to measure the phases with a specific crystallographic orientation within the coating. The inclination around the azimuth angle was performed from $\psi = 0$ to 90°, in 1° steps. The diffraction spectra are shown as a contour plot in Figure 42. The azimuth angles at which intensity is measured for the ferrite peaks α-110, α-200 and α-211 correspond exactly to the angles between the preferred <311> orientation and the specific lattice planes as calculated in Section 4.2.4.2 and presented in Table 7. This supports the result of the quantitative crystallographic texture analysis presented in Manuscript I. The additional peak for the phase (not being ferrite) is measured only for an applied azimuth angle between 0 and 12°. The d-spacing was measured to 0.237 nm at $\psi = 0°$, which is in good agreement with the result from manuscript I. The measurement did not detect additional peaks for the “nameless phase”. The measurement also shows that the peaks of the “nameless phase” and the α-110 decrease in intensity in a similar manner from $\psi = 0$ to 12° and this indicates an orientation relationship between these two phases.

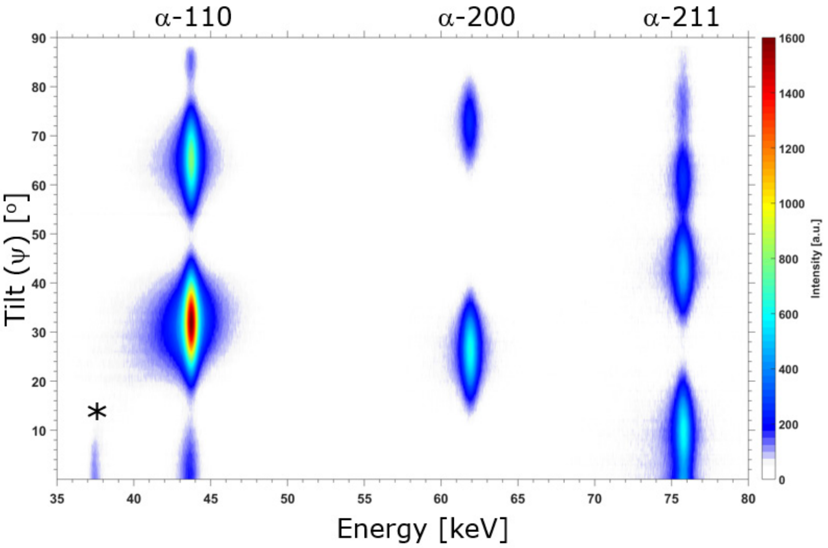

*Figure 42: Contour plot of EDD spectra using 2Θ = 8° of as-deposited Fe-C coating inclined around the azimuth angle ψ from 0 to 90°. α corresponds to ferrite and * corresponds to the "nameless phase".*

6.1.3.1.2 Depth resolved phase analysis

The Fe-C coating was deposited with a thickness of 360 µm on a brass substrate and was afterwards deposited with a thin layer of nickel. The brass substrate was used to have a clear transition from the Fe-C coating to the substrate and the nickel coating was applied to protect the samples from corrosion during the sample preparation, which was needed for the depth-resolved measurements. The sample was cut as cross section to receive a thin slice of 1 mm using a Struers Accutom-50 with a low feed rate and applying cooling fluid. The cutting was performed with the sample being fixed on a steel plate for support as shown in Figure 43.

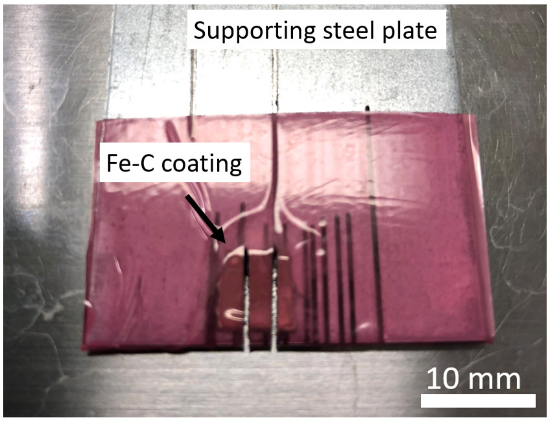

Figure 43: Sample preparation for depth-resolved EDD measurement in transmission geometry.

An illustration of the cross section of the sample used for the depth resolved phase analysis is shown in Figure 44, where the diamonds represent the measurement gauge of the synchrotron beam, which was reduced to a height of 10 µm. By moving the sample through the beam in transmission geometry, depth-resolved phase analysis was possible. A distance in height between each measurement position of 40 µm was used and the first measurement was acquired 20 µm below the interface of the Ni layer and the Fe-C coating. The stage was used to increase the height of the sample to access different measurements positions. The diffraction angle was set to 2Θ = 20° in order to measure also the higher order reflections of α-Fe. The diffraction peaks were fitted using a pseudo Voigt function. A gold standard was measured in reflection to correct for energy offset using otherwise identical diffraction conditions.

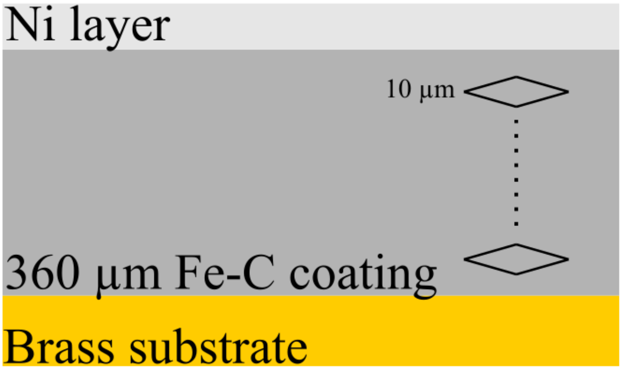

Figure 44: Illustration of the cross section of the sample being used for depth resolved phase analysis. The diamond represents the EDD measurement gauge.

The lattice spacings for α-Fe peaks of high intensity measured as a function of the distance from the surface are shown in Figure 45. For these peaks, reliable peak fitting was achieved. The lattice spacings are relatively uniform as a function of depth with an outlier being measured at 60 µm from the surface for all measured reflections and an outlier measured for α-310 at 220 µm from the surface. There is no clear explanation for these values. The lattice spacings are slightly lower for the measurements closest to the brass substrate, which could be related to the mismatch between the unit cells of the substrate and the coating.

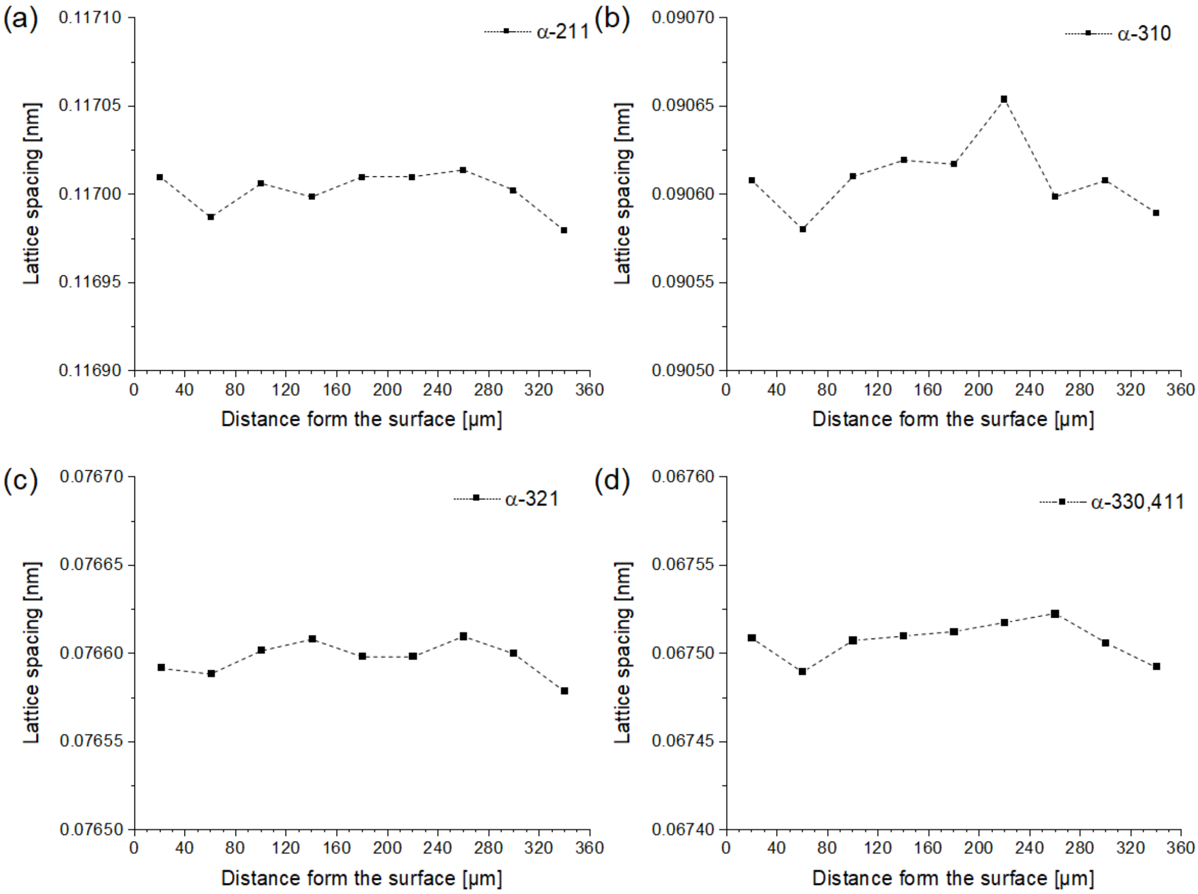

Figure 45: Depth resolved energy-dispersive diffraction in transmission on an as-deposited Fe-C coating. The height of the measurement gauge was 10 µm. The measured peaks correspond to α-211 (a), α-310 (b), α-321 (c), and α-330,411 (d).

6.1.3.1.3 $\sin^2\psi$ method

The macrostress state of the as-deposited Fe-C coating was attempted to investigate using the $\sin^2\psi$ method as described in Section 4.2.4.1 using a diffraction angle of $2\Theta = 20°$ in order to measure the higher order reflections of α-Fe. The inclination around the azimuth angle was performed from $\psi =$ 0 to 75°, in 1° steps. The diffraction spectra are shown as a contour plot in Figure 46. The α-Fe peaks were fitted with a pseudo Voight function and corrected for energy offset using a gold standard that was measured at each of the azimuth angles.

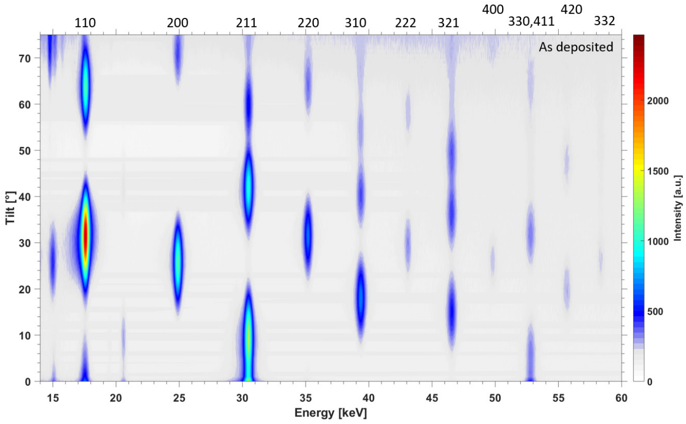

Figure 46: Contour plot of EDD spectra using $2\Theta = 20°$ of as-deposited Fe-C coating inclined around the azimuth angle ψ from 0 to 75°

The strain has been calculated using the Equation (19) with the strain-free lattice spacing measured for the Fe-C coating in the strain-free direction (cf. Table 6). The azimuth angle closest to the strain-free direction was used to obtain d_0 and the difference between the measured angle and the calculated angle of ψ_0^{hkl} corresponds to a maximum of 0.5°. The α-200 peak is not included in the analysis as there is no intensity measured for this peak in its strain-free direction corresponding to ψ_0^{200}= 45.6°. The $\sin^2\psi$ plot is shown in Figure 47. Clearly, a linear regression between the points, as requested for the $\sin^2\psi$ analysis, is not possible for the present data. The large variation between the measurement values is expected to be caused by the strong fiber texture. The $\sin^2\psi$ method is therefore not investigated further.

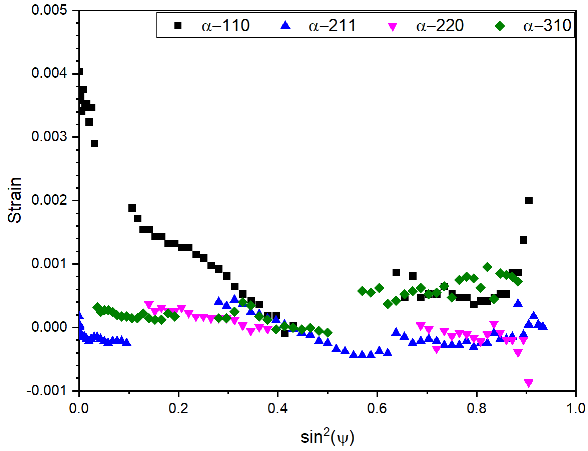

Figure 47: Energy-dispersive diffraction analysis applying the $\sin^2\psi$ method using several α-Fe peaks on as-deposited Fe-C coating.

6.1.3.1.4 Crystallite group method

The crystallite group method was introduced to analyze the macrostresses within the textured Fe-C coating [42]. The crystallite group method uses only the measured lattice strain from the grains of main crystallographic orientation being <311>. The angles between the α-311 lattice plane and the different lattice planes for α-Fe used in the analysis are shown in Table 7. The strain values for the α-Fe peaks are plotted as a function of the $\sin^2\psi$ along with the linear regression between the points as shown in Figure 48. The variation between the measured strain values produces a large standard deviation for the linear regression and hinders the crystallite group method in being a suitable method to determine the macrostresses for the Fe-C coating.

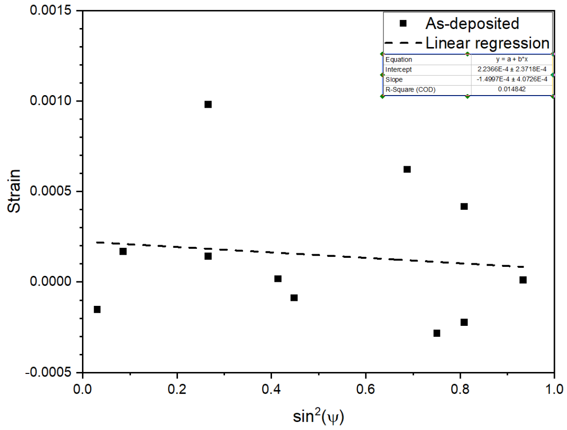

Figure 48: Energy-dispersive diffraction macrostress analysis applying the crystallite group method on as-deposited Fe-C coating.

By mechanical means instead of XRD, the residual stresses of the Fe-C coating were quantified as compressive stresses below 200 MPa by the stress deposit analyzer in Section 6.1.2.3. The residual stresses measured by the crystallite group method only relate to ferrite while the stress deposit analyzer measures the total residual stresses. The difficulty of obtaining results from XRD for residual stresses with the crystallite group method may be related to the rather weak stresses expected in ferrite.

6.1.3.2 Hardness depth profile

Another part of the Fe-C coating on a brass substrate and Ni deposited on the surface, as described in Section 6.1.3.1.2, was also used for hardness depth profile measurements in order to complement the different methods of characterizations. The sample was cold embedded in epoxy and the cross section was metallographically prepared as described in Section 4.3.1. To obtain a good measurement resolution, the depth profiles was acquired using 4 measurement rows where the distance to the interface of the Ni layer and the Fe-C coating was slightly shifted for each of the first measurement point in a row, as described in Section 4.6.1. The depth-resolved measured microhardness values are shown in Figure 49. On average over the whole coating thickness, they result in a value of around 780 HV0.025. The measurement indicates that the microhardness may be slightly higher at the surface although the variation does not clearly allow for such a conclusion.

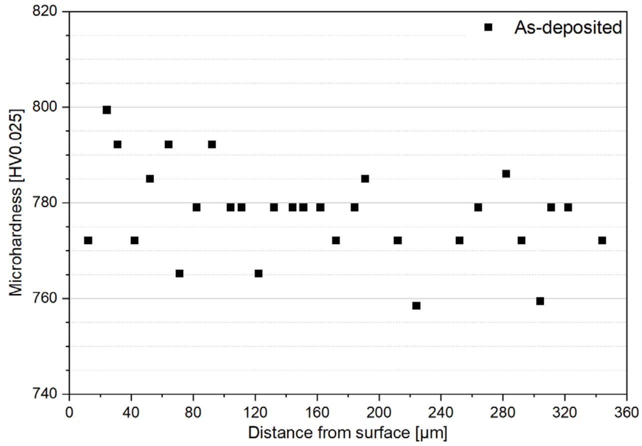

Figure 49: Microhardness depth profile of an as-deposited Fe-C coating.

6.2 The study of the current density, iron concentration and citric acid concentration

6.2.1 Manuscript II

Study of Fe-C coatings electrodeposited using specific operation conditions to control the mass transfer rate[6]

Jacob Obitsø Nielsen*, Karen Pantleon

Technical University of Denmark, Department of Mechanical Engineering, Produktionstorvet, building 425, DK – 2800 Kongens Lyngby, Denmark

Abstract

Fe-C coatings were deposited from an iron(II)sulfate or an iron(II)chloride based electrolyte using citric acid as an additive. Different concentrations of iron(II)sulfate were applied and the increase in iron concentration was accompanied by an increase in the applied current density. The iron(II)chloride based electrolyte was mixed with the same iron concentration as the iron(II)sulfate based electrolyte with the lowest iron concentration to investigate the influence of the different anions. The samples were investigated using X-ray diffraction and chemical analysis along with microhardness measurements. The appearance of the Fe-C coatings was dark grey and mirror bright independent of the applied operation conditions. The carbon content and hardness of the Fe-C coatings were also independent of the operation conditions. The phase constitution was the same for the Fe-C coatings deposited using different operation conditions from the iron(II)sulfate based electrolyte, but different from the Fe-C coating from the iron(II)chloride based electrolyte. The highest deposition rate and current efficiency were measured for the Fe-C coating deposited in the electrolyte with the highest iron concentration. The results demonstrate that similar Fe-C coatings can be deposited when the ratio between the iron concentration and current density is maintained and using a higher iron concentration will increase the current efficiency, which is desirable for a large-scale long term industrial operation.

1. Introduction

The electrodeposited Fe-C coatings are potential candidates to replace hard chrome coatings in lubricated environments as the as-deposited coating hardness is around 800 HV and the coating can be deposited in thick layers [1-5]. The electrolyte used to deposit Fe-C coatings is based on iron-sulfate and the addition of at least one carboxylic acid [6]. The carboxylic acid has multiple purposes as carbon source, buffer and to avoid solid precipitates in the electrolyte by complexing with iron. The influence of the electrolyte's chemical composition on the resulting microstructure and the mechanical properties of the Fe-C coating has been examined in multiple articles [3,7,8]. The evaluation of the influence of each parameter can lead to ambiguities when comparing results as the remaining operation conditions in the publications are not identical.

There are many adjustable parameters for an electrochemical deposition that influence the resulting microstructure obtained on the cathode surface [9]. Some of the adjustable parameters

---

[6] Manuscript in preparation for publication.

are the current density, temperature, pH-value, cathode material, additive, and complexation. The effect of each operation condition can be subdivided into the charge transfer, diffusion, reaction, and crystallization overpotentials. However, the determination of the overpotentials is experimentally difficult and the evaluation of the individual contributions to the total overpotential as a single parameter lacks the correlation to the resulting microstructure of the coating [9]. The total overpotential can be estimated based on the morphology of the coating and the inhibition intensity along with the mass transfer parameter being the ratio between the current density and the equilibrium metal ion concentration. However, the chemical composition of an electrolyte can change during deposition as different partial reactions occur simultaneously. The concentration of iron, for example, will increase when the cathodic current efficiency is below 100 % and a sacrificial iron anode is applied.

It is therefore necessary to ensure that the Fe-C coatings can be deposited with similar and reproducible properties over a range of iron concentrations as the current efficiency of the process is well below 100 % when a thick coating is deposited [10]. The increase in the metal ion concentration will require an increase in the current density to maintain the mass transfer parameter and ensure that the electrodeposited coatings have consistent growth characteristics [9].

The present work reports on systematic studies of Fe-C coatings that were electrodeposited from an iron-sulfate electrolyte with citric acid as additive. The effect of the operation conditions was studied by varying the chemical composition of the electrolyte and the current density simultaneously. The difference between a Fe-C coating from an iron-chloride and an iron-sulfate electrolyte, having the same iron concentration and otherwise similar operation conditions, was investigated to measure the effect of the anions. The Fe-C coatings' appearance, hardness, and crystal structure were examined, along with the process deposition rate and the current efficiency.

2. Materials and methods

2.1 Electrodeposition

The operation conditions of the four setups that were investigated are shown in Table 10. The operation conditions 1 and 2 had the same iron concentration (8 g/L) but used different iron-salts. The iron concentration and current density were increased for operation conditions 3 and 4. The temperature of the electrolyte amounted to 50 °C for all depositions. The pH-value was kept between 2.5-2.8 and was adjusted during deposition, using either hydrochloric acid (HCl) for the iron-chloride electrolyte or sulfuric acid (H_2SO_4) for the iron-sulfate electrolytes.

Table 10: Electrolyte composition and operation conditions for different electrolytes used for electrodeposition of Fe-C coatings.

Operation conditions	**1**	**2**	**3**	**4**
Iron-chloride ($FeCl_2 \cdot 4H_2O$) [g/L]	28	-	-	-
Iron-sulfate ($FeSO_4 \cdot 7H_2O$) [g/L]	-	40	80	120
Citric acid ($C_6H_8O_7 \cdot H_2O$) [g/L]	1.2	1.2	1.2	1.2
Current density [A/dm^2]	3.0	3.0	3.5	4.0
Deposition time [hour]	7	7	12	12

The cathode design was identical for all depositions with three hardened steel strips being fixed to one side of a 10 x 9 cm steel plate using lead tape as illustrated in Figure 1. The hardened steel strips were introduced as cathode material, because they ensure a low adhesion to the Fe-C coatings and can easily to be removed to obtain a free-standing coating for materials characterization. The strips of hardened steel were positioned 1 cm away from the edge of the cathode to avoid any possible edge effects. The lead tape was applied in a matrix such that different areas of the cathode could be examined separately. This allowed the investigation of potential variations between the deposits from the center (labeled 3 in Figure 1) and the deposit closer to the edge (labeled 1 in Figure 1). The lead tape had the advantage of being electrical conductive and did not alter the current field lines, because the whole cathode surface was electrically conductive. A single IF steel anode was used and the backside of the cathode was covered with an isolating electrolyte-resistant tape to ensure that only the side towards the anode was deposited. The measurement positions 1, 2, and 3, shown in the illustration of the cathode in Figure 1, are used to indicate the various measurement positions during materials characterization as described below.

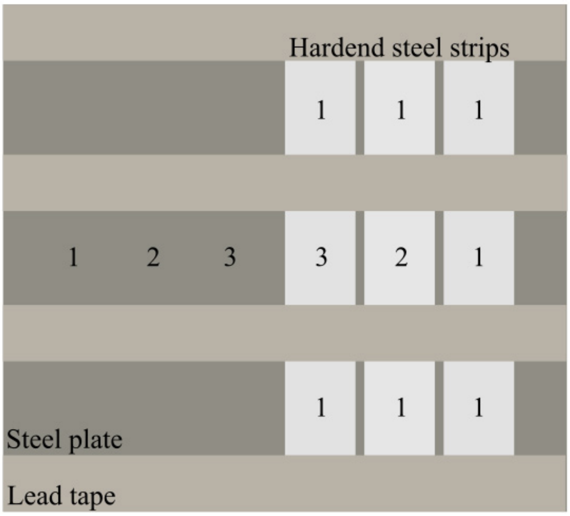

Figure 1: Illustration of the cathode consisting of hardened steel strips attached to a steel plate using lead tape. The numbers 1, 2, and 3 are explained in the text.

2.2 Determination of the current efficiency

The thickness of the coating deposited on the steel plate was measured at position 1, 2 and 3 for each sample using a micrometer screw gauge.

The current efficiency of the system was calculated by dividing the measured thickness of the coating with the theoretical thickness (*d*) calculated according to [11],

$$d = \frac{I \cdot t \cdot M}{z \cdot F \cdot \rho \cdot A}$$

where m is the total mass gain, I is the current, t is the deposition time, M is the molar mass, z is the amount of electrons transferred and F is Faradays number, ρ is the density of the coating and A is the cathode surface area.

2.3 Chemical composition

The carbon content of the Fe-C coatings was determined by the evolved-gas-analysis using a carbon analyzer LECO CS230. The measurements were performed using 0.1 g of the free-standing coating. The carbon content was measured twice per sample from measurement position 1. The extended deposition time and higher deposition rate for the operation conditions 3 and 4 provided the 0.1 g of free-standing coating from measurement position 3 where a thinner coating is deposited compared to the edges.

2.4 Hardness measurement

The microhardness was measured using a Struers DuraScan on the free-standing coatings from position 1 that have been cold embedded in epoxy and metallographically prepared to allow the indent to be positioned in the middle of the coatings cross section. The microhardness was determined using a Vickers indent and a load of 25 g. The values are presented as the average value of five measurements per sample.

2.5 Energy-dispersive diffraction phase analysis

Qualitative phase analysis was performed by means of energy-dispersive diffraction (EDD) with a dedicated diffractometer operated in the energy-dispersive mode using a laboratory tungsten X-ray tube (LEDDI diffractometer at HZB, Berlin). The white X-ray beam with a continuous photon energy spectrum is used at a fixed diffraction angle 2θ, and diffraction occurs for crystallographic lattice planes with spacing (d_{hkl}) at a photon energy (E_{hkl}) according to [12],

$$E_{hkl} = \frac{h\,c}{2\sin\theta} \cdot \frac{1}{d_{hkl}}$$

where h is Planck's constant and c is the speed of light. The X-ray fluorescence lines for the elements within the sample and in the experiment setup are also measured at their respective characteristic energies. The white beam was generated by a tungsten X-ray tube. A symmetric diffraction geometry was applied with a fixed diffraction angle of $2\theta = 21.5^\circ$ in order to measure the higher order reflections. The EDD spectra were measured for all samples on the steel substrate at positions 1, 2, and 3.

3. Results and discussion

3.1 Appearance

The appearance of the as-deposited Fe-C coatings was dark-grey and mirror bright as shown in Figure 2. The upper left corner of the Fe-C coating from the iron chloride electrolyte has a higher surface roughness compared to the remaining samples. This roughness was developed by hydrogen bubbles that were produced on the cathode surface and increased in size at the position where the lead tape had released from the steel plate. The gas bubbles traveled near the cathode towards the surface and changed the current field lines in their path. The surface roughness was developed over time and acted as favorable tracks for the succeeding bubbles and reinforced the effect. The development of dendrites on the edge of the cathode plates was seen on all samples. The majority of dendrites broke off during drying the sample after deposition and they are therefore not seen in Figure 2.

There was no difference in the appearance of the Fe-C coatings deposited using the different operation conditions when disregarding the development of the surface roughness caused by the detachment of the lead tape. It was noted that the Fe-C coating deposited using the iron-chloride electrolyte fractured more easily compared to the Fe-C coating deposited under similar condition but from an iron-sulfate electrolyte when the coatings were removed from the hardened spring steel. The fracture of the coating was not a consequence of a stronger adhesion to the substrate, but may indicate that the brittleness is higher for the chloride based Fe-C coating.

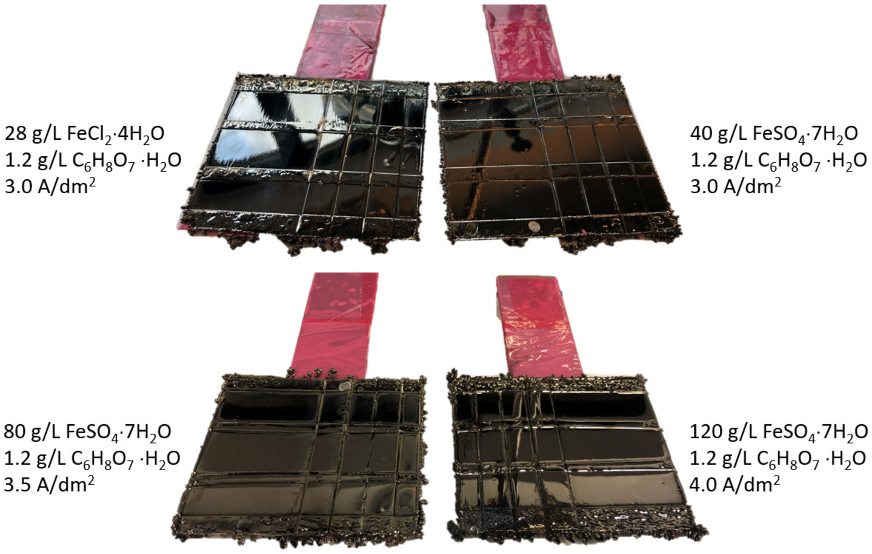

Figure 2: Images of Fe-C coatings deposited using different operation conditions.

3.2 Deposition rate and current efficiency

The average deposition rate and current efficiency for the applied operating conditions are shown in Figure 3a and 3b, respectively. The deposition rate was highest closest to the edge of the sample (position 1) as was expected for a planar cathode geometry under normal plating conditions. The average deposition rate and current efficiency are nearly identical for the iron-sulfate and iron-chloride electrolyte with the same iron-concentration. The deposition rate was increased for the electrolyte with an iron-sulfate concentration of 80 g/L as a higher current density was applied. However, the current efficiency was the same as for the electrolytes with a lower iron concentration. The deposition rate was highest for the iron-sulfate concentration of 120 g/L as the current density was increased further. The increased iron concentration and current density resulted in an increased current efficiency for the iron-sulfate concentration of 120 g/L.

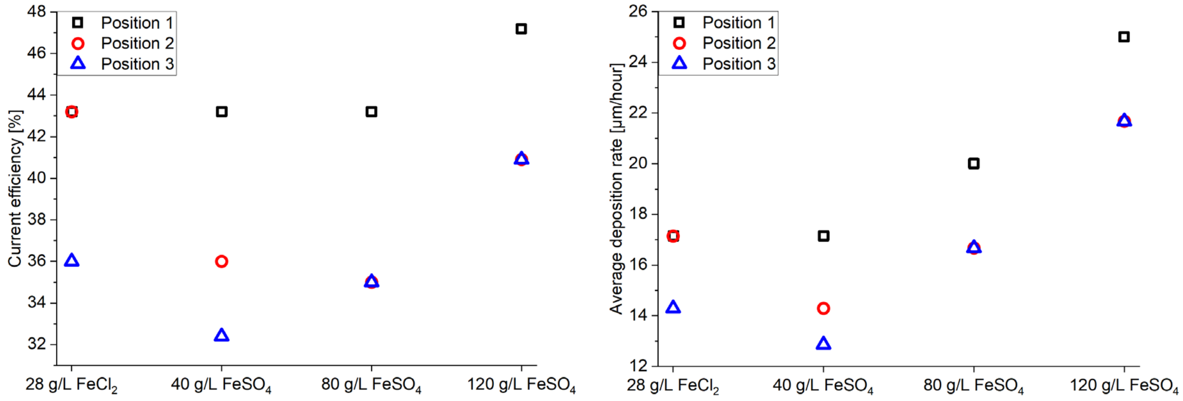

(a) (b)

Figure 3: The deposition properties calculated from the three measured position on the Fe-C coatings deposited using different operation conditions. (a) The average deposition rate. (b) The current efficiency.

3.3 Carbon content and microhardness

The carbon content and microhardness for all deposits are shown in Table 1. The carbon content was measured around 1 wt% independent of the operation conditions. The variation of the carbon content in the center of the sample and the outer region was insignificant. The average microhardness for all samples amounted to around 775 HV0.025.

The carbon content of around 1.0 wt% measured for all samples is higher compared to the value of 0.88 wt% published previously for the Fe-C coating deposited using the same operation conditions [10]. The same instrument setting was applied to the LECO CS230 and the calibration method and sample size of both sets of measurements have been identical. The measurements were conducted with more than a year in between, which should not influence the results. There is no clear explanation for this difference at the moment.

Table 1: Carbon concentration and average microhardness of Fe-C coatings deposited using different operations conditions.

Electrolyte composition	**28 g/L $FeCl_2$**	**40 g/L $FeSO_4$**	**80 g/L $FeSO_4$**	**120 g/L $FeSO_4$**
Carbon concentration position 1 [wt%]	1.027 ± 0.001	1.031 ± 0.041	0.975 ± 0.034	0.998 ± 0
Carbon concentration position 3 [wt%]	-	-	0.963	0.998
Microhardness [HV0.025]	774 ± 25	777 ± 5	787 ± 17	770 ± 26

3.4 Phase analysis

The measured diffraction spectra at the three positions for all samples are shown in Figure 4. The three diffraction spectra for each coating were nearly identical in terms of intensity, peak position, and peak profile and showed that there was no significant variation. There are two peaks measured at low energy that have a much smaller breadth compared to the remaining peaks and these have been identified as X-ray fluorescence peaks and are related to the experimental method. The phase analysis revealed that the microstructure mainly consists of α-Fe (JCPDS 6-696). The intensity of α-110 and α-211 was higher for the iron-chloride based coating compared to the iron-sulfate based one and suggested a different crystallographic texture of this coating. A minor second phase, in addition to ferrite, was measured for all samples by the additional peak around 14 keV. This peak has been repeatedly measured using both conventional laboratory X-ray diffraction techniques using a fixed wavelength and energy-dispersive synchrotron diffraction using a white beam [5,8,10,13]. However, the phase identification is hindered and even impossible by only having measured a single peak and therefore, the second phase is referred to as the "nameless phase" and (at the moment) remains unidentified. The difference in chemical composition of the two types of electrolytes, i.e. sulfate- and chloride-based, contributes to understanding the "nameless phase". The results revealed that the "nameless phase" does not include the element sulfur, as the iron-chloride electrolyte did not contain this element in the operation conditions. The intensity of the "nameless phase" was lower for the iron-chloride based coating, which either could indicate a smaller amount of that phase and/or could be an effect of a different crystallographic texture, which also was suggested for the ferrite phase as mentioned above.

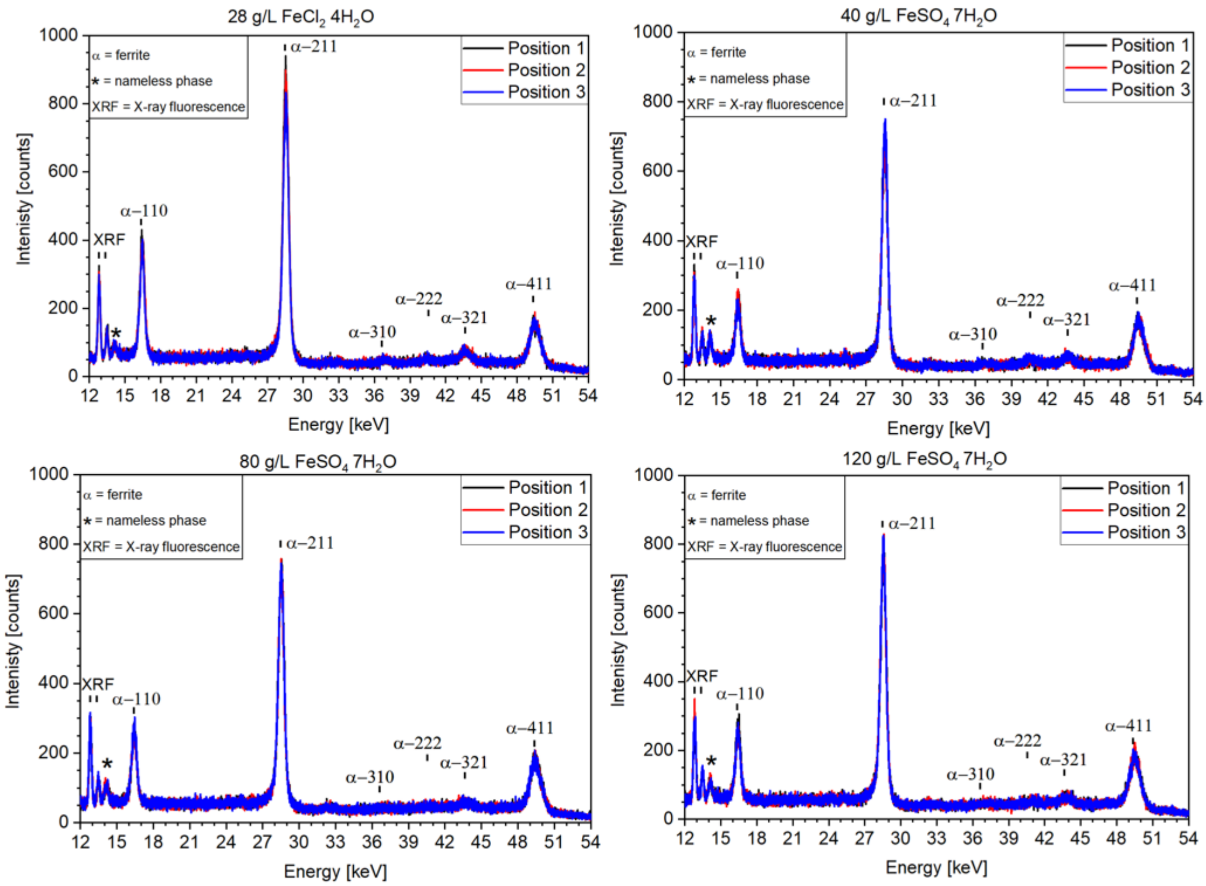

Figure 4: Energy-dispersive diffraction spectra measured at different positon on the Fe-C coatings deposition using different operation conditions.

4. Conclusion

The Fe-C coatings deposited from the iron-chloride and iron-sulfate based electrolyte using otherwise identical operation conditions have the same appearance, carbon content, and microhardness but a slight change in the crystallographic texture is indicated. Further, the deposition rate and current efficiency of the deposition processes are also the same. The Fe-C coating from the iron-chloride electrolyte performed more brittle compared to the Fe-C coating from the iron-sulfate electrolyte, which is a disadvantages for wear applications.

The simultaneously increase in iron-sulfate concentration and current density resulted in Fe-C coatings with the same carbon content, microhardness, phase constitution and appearance for all the applied operation conditions. The phase constitution is homogenous over the measured surface area. The increase in iron-sulfate concentration and current density resulted in a higher current efficiency and deposition rate, which is beneficial for an industrial process. The results show that it is possible to deposit Fe-C coating with the same material properties over a wide range of iron sulfate concentrations when the current density is managed accordantly.

Acknowledgement

M. Klaus, D. Apel, and C. Genzel from Helmholtz Zentrum für Materialien und Energie (HZB, Germany) are acknowledged for their valuable support with energy-dispersive diffraction measurements and during subsequent data analysis.

References

[1] M. Izaki, H. Enomoto, T. Omi, Hardness and Carbon Content of Fe Electroplate from Sulfate Bath Containing l-Ascorbic Acid and Citric Acid, J. Surf. Fin. Soc. Jpn. 40 (1989) 1304–05.

[2] M. Izaki, H. Enomoto, A. Nakae, S. Terada, Y. Eiko, T. Omi, Phase Transformations and Hardness Changes in Electrodeposited Alloy Films Iron-carbon alloy films., J. Surf- Fin. Soc. Jpn. 45 (1994) 1303–1309.

[3] Y. Fujiwara, M. Izaki, H. Enomoto, T. Nagayama, E. Yamauchi, A. Nakae, Optimization of bath composition for hard Fe-C alloy plating, J. Appl. Electrochem. 28 (1998) 855–862.

[4] M. Panayotova, Deposition of Fe–C alloy on structural steel and cast iron for repair of worn machine parts, Surf. Coat. Technol. 124 (2000) 266–271.

[5] J.O. Nielsen, K. Pantleon, Evolution of hard Fe–C electrodeposits with temperature, Surf. Eng. (2019), in press. Published online in October 2019.

[6] Y. Fujiwara, M. Izaki, H. Enomoto, A. Nakae, Effects of Hydroxycarboxylic Acids on the Electrodeposition of Fe-C Alloys, Denki Kagaku. 7 (1993) 840–842.

[7] A.S.M.A. Haseeb, M.Z. Huq, Electrodeposition of martensitic iron-carbon alloy coatings at room temperature, Met. Finish. 95 (1997) 30–34.

[8] T. Müller, J. Grimwood, A. Bachmaier, R. Pippan, Electrodeposition of Fe-C alloys from citrate baths: Structure, mechanical properties, and thermal stability, Metals (Basel). 8 (2018) 1–13.

[9] R. Winand, Electrocrystallization - theory and applications, Hydrometallurgy. 29 (1992) 567–598.

[10] J.O. Nielsen, P. Møller, K. Pantleon, Electrodeposition of Iron with Co-deposition of Carbon: On the Nature of Nanocrystalline Fe-C Coatings, Metall. Mater. Trans. A. 50A (2019) 3785–3793.

[11] M. Panunovic, M. Schlesinger, Fundamentals of Electrochemical Deposition, Wiley, 2006.

[12] C. Genzel, I. A. Denks, J. Gibmeier, M. Klaus, G. Wagener, The materials science synchrotron beamline EDDI for energy-dispersive diffraction analysis, Nucl. Instruments Methods Phys. Res. A. 578 (2007) 23–33.

[13] A.S.M.A. Haseeb, Y. Hayashi, M. Masuda, M. Arita, On the nature of the electrochemically synthesized hard Fe-0.96 mass pct C alloy film, Metall. Mater. Trans. B. 33B (2002) 921–927.

6.2.2 Supplementary material regarding operation conditions.

The difference in appearance of the as-mixed iron-sulfate and iron-chloride electrolyte is shown in Figure 50. The blurred appearance of the iron-chloride based electrolyte suggests the presence of solid precipitates. The appearance of the Fe-C coating deposited from the iron-chloride electrolyte was not influenced by the solid precipitates and, with the applied characterization methods, neither an incorporation of the precipitates in the coating (which would have affected, for example, the hardness) was revealed.

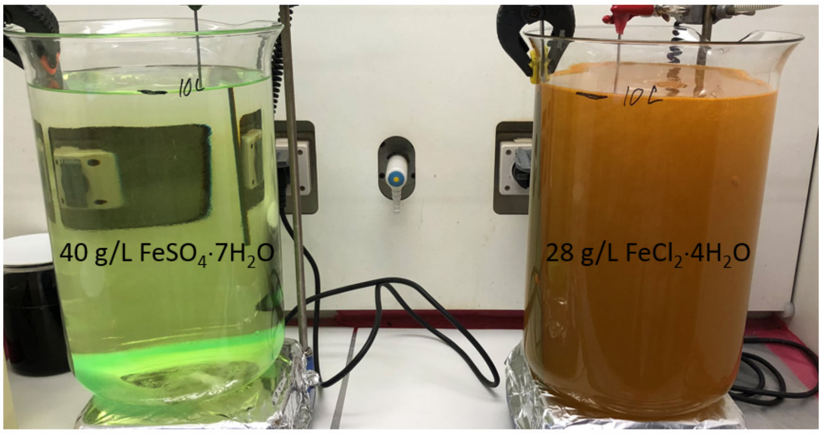

Figure 50: Image of Fe-C electrolytes mixed using FeSO$_4$ or FeCl$_2$ salts.

Screening the operation conditions

The mechanical properties of a coating are not the only important parameter for an industrial surface treatment. The appearance is vital for industrial applications as the ability to produce a uniform and reproducible look may be required to convince a customer of the quality of a new surface treatment.

The present work reports on systematic studies of Fe-C coatings, which where electrodeposited from an iron-sulfate electrolyte with citric acid as additive.

The statistical design and analysis of experiments (DOE) using a definitive screening design[7] was applied to reduce the number of samples without losing the ability to investigated the correlated effects. The parameters of the operation conditions that were varied include the iron concentration, citric acid concentration and the current density and each parameter was applied in three values as shown in Table 11. The temperature amounted to 50 °C for all depositions. The initial pH-value was as mixed (between 2.4 and 2.7) and a deposition time of 2 hours was applied. An iron anode was positioned on one side of a 5 x 5 cm steel plate used as cathode. One side of the cathode was covered with an electrolyte-resistant tape to ensure deposition only on the side toward the anode.

Table 11: The three parameters and three values applied during the definitive screening design for optimizing the operation condition for Fe-C coatings.

Three parameters	**Three values**
Iron-sulfate ($FeSO_4 \cdot 7H_2O$) [g/L]	40, 80, 120
Citric acid ($C_6H_8O_7 \cdot H_2O$) [g/L]	1.2, 2.4, 3.6
Current density [A/dm^2]	3.0, 4.5, 6.0

---

[7] The definitive screening design was generated by the software SAS JMP.

Supplementary material regarding operation conditions.

A new electrolyte was mixed for each sample to avoid the influence of oxidation of Fe^{2+} to Fe^{3+} by air and to follow the randomly generated experimental plan. The coatings were rinsed in water immediately after deposition, followed by rinsing in ethanol, and then carefully dried to avoid oxidation. The samples were protected from any contact with oxidizing environments during storage.

Appearance

The surface on some of the samples shown in Figure 51 indicates signs of oxidation after deposition, as visible by the brown to blue areas. The oxidation of the samples could have been avoided by applying a thin layer of oil following deposition, which has been proofed to be efficient for corrosion protection and can be considered for industrial applications. However, a thin layer of oil poses a risk of influencing the results in a scientific investigation and was therefore not applied.

The appearance of the Fe-C coating was uniform, dark-grey and mirror bright when using the lowest parameter values described in Table 11. These operation conditions were also used in the published manuscripts shown in Section 6.1.1.

Increasing one parameter

- The increase in current density produced a uniform mirror-bright appearance.
- The increase in iron concentration produced a matte appearance.
- The increase in citric acid produced a dark-grey and matte appearance with burnt edges.

The correlated effect of increasing two parameters

- The increase of the current density and the iron concentration produced a uniform mirror-bright appearance.
- The increase of the current density and the citric acid concentration produced a dark-grey and matte appearance with burnt edges.
- The increase of the iron concentration and the citric acid concentration produced a dark-grey and matte appearance with burnt edges.

The correlated effect of increasing three parameters

- The use of the highest parameter values produced a dark-grey and matte appearance with burnt edges.

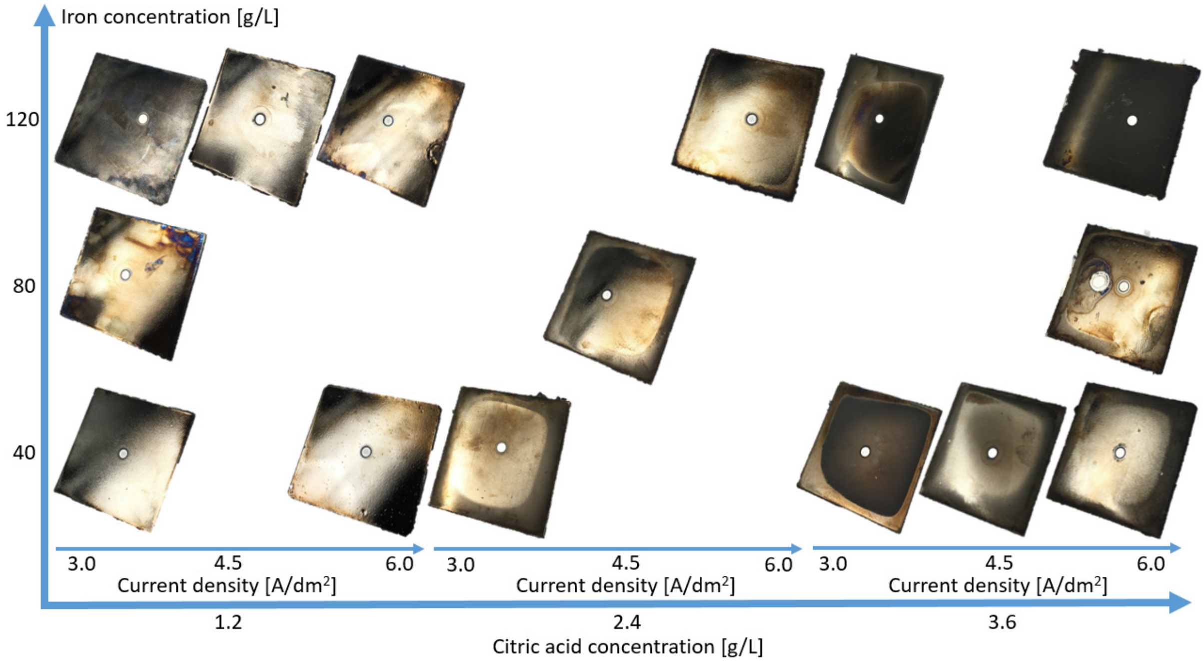

Figure 51: Appearance of Fe-C coatings deposited from electrolytes of different chemical composition of iron-sulfate and citric acid, using various current densities.

The screening revealed that the parameter having the largest influence on the appearance was the citric acid concentration. The citric acid appeared to increase the inhibition intensity and resulted in hydrogen evolution at the edges of the cathode, where the current density was highest. It is not beneficial to increase the concentration above 1.2 g/L as it results in burnt edges and an inconsistent appearance independent of the iron-sulfate concentration and the applied current density.

The increase in current density produced a uniform and mirror bright appearance. The increase in current density is associated with a smaller crystallite size, but can lead to hydrogen evolution and burnt edges if the cathode geometry includes an area susceptible for a high local current density.

The appearance of the deposit became matte when the iron-sulfate concentration was increased. The increase in ion concentration can be associated with a larger average crystallite size, which can influence the topography of the deposits.

The brightness reappeared from the correlated effect of a high current density and iron concentration. The mass transfer parameters consist of the ratio between the current density and metal ion concentration and a fixed ratio predicts consistent growth characteristics as described in Section 2.1.

6.3 The influence of the pH-value of the electrolyte

6.3.1 Manuscript III

The influence of the electrolytes pH-value on the material properties of the electrodeposited Fe-C coating[8]

Jacob Obitsø Nielsen, Karen Pantleon

Technical University of Denmark, Department of Mechanical Engineering, Produktionstorvet, building 425, DK – 2800 Kongens Lyngby, Denmark

Abstract

The Fe-C coatings were deposited in different pH-region using an iron(II)sulfate based electrolyte and citric acid as an additive. The samples were systematically investigated applying X-ray diffraction and chemical analysis, which were supplemented by microhardness measurements. The current efficiency was calculated to nearly 100 % for the deposition conducted in the pH-region above 2.5. The appearance of the coating was dark grey and mirror bright for the samples deposited using a pH-value below 3.2 and no oxides developed on the surface after deposition, in contrast to samples deposited using a pH-value above 3.4. The measured oxygen content was independent of the pH-value but could not be quantified. The maximum carbon content around 1 wt% was measured for the coating deposited in the pH-region around 3.0 and the content decreased outside this pH-region. The X-ray patterns identified ferrite and a single free standing diffraction peak not being ferrite, for which the measured intensity changed as a function of the pH-value used during deposition, while at pH-values above 3.4 this peak was not detected. The hardness of the coating was measured around 780 HV independent of the pH-value. The results establish that Fe-C coatings with the same hardness can be deposited in different pH-regions, but the electrolyte should be controlled to ensure that the pH remains between 2.5 and 3.0 for long term operations to obtain the highest current efficiency and avoid oxidation after deposition.

1. Introduction

The pH-value of the electrolyte is an important parameter within electrochemical deposition. It can be a determining factor for the partial cathodic reactions and it affects the current efficiency of the process, when the current is consumed by the evolution of hydrogen instead of the reduction of the metallic ions on the cathode. The Pourbaix diagram for iron in aqueous solution indicates the presence of possible compounds and ions in thermodynamic equilibrium as a function of the pH-value and the electrode potential. It reveals that the precipitation of oxides and hydroxides within the electrolyte is thermodynamically favored in slightly acidic and neutral conditions [1] and, thus, provides a tool for avoiding the co-deposition of such oxides or hydroxides, which normally are undesired.

The Fe-C coatings having a hardness of nearly 800 HV and a high carbon content between 0.8 to 1.0 wt% can be deposited in an electrolyte consisting of iron-sulfate and a carboxylic acid used as buffer, complexing agent and carbon source [2-5]. The electrolyte is normally operated at a pH-value of 2.5, but during deposition, the partial cathodic reactions can reduce the current efficiency and complicate the regulation of the pH-value, which is required to be a stable

---

[8] Manuscript in preparation for publication.

process parameter. The influence of the electrolytes pH-value on several material properties and its effect on further process parameters has been investigated for the electrodeposition of Fe-C coatings [3,6], although the comparison of different studies is hindered by the difficulty to consider solely the pH-value, as different process parameters have been applied. The general trend shows that lowering the pH-value from 3.0 to 2.0 decreases the current efficiency from around 100 % to 80 % [3,6]. The carbon content has been shown to increase when the pH-value of the electrolyte decreases [3]. The hardness of the deposit is either independent of the pH-value within 2.0 and 3.5 [3] or slightly increased for higher pH-values [6].

The present work investigates the influence of the pH-value of an iron-sulfate based electrolyte using citric acid as an additive. The same electrolyte is used for all depositions to study the consumption of the additive during deposition and its impact on the resulting coating. The electrodeposited Fe-C coatings are characterized with different methods to reveal systematic changes in the optical appearance, current efficiency, chemical composition, phase constitution, and hardness.

2. Materials and experimental methods

2.1 Electrodeposition at different pH-values

A series of Fe-C coatings was deposited in different pH-regions from the same electrolyte using the operation conditions as shown in Table 1.

Table 1: Operation conditions for electrodeposition of Fe-C coatings as a function of pH-value

Operation conditions	
Temperature	50 °C
Electrolyte volume	4 L
Electrolyte composition	80 g/L $FeSO_4 \cdot 7H_2O$ 1.2 g/L $C_6H_8O_7 \cdot H_2O$
pH-value	Varied from 2.0 to 3.7 (see Figure 1)
Current density	3.5 A/dm^2
Anode	IF steel plate
Cathode	5 x 5 cm steel plate
Deposition time	1 hour

An IF steel anode was placed on both sides of the cathode positioned in the middle of the bath, so that deposition proceeded on both sides of the cathode. The weight of the steel plate used as cathode was measured precisely using a laboratory scale prior to each deposition and after deposition for 1 hour. Weighing occurred after cleaning the samples and in dried conditions, but without removing dendrites, which may have formed. The current efficiency of the system is calculated using the measured mass gain and the theoretical mass gain (m) calculated using Equation (1),

$$m = \frac{I \cdot t \cdot M}{z \cdot F} \qquad (1)$$

where I is the current, t is the deposition time, M is the molar mass, z is the amount of electrons transferred with $z = 2$ as the electrolyte consist of iron in the oxidation state $Fe^{2+}$and F is Faradays number. The theoretical mass gain for the applied operation conditions described in Table 1 corresponds to 1.823 g.

The experimental procedure used to study the pH-value influence on the electrolyte and the consumption of the additive is illustrated in Figure 1 along with the sample designation referring to the pH-region of the electrolyte at which the samples were deposited. The pH-value of the system was measured using a calibrated pH-electrode connected to a Mettler Toledo Seven Excellence pH-meter prior to deposition and after deposition of each sample. The initial pH-value of the electrolyte amounted to 2.5 and a deposition of 6 hours was intentionally carried out to increase the pH-value to values outside the normal operation conditions of 2.5 to 3.0, which resulted in a pH-value of 3.5, at which the first sample then was deposited for 1 hour. Afterwards the pH-value of the electrolyte was lowered to 2.0 using diluted sulfuric acid where the second deposition for 1 hour was initiated. Further nine samples were deposited for 1 hour each before a pH-value of 3.5 was measured. There was at no time any indication of solid precipitates in the electrolyte during the experimental procedure.

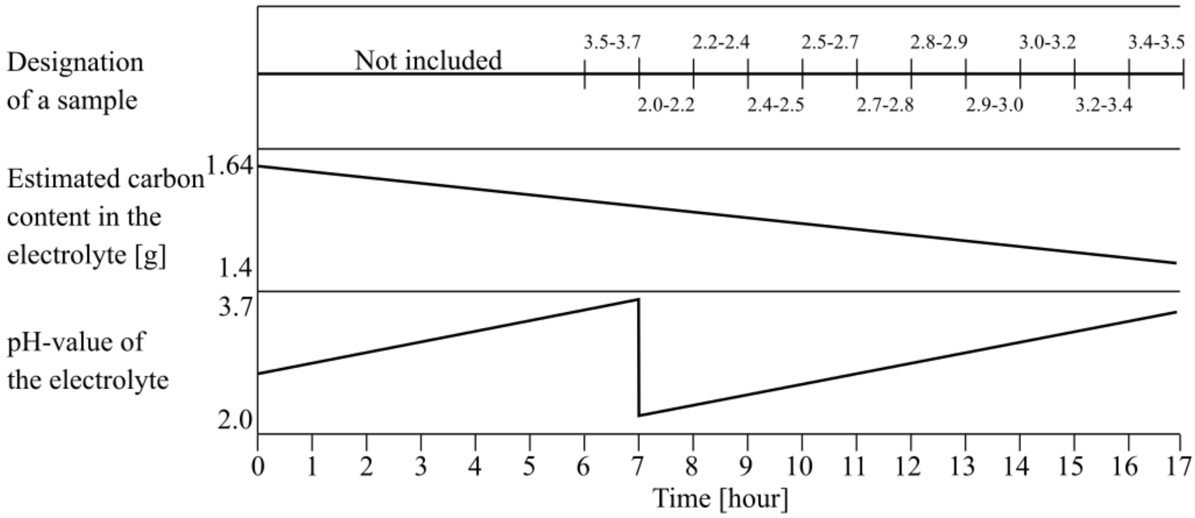

Figure 1: Experimental procedure illustrating the change in the electrolytes pH-value and the estimated carbon content as a function of the amount of hours that the electrolyte has been used for deposition. The designation of samples is included and the values represent the pH-region of the electrolyte during deposition. The change in pH-value after 7 hours of deposition corresponds to the deliberate adjustment using sulfuric acid as described in the text.

2.2 Chemical analysis

The chemical composition of the coatings deposited in different pH-regions was investigated by glow discharge optical emission spectroscopy (GDOES) using a Horiba equipment GD profiler 2 with Quantum XP software to measure the content of carbon and oxygen. The GDOES instrument was calibrated prior to the measurement using multiple standards having different carbon content up to 1.3 wt%. The oxygen content is presented as qualitative values using the measured signal in [V], as a calibration curve could not be obtained due to the lack of reference samples. For both elements, calculated averages over the measured region covering most of the coating thickness, but disregarding the running-in period of the equipment and the transition from the coating to the substrate, are used for comparing the different samples. The average oxygen content has a large standard deviation, as the signal to noise ratio is high.

2.3 X-ray diffraction

A Bruker AXS D8 Discover X-ray diffractometer operated with Cr-K_α radiation was used for qualitative phase analysis. The use of a Göbel mirror allowed obtaining a high intense parallel beam. The calculated penetration depth in iron corresponds to a maximum of about 6 µm within the measured range of diffraction angles.

The samples were measured twice. The first measurement was dedicated to phase analysis by investigating the full diffraction pattern of all samples using a step size of 0.05 °2Θ and a measurement time of 3 seconds per step at diffraction angles between 50 and 160 °2Θ. The second measurement dedicated to line profile analysis, which was carried out with a finer step size of 0.04 °2Θ and a higher measurement time of 40 seconds per step within the measured range of diffraction angles between 45 and 75 °2Θ to obtain a better resolution and counting statistics.

The measured diffraction patterns from the second measurement were fitted using a pseudo-Voigt function with the software Topas from Bruker AXS. Fitting with the pseudo-Voigt function revealed the following parameters for further analysis: The peak position (used for phase analysis), the full-width-half-maximum (FWHM) and the shape of the peaks with the corresponding Gaussian and Lorentzian contributions to the peak profile (from both, the integral breadths β was calculated and used for line profile analysis) and the integrated intensity of the measured peaks.

2.4 Hardness

The microhardness of the coatings was measured using a Struers DuraScan with a Vickers indent applying a load of 25 g placed in the middle of the coating on the cross section of samples that prior to the measurement were cold embedded in epoxy and metallographically prepared. On the thinnest coatings, instead, a load of 10 g was applied, as the diameter of the indent when using 25 g would exceed the minimum distance of 2.5 times the diameter from the center of the indent to the substrate and surface of the coating as required for microhardness tests. The microhardness value can slightly depend on the applied load. The microhardness is presented as the average value of five measurements per sample.

3. Results and discussion

3.1 Appearance

An overview on the different visual appearance of the samples deposited in the different pH-regions is shown in Figure 2. The images were captured after the samples had been stored in separate plastic bags without further protection against oxidation. The appearance of the Fe-C coating deposited at pH-values below 3.2 had a similar dark grey mirror-bright appearance without indications of oxidation during storage. The sample deposited in the pH-region of 3.2-3.4 was grey and matte and without any indications of oxidation during storage. The samples deposited at pH-values above 3.4 appeared grey and matte and oxidation products on the surface were visible for the naked-eye shortly after deposition and evolved during storage.

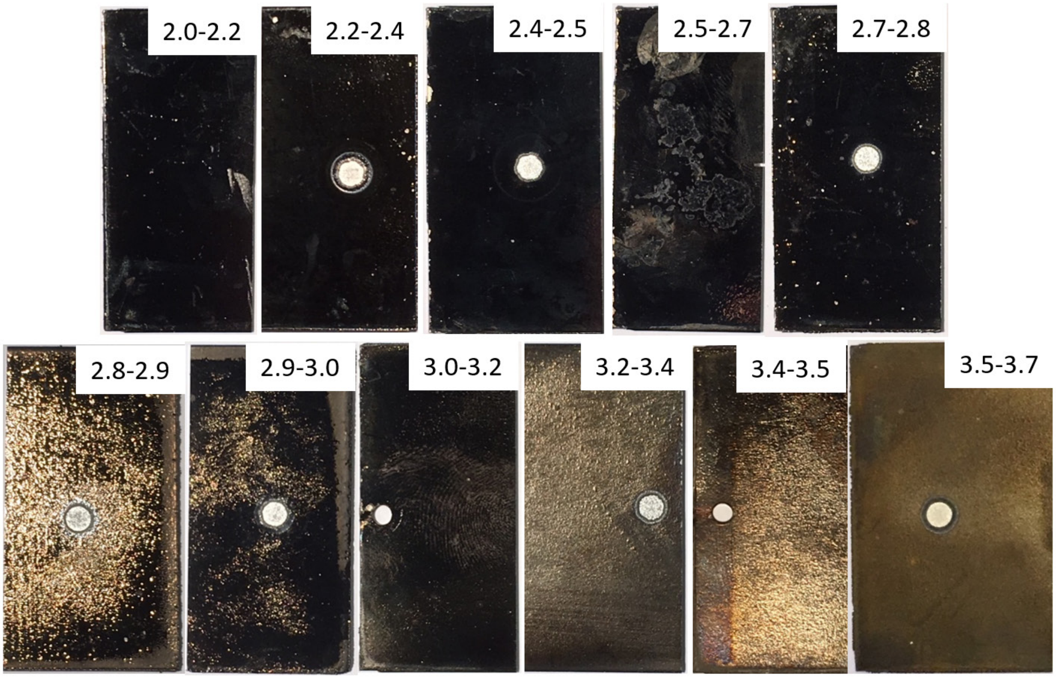

Figure 2: Photographs of Fe-C coatings after deposition in different pH-regions for the electrolyte. The circle on the surface of most samples is the GDOES measurement crater.

3.2 Current efficiency

The calculated current efficiency for the various Fe-C coatings is shown in Figure 3. The current efficiency is calculated to around 80 % in the most acidic region below a pH-value of 2.2 and increases linearly to around 100 % at a pH-value of 2.5, where it remains at high value of nearly 100 % for the samples deposited at higher pH-values.

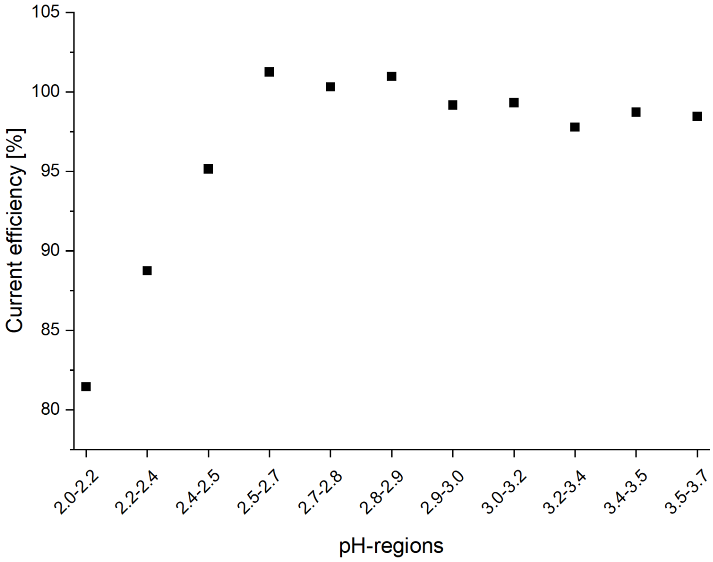

Figure 3: Calculated current efficiency for Fe-C coating deposited for 1 hour in different pH-regions.

The lowered current efficiency in the most acidic region is most likely an effect of cathodic hydrogen evolution as described in Equation (2). The cathodic hydrogen evolution requires electrons to occur and the consumption of electrons lowers the current efficiency as fewer iron ions can be reduced at the cathode.

$$2H^{+} + 2e^{-} \rightarrow H_2(g) \qquad (2)$$

However, the calculated current efficiency is nearly 100% at a pH-value above 2.5 and suggests that the cathodic hydrogen evolution is not proceeding in this pH-region. The increasing pH-value during deposition with a 100% current efficiency independent of the pH-value requires another partial reaction that consumes the H^+ ions. The consumption of H^+ within the electrolyte could follow the Equation (3), because iron is present in the electrolyte.

$$Fe(s) + 2H^+ \rightleftharpoons Fe^{2+} + H_2(g) \qquad (3)$$

However, the steel cathode is catholically protected from the reaction described in Equation (3) during deposition and the anodic reaction using sacrificial anodes progresses according to Equation (4) and does not consume H^+.

$$Fe(s) \rightleftharpoons Fe^{2+} + 2e^- \qquad (4)$$

The presence of hydrogen often is speculative, because the light element cannot be quantified straightforwardly, but hydrogen evolution during electrodeposition and its incorporation into the coating is well accepted. In case of hydrogen, recent annealing experiments of as-deposited Fe-C coatings revealed that hydrogen constitutes different phases in the Fe-C coating, which evolve differently with temperature, depending on whether hydrogen is incorporated as atoms/molecules or chemical compounds [7,8].

The revealed current efficiency as a function of the pH-values (cf. Figure 3) is in good agreement with the results published previously [3,6], however thorough understanding of the mechanism of co-deposition and consumption of hydrogen is still lacking.

3.3 Chemical composition

Instead of solely carbon atoms, which are aimed to be co-deposited from the present electrolyte and cause the formation of Fe-C coatings, also hydrogen and oxygen have been reproducibly confirmed experimentally in the coatings [7,8]. Figure 4 reveals the effect of the pH-value in the electrolyte on the resulting carbon and oxygen content. Although oxygen cannot be quantified from the present study, the recorded average oxygen signal is similar for all the samples, which suggests that the co-deposition of oxygen in the coating is independent of the pH-value (see Figure 4b).

The average carbon content (see Figure 4a) amounts to about 0.8 wt% for the samples deposited at a pH-value below 2.5. For higher pH-values, the carbon content increases to a maximum with about 0.96 wt% for the sample deposited in the pH-region around 3.0. A further increase of the pH-values results in a decrease of the carbon content with the lowest value of 0.7 wt% measured at a pH-value of around 3.5. The decrease in the carbon content could be related to a change in the complex ability between the citric acid and the iron ions. An equilibrium study of Fe^{2+} complexes with citric acid in an aqueous solution has been conducted at 37 °C in the pH-region 2.8-10.0 [9]. The study revealed that three species being Fe^{2+}, $FecitH^0$ and $FecitH_2^+$ exist in different distributions in the pH-region of the present study. The negative charge of the cathode will only attract the Fe^{2+} ions and the $FecitH_2^+$. The distribution of $FecitH_2^+$ complex as a function of the pH-value has its maximum around 2.9. The co-deposition of this complex could explain the trend in the carbon content for the as-deposited Fe-C coatings.

The three outliers in the measurements (cf. Figure 4a), being the samples deposited in the pH-region of 2.0-2.2, 2.8-2.9 and 3.5-3.7, do not contradict this general trend. There is not a clear explanation for the higher carbon content in the sample deposited in the pH-region of 2.0-2.2

compared to 2.2-2.4 at the moment, but the two remaining outliers are explained as follows. During the GDOES analysis of the sample from the pH-region 2.8-2.9, multiple short-circuits occurred, which affected the recorded signals as reflected in a high standard deviation. The higher carbon content of the sample from the pH-region 3.5-3.7 compared to the sample deposited in the pH-region from 3.4-3.5 relates to the following: The sample from the pH-region 3.5-3.7 was the first deposition (cf. Figure 1), and the sample from the pH-region 3.4-3.6 was the final deposition. It is likely, that this corresponds to a higher citric acid concentration in the electrolyte during the deposition at the pH-region of 3.5-3.7 as the additive is the only carbon source and will gradually be consumed during deposition, as illustrated in Figure 1. The mass of the deposits and their average carbon contents can be used to estimate the consumption of citric acid during deposition and this allows estimating the changes of the chemical composition of the electrolyte, i.e. the amount of citric acid consumed during deposition. For the two samples deposited at a pH-value above 3.4, but at different age of the electrolyte, the resulting carbon concentration is discussed as follows. The initial amount of citric acid ($C_6H_8O_7{\cdot}H_2O$, M = 210.14 g/mol) applied to the 4L electrolyte was 4.8 g, where carbon amounts to 34.3 % of the molar ratio of citric acid, which results in 1.64 g carbon in the electrolyte. The amount of carbon consumed is estimated by multiplying the deposits mass with the average carbon content for each deposit and the consumption of carbon during deposition for 1 hour is between 0.012 to 0.018 g. The initial running in period where a sample was deposited for 6 hours to reach the pH-value of 3.5 is estimated to have consumed a similar amount of carbon as the samples deposited for 1 hour each in the same pH-region being 0.094 g. The estimated concentration of carbon in the electrolyte prior to the first deposition for 1 hour in the pH-region between 3.5-3.7 is 1.546 g. The estimated carbon content in the electrolyte prior to the final deposition for 1 hour in the pH-region between 3.4-3.5 is 1.397 g. The carbon content in the electrolyte is nearly 10 % lower for the final deposition for 1 hour and, correspondingly, the average carbon content indeed is measured to be 12.5% lower. The estimated carbon consumption during the measurement likely clarifies the difference of the average carbon content for the two samples with pH-value above 3.4. The observed trend in Figure 4a that the carbon content shows a maximum in the middle pH-region demonstrates that the carbon content is influenced by the pH-value as the carbon consumption in the electrolyte will result in a linear decrease in carbon content as a function of the time the electrolyte has been applied for deposition (cf. Figure 1).

The result for the average carbon content differs from what has been presented by other authors where the carbon content was found to increase linearly when the acidity of the electrolyte is increased [3]. All the co-deposited elements (carbon, oxygen, and hydrogen) are supplied by the citric acid, applied as an additive and forming complexes with Fe^{2+} within the electrolyte. Although qualitatively (and quantitatively) detected in the Fe-C coatings, the nature and type of the incorporation of these elements in the coating are not well understood.

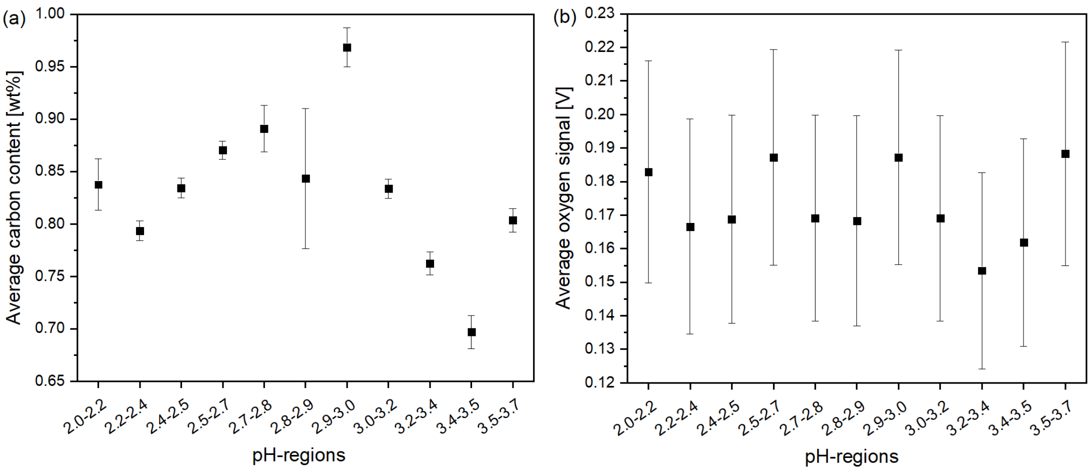

Figure 4: GDOES measurement of Fe-C coating deposited for 1 hour in different pH-regions. (a) The average carbon content. (b) The average signal measured for oxygen in sample.

3.4 Phase analysis

The measured XRD patterns shown in Figure 5 and 6 are used for qualitative phase analysis. Figure 5, representing the full measurement range from 50 to 160 °2Θ, reveals that the main phase for all samples corresponds to α-iron. The absence of peaks related to an oxide in the diffraction range is surprising as a clear indication of the oxidation product can be seen with the naked eye as shown in Figure 2 for the samples deposited at pH-values above 3.4. Possibly, the oxide layer is very thin and therefore not detectable. The XRD patterns indicate a crystallographic texture (deviation from theoretical intensity ratios) and that this is different for a Fe-C coating deposited at low pH-values compared to a Fe-C coating deposited at a higher pH-value. The Fe-C coating has been deposited previously under similar operation condition in the pH-region of 2.5-2.8 and a quantitative crystallographic texture analysis showed that a <311> fiber texture is developed during deposition [5]. The changing intensity ratios for the measured peaks of α-iron at high pH-values suggest a decrease in the strength of the <311> fiber texture, however a full texture measurement is required to confirm this trend. One additional peak, not being ferrite, is measured at 57.9 °2Θ for the samples deposited using a pH-value below 2.8. This additional peak has been repeatedly measured [4,5,7,10], but a phase identification is hindered by the lack of supplementary peaks. As a consequence of the incomplete phase identification, the additional peak is referred to as the "nameless peak" and originates from the "nameless phase". The lack of intensity from the "nameless peak" in specific samples (see Figure 5) strongly indicates that the "nameless phase" indeed does not form at increased pH-values, although changes of the crystallographic texture may affect its visibility with the present measurements. The XRD patterns used for line profile analysis are shown in Figure 6 and confirm that no additional peaks are measured and that the decreasing trend for the "nameless peak", being suggested by Figure 5, is correct.

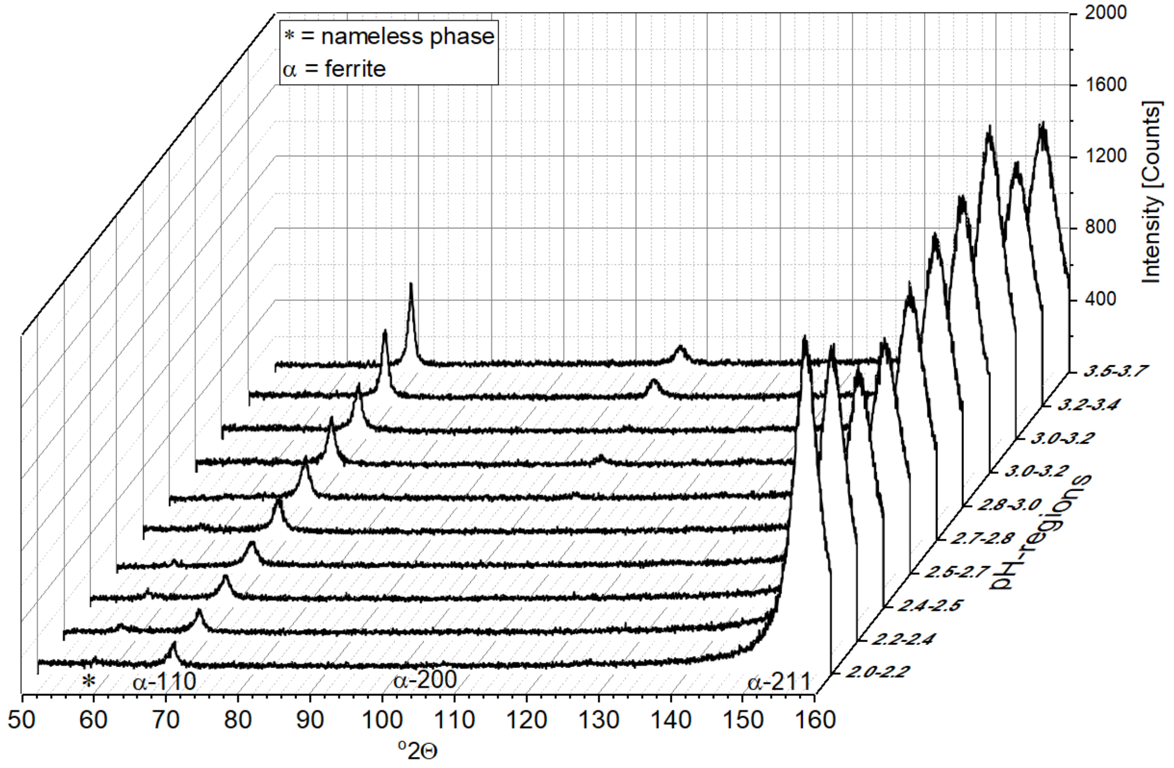

Figure 5: XRD patterns of Fe-C coatings deposited for 1 hour in different pH-regions for the electrolyte.

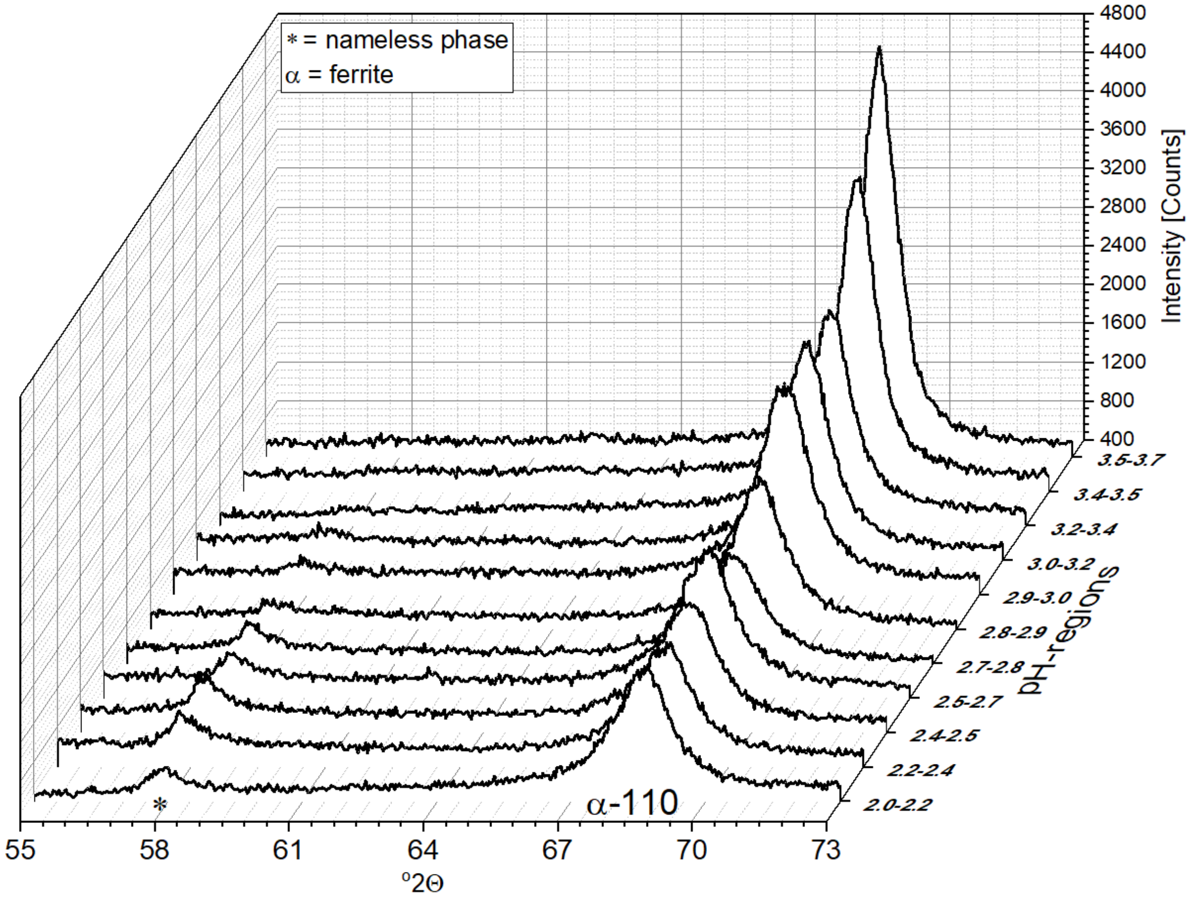

Figure 6: XRD patterns measured using a counting time of 40 seconds of Fe-C coatings deposited for 1 hour in different pH-regions for the electrolyte.

Both the “nameless peak” and the peak corresponding to α-110 shown in Figure 6 were subjected to peak profile fitting using a pseudo-Voigt function and the resulting peak position, integrated intensity and the integral breadth are shown in Figure 7a and 7b. The increased counting time provided a better counting statistics, however the low intensity of the “nameless peak” still provides a challenge for reliable peak fitting and consequently the interpretation based on its evolution is hindered. The low intensity of the “nameless peak” is seen in the scattered data of the peak position and integral breadth and these values are not suitable for interpretation. The integrated intensity of the “nameless peak” is also somewhat scattered, but it is clear from Figure 6 and 7a that its intensity is lower for the Fe-C coatings deposited using a pH-value of above 2.9 and the “nameless peak” is not measured at pH-values above 3.4. The trend does not indicate a relation to the carbon content; for example, the same carbon content of 0.8 wt% can be achieved from both the deposition with a low pH-value, where the “nameless peak” is present (e.g. pH-region 2.2-2.4), and with high pH-value, where the “nameless phase” is absent (e.g. pH-region 3.5-3.7). The two samples deposited at pH-values above 3.4 are the only samples that visibly show surface oxidation after deposition and these are the same samples where the “nameless peak” is not measured.

The intensity of the α-110 permits accurate peak fitting and a clear trend is seen for the peak position, integrated intensity and integral breadth as a function of the pH-region during deposition (cf. Figure 7b).

The integrated intensity for α-110 is almost stable when the electrolytes pH-value was below 2.9 and increases for the higher pH-values. The increase in intensity is associated with a change in the crystallographic texture as also suggested from Figure 5, but a full texture measurement would be required for further evaluation.

The peak position is relatively stable around 68.5 °2Θ when the pH-value was below 2.9 and shifts towards higher diffraction angles of about 68.7 °2Θ for the higher pH-values. The shift in peak position is either related to the macrostresses within the material or a result of a change in the size of the unit cell related to chemical changes of the measured phase (e.g. the unit cell is increased by interstitial atoms). The strain-free lattice spacings d_0 of ferrite that have been measured for the as-deposited Fe-C coatings and matched carbon-free ferrite (JCPDS 6-696) [7,8]. The strain-free lattice spacings d_0 of ferrite [7,8] opposes that the shift in peak position is related to an increase in the size of the unit cell related to interstitial atoms and points towards residual stresses as a cause of peak shifts.

The integral breadth is stable at pH-values below 2.8 and decreases for higher pH-values. The peak breadth is associated with the crystallite size and microstrain of the measured phase and will decrease when the crystallite size increases and/or when the microstrain decreases. The Hall-Petch relation couples an increase in crystallite size with a decrease in hardness [11]. Similar will a decrease in microstrain also reduce the hardness of an electrodeposited coating [12].

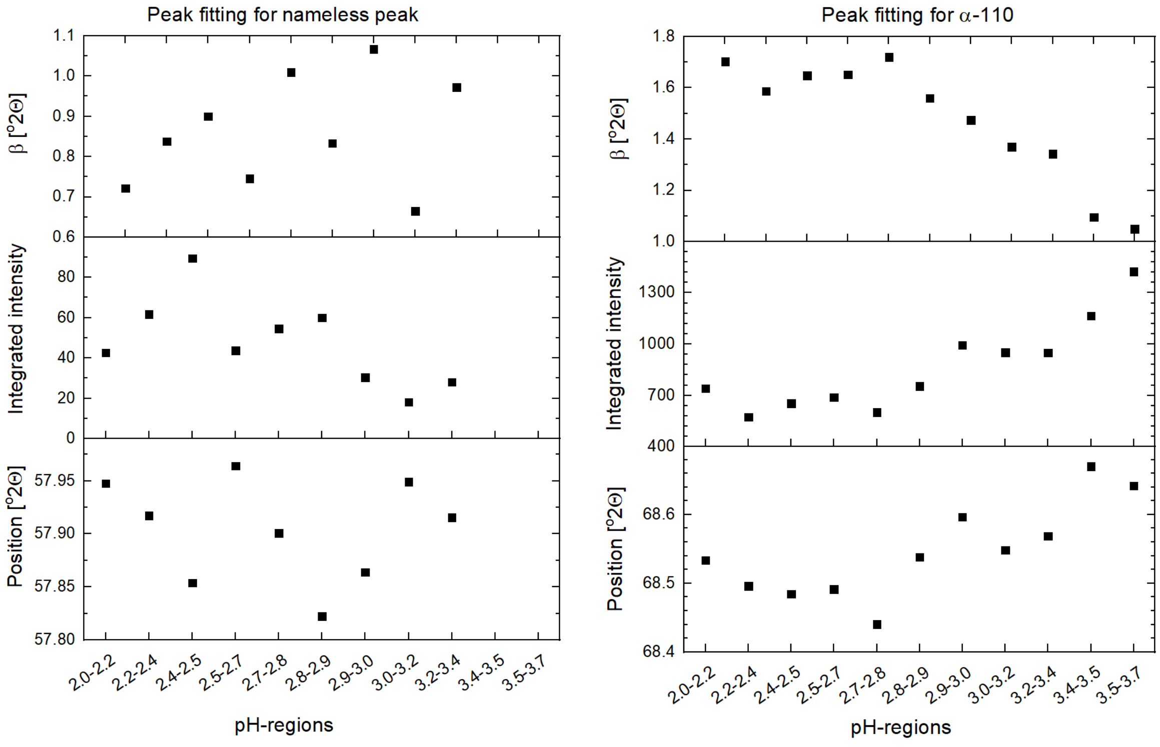

(a) (b)

Figure 7: The peak position, integrated intensity, and integral breadth for the "nameless peak" being of low intensity (a) and the peak for α-110 (b) obtained using pseudo-Voigt fitting of the XRD patterns measured for Fe-C coatings deposited at different pH-region shown in Figure 6.

The shift in peak position and the decrease in integral breadth of α-110 when the pH-value is increased does not appear to be related to the carbon content as samples deposited at 2.2-2.3 and 3.5-3.7 have the same average carbon content (cf. Figure 4). However, the evolution of the α-110 peak seems to be connected with the reduction of intensity for the "nameless peak" (cf. Figure 7a). These observations point towards a correlation between the "nameless phase" and ferrite phase that is not yet understood. Previous results have described an orientation relationship between the two individual phases along with a correlated peak shift [5]. The correlation of the phase constitution and crystallographic texture of the Fe-C coating and the electrolytes pH-value along with the visual surface oxidation requires further study.

3.5 Hardness

The average microhardness measured for all samples is shown in Figure 8. The values of around 780 HV0.025 appear to be not significantly affected by the pH-values during deposition, when taking into account the differences in the applied load during hardness measurements. However, the standard deviation is high for all measurements and impedes such a conclusion.

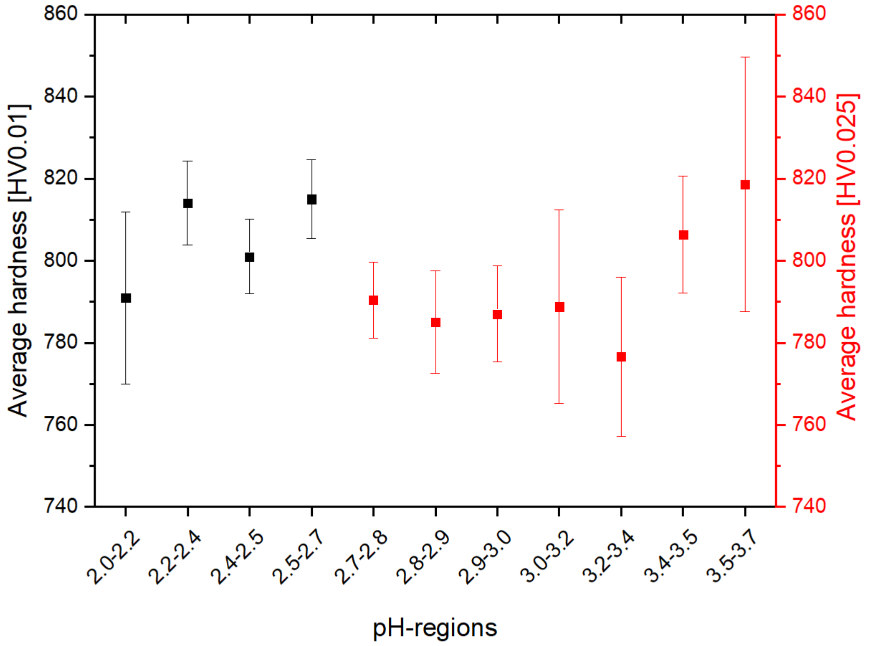

Figure 8: Average microhardness of Fe-C coatings deposited in different pH-regions.

The result suggest that the high microhardness of around 780 HV0.025 is independent of the presence of the “nameless phase”, if its disappearance for pH-values above 3.4 is not coupled to a change in texture. The change measured for the average carbon content (cf. Figure 4) also does not influence the microhardness. The decrease in integral breadth for α-110 (cf. Figure 7b) was expected to decrease the microhardness, from either an increase in the crystallite size or a decrease in the microstrain. However, the line profile analysis only reflects data for ⟨110⟩-oriented grains, which constitute a minority of all grains in the coating with <311> preferred orientation and therefore will only slightly influence the average hardness.

The results presented for the average microhardness of the Fe-C coatings being independent of the pH-value of the electrolyte is in good agreement with the findings of Izaki [3], which found that there is no influence on the hardness up to a pH-value of 3.5, whereas Panayotova [6] measured that the hardness increased linearly with the pH-value between 2.0 and 3.0.

4. Conclusion

The regulation of the pH-value of the electrolyte is very important for the electrodeposition of Fe-C coatings as a feasible industrial process, because it not only influences the appearance of the coating and the current efficiency of the process, but also the chemical composition, crystallographic texture and phase constitution of the as-deposited coating.

The pH-value of the electrolyte influences the content of co-deposited carbon and a maximum value of nearly 1 wt% is measured when the electrolyte is operated at a pH-value of 3.0. The trend of the carbon content is similar to the expected distribution of a $\mathrm{FecitH_2^+}$ complex as a function of the pH-value and suggests that this specie in the electrolyte regulates the co-deposition of carbon. The lower carbon content for samples deposited within a similar pH-region can be related to the consumption of citric acid during the course of deposition. The amount of co-deposited oxygen was not possible to quantify, but the measured signal is independent of the pH-value.

The XRD analysis shows that the "nameless peak" decreases in intensity when the electrolytes pH-value is above 3.0 and is absent for pH-values above 3.4. The integral breadth of the α-110 is similar for the coatings deposited in the pH-region below 3.0 and decreases when the pH-value is above 3.0. The decrease in the measured breadth for α-110 is not accompanied by a decrease in hardness.

The applied pH-value does not influence the resulting hardness of the as-deposited Fe-C coating, but should be maintained between 2.5 and 3.0 for industrial application as the current efficiency for 1 hour depositions is around 100 % and no visible oxidation is seen after deposition.

Acknowledgement

The authors gratefully acknowledge OCAS NV, ArcelorMittal Global R&D Gent (Belgium), a. h. nichro Haardchrom (Denmark), and Fast Track - Societal Partnership (Denmark), funded by the Innovation Fund Denmark (IFD), for financial support.

References

[1] M. Pourbaix, Atlas of electrochemical equilibria in aqueous solutions, 1974.

[2] M. Izaki, H. Enomoto, A. Nakae, S. Terada, Y. Eiko, T. Omi, Phase Transformations and Hardness Changes in Electrodeposited Alloy Films Iron-carbon alloy films., J. Surf- Fin. Soc. Jpn. 45 (1994) 1303–1309.

[3] Y. Fujiwara, T. Nagayama, A. Nakae, M. Izaki, H. Enomoto, E. Yamauchi, Electrodeposition of Fe-C Alloys from Baths Containing Dicarboxylic Acids with a Linear Alkyl Chain, J. Electrochem. Soc. 143 (1996) 2584–2590.

[4] A.S.M.A. Haseeb, Y. Hayashi, M. Masuda, M. Arita, On the nature of the electrochemically synthesized hard Fe-0.96 mass pct C alloy film, Metall. Mater. Trans. B. 33B (2002) 921–927.

[5] J.O. Nielsen, P. Møller, K. Pantleon, Electrodeposition of Iron with Co-deposition of Carbon: On the Nature of Nanocrystalline Fe-C Coatings, Metall. Mater. Trans. A. 50A (2019) 3785–3793.

[6] M. Panayotova, Deposition of Fe–C alloy on structural steel and cast iron for repair of worn machine parts, Surf. Coat. Technol. 124 (2000) 266–271.

[7] J.O. Nielsen, K. Pantleon, Evolution of hard Fe–C electrodeposits with temperature, Surf. Eng. (2019) in press. Published online in October 2019.

[8] J.O. Nielsen, T.L. Christiansen, K. Pantleon, In-situ analysis of the thermal evolution of electrodeposited Fe-C coatings, under review in revised state in Acta Materialia since March 2020.

[9] P. Amico, P.G. Daniele, V. Cucinotta, E. Rizzarelli, S. Sammartano, Equilibrium study of iron(II) and manganese(II) complexes with citrate ion in aueous solution: Relevance to coordination of citrate to the active site of aconitase and to gastrointestinal absorption of some essential metal ions, Inorganica Chim. Acta. 36 (1979) 1–7.

[10] T. Müller, J. Grimwood, A. Bachmaier, R. Pippan, Electrodeposition of Fe-C alloys from citrate baths: Structure, mechanical properties, and thermal stability, Metals, 8 (2018) 1–13.

[11] E.O. Hall, The deformation and ageing of mild steel: III Discussion of results, Proc. Phys. Soc. Sect. B. 64 (1951) 747–753.

[12] R. Sard, H. Leidheiser, F. Ogburn, Correlation of Microstrain and Hardness of Electrodeposits, in: R.S. Oswald, R. Weil (Eds.), Prop. Electrodeposits, Their Meas. Significance, Princeton, N.J. : Corrosion, Electrodeposition, and Electronics Divisions, Electrochemical Society, 1975: pp. 246–254.

6.4 Adhesion testing

6.4.1 Manuscript IV

Screening of pre-treatments using the interface indentation test for optimizing the adhesion between the Fe-C coating and hardened tool steel[9]

Jacob Obitsø Nielsen, Karen Pantleon

Technical University of Denmark, Department of Mechanical Engineering, Produktionstorvet, building 425, DK – 2800 Kongens Lyngby, Denmark

Abstract

A Fe-C coating was deposited on a hardened tool steel using the iron(II)sulfate based electrolyte with citric acid used as additive. Different pre-treatment strategies were applied prior to deposition to activate the substrates surface and enable the coating to adhere to the substrate material. The interface indentation test was used to estimate the work of adhesion between the coating and the substrate to benchmark the pre-treatments. A new method for the interface indentation test is proposed that applies a single load that can initiate a crack in the interface and the length of the crack on both sides of the Vickers indent is taken into account. The results show that two out of the five pre-treatments produced a lower work of adhesion between the coating and the substrate compared to the highest mean value measured. The proposed method of estimating the work of adhesion using the interface indentation test is simple and reproducible and can be applied for benchmarking different pre-treatments when a new coating/substrate combination is required.

1. Introduction

For all electrodeposited coatings, the pre-treatment of the substrate is essential to achieve a good product finish and is performed in several steps depending on the conditions of the substrate and the type of material. Usually, the pre-treatment of a specific material is chosen by the supplier, from experience or from textbook specifications. However, the rapid development of new materials, new treatments of existing materials and new coatings makes it essential to have a reliable method to evaluate the effect of the pre-treatments. The removal of greases and oils from the substrate can easily be evaluated by submerging the sample in water and inspecting the uniformity of the thin water film while draining. The development of dry spots on the substrate surface refers to the hydrophilic properties of the oils still contaminating the surface. The activation of the surface is required to remove the alkaline residues from the prior pre-treatments and to remove a possible oxide layer on the surface to finally allow the coating to adhere to the substrate material. The evaluation of the activation is however not straightforward as the alkaline residual and oxide layer are often invisible to the naked eye. A poor activation can result in an unsatisfactory surface finish and a low adhesion between the substrate and the coating. Tailoring the activation procedures for improved adhesion is most problematic as its required level is determined by the coatings purpose. The techniques to test the adhesion are destructive and either require a special equipment to ensure a reproducible examination and quantitative result, like for example with the scratch test and peel test, or use common equipment with a lower reproducibility as the cross hatch tape test or the bend adhesion test [1,2].

---

[9] Manuscript in preparation for publication.

An alternative and elegant approach to reliable and reproducible measure the adhesion between a coating and a substrate bases on the apparent interface toughness, which can be measured by interface indentation tests [3-5]. The test is performed on a metallographically prepared cross section of a coated sample by placing a Vickers hardness indent into the interface of the substrate and the coating to generate and propagate a crack parallel with the interface. The length of the generated crack is proportional to the force applied during indentation and by investigating this relation, a critical force is obtained that can be converted to the apparent interface toughness. However, for many applications the absolute value of the adhesion is not required.

A simplified interface indentation test is proposed in the present work, to evaluate the work of adhesion between a coating and a substrate. The method is conducted using a fixed indentation force that is able to initiate a crack in the interface of the coating and the substrate. The test is repeated on each sample to obtain good statistics that allows the estimation of the difference between the mean values. The screening takes advantages of the two sample t-test [6] to evaluate the confidence level when comparing the obtained results. The limitation of the method is that it does not allow comparing results of coatings with different thicknesses, different types of coatings on the same substrate or the same coating on different substrates. However, the proposed test is appropriate for screening the level of adhesion achieved by varying only the pre-treatments and designate the best performing candidates for specific pre-treatments from a list of many potential ones.

The Fe-C coatings electrodeposited from an iron-sulfate electrolyte with the addition of an additive acting as the carbon source have a hardness of nearly 800 HV and the coatings can be deposited in thick layers up to several hundreds of micrometers [7-13]. These material properties make the Fe-C coatings a promising solution for the restoration of worn machine parts or as a wear resistant coating. However, the corrosion properties of the Fe-C coating limit its use to lubricated environments. A typical substrate material required to be restored or coated could be a hardened tool steel. The low temperature of the electrodeposition will not influence the microstructure of the hardened steel and the hardness of the coating is only slightly higher than the worn component. However, obtaining a good adhesion on hardened steels can be a challenge. The carbides developed at high temperature in a steel containing chromium, molybdenum and vanadium are insoluble in the most acid solutions, and their presence in the surface will influence the level of adhesion that can be realized.

The challenge of selecting an activation method that ensures that specific coatings will adhere to the hardened tool steel is evident. The different approaches examined to activate the surface and their interaction with the substrate are as follows: (1) Disregarding the activation will require the pH-value of the electrolyte used for deposition to be low enough to dissolve the oxide layer by itself. (2) Activation of the substrate in a sulfuric acid solution will dissolve the oxide layer, mildly etch the iron and expose the carbides to the surface. (3) The introduction of a counter electrode and an applied current to the sulfuric acid solution will allow the substrate to act as cathode and the electrolysis on its surface will generate hydrogen bubbles and clean the surface during activation. (4) Activation of the surface in a dry acid solution that contains a small amount of fluoride salts will be more aggressive on the ferrous substrate, but will to some extend also dissolve the carbides that are exposed by the etching [14]. In addition to the specific chemical solution, also the duration and temperature of the pre-treatments can be adjusted to optimize the activation. However, it is difficult to predict the consequence of choosing a longer exposure to the acidic environment or the influence of the increased reaction rate for increased temperatures.

The present work reports on systematic studies of Fe-C coatings, which were electrodeposited from an iron-sulfate electrolyte with citric acid as additive onto a hardened calmax steel substrate that was pre-treated using different conditions. The Fe-C coatings were deposited with the same thickness that allowed a microhardness indentation to be precisely positioned in the interface of the coating and substrate on their metallographically prepared cross sections. The interface indentation test was repeated several times on each sample using a fixed load that allowed the evaluation of the work of adhesion obtained using the different pre-treatments.

2. Materials and methods

2.1 Electrodeposition

The electrolytes were prepared with a volume of 4 L from chemicals of analytical grade with a concentration of 0.286 mol/dm^3 iron(II) sulfate heptahydrate, 6.2 x 10^{-3} mol/dm^3 citric acid monohydrate, and deionized water. The electrolytes were freshly mixed for each sample to avoid any possible oxidation or change in chemical composition as an additional influence. The temperature of the electrolyte amounted to 50 °C and mechanical stirring was applied during deposition. The pH-value of the electrolyte was maintained between 2.5 and 2.8 during deposition using a 10% sulfuric acid solution. The anode consisted of an IF steel plate, and the cathode was a hardened calmax steel plate with dimensions of 5 x 5 cm. One side of the substrate was covered with an electrolyte-resistant tape to ensure deposition only on the side toward the anode.

The pre-treatment of the substrate started with the same procedure for all samples with 2 min of anodic degreasing at 5 V followed by rinsing in water. Then, one of the following activations was applied for the various samples: (1) no activation, (2) 2 min in dry acid, (3) 5 min in dry acid, (4) 2 min in 15% sulfuric acid or (5) 2 min cathodic treatment in 15% sulfuric acid at 5 V. The pre-treatment solutions were kept at room temperature. The substrates were rinsed in water after the activation and the electrodeposition was carried out at a constant current density of 3.5 A/dm^2, which was applied for a deposition time of 360 minutes. The coatings were rinsed in water immediately after deposition, followed by rinsing in ethanol, and then carefully dried to avoid oxidation. The samples were protected from any contact with oxidizing environments during storage.

2.2 Interface indentation test

2.2.1 Apparent interface toughness

The interface indentation test is used to determine the adhesion between the coating and the substrate [3]. The test is performed on a metallography prepared cross section of a coated sample by placing a Vickers indent with the force (F) into the interface of the substrate and the coating to generate and propagate a crack parallel with the interface as shown in Figure 1.

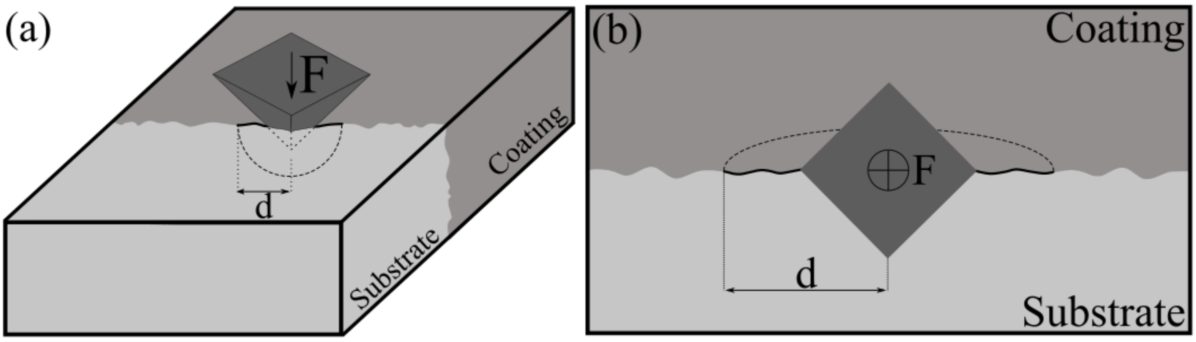

Figure 1: Illustration of the interface indentation test using a Vickers indent (a) 3. dimensional representation and (b) 2. dimensional representation.

The generated crack has a semi-circular geometry and is localised in the interface plane [3,15]. The length of the crack (d) is measured from the center of the indent to the tip of the crack in each direction, named (d) in Figure 1. The adhesion is represented as the apparent interface toughness (K_{ca}) between the substrate and the coating and can be calculated from Equation (1) [3],

$$K_{ca} = 0.015 \frac{F_c}{d_c^{3/2}} \cdot \left(\frac{\left(\frac{E_S}{H_S}\right)^{\frac{1}{2}}}{1 + \left(\frac{H_S}{H_R}\right)^{\frac{1}{2}}} + \frac{\left(\frac{E_R}{H_R}\right)^{1/2}}{1 + \left(\frac{H_R}{H_S}\right)^{1/2}} \right) \tag{1}$$

where F_c is the critical load, d_c is critical half indent, E is the Young's modulus, and H is the hardness. The R and S in subscript represent the materials properties of the coating and substrate, respectively. The value of d_c is half the diagonal of the indent when no crack formation has occurred. The critical load represents the minimum load where it is possible to break the link between the substrate and the coating.

2.2.2 Estimated work of adhesion for screening of pre-treatments

The emphasis of the screening of pre-treatments is not to determine the absolute value of the apparent interface toughness, but to have a statistic basis for selecting which treatments would be desirable to investigate further. Equation (1) becomes simpler when the coating and the substrate is not varied, as the final term becomes a constant. The force of the indentations is fixed and is required to exceed the critical load ($F > F_c$) that will initiate a crack. The proposed simplified equation for the estimated work of adhesion (a) between a coating and a substrate is shown in Equation (2),

$$a = \frac{F}{A_C^{1/2}} \tag{2}$$

where A_c is the area of the propagated crack as illustrated in Figure 2b. The estimated work of adhesion shown in equation (2) shares the unit with the work of adhesion [J/m^2]. The applied force will be converted into the initiation and propagation of the crack as well as the plastic deformation of the substrate and the coating. The estimation of the force contributing to the plastic deformation is extensive and requires a thorough understanding of the materials properties of the substrate and the coating. The force that goes into plastic deformation is not taken into account as the screening of pre-treatments does not alter the substrate material, the coating material, or the thickness of the coating and therefore the value can be considered as a constant. The thickness of the coating does not influence the surface energy between the substrate and the coating. However, the cracking ability during the interface indentation test is dependent on the coating thickness and a thick coating is more resistant to initiate a crack compared to a thin one [3]. The simplified equation for screening of pre-treatments, therefore, only allows comparing the same substrate coated by the same type of coating that has the same thickness, which all applies for the present work.

The formation of the ideal crack with a semi-circular geometry was only measured occasionally and more often was the length in one direction different than in the other direction, as shown in Figure 2a.

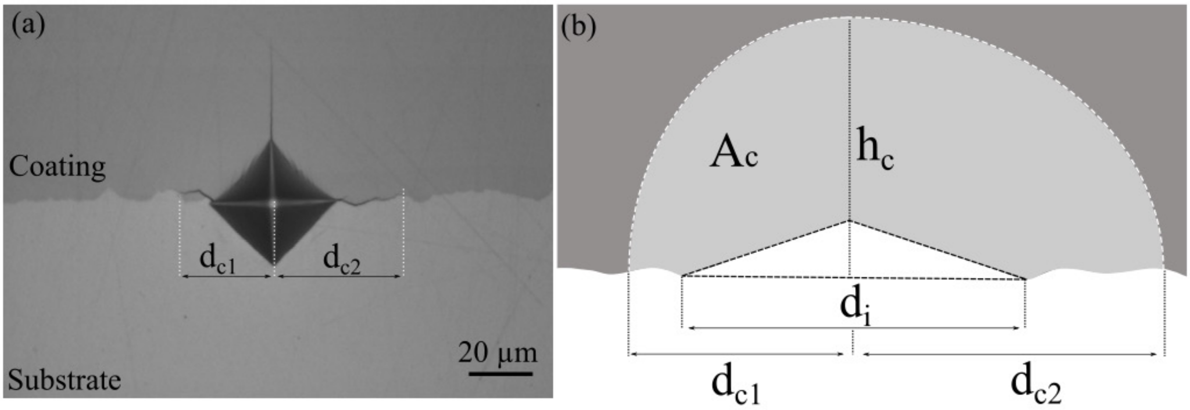

Figure 2: (a) Interface indentation test of a Fe-C coating on a hardened calmax substrate. (b) Illustration of the geometry in the interface where the crack has propagated. The d_{c1} and d_{c2} are the length of the visible cracks, d_i is the diagonal of the indentation, h_c is the depth of the propagated crack, and A_c is the area of the propagated crack.

The length of the cracks is measured from the visible crack tip to the center of the indent. The value A_c can be calculated by dividing the interface where the crack has propagated into two areas that share the boarder h_c. Each area is calculated as one quarter of an ellipse ($\frac{\pi\cdot a\cdot b}{4}, a = d_c, b = h_c \approx \frac{d_{c1}+d_{c2}}{2}$). The two areas are added and the plastically deformed area generated by the Vickers indent ($\frac{a\cdot b}{2}, a = d_i, b \approx \frac{d_i}{7}$) is subtracted as shown in Equation (3).

$$A_c = \frac{\pi \cdot d_{c1} \cdot h_c}{4} + \frac{\pi \cdot d_{c2} \cdot h_c}{4} - \frac{d_i^2}{14} \qquad (3)$$

2.3 Metallographic preparation

The coated samples were cut precisely in half to provide access to the cross section in an area where the coatings have the same thickness. The cutting was performed using a Struers Accutom-50 and cooling liquid was applied to avoid thermal evolution of the coating. The samples were fixed in a sample holder that allowed metallographic preparation of the cross section without embedment using a Struers Abramin. The metallographic preparation ensured that the samples cross sections were plane parallel with the sample stage of the microhardness indentation equipment.

2.4 Microhardness indentation

A Future Tech Inc. FM700 was used for the microhardness indentations using a Vickers indent that could be positioned precisely in the interface of the substrate and the coating of the prepared cross section. A load of 500 g (4.903 N) was applied for all samples and 10 indentations were acquired per sample. The distance between each indentation was at least three times the distance of the measured length of the interface crack. The indentations were posited in relatively flat areas in the interface to minimize the risk of surface roughness features that would interrupt the crack propagation. The length of the cracks was determined by the light optical microscopy using a Struers DuraScan.

3. Results and discussion

The interface indentation test allowed for the screening of the pre-treatments and determines which method of activation resulted in the highest mean values of adhesion. The activation of the substrate in 15% sulfuric acid for 2 min did not provide a level of adhesion that could be investigated as the interface indentation test caused the Fe-C coating to delaminate. However, the Fe-C coating that was not activated provide a level of adhesion that could be measured by the interface indentation test and suggest it is not an surface oxide layer that results in the low adhesion obtained for the activation using 15% sulfuric acid for 2 min, but rather carbides that are etched free and does not dissolve in this solution. The remaining activations provided a level of adhesion between the coating and substrate that allowed the length of the cracks to be measured and to evaluate the area of the propagated crack. The indents were positioned in areas that appeared flat to minimize obstacles for the propagation of the crack. Still, it is noted that the surface roughness of the substrate hindered crack propagation at the onset of steep changes as shown in Figure 3a. The measured cracks also appear to propagate into the Fe-C coating as shown in Figure 3b-d. However, the influence of the surface roughness in the direction perpendicular to the cross section cannot be evaluated and is considered as a source of error and lead to a considerable variation between the measured crack lengths as shown in Figure 3.

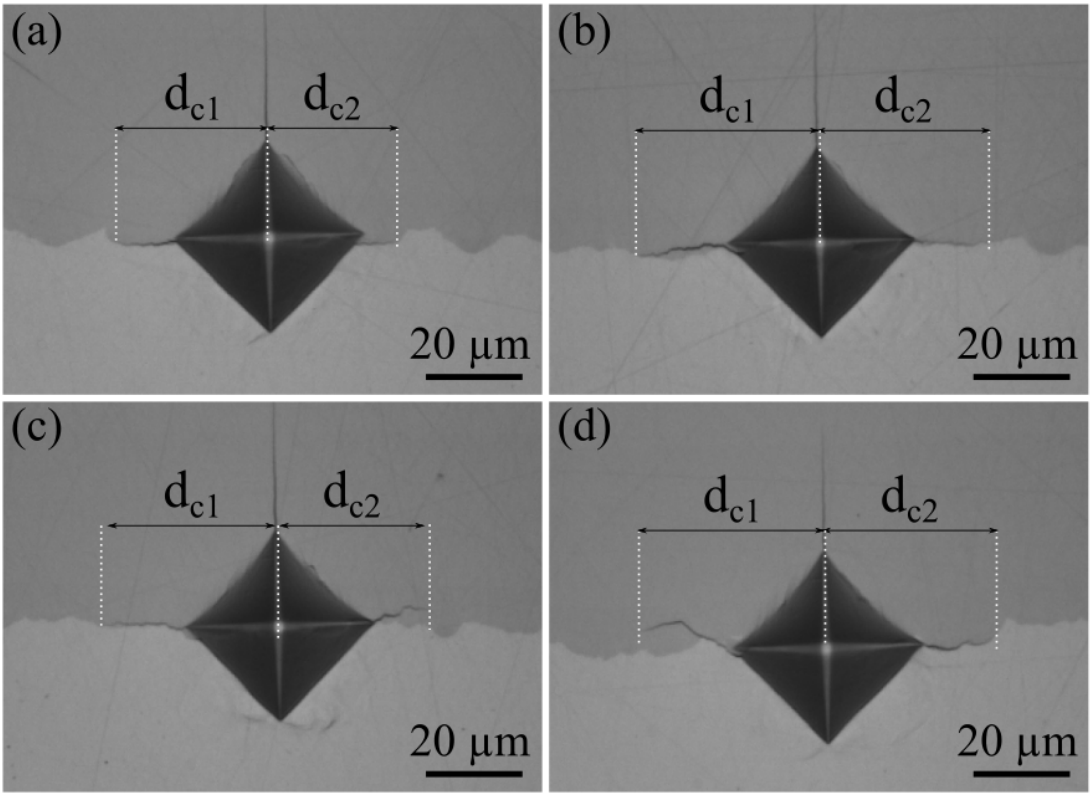

Figure 3: Interface indentation tests on the Fe-C coating on a hardened calmax steel activated using 2 min cathodic sulfuric acid. (a-d) Represent how the crack can propagate and how the crack length was measured.

The mean values of the estimated work of adhesion between the Fe-C coatings and the hardened calmax steels that were obtained for the different pre-treatments are shown in Figure 4. The mean value represents 10 interface indentation tests using a fixed load. The surface roughness is suggested as the main source of error that resulted in the high standard deviation for the interface indentation test. The two-sample t-test [6] is used to determine the confidence level of the differences in the mean values of the estimated work of adhesion. The power curve from the two-sample t-test [6] is used to estimate the sample size required to obtain a confidence level of 95 %.

The results showed that the highest mean value was obtained for the activation using 2 min of cathodic treatment in sulfuric acid. It can be stated with a confidence level above 95 % that this activation provides a better adhesion compared to an activation of 5 min in dry acid.

However, the confidence level is below 95 % that the activation using 2 min cathodic treatment in sulfuric acid provides a better adhesion compared to no activation at all. The power curve for the t-test estimates that using 15 measurements per sample (compared to 10 as currently used) will provide a confidence level above 95 % whether the activation for 2 min cathodic in sulfuric acid will improve the adhesion.

The confidence level is below 30% that the activation using 2 min cathodic treatment in sulfuric acid will improve the adhesion compared to the activation using dry acid for 2 min. The power curve estimates that above 100 measurements per sample are required to realize a confidence level at 95 % to state whether the activation for 2 min cathodic in sulfuric acid provides a better adhesion compared to the activation in dry acid.

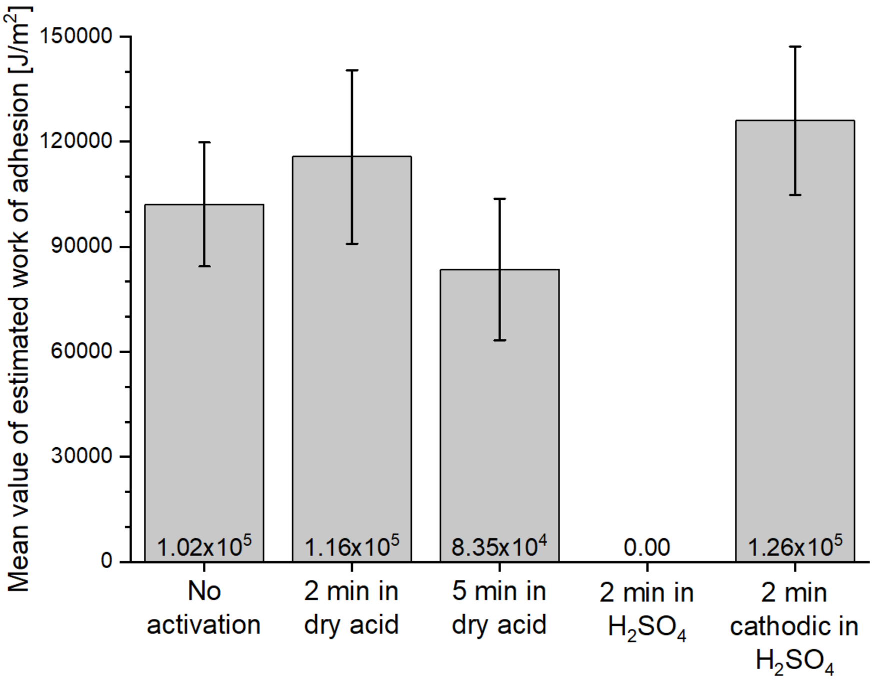

Figure 4: The mean values of the estimated work of adhesion between the Fe-C coating and the hardened calmax steel that was obtained using different activations. The mean value is calculated from 10 interface indentation tests using a fixed load of 500 g.

The difference between the activation in sulfuric acid when the substrate is connected as cathode compared to simply being submerged is compelling. The activation using 2 min in 15% sulfuric acid did not provide a level of adhesion to conduct the interface indentation test without delamination of the coating whereas the activation using 2 min cathodic treatment in sulfuric acid provided the highest mean value. It is evident that rinsing the substrate does not remove the contamination on the surface of carbides being etched free and hinders the coating to obtain a good adhesion towards the substrate. The contaminations are removed during activation using 2 min cathodic treatment in sulfuric acid by the hydrogen bubbles formed by electrolysis of water on the surface of the substrate.

The lower value of adhesion achieved by the extended duration in dry acid is suggested as a contamination of the surface from carbides being etched free and were not removed by rinsing in water or dissolved in the dry acid solution. The outcome of connecting the substrate as cathode in sulfuric acid showed the surface is cleaned during the activation by electrolysis of water on the surface of the substrate. The activation in dry acid for 2 min only had a slightly lower mean value compared to the 2 min cathodic treatment in sulfuric acid and suggests that such activation could be of interest.

4. Conclusion

The results does not allow with a statistical confidence to state which activation will provide the highest value of the estimated work of adhesion. However, it has proven that 2 out of the 5 pre-treatments do not provide the same value of adhesion and, therefore, are not essential for further investigation. A relatively small amount of measurements is required to state with a statistical confidence that disregarding the activation is not beneficial to obtain a high value of adhesion. The screening of pre-treatments using the interface indentation test has successfully limited the amount of activations being of significant interest and propose a new activation method of interest.

Acknowledgement

The authors gratefully acknowledge OCAS NV, ArcelorMittal Global R&D Gent (Belgium), a. h. nichro Haardchrom (Denmark), and Fast Track - Societal Partnership (Denmark), funded by the Innovation Fund Denmark (IFD), for financial support.

References

[1] D. Driver, Handbook on Adhesion, 2nd ed,. Wiley,1993.

[2] P. Møller, L.P. Nielsen, Advanced Surface Technology,1st ed,. Møller&Nielsen, 2013.

[3] D. Chicot, P. Demarecaux, J. Lesage, Apparent interface toughness of substrate and coating couples from indentation tests, Thin Solid Films. 283 (1996) 151–157.

[4] G. Marot, J. Lesage, P. Démarécaux, M. Hadad, S. Siegmann, M.H. Staia, Interfacial indentation and shear tests to determine the adhesion of thermal spray coatings, Surf. Coat. Technol. 201 (2006) 2080–2085.

[5] M. Hadad, G. Marot, P. Démarécaux, D. Chicot, J. Lesage, L. Rohr, S. Siegmann, Adhesion tests for thermal spray coatings: correlation of bond strength and interfacial toughness, Surf. Eng. 23 (2007) 279–283.

[6] D.C. Montgomery, Analysis of variance, in: Des. Anal. Exp., 8th ed., Wiley, 2013: pp. 65–130.

[7] M. Izaki, H. Enomoto, T. Omi, Hardness and Carbon Content of Fe Electroplate from Sulfate Bath Containing l-Ascorbic Acid and Citric Acid, J. Surf. Fin. Soc. Jpn. 40 (1989) 1304–05.

[8] Y. Fujiwara, T. Nagayama, A. Nakae, M. Izaki, H. Enomoto, E. Yamauchi, Electrodeposition of Fe-C Alloys from Baths Containing Dicarboxylic Acids with a Linear Alkyl Chain, J. Electrochem. Soc. 143 (1996) 2584–2590.

[9] M. Panayotova, Deposition of Fe–C alloy on structural steel and cast iron for repair of worn machine parts, Surf. Coat. Technol. 124 (2000) 266–271.

[10] T. Müller, J. Grimwood, A. Bachmaier, R. Pippan, Electrodeposition of Fe-C alloys from citrate baths: Structure, mechanical properties, and thermal stability, Metals. 8 (2018) 1–13.

[11] A.S.M.A. Haseeb, Y. Hayashi, M. Masuda, M. Arita, On the nature of the electrochemically synthesized hard Fe-0.96 mass pct C alloy film, Metall. Mater. Trans. B. 33B (2002) 921–927.

[12] J.O. Nielsen, P. Møller, K. Pantleon, Electrodeposition of Iron with Co-deposition of Carbon: On the Nature of Nanocrystalline Fe-C Coatings, Metall. Mater. Trans. A. 50A (2019) 3785–3793.

[13] J.O. Nielsen, K. Pantleon, Evolution of hard Fe–C electrodeposits with temperature, Surf. Eng. (2019), in press. Published online in October 2019.

[14] W.H. Philipp, Chemical Reactions of Carbides, Nitrides, and Diborides of Titanium and Zirconium and Chemical Bonding in These Compounds, 1966.

[15] G. Liu, A. Mouftiez, J. Lesage, S. Panier, A numerical fracture analysis of a stationary semi-circular interface crack during interfacial indentation test G., Surf. Coat. Technol. 2001 (2006) 2086–2091.

7 Results regarding the annealed Fe-C coatings

7.1 Evolution of ex-situ annealed Fe-C coating

7.1.1 Manuscript V

Evolution of hard Fe-C electrodeposits with temperature[10]

Jacob Obitsø Nielsen*, Karen Pantleon

Technical University of Denmark, Department of Mechanical Engineering, Produktionstorvet, building 425, DK – 2800 Kongens Lyngby, Denmark

*Corresponding author: jacobon@mek.dtu.dk

ABSTRACT

The high microhardness of electrodeposited Fe-C coatings with around 800 HV after electrodeposition increased to about 1300 HV by dedicated annealing, reflecting a huge potential for surface engineering. The coatings remain nanocrystalline during annealing, but co-deposited carbon and oxygen result in temperature induced phase transformations. Energy-dispersive synchrotron diffraction revealed that carbides and oxides form during annealing of the as-deposited coating, which consisted mainly of carbon-free ferrite. The understanding of occurring precipitations was supplemented and verified by in-situ thermal analysis, which revealed the temperatures of thermal events related to decomposition reactions, the evolution of gasses and associated mass changes during annealing.

Introduction

Despite the enormous attention on iron-carbon alloys for a wide range of surface engineering applications, their synthesis by electrodeposition is still less in focus compared to, for example, thermo-chemical treatments. The addition of organic species, like carboxylic acids, to traditional iron-sulphate electrolytes provides the carbon source that enables the co-deposition of carbon together with iron, resulting in Fe-C coatings with thicknesses of up to several hundreds of micrometers. The structure and functional groups of various carboxylic additives influence the amount of co-deposited carbon and, to some extent, the morphology and associated properties of the Fe-C coatings [1-6]. High microhardness values (up to around 800 HV) [7] are consistently reported for electrodeposited Fe-C coatings and, hence, the coatings provide a favourable alternative to hardened steels. The more versatile process of electrodeposited Fe-C compared to (surface) hardening of steels allows producing hard and wear-resistant coatings on a variety of different substrates, performing site-specific deposition for repairing surfaces and tailoring the internal structure of the coatings according to the deposition process parameters, and it offers a huge potential for surface engineering by post-deposition treatment. In this respect, not only the nature of as-deposited coatings, but also their thermal stability including the evolution of the microstructure and occurring phase transformations are of interest.

---

[10] Surface Engineering, in press. Published online in October 2019. The format of the published article was adapted to the format of the doctoral thesis.

In our recent work [6], we have shown that as-deposited Fe-C coatings consist of nanocrystalline grains and form strong <311> fibre textures independent of the coating thickness. Despite the high concentration of carbon, which amounts to 0.88 wt-% in the as-deposited coatings, the majority of grains correspond to ferrite with bcc crystal structure and the strain-free lattice spacing as measured by X-ray diffraction (XRD) does not indicate any (supersaturated) solid solution of carbon [6]. The presence of a minor second phase has been suggested by XRD, but thorough identification of that phase is hindered by the limited number and weak intensity of corresponding peaks: only a single peak, in addition to ferrite, can be detected clearly [5,6,8,9]. This second phase may originate from the co-deposited carbon (e.g. Fe_2C carbides [6,8]), but it also may be related to further elements like oxygen and hydrogen, which indeed are detected although not quantifiable in as-deposited coatings, and/or a combination of all present elements being iron, carbon, oxygen and hydrogen. To reveal the role of these elements, which reproducibly are detected in electrodeposited Fe-C coatings [2,6-8,10,11], the present work investigates the evolution of as-deposited coatings during annealing and reveals corresponding phase transformations by means of complementary thermal analysis and diffraction analysis, further supplemented with transmission electron microscopy.

Material and methods

Electrodeposition

The same Fe-C coatings, which previously have been studied in their as-deposited state [6], have been used for the present annealing study. Deposition from an iron-sulphate electrolyte with citric acid as an additive (0.143 mol/dm^3 $FeSO_4 \cdot 7H_2O$, 6.2 x 10^{-3} mol/dm^3 $C_6H_8O_7 \cdot H_2O$) occurred with a constant current density of 3.0 A/dm^2 (for details, see [6]). As cathode, thin brass strips and lead-tape were attached on a steel plate such that deposition occurred simultaneously on lead and brass, thus, under exact same conditions. The substrate material does not play a role for the present study, because the long deposition with 15 h resulted in a thick coating of 360 µm. Low adhesion of the coating on lead allowed easy detaching from the substrate to obtain stand-alone coatings for in-situ thermal analysis, while coatings on brass were used for ex-situ annealing.

Characterization methods

Simultaneous thermogravimetry (TGA) and differential thermal analysis (DTA) were performed in a Netzsch STA 449F3 coupled with a Netzsch QMS 403 Aëolos quadrupole mass spectrometer (MS). The setup enables the detection and identification of evolved gases in time correlation with enthalpy and mass changes. For each measurement, a piece of substrate-free coating material, detached from the lead-tape and weighing 250-260 mg, was placed in an alumina crucible. Isothermal annealing experiments were carried out at temperatures of 200, 250 and 300 °C, respectively, with a holding time of 24 h at each temperature. Each of the isothermally treated samples, was subsequently further subjected to two cycles of isochronal annealing from 40 °C to 800 °C, using a heating rate of 2 K min^{-1} and a cooling rate of 40 K min^{-1}, whereby the second isochronal annealing was used to correct for the instrumental background of the first isochronal annealing. As a reference, an as-deposited coating was subjected to the two isochronal heating cycles. Annealing was carried out in an inert atmosphere of argon gas (99.999 mol-% purity).

Identical counterparts of the coating on brass substrates were used for furnace annealing in a lower temperature range up to a maximum of 300 °C. Such furnace annealing was carried out for 24 h at isothermal temperatures of 200, 250 and 300 °C, respectively, in an inert argon (99.999 mol-% purity). Qualitative phase analysis was carried out for each sample at the synchrotron diffraction facility BESSY II using energy-dispersive diffraction (EDD) at the EDDI beamline [12]. EDD spectra were recorded for 600 s applying a symmetric diffraction geometry with a constant scattering angle $2\theta = 14°$, corresponding to a maximum information depth of about 100 µm. For phase analysis, the diffraction lines were fitted with pseudo-Voigt functions. A gold reference standard was used for calibration of the energy offset.

Fe-C coatings in both the as-deposited state and after annealing at 300 °C for 24 h have been prepared for transmission electron microscopy (TEM) analysis. Applying the FIB lift-out technique in a dual beam FEI Helios EBS3 microscope, samples were prepared in plan view at about half of the total thickness of the 360 µm thick Fe-C coatings. TEM investigation applying bright field imaging (BF) and selected area electron diffraction (SAED) was carried out with an accelerating voltage of 300 kV using a Joel 3000F microscope.

Microhardness measurements were performed on metallographically prepared cross sections of the exact same Fe-C coatings of the present diffraction analysis. A Future Tech Inc. FM700 microhardness tester with Vickers geometry was applied with a load of 25 g and represented data average over five measurements per sample.

Results and discussion

The EDD spectra of the as-deposited and ex-situ annealed Fe-C coatings are shown in Figure 1. Consistent with results from conventional laboratory XRD [6], the as-deposited coating mainly consists of α-iron and a second phase is indicated by one additional peak at 21.51 keV (Figure 1(a)) corresponding to a d-spacing of 0.2365 nm, which confirms our previous measurements. Although this single peak of an additional phase is reproducibly measured and also reported in literature [5,6,8], the corresponding phase analysis has not yet been unambiguously, as mentioned above (therefore, here, it is referred to ‘nameless peak’), and it is of interest to follow the evolution of this peak/phase by annealing. Figure 1(b) shows that the nameless peak remains unchanged even after annealing of 24 h at 250 °C, and its position, intensity and width are identical to the ones for the as-deposited coating. In the same temperature range, where the nameless peak still is unaffected, Fe_3O_4 (magnetite) develops (cf. Figure 1(b)). As the applied inert gas excludes oxidation from the furnace and no oxide layer has been found on the surface, the formation of magnetite has occurred throughout the coating. This confirms that oxygen has been present already in the as-deposited coating, which agrees with the detection of oxygen by chemical analysis with glow discharge optical emission spectroscopy and electron energy loss spectroscopy, although quantification of the as-deposited oxygen concentration has not been possible yet [6]. While the oxide is detected already at 200 °C, still there is no clear indication for a carbon-containing phase (except from the vague relation to the nameless peak) and first at 250 °C, carbides of Fe_3C (cementite) are clearly detected (cf. Figure 1(b)). With further increasing temperature to 300 °C, both magnetite and cementite further evolve towards higher intensities, while the nameless peak simultaneously reduces in intensity. Although of low intensity, the nameless peak is still present after annealing at 300 °C, as indicated by the observed asymmetry of the higher intense peak of Fe_3C at about the same position (cf. Figure 1(b)). The decrease in intensity of the nameless peak, simultaneously with a significant increase in the intensities of all peaks related to both Fe_3C and Fe_3O_4 suggest that the phase related to the nameless peak contains carbon and oxygen.

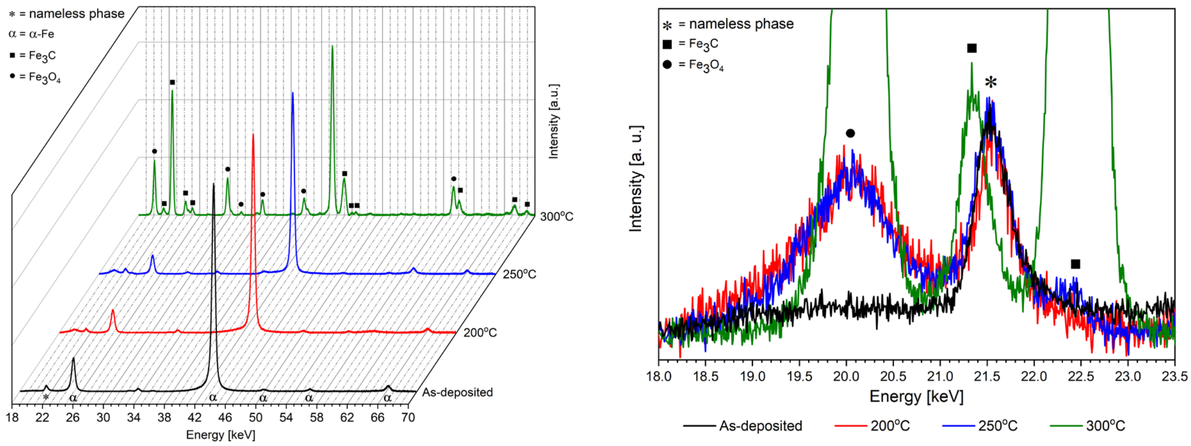

(a) (b)

Figure 1: Energy-dispersive diffraction spectra of Fe-C coatings: as-deposited (black) and after isothermal annealing for 24 hours at 200 °C (red), 250 °C (blue) and 300 °C (green). (a) Overview (b) Magnified region to indicate phase transformations, see details in the text. Note: The peak at 33.61 keV corresponds to an escape peak from α-211.

To verify the phase transformations as revealed by diffraction analysis and to understand the nature and evolution of the nameless peak/phase of the as-deposited coatings, thermal analysis during isochronal annealing of both an as-deposited coating and previously isothermally annealed coatings for 24 h at 200, 250 and 300 °C has been carried out by simultaneous DTA, TGA and MS analysis. Figure 2 shows, on the example of occurring weight changes, the thermal desorption of H_2O (related to desorption of hydrogen), and the enthalpy changes, that the as-deposited Fe-C coating undergoes four thermal events at distinct temperatures during isochronal annealing.

The first event at around 115 °C is defined by an exothermic peak (cf. Figure 2), a desorption of hydrogen and corresponding mass loss, which is related to dehydrogenation of adsorb hydrogen originating from the electrolysis of water during the deposition process. The entrapment of hydrogen into the growing coating is typical for electrodeposition and manifests in reduced current efficiency, which indeed for the present samples amounted to 60.5 %. This atomic or molecular hydrogen can easily evaporate and, accordingly, this reaction only is measured for the as-deposited coating and not for the already annealed samples. The second event at around 275 °C (cf. Figure 2) is visible for the as-deposited sample and for samples annealed at 200 °C and 250 °C, and relates to a thermal decomposition, which is characterized by a further release of hydrogen and a mass loss. The observation that the hydrogen release in the second event is lower for the 250 °C annealed sample compared to 200 °C and not occurring after higher annealing temperature of 300 °C, indicates that the corresponding phase still is intact after isothermal annealing at 200 °C, partly decomposed after 250 °C annealing and fully decomposed at 300 °C. The precipitation of Fe_3C for samples annealed at 250 °C and 300 °C, respectively, as measured by EDD (cf. Figure 1(b)), further reveals that carbon originally is bound to the phase decomposing at the second event. As the nameless peak/phase still is recorded by EDD after isothermal annealing at 250 °C without any changes compared to its as-deposited state, the occurring thermal decomposition in the second thermal event does not seem to relate to that phase. The third event at around 360 °C (cf. Figure 2) is identified as a thermal decomposition by an exothermic reaction, a further release of hydrogen and a mass loss. This thermal decomposition at 360 °C is measured for all samples, but is much less prominent for the 300 °C annealed sample, where only the mass loss and a release of hydrogen indicate the reaction. This could be associated with the nameless peak/phase measured by EDD, since the intensity of the peak has decreased significantly after isothermal annealing at 300 °C (cf. Figure 1b). Such a correlation would reject the hypothesis that the nameless peak originates from Fe_2C (either ε- or η-phase, as previously suggested [6,8]), since its transformation into Fe_3C cannot be associated with a mass loss or release of hydrogen [13]. The temperature of 360 °C is also higher than the reported transformation temperature of ε/η-Fe_2C to Fe_3C [13], but is in good agreement with a former study of the decomposition of ferrihydrite [14]. The suggestion of the nameless phase being a hydroxide would be supported by the observed release of hydrogen during annealing and the measured d-spacing of the nameless peak with d = 0.2365 nm (E = 21.51 keV, Figure 1) would correspond to d_{004} = 0.234 nm of FeOOH (ferrihydrite), although this is the only observable peak of that phase, as mentioned above. However, ferrihydrite, as the possible second phase in the as-deposited Fe-C coating, only consists of iron, oxygen and hydrogen, but not carbon. Accordingly, its decomposition would not account for the release of carbon required for the growth of Fe_3C. Instead, the carbon required for the growth of Fe_3C may originate from the phase decomposing in the second event. Accordingly, the 300 °C annealed sample has already underwent that decomposition fully, which has supplied carbon for the growth of Fe_3C, and, simultaneously, ferrihydrite related to the third event has partly decomposed and released oxygen for the growth of Fe_3O_4. The fourth event at around 505 °C (cf. Figure 2) is revealed as a small exothermic reaction for the as-deposited sample only. This event is not associated with any mass loss or release of hydrogen. The observed temperature of that event does not relate to any expected transformation of α-Fe, Fe_3C or Fe_3O_4 [15-17], but a second exothermic reaction has been reported for ferrihydrite [14], which explains that only the as-deposited coating further evolves at that temperature.

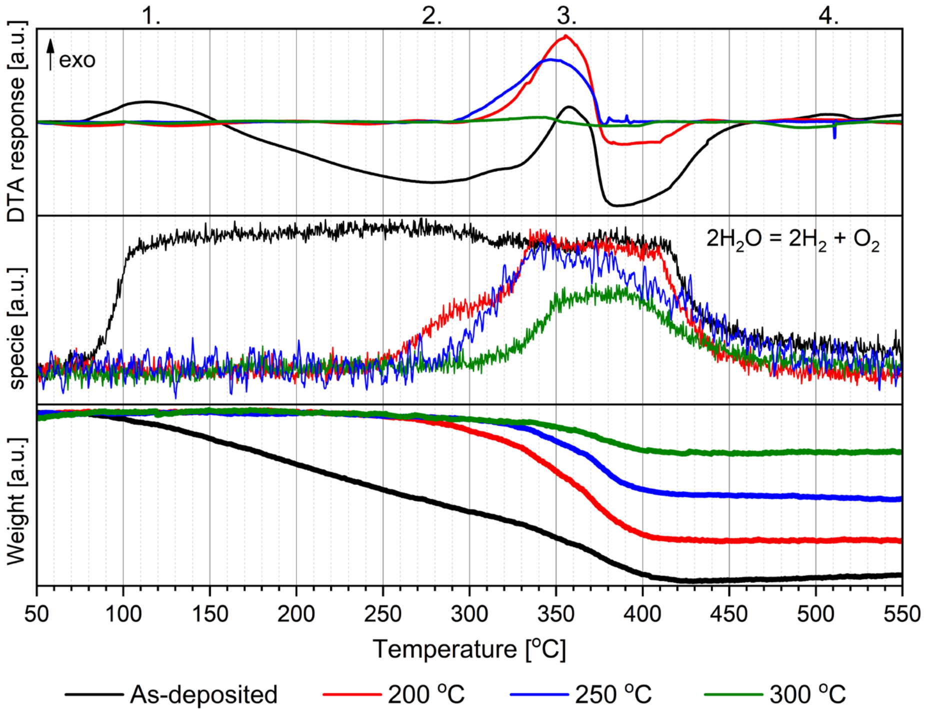

Figure 2: Thermal analysis by DTA, MS and TGA for Fe-C coatings: as-deposited (black) and after isothermal annealing for 24 hours at 200 °C (red), 250 °C (blue) and 300 °C (green). The signal from H_2O^+ is used as a marker for the desorption of hydrogen, since hydrogen released from the sample will reacts with the oxygen impurity in the argon ($2H_2 + O_2 \rightarrow 2H_2O$) and produces an increased signal of H_2O. The numbers 1 to 4 corresponds to the thermal events described in the text.

Supplementing the results from diffraction analysis and thermal analysis regarding the presence and thermal evolution of phases in the Fe-C coating, TEM reveals that the as-deposited coating is nanocrystalline. The applied plan-view investigations show average grain sizes of 15-40 nm for the as-deposited coating, as shown in Figure 3(a). These grains result in fine rings in the SAED pattern shown in Figure 3(b), which correspond to the ferrite phase, in agreement to the results from synchrotron diffraction for the as-deposited coating (cf. Figure 1). In addition to ferrite, also a uniformly occupied diffraction ring indicating magnetite Fe_3O_4 is detected, which has not been revealed by synchrotron diffraction. Based on the knowledge of co-deposited oxygen [6], the oxide may have formed during electrodeposition but with too low volume fraction for being detected by synchrotron diffraction covering a larger sample volume, but it also may indicate the challenges of preventing oxidation of ferrite during preparation, handling or storage of the thin TEM lamella. Interestingly, there are no diffraction spots matching the d-spacing of the nameless peak or other spots related to the nameless phase, which is known to be present in the as-deposited coating based on EDD (cf. Figure 1); however, both diffraction methods relate to a different measurement direction in the coating.

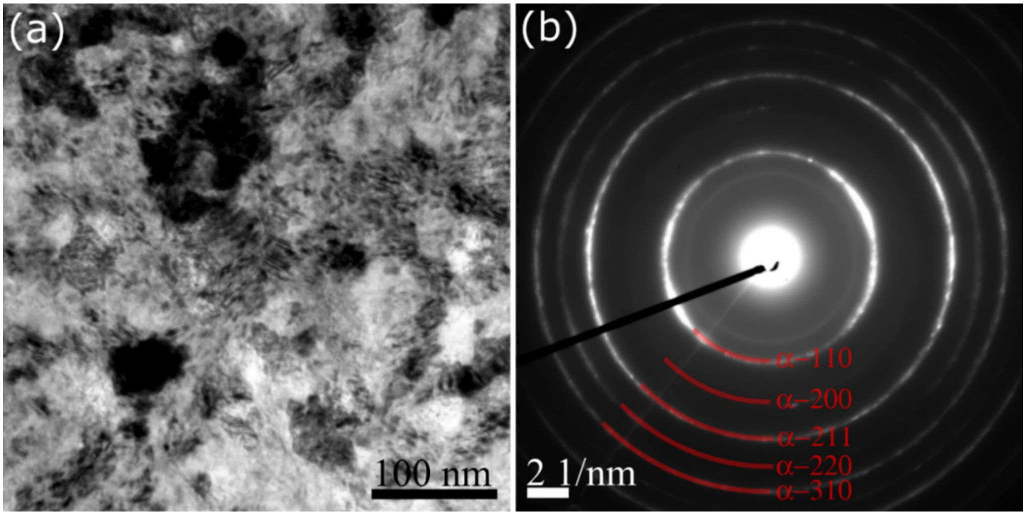

Figure 3: TEM micrograph (a) and corresponding selected area electron diffraction pattern (b) of the as-deposited Fe-C coating in plan-view.

After ex-situ annealing at 300 °C for 24 h (same sample as used for EDD), the ferrite grains are still nanocrystalline and Figure 4(a) in plane-view reveals an average size of the grains in the order of 30-50 nm. The corresponding SAED pattern (Figure 4(b)) for this annealed Fe-C coating clearly reveals that cementite Fe_3C and magnetite Fe_3O_4 have formed during annealing. This is consistent with synchrotron diffraction results of the annealed coatings, which reveal magnetite formation already after annealing at 200 °C with nanocrystalline dimensions as indicated by the fairly broad peaks (cf. Figure 1).

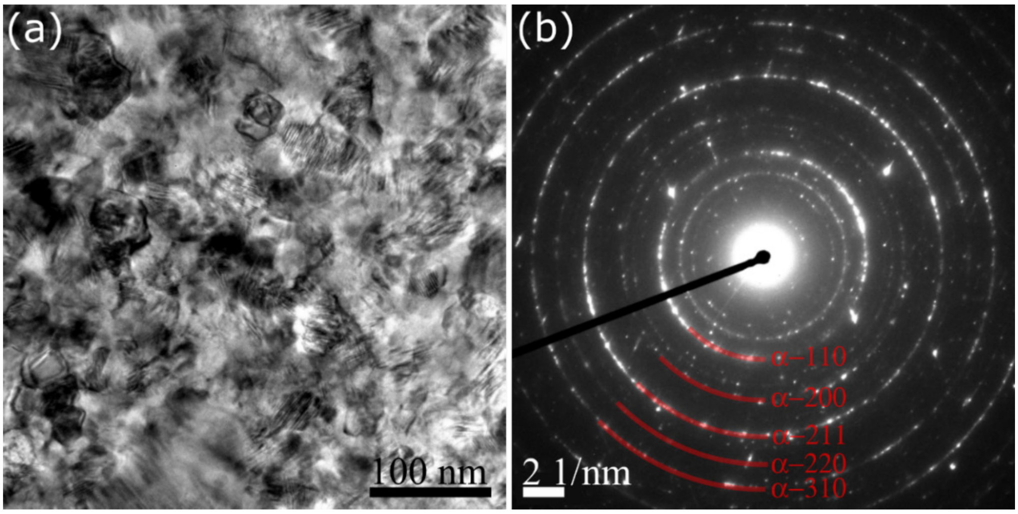

Figure 4: TEM micrograph in plan view (a) and corresponding selected area electron diffraction pattern (b) of the Fe-C coating ex-situ annealed at 300 °C for 24 hours.

Microhardness measurements on cross sections of the nanocrystalline Fe-C coatings revealed high microhardness of 784±12 HV0.025 for the as-deposited coating. The occurring phase transformations during annealing suggest a further hardness increase. Indeed, isothermal annealing at 200, 250 and 300 °C increased the microhardness of the Fe-C coatings to 883±28 HV0.025 (200 °C), 957±17 HV0.025 (250 °C) and 1286±27 HV0.025 (300 °C). The absence of significant grain growth of ferrite and the evolving oxide and carbide phases being of small dimensions and distributed within the whole coating according to the origin of carbon and oxygen from the electrodeposition process, essentially contribute to the observed increase of the hardness by annealing.

Conclusion

The applied complementary methods of microscopy, diffraction analysis and thermal analysis strongly support the understanding of both the as-deposited Fe-C coatings as well as their evolution during annealing. The results reveal the important role of carbon, oxygen and hydrogen, which previously have been detected in as-deposited coatings, but are challenging to be quantified by chemical analysis. The origin of carbon, oxygen and hydrogen strongly relates to the deposition process with citric acid as an additive and complexing agent in the iron sulphate electrolyte. Although mainly the co-deposition of carbon has been intended for the electrodeposited Fe-C coatings, the formation of phases during deposition and the occurring phase transformations during annealing are clearly governed by more than just carbon and iron. The synergetic effect of all these elements together with the nanocrystalline nature of the coatings explain the excellent mechanical properties of the electrodeposited Fe-C coatings and make them a favourable candidate for wear resistant surfaces.

Acknowledgements

The authors are grateful to Christoph Genzel, Manuela Klaus and Daniel Apel (HZB, Germany) for experimental support at the beamline EDDI of BESSY II. Flemming Bjerg Grumsen (DTU, Denmark) is acknowledged for TEM analysis and Thomas Lundin Christiansen (DTU, Denmark) is acknowledged for discussions on thermal analysis. Financial support by OCAS NV, ArcelorMittal Global R&D Gent (Belgium), a. h. nichro Haardchrom (Denmark) and Fast Track - Societal Partnership (Denmark), funded by the Innovation Fund Denmark (IFD), is kindly acknowledged.

References

[1] Fujiwara Y, Izaki M, Enomoto H, et al. Effects of Hydroxycarboxylic Acids on the Electrodeposition of Fe-C Alloys. Denki Kagaku. 1993;7:840–842.

[2] Fujiwara Y, Nagayama T, Nakae A, et al. Electrodeposition of Fe-C Alloys from Baths Containing Dicarboxylic Acids with a Linear Alkyl Chain. J. Electrochem. Soc. 1996;143:2584–2590.

[3] Fujiwara Y, Izaki M, Enomoto H, et al. Optimization of bath composition for hard Fe-C alloy plating. J. Appl. Electrochem. 1998;28:855–862.

[4] Panayotova M. Deposition of Fe–C alloy on structural steel and cast iron for repair of worn machine parts. Surf. Coat. Technol. 2000;124:266–271.

[5] Müller T, Grimwood J, Bachmaier A, et al. Electrodeposition of Fe-C alloys from citrate baths: Structure, mechanical properties, and thermal stability. Metals. 2018;8:1–13.

[6] Nielsen JO, Møller P, Pantleon K. Electrodeposition of iron with co-deposition of carbon – on the nature of nanocrystalline Fe-C coatings. Metall. Mater. Trans. A. 2019;50A:3785-3793

[7] Izaki M, Omi T. Structural characterization of martensitic iron-carbon alloy films electrodeposited from an iron(ll) sulfate solution. Metall. Mater. Trans. A. 1996;27A:483–486.

[8] Haseeb ASMA, Hayashi Y, Masuda M, et al. On the nature of the electrochemically synthesized hard Fe-0.96 mass pct C alloy film. Metall. Mater. Trans. B. 2002;33B:921–927.

[9] Miyamoto N, Sakamoto S, Tamura H, et al. Effect of Carbon Content on Structural and Mechanical Properties of Fe-Co-C Alloy Electrodeposited from Aqueous Solutions. J. Electrochem. Soc. 2005;152:C488–C492.

[10] Haseeb ASMA, Nishida T, Masuda M, et al. Mössbauer investigation on electrodeposited Fe-C and Fe-Ni-C alloys. Scr. Mater. 2001;44:519–523.

[11] Haseeb ASMA, Arita M, Hayashi Y. Thermal decomposition study of electrodeposited Fe-C and Fe-Ni-C alloys by differential scanning calorimetry. J. Mater. Sci. 2001;6:4739–4743.

[12] Genzel C, Denks I. A, Gibmeier J, et al. The materials science synchrotron beamline EDDI for energy-dispersive diffraction analysis. Nucl. Instruments Methods Phys. Res. A. 2007;578:23–33.

[13] Cheng L, Brakman CM, Korevaar BM, et al. The Tempering of Iron-Carbon Martensite; Dilatometric and Calorimetric Analysis. Metall. Trans. A. 1988;19A:2415–2426.

[14] Campbell AS, Schwertmann U, Campbell PA. Formation of cubic phases on ferrihydrite heating. Clay Miner. 1997;32:615–622.

[15] Chipman J. Thermodynamics and Phase Diagram of the Fe-C System. Metall. Trans. 1972;3:55–64.

[16] Yakel HL. Crystal structures of stable and metastable iron-containing carbides. Int. Met. Rev. 1985;30:17–40.

[17] Wriedt HA. The Fe-O (Iron-Oxygen) System. J. Phase Equilibria. 1991;12:170–200.

7.1.2 Supplementary material regarding the hardness and phase constitution

The applied letter format for Manuscript V did not allow all the words that were required to describe and analyze all the ex-situ isothermal annealed samples that were produced during the experimental process.

The present chapter supplements the systematic studies of Fe-C coatings described in Manuscript V using samples from the same electrodeposition. The ex-situ annealing procedure was identical to the procedure described in Manuscript V, with the exception of the isothermal holding time at elevated temperature for some samples. The methods of identifying the phase constitution using energy-dispersive synchrotron diffraction and determining the microhardness of the coating were the same as described in Manuscript V. The diffraction spectra of the samples described in Manuscript V are included in Figure 52 to allow straightforward comparison between the spectra of the annealed samples, but will not be discussed. The microhardness value of the samples presented in Manuscript V are included in Figure 54, but will not be discussed.

Diffraction analysis

The diffraction spectra of the ex-situ isothermal annealed Fe-C coatings are shown in Figure 52 as an overview and a magnified region of selected spectra is shown in Figure 53. The overview supports the conclusion in Manuscript V, that magnetite is measured as a broad peak of low intensity after annealing at 200 °C for 24 hours and up to 250 °C for 24 hours. The peak related to magnetite grows in intensity and decreases in breadth when the coating is annealed at 300 °C for 3 hours, which indicates a higher phase fraction and an increase in crystallite size and/or decrease in microstrain. The phase fraction of magnetite increases further for the coating annealed at 400 °C for 3 hours. The diffraction spectrum for the coating annealed at 250 °C for 3 hours does not contain peaks related to cementite and confirms that its precipitation rate at this temperature is low. The peaks related to cementite are of high intensity for the coating annealed at 300 °C for 3 hours. The selected spectra shown in Figure 53 display the challenge of analyzing the transformation of the “nameless peak”, which is described in Manuscript VI and VII for the in-situ diffraction analysis. The as-deposited diffraction spectrum (black) shows the “nameless peak” in its as-deposited state at 21.51 keV, while the coating annealed for 400 °C for 3 hours (red) does not include the “nameless peak”, but a peak related to cementite developed at 21.30 keV. The diffraction spectrum for the coating annealed at 300 °C for 3 hours (blue) includes a peak measured at 21.41 keV being an overlap of the “nameless peak” and the cementite peak.

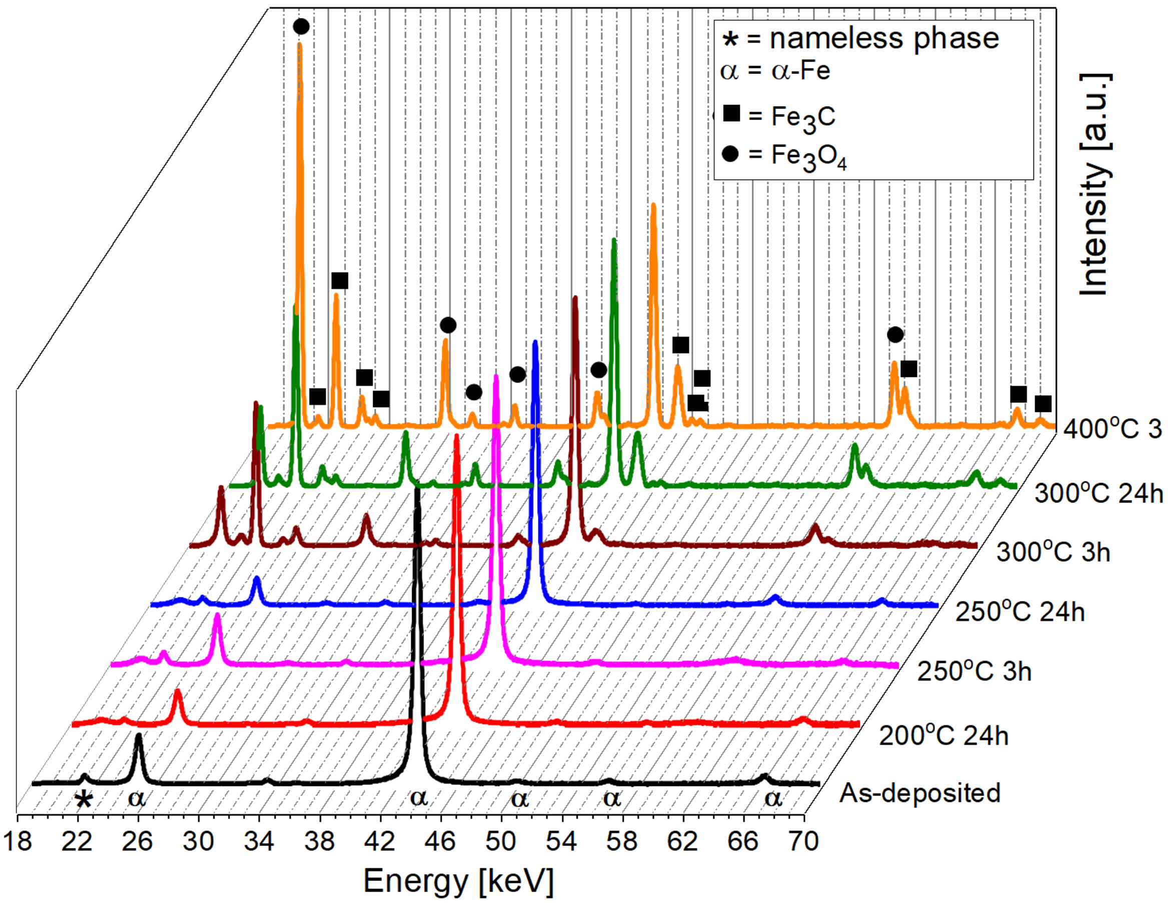

Figure 52: Energy-dispersive diffraction spectra of Fe-C coatings: as-deposited (black) and ex-situ isothermal annealing for different times and temperatures. The peak at 33.61 keV corresponds to an escape peak from α-211.

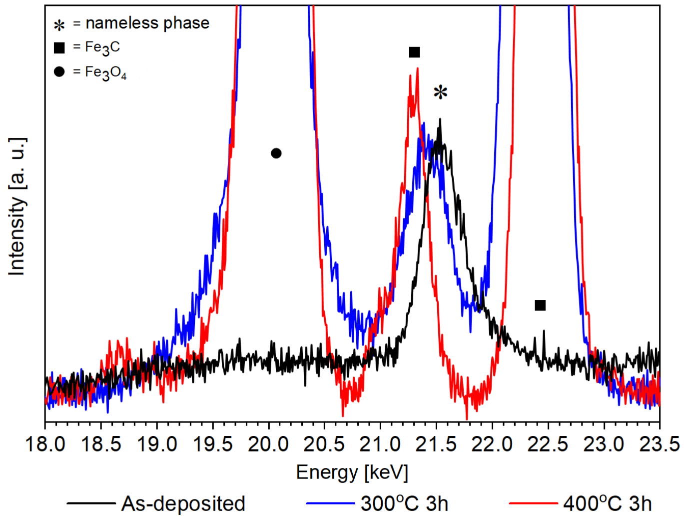

Figure 53: Energy-dispersive diffraction spectra of Fe-C coatings: as-deposited (black) and ex-situ isothermal annealing for different times and temperatures. Magnified region to indicate phase transformations.

Hardness

The microhardness values measured for the ex-situ annealed coatings are shown in Figure 54. The microhardness of the coatings where only magnetite has developed, i.e. coatings after annealing at 200 and 250 °C for 3 hours and 200 °C for 24 hours, is increased to nearly 900 HV0.025. The microhardness of the coating increased further to around 960 HV0.025 when magnetite and cementite developed and the “nameless phase” is still clearly measured in the diffraction spectra after annealing at 250 °C for 24 hours and 300 °C for 3 hours. The coatings annealed above the temperature of the transformation of the “nameless phase”, which occurs at around 328 °C (as described in Manuscript VI), have a hardness of more than 1000 HV0.025, with the highest hardness above 1100 HV0.025 for the sample annealed for the shortest duration of 3 hours. The decrease in hardness measured for the coating annealed at 400 °C compared to the sample annealed at 300 °C for 24 hours is related to grain coarsening of ferrite and will be discussed in Manuscript VII.

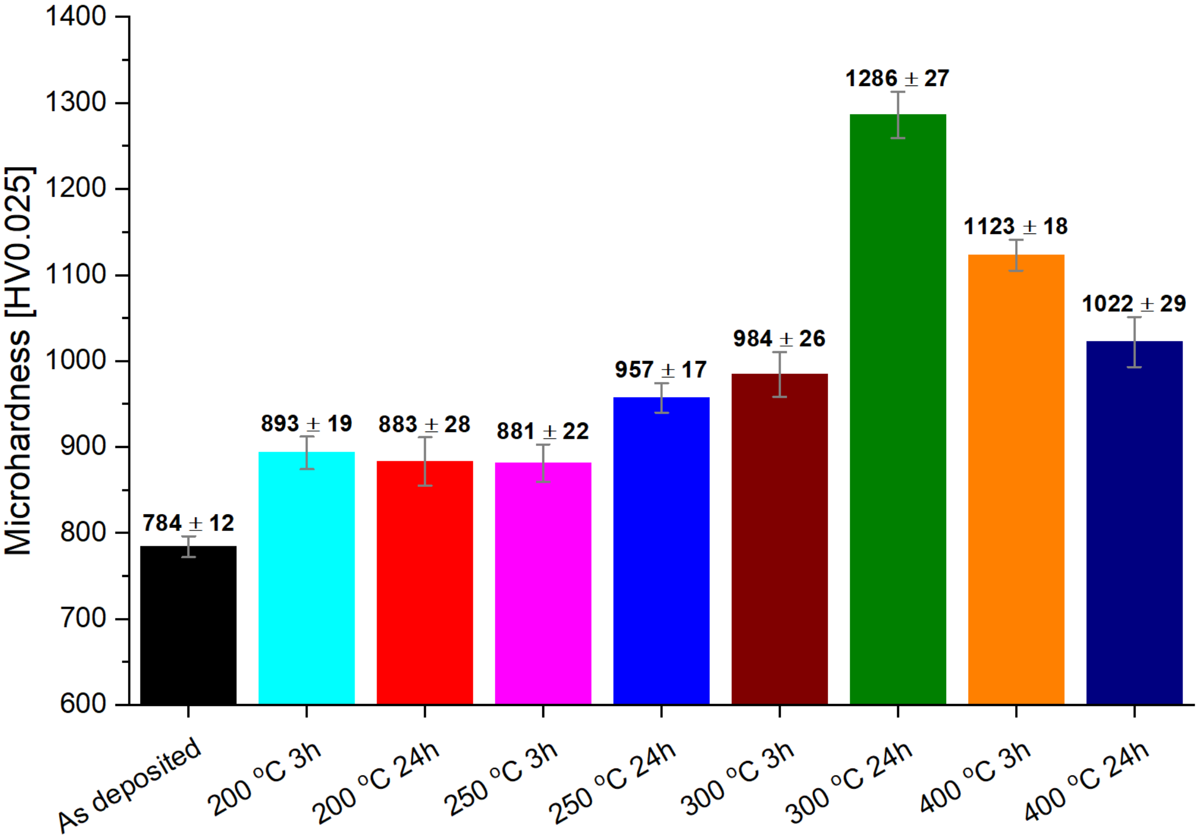

Figure 54: Average microhardness of 5 measurement close to the surface of the as-deposited Fe-C coating and Fe-C coatings annealed at different times and temperatures.

7.2 Evolution of in-situ annealed Fe-C coatings

7.2.1 Manuscript VI

In-situ analysis of the thermal evolution of electrodeposited Fe-C coatings[11]

Jacob Obitsø Nielsen*, Thomas Lundin Christiansen, Karen Pantleon

Technical University of Denmark, Department of Mechanical Engineering, Produktionstorvet, building 425, DK – 2800 Kongens Lyngby, Denmark

*Corresponding author: jacobon@mek.dtu.dk, +45 60171310

Abstract

Fe-C coatings with a high amount of carbon were electrodeposited from an iron-sulfate electrolyte. Citric acid was used as an additive in the electrolyte, which not only served as carbon source during electrodeposition, but also caused the reproducible co-deposition of oxygen and hydrogen. The various co-deposited elements (C, O, H) result in a complex nature of the as-deposited coatings and allow for deliberate alterations of the coating properties by post-deposition annealing. The thermal evolution of electrodeposited Fe-C coatings was investigated *in-situ* during isochronal annealing. *In-situ* synchrotron diffraction analysis revealed temperature dependent phase transformations, and was supplemented with *in-situ* thermal analysis for investigating the evolution of co-deposited elements and associated mass changes during annealing. Based on the determined activation energies of identified thermal events, the underlying mechanisms are discussed. The results clearly indicate the role of co-deposited elements in the coatings and suggest that they partly exist in form of organic compounds, which decompose during annealing. In addition to revealing the thermal stability of the coatings and quantifying the coating's thermal evolution, the complementary methods of *in-situ* analysis considerably improved the understanding of the as-deposited Fe-C coatings – both are essential prerequisites for the successful application of the Fe-C coatings.

1. Introduction

The electrodeposition of iron and carbon (Fe-C) coatings implies a number of advantages for improving the hardness and wear resistance of surfaces. The deposition process is industrially feasible, it uses an inexpensive and environmental friendly electrolyte and Fe-C coatings can easily be deposited with thicknesses up to several hundreds of micrometers. Moreover, excellent mechanical properties are consistently reported for as-deposited Fe-C coatings [1-7]. In particular the ability of producing very hard coatings with microhardness values as high as for hardened steels makes the electrodeposited Fe-C coatings very attractive for various engineering applications where high hardness and good wear resistance are important. This entails both the dedicated electrodeposition of Fe-C coatings as a final process in the fabrication of components and the repair of worn or damaged surfaces by site-specific repeated deposition. In addition to the application of Fe-C coatings in their as-deposited state, a further potential for surface engineering is provided by the chemical nature of the coatings. The co-deposited carbon and other elements, like oxygen and hydrogen originating from the applied electrolyte, play a decisive role during post-deposition heat treatments, whereby the as-deposited microstructure can be deliberately altered [4,5,7-9]. Thermal treatment of the electrodeposited

---

[11] Under review in revised state in Acta Materialia since March 2020.

Fe-C coatings, which already in their as-deposited state are fairly hard with about 800 HV [6,7] is associated with a further hardness increase of up to 1300 HV after 24 h of isothermal annealing at 300 °C [7]. Hence, from an application point of view, the mechanical properties are very convincing and pave the way for a number of applications of Fe-C coatings. From a scientific point of view, thorough understanding of the as-deposited microstructure has hitherto not been obtained and despite good reproducibility of the electrodeposition process with consistent results in literature, the nature of as-deposited Fe-C coatings and the role of the co-deposited carbon are subject of different interpretations.

Previous studies of Fe-C coatings refer to an iron-sulfate electrolyte, which was optimized to resist the oxidation of Fe^{2+} to Fe^{3+} by the addition of a carboxylic acid that also act as a buffer, carbon source and complexing agent [5,10]. The composition and functional groups of the carboxylic acid have been found to influence the amount of co-deposited carbon, the morphology and the associated properties of the Fe-C coatings [2,3,5,11-14]. In addition, the applied electrodeposition conditions, like the cathode current density, the pH value and the temperature of the electrolyte [2,3,5,15], influence the current efficiency and, hence, the chemical composition, microstructure and properties of the as-deposited coatings. Typically, the electrodeposited Fe-C coatings contain high concentrations of carbon up to about 1 wt%. Such high amount of carbon considerably exceeds the solubility of carbon in iron at room temperature, which, typically for Fe-C alloys, suggests either the formation of iron carbides or the presence of carbon in supersaturated solid solution in the iron lattice. Previous investigations of electrodeposited Fe-C coatings by means of diffraction analysis consistently revealed the presence of one major phase in as-deposited coatings, which is interpreted either as ferrite (not containing carbon in thermodynamic equilibrium) [5-7,13] or as martensite (with carbon in supersaturated solid solution) [2,3,11,12,15]. The similarity of both lattices and the strong crystallographic texture of as-deposited Fe-C coatings complicate the phase analysis. The presence of a supersaturated solid solution would provide an immediate explanation for the location of carbon in the coatings, i.e. carbon would be interstitially dissolved. However, the very high measured carbon concentration would need to result in enormous changes of the iron lattice and this should cause either very broad and shifted diffraction peaks or asymmetric and even split diffraction peaks (apparently, both observations are reported). On the other hand, in case of ferrite without any carbon in its bcc lattice, the nature of the measured high amount of carbon would require the presence of a second phase in as-deposited Fe-C coatings. Indeed, diffraction analysis repeatedly revealed a second phase, but thorough phase identification is considerably hindered by the limited number of peaks; in addition to α-Fe, only one further peak is clearly evident [4-7] with only low diffracted intensities. As a consequence, phase analysis has not yet been unambiguous. As an attempt to clarify the location of the measured carbon, this second phase in the as-deposited Fe-C coatings has previously been explained as Fe_2C transition carbides [4,8,9], but alternative explanations including other co-deposited elements are possible [7]. The ambiguity of phase analysis based on the single additional peak, which consistently corresponds to a lattice spacing of $d = 0.237$ nm, is reflected in its present terminology as “nameless” peak referring to the not yet identified, “nameless”, phase in the as-deposited Fe-C coatings. A recent *ex-situ* isothermal annealing study revealed that this phase is present up to a temperature of about 300 °C [4,7,8]. Tracing the evolution of this phase by an *in-situ* annealing study and investigating the occurrence of further phase transformations is the purpose of the present work.

The thermal stability of Fe-C coatings with a high carbon content of 0.88±0.02 wt% is followed *in-situ* during isochronal annealing from room temperature to above the austenitization temperature. The occurring phase transformations are revealed by *in-situ* diffraction analysis and discussed in relation to the evolution of co-deposited elements and associated mass changes obtained from *in-situ* thermogravimetric analysis in combination with mass spectroscopy.

2. Method

2.1 Electrodeposition of Fe-C coatings

The electrolyte was prepared from chemicals of analytical grade with a concentration of 0.143 mol/dm^3 iron (II) sulfate heptahydrate, 6.2 x 10^{-3} mol/dm^3 citric acid monohydrate and deionized water. A 10 Liter electrolyte was used to minimize the change in chemical composition of the electrolyte during deposition. The electrolyte temperature was kept at 50 °C and mechanical stirring was applied during deposition. The pH-value of the electrolyte was controlled during deposition and maintained between 2.5 and 2.8 using a H_2SO_4-diluted solution. An interstitial-free steel plate was used as anode. The cathode consisted of a 10 x 9 cm low carbon steel plate covered with a conductive lead tape, such that deposition occurred both on lead and on the steel substrate simultaneously. The backside of the cathode was covered with an isolating electrolyte-resistant tape to ensure that only the side towards the anode was deposited. Prior to electrodeposition, the cathode was pre-treated by 2 min cathodic degreasing at 5 V followed by 2 min activation in commercial dry acid 629 SV from EngTech Scandinavia. Electrodeposition was carried out at a constant current density of 3.0 A/dm^2 applied for 15 hours resulting in 360 μm thick Fe-C coatings. The Fe-C coatings were immediately after deposition rinsed in water, then rinsed in ethanol and carefully dried to avoid oxidation. The Fe-C coatings were protected from any contact with oxidizing environments during storage.

The abovementioned design of the cathode ensured that multiple identical samples were obtained from the same deposition event, in which the substrate (lead or low carbon steel) is unimportant for the finally 360 μm thick Fe-C coatings, but allows to obtain dedicated samples for annealing. Due to low adhesion of the Fe-C coatings on the lead tape, the coating could easily be detached from the tape, thus providing free-standing coatings. They were used for *in-situ* thermal analysis, where it was essential to quantify the chemical species that evolved in the coating material. The Fe-C coatings on low carbon steel allowed better sample handling for *in-situ* diffraction analysis during annealing. The various sample pieces used for the present study were collected at least 1 cm away from the edge of the electrodeposited plate to avoid any potential edge effect from electrodeposition.

2.2 In-situ annealing experiments

2.2.1 Synchrotron diffraction

Energy-dispersive diffraction (EDD) was performed *in-situ* at the synchrotron facility BESSY II at the EDDI beamline. In EDD, a white X-ray beam with a continuous photon energy spectrum is used at a fixed diffraction angle 2θ, and diffraction occurs for crystallographic lattice planes with spacing d_{hkl} at a photon energy E_{hkl} according to [16]

$$E_{hkl} = \frac{h\,c}{2\sin\theta} \cdot \frac{1}{d_{hkl}}$$

where h is Planck's constant and c is the speed of light.

Compared to angle dispersive diffraction, the EDD mode has significant advantages, in particular for time- and/or temperature-resolved *in-situ* measurements. Complete diffraction patterns with a multitude of diffraction lines, E_{hkl}, are recorded simultaneously under fixed geometrical conditions, i.e. without scanning the 2θ angle. In addition, the very intense synchrotron radiation allows for short recording times for a complete diffraction pattern with good counting statistic. Owing to the different photon energies, the structural information contained in each diffraction line at the energy E_{hkl} has to be assigned to different average information depths [16]. For the applied symmetric diffraction geometry and a diffraction angle of $2\theta = 8°$, for example, the 211 reflection of iron corresponds to an information depth of about 67 μm.

In-situ annealing experiments during EDD analysis were performed in an Anton Paar DHS 1100 Domed Hot Stage under continuous flow of inert argon gas (99.999 mol% purity) at a constant pressure of 1.4 bar. Fe-C coatings on low carbon steel, were placed on the heating element (alumina plate) onto which they were mounted by mild clamping. The temperature was measured with a Pt-Pt10Rh thermocouple fixed to the stage. Isochronal annealing was performed from 30 °C to 800 °C using a heating rate of 2 K/min and an acquisition time of 30 seconds per EDD spectrum, resulting in a high resolution of one diffraction pattern per Kelvin. For qualitative phase analysis, the diffraction lines were fitted with pseudo-Voigt profile functions. A gold reference standard was used for calibration of the energy offset. The peak position was corrected for thermal expansion using the linear thermal expansion coefficient for ferrite of $\alpha = 15.1$ (10^{-6} K^{-1}), which was obtained for the present samples from their EDD spectra measured during cooling from 800 °C to room temperature after isochronal annealing.

2.2.2 Thermal analysis

Simultaneous thermogravimetry (TGA) and differential thermal analysis (DTA) were performed in a Netzsch STA 449F3 coupled with a Netzsch QMS 403 Aëolos quadrupole mass spectrometer (MS). The setup enables the detection and identification of evolved gases in time correlation with enthalpy and mass changes. For each measurement, a substrate-free coating weighing about 250 mg was placed in an alumina crucible. The sample chamber was pumped to vacuum and flushed with argon three times prior to each measurement. Heating was carried out in an inert atmosphere created by flowing argon gas (99.999 mol% purity) through the chamber with a rate of 30 mL/min.

A sample was subjected to three cycles of isochronal heating from 40 °C to 1000 °C using a heating rate of 2 K/min. Before the experiment and in between the sequential heating cycles, the sample was hold for 2 hours at 40 °C to ensure a stable and consistent environment. The cooling rate was set to 40 K/min. The applied heating sequences are illustrated in Figure 1. The first and second isochronal annealing were adjusted for instrumental background by using the second and third isochronal annealing, respectively.

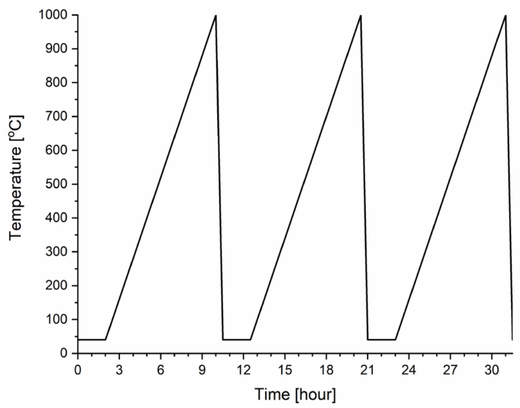

Figure 1: Subsequent heating cycles for isochronal annealing used for simultaneous thermogravimetry and differential thermal analysis coupled with a mass spectrometer.

From isochronal annealing experiments applying different heating rates, the activation energies for thermal events measured by DTA were evaluated by means of a Kissinger analysis applying different heating rates [17]. For each thermal event, the activation energy was determined from the slope of the straight line obtained by plotting $\ln(T^2_{f'}/\Phi)$ versus $1/T_{f'}$, where Φ corresponds to the applied constant heating rates of 2 K/min, 10 K/min, 20 K/min and 40 K/min, respectively. $T_{f'}$ corresponds to a fixed stage of transformation f' measured for the various heating rates. The values for $T_{f'}$ refer to the maxima of exothermic peaks, which were determined by fitting a Gaussian function to the background subtracted peaks.

3. Results

3.1 Diffraction analysis

In-situ diffraction analysis during isochronal annealing of an as-deposited Fe-C coating using a heating rate of 2 K/min revealed the as-deposited phases, along with the temperature induced phase transformations from room temperature to above the austenitization temperature. The acquired EDD spectra with high temperature resolution (one diffraction spectrum per Kelvin) are shown as a contour plot in Figure 2.

The as-deposited coating mainly consists of α-Fe (JCPDS 6-696). According to the strong <311> fiber texture of the as-deposited Fe-C coating [6], only the 110 and 211 reflections of α-iron are detected, while the 200 reflection is absent. The strain-free lattice spacings d_0 for the 110 and 211 reflections of α-Fe were determined for the as-deposited coating by tilting the sample around the strain-free direction ($\psi_0 = 41.16$ °), providing $d_{0\_110} = 0.20273$ nm and $d_{0\_211} = 0.11706$ nm, respectively. Both d-spacings match the corresponding values for carbon-free α-Fe (JCPDS 6-696 with $d_{110} = 0.20269$ nm and $d_{211} = 0.11702$ nm), which indicates that carbon-free bcc ferrite is present in the as-deposited coating. The measured peaks are broadened corresponding to the nanocrystalline nature of the coating, which previously has been quantified with an average crystallite size of 15-40 nm [7]. Apart from ferrite, only one additional peak is detected in the as-deposited coating, namely at 37.5 keV (cf. Figure 2). This peak corresponds to a d-spacing of 0.237 nm and has previously been reported from conventional laboratory X-ray diffraction phase analysis [4-6,8]. But, as mentioned above, no clear phase identification is possible based on that single peak only and, therefore, in the following, it is referred to as the "nameless phase".

During annealing, a sudden drop of the intensity of all peaks was observed at around 100 °C. After careful consideration and exclusion of any experimental reason for this intensity drop, the only explanation is a sudden change of the sample height (related to the occurring evolution of the coating with temperature, as discussed later in this manuscript) and accordingly, the sample was repositioned by adjusting the stage height. This is reflected in slight fluctuations of the diffracted intensities in Figure 2 until they stabilized at around 144°C. At that temperature, still only α-Fe and the "nameless phase" are present.

With continued heating, the formation of magnetite Fe_3O_4 (JCPDS 76-0957) is detected at about 259 °C and cementite Fe_3C (JCPDS 77-0255) forms at about 310 °C (cf. Figure 2). The formation of both phases confirms the presence of oxygen and carbon in the as-deposited coating, which are known to be co-deposited during electrochemical deposition [6], although the nature and location of these light elements in the as-deposited coatings could not be clarified yet. The formation of magnetite and cementite, as revealed during *in-situ* annealing in the present study, is consistent with previous *ex-situ* observations after isothermal furnace annealing of Fe-C coatings, where both phases were detected by synchrotron diffraction as well as selected area diffraction in the transmission electron microscope after *ex-situ* annealing [7].

With increasing temperature, the precipitation of magnetite and cementite proceeds as indicated by continuously increasing intensities of their corresponding diffraction peaks (cf. Figure 2). A remarkable change is observed at a temperature of 328 °C, which seems to be related to the transformation of the "nameless" phase. The intensity of its corresponding peak at 37.5 keV drops suddenly and the peak finally disappears, while at the same time a new peak develops near the original one. The partly overlapping intensities of the "nameless" peak and the new one cause some asymmetry of the measured peak profile. This hinders accurate peak fitting at this temperature and, therefore, the intensity decrease of the "nameless" peak and the corresponding transformation temperature of the "nameless phase" cannot be quantified precisely. In accordance with a further evolution of cementite Fe_3C, the newly arising peak certainly originates from Fe_3C. At about the same temperature of the disappearance of the single peak related to the "nameless phase", another observation from the diffraction results is of interest. Again, similarly as observed at about 100 °C as mentioned above, changes of the sample height and associated intensity changes of all peaks were recorded and required repositioning of the sample by readjusting the stage height (also this observation is related to the evolution of the coating and will be discussed together with results from the thermal analysis later in this manuscript).

At a temperature of about 571 °C, the transformation of Fe_3O_4 to wüstite FeO (JCPDS 77-2355) occurs (cf. Figure 2). Finally, at about 727 °C, the initial phase α-Fe ferrite transforms to γ-Fe austenite (JCPDS 31-0619) and, simultaneously, the peaks corresponding to Fe_3C drop in intensity, because carbides dissolve and carbon goes into solid solution in austenite. Peaks corresponding to FeO are still present above the austenitization temperature.

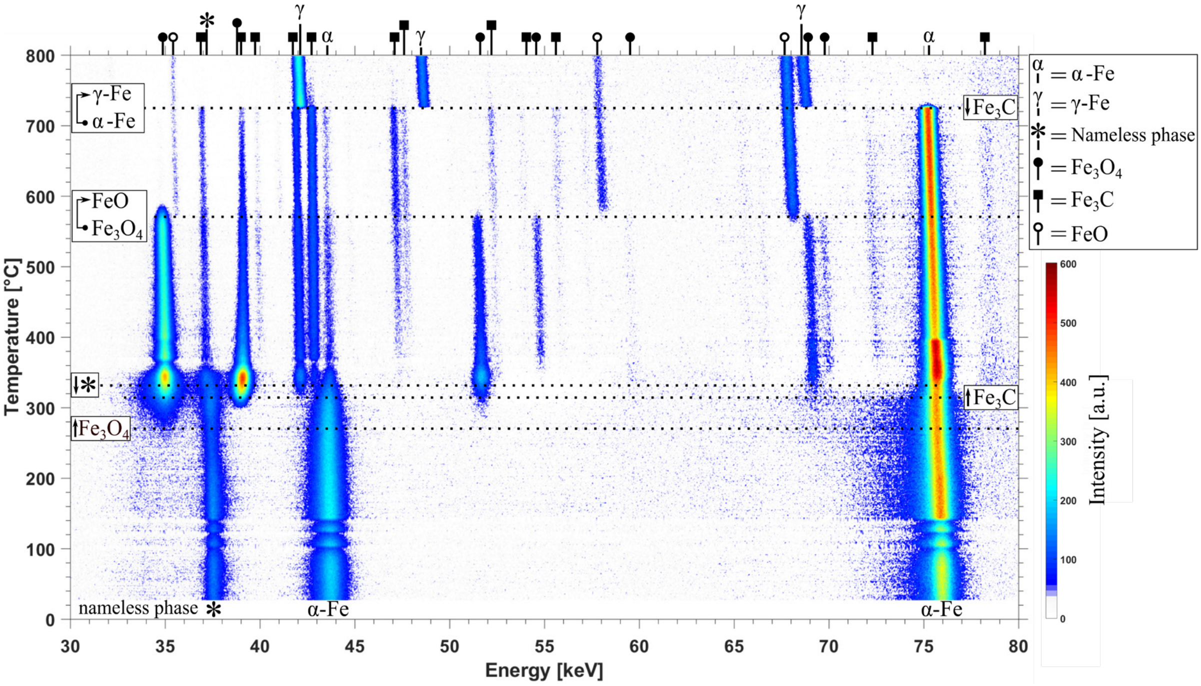

Figure 2: Synchrotron energy-dispersive diffraction spectra of in-situ annealing of an as-deposited Fe-C coating using a heating rate of 2 K/min from 30 to 800 °C.

3.2 Thermal analysis

3.2.1 Thermogravimetry, differential thermal analysis and mass spectrometry

The *in-situ* isochronal annealing by simultaneous DTA and TGA coupled with MS, using a heating rate of 2 K/min (i.e. the same as applied during *in-situ* diffraction analysis), revealed further information on the thermal stability of the as-deposited Fe-C coating. The results in Figure 3a and 3b correspond to the first annealing to 1000 °C and the subsequent annealing of the same sample to 1000 °C, respectively. The signals recorded by MS have been correlated to the individual elements using their ion mass. The measured species involved H_2^+, O_2^+ and CO_2^+ having a mass/charge ratio of 2 amu, 32 amu and 44 amu, respectively. Although the measurement was carried out in an inert Ar atmosphere, a low concentration of impurities in the gas such as O_2 and H_2 is seen as background in the beginning of the experiment. An increase in the DTA signal in Figure 3 relates to an exothermic reaction and a decrease indicates an endothermic reaction.

The first annealing cycle to 1000 °C (cf. Figure 3a) shows a mass loss just prior to an exothermic reaction at about 114 °C. The relatively low temperature and the increase in intensities of H_2 suggest that the reaction is related to dehydrogenation of absorbed hydrogen trapped in the as-deposited coating, which is a typical phenomenon during electrodeposition. This hydrogen originates from electrolysis at the cathode surface and results in a current efficiency of the deposition process below 100% (in fact, a current efficiency of only 60 % applies for the present deposition [7]). The simultaneous decrease in O_2 is likely related to its reaction with the desorbed H_2 from the sample and the corresponding formation of H_2O before reaching the MS detector. Energy is removed from the system in the temperature range following the exothermic reaction at 114 °C, which is interpreted as hydrogen desorption.

At around 250 °C an increase in CO_2 is detected, but at this temperature neither the DTA signal nor the mass loss gradient change.

At 310 °C a relatively small exothermic peak is measured and directly followed by a more pronounced exothermic peak of much higher intensity with a maximum at 360 °C. These exothermic reactions are accompanied by a small increase in O_2 and CO_2 at around 340 °C along with a change in the mass loss gradient. Simultaneously, the intensity of H_2 increases significantly and reveals a maximum at 375 °C. The associated desorption of hydrogen continues until a temperature of around 436 °C is reached. Energy is removed from the system in the temperature range following the exothermic reaction at 360 °C, which is interpreted as hydrogen desorption.

A relatively small exothermic peak is measured at 505 °C, without a notable change in the TGA or MS signals. An endothermic peak at 570 °C indicates the phase transformation of Fe_3O_4 to FeO, in accordance with diffraction analysis (cf. Figure 2). At the same temperature, a change in intensity for CO_2 is measured, along with an increased mass loss, which is related to decarburization. At 705 °C a small peak in the CO_2 intensity is measured, which is followed by a pronounced endothermic peak at 725 °C corresponding to the austenitization temperature, thus, the transformation of α-Fe ferrite to γ-Fe austenite, as also detected by diffraction analysis at that temperature.

The second heating cycle to 1000 °C (cf. Figure 3b) reveals an exothermic peak at 295 °C and endothermic peaks at 585 °C and 725 °C corresponding to the phase transformation of FeO (which is still present after the first heating cycle) to Fe_3O_4, the phase transformation of Fe_3O_4 to FeO and the formation of austenite, respectively. There is no apparent mass change, before decarburization is measured by an increased intensity for CO_2 at around 590 °C.

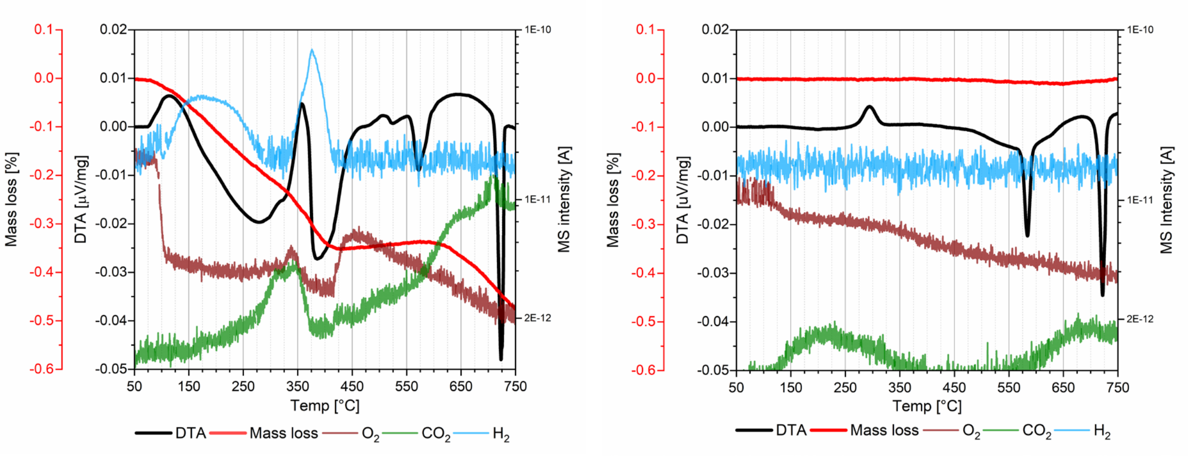

(a) (b)

Figure 3: Simultaneous thermogravimetry, differential thermal analysis and mass spectrometry to detect and identify thermal events, in correlation to the evaporated gases. The black left axis corresponds to the DTA signal and the red left axis corresponds to the measured mass loss. The right axis corresponds to the various desorbed gasses measured by MS. Figure 3a refers to the first annealing cycle and Figure 3b reflects the second annealing cycle of the same coating. The applied heating rate corresponds to 2 K/min.

3.2.2 Determination of activation energies

Applying different heating rates for isochronal annealing of as-deposited Fe-C coatings (similar to the example shown for 2 K/min in Figure 3a), three separate thermal events are recorded as exothermic peaks by DTA in the temperature range up to 500 °C, which is shown in Figure 4a. The heating rate affects both the temperatures of the occurring thermal events and their corresponding intensities in the DTA curves: with increasing heating rate, the peak temperature and the recorded intensities increase. The corresponding Kissinger plot in Figure 4b provides the activation energies of the three thermal events. The relatively small exothermic peak measured at 310 °C for 2 K/min (and correspondingly higher temperatures for increased heating rates, cf. Figure 4a) is not included in the Kissinger analysis as it overlaps with the exothermic peak of much higher intensity, which hinders an accurate peak fit. The thermal events relate to the desorbed gasses measured by MS, as explained below.

The first thermal event (at around 114 °C for $\Phi = 2$ K/min) corresponds to dehydrogenation, where the co-deposited hydrogen originating from electrolysis at the cathode surface (see above) is released from the sample. The calculated activation energy of this first thermal event amounts to 40 kJ/mol.

The second thermal event is indicated by an exothermic peak (at around 284 °C for $\Phi = 10$ K/min) and corresponds to an activation energy of 98 kJ/mol. For the low heating rate of 2 K/min the second thermal event cannot be verified experimentally due to too low peak intensity (cf. Figure 4a) and therefore it cannot be related to the desorbed elements according to Figure 3a.

The third thermal event (at 360 °C for $\Phi = 2$K/min) was clearly detected by its exothermic peak for all heating rates and corresponds to an activation energy of 151 kJ/mol. This event is characterized as a thermal decomposition, which relates to a mass loss, enthalphy change and the release of H_2 (cf. Figure 3a). Furthermore, the increased intensities of O_2 and CO_2 measured at 340 °C (cf. Figure 3a) suggest that also carbon and oxygen are released during this third thermal event.

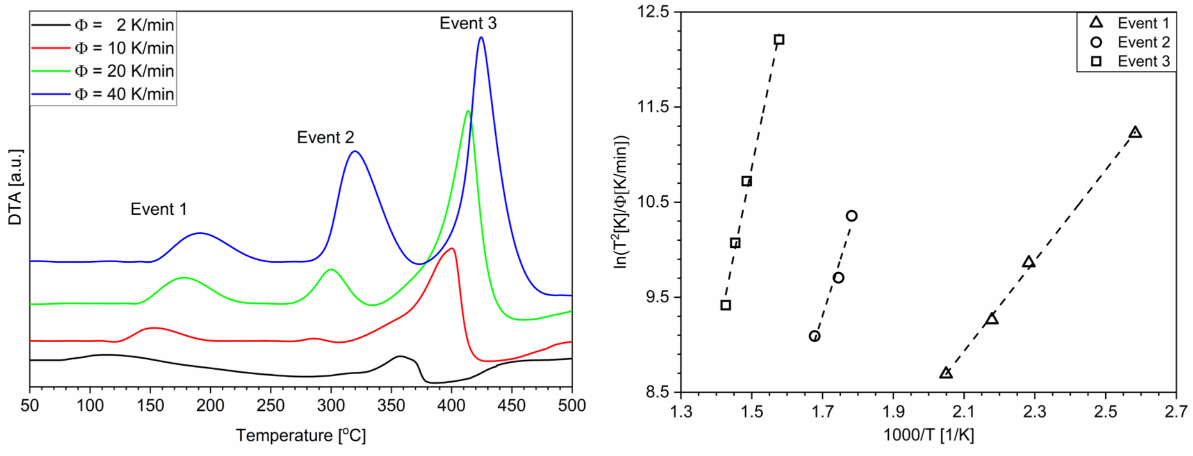

(a) (b)

Figure 4: Isochronal Kissinger analysis (a) differential thermal analysis during isochronal annealing of an as-deposited sample applying heating rates of 2, 10, 20 and 40 K/min (b) Kissinger plot for different thermal events measured for isochronal annealing with heating rates of 2, 10, 20 and 40 K/min.

4. Discussion

For the present samples, carbon-free ferrite is clearly detected as the major phase in as-deposited coatings, but XRD also indicates an additional crystalline phase, which cannot be identified from the measured single peak and therefore, so far, is called the “nameless phase”. As an approach to discover the nature of this phase, synchrotron diffraction has been carried out also in transmission and under various sample tilts and rotations (not shown here), but no additional reflections could be revealed. The applied *in-situ* analysis during isochronal annealing by means of energy-dispersive synchrotron diffraction allows tracing the occurring phase transformations with an excellent temperature resolution. Although such *in-situ* diffraction analysis provides the thermal stability of the electrodeposited Fe-C coatings and supports an interpretation of the as-deposited nature of the coatings, in fact, it only can detect crystalline phases. The combination of *in-situ* diffraction analysis with *in-situ* thermal analysis for the same as-deposited Fe-C coatings, as in the present work, supports the interpretation by cross-linking with the temperature-dependent evolution of co-deposited elements (carbon, oxygen, hydrogen) during annealing. The complementary results obtained from both methods of *in-situ* analysis allow the following interpretation of the thermal stability of Fe-C coatings and also give an improved understanding of the as-deposited Fe-C coatings, as discussed below. The specific temperatures stated in the discussion refer to the data obtained for in-situ isochronal annealing experiments using a heating rate of 2 K/min unless otherwise noted.

4.1 Low temperature range – below 200 °C

Already at a relatively low temperature of about 114 °C, co-deposited hydrogen desorbs from the coating (cf. Figure 3a). This confirms that hydrogen indeed is present in as-deposited coatings, which previously has been suggested from chemical analysis (although hydrogen could not be quantified [6,7]) and is reflected in a low current efficiency of only 60.5 % for the applied deposition process. The determined activation energy of 40 kJ/mol for this first thermal event indicates that this hydrogen, which originates from electrolysis at the cathode during deposition, has been trapped in either microvoids or grain boundaries, for which trap activation energies for hydrogen evolution of 35.15 kJ/mol or 17.2 kJ/mol [18], respectively, are reported for pure iron. The nanocrystalline microstructure of the as-deposited Fe-C coating [6,7] provides a high number of grain boundaries for trapping and the reported temperature of hydrogen evolution from grain boundaries (105 °C for a heating rate of 3.06 K/min [18]) agrees well with the present observation of dehydrogenation.

Diffraction analysis did not immediately indicate this first thermal event of dehydrogenation, because no phase transformations are detected and still only ferrite and the nameless phase are present (cf. Figure 2) at these low temperatures. However, the observation of a sudden change in the sample height, reflected by sudden intensity changes and the need of readjusting the sample as described above, clearly relates to the release of hydrogen.

In earlier studies of Fe-C coatings [4,9], the exothermic reaction, which clearly relates to dehydrogenation as described above, was also observed, but it was interpreted as the first stage of tempering martensite, where carbon atoms are redistributed resulting in carbon segregation and clustering in an apparent martensite matrix. Although the temperature is similar to the first step of tempering martensite, the release of hydrogen at that temperature as observed in the present work and the missing indication of martensite in the as-deposited coating exclude that the exothermic peak is caused by a redistribution or clustering of carbon. Furthermore, the activation energy for carbon clustering is reported to be significantly higher with about 80 kJ/mol [19].

In conclusion, the present *in-situ* analysis confirms that the Fe-C coatings remain fairly stable up to a temperature of 200 °C, because only some release of the loosely bound hydrogen occurs without other changes of the chemical composition and phase constitution of the Fe-C coatings. This explains previous observations from *ex-situ* annealing studies, which revealed that the microhardness after annealing at 200 °C still was as high as after deposition [5,8] or even slightly increased for longer isothermal holding at 200 °C [7], which also contradict the interpretation of tempering martensite [4,9]. Consequently, the internal structure of the coatings at 200 °C still corresponds to their deposition-related characteristics, which causes the excellent hardness of the Fe-C coatings.

4.2 Medium temperature range – between 200 °C and 380 °C

After co-deposited hydrogen from electrolysis during deposition is released (first thermal event), subsequent chemical changes imply the desorption of CO_2 at a temperature of about 250 °C (cf. Figure 3a), which indicates the second thermal event. At the same temperature of 250 °C, a previous study on the same as-deposited Fe-C coatings, which however were investigated by *in-situ* isochronal annealing after preceding *ex-situ* isothermal furnace annealing [7], revealed a characteristic desorption of hydrogen. This desorption of hydrogen at 250 °C is clearly not related to the hydrogen from electrolysis, which was already released during the *ex-situ* isothermal annealing. The present *in-situ* analysis could not detect the characteristic desorption of hydrogen at 250 °C as part of the second thermal event, due to the ongoing desorption from the first thermal event and a corresponding broad peak of hydrogen evolution in a wide temperature range (cf. Figure 3a). Although the temperature of the second thermal event could not be experimentally determined for a heating rate of 2 K/min (cf. Figure 4a), linear regression from the three measured values at higher heating rates (cf. Figure 4b) allowed to calculate the corresponding temperature to amount 250 °C and the recorded signals for H_2 and CO_2 support that (cf. Figure 3a). The detected desorption of both CO_2 and H_2 associated with the second thermal event suggest a relation between hydrogen, oxygen and carbon in the as-deposited coating. The observation that hydrogen still evolves at this temperature indicates that the element is not just present as trapped atoms or molecules in microvoids or grain boundaries (as described above for hydrogen from electrolysis, released in the first thermal event), but additionally constitutes a phase in the as-deposited coating, which is stable up to higher temperature.

All the elements involved in the second thermal event are provided by the citric acid in the electrolyte, which seems to promote the incorporation of an organic compound consisting of carbon, oxygen and hydrogen during electrodeposition, which decomposes at 250 °C. A previous study on as-deposited Fe-C coatings revealed by photoelectron spectroscopy that carbon is bound to both hydrogen and oxygen and found that an organic compound is incorporated in the coating in the form of (COOH) [8]. With EDD, this organic phase is not revealed, indicating that it either is not crystalline or of too low volume fraction for measureable diffracted intensities and therefore the present study does not allow an interpretation of the chemical structure of the organic compound. However, the precipitation of magnetite and cementite is a consequence of the decomposition of the organic compound and identified by the *in-situ* diffraction analysis in the corresponding temperature range. The first presence of an oxide phase, namely magnetite Fe_3O_4, is revealed by diffraction analysis at a temperature of 259 °C, hereafter it evolves with increasing temperature. The slow growth rate of magnetite during heating with 2 K/min, as indicated in Figure 2 by the slowly evolving diffraction intensities for the Fe_3O_4 reflection around 34.8 keV at temperatures below 320 °C, could explain the absence of an exothermic peak in DTA for this low heating rate. Together with oxygen used for the formation of oxides, also carbon is provided by the decomposition of the organic compound in the second thermal event and results in the formation of carbides as Fe_3C at 310 °C (cf. Figure 2). A relatively small exothermic peak is measured around 310 °C in the first heating cycle to 1000 °C by DTA as a shoulder of the exothermic peak related to the third thermal event at 360 °C (cf. Figure 3a) and suggests a relation the Fe_3C formation. The proceeding formation of oxides and carbides results in a microhardness increase of the Fe-C coatings during annealing in the here considered temperature range [5,7,8], with a particular increase observed above 250 °C [7] where the organic phase decomposes. Despite the general difficulty to relate the occurring phase transformations, as revealed by the present *in-situ* isochronal annealing study, to the microstructure and hardness of the coatings, as observed after *ex-situ* isothermal annealing at various temperatures, the results indicate several influences on the hardness of the annealed Fe-C coatings. In addition to the newly formed oxides and carbides, which are fine dispersed within the annealed coating [7], the ferrite phase still consists of nanocrystalline grains even at temperatures above 250 °C (cf. [7], further details will be published elsewhere), and, together with the still present "nameless phase", determine the hardness of the coatings.

It is noted that the "nameless phase", which previously was considered an explanation for the location of the measured high concentration of carbon in the as-deposited coatings [4,8,9], still is present at 250 °C (cf. Figure 2). A previous study further revealed that the as-deposited "nameless phase" is still present even after *ex-situ* isothermal annealing for 24 h at 250 °C, thus, it does not decompose with the second thermal event [7] and is not responsible for the formation of magnetite and cementite at this temperature. From the present *in-situ* study it is known that the "nameless phase" remains stable up to a temperature of 328 °C.

Although missing a clear experimental verification, it has been suggested previously that ε/η-Fe_2C transition carbides could be present as minor phase in the otherwise ferritic as-deposited Fe-C coatings [4,8,9], because they would explain the "nameless phase", although the similarity of the two possible carbides, ε-Fe_2C and η-Fe_2C [20,21], does not allow their distinction from the present data. Assuming meta-stable ε/η-Fe_2C in the as-deposited coating, a transformation to Fe_3C would be expected during annealing. The reported enthalpy change and the temperature range of 260 °C to 350 °C for that transformation would be associated with an activation energy of 200 kJ/mol [19]. For the present Fe-C coatings, such transformation is not indicated by the second thermal event having a much lower activation energy of 98 kJ/mol. The third thermal event, which occurs at a temperature of 360 °C with an activation energy of 151 kJ/mol is associated with a mass loss and desorption of at least hydrogen (cf. Figure 3a). This rejects that it is related to the transformation of Fe_2C to Fe_3C and, thus, questions the presence of Fe_2C at all.

The complementary results from *in-situ* diffraction analysis and thermal analysis indicate that the disappearance of the "nameless phase" at about 328 °C (cf. Figure 2) is related to the third thermal event, which is recorded by a strong exothermic peak with a temperature maximum at 360 °C. The pronounced release of hydrogen strongly suggests that hydrogen is included in the "nameless phase". This evolution of hydrogen marks the decomposition of the "nameless phase" and, at the same time, explains the abovementioned observation of the sudden change in the sample height during *in-situ* diffraction analysis in that temperature range (similar to the sample height changes at low temperature in relation to dehydrogenation during the first thermal event, see above). In addition to hydrogen, to a lesser extent also O_2 and CO_2 evolve during the third thermal event (cf. Figure 3a), which suggests also oxygen and/or carbon as elements in the "nameless phase". The simultaneous desorption of hydrogen and oxygen indicates that it originates from the family of hydroxides, e.g. ferrihydrite as previously suggested [7]. Ferrihydrite is reported as being nanocrystalline with an average domain size of around 2.7 nm and poor crystallinity [22-24]. The formation of ferrihydrite is known to be favored [25], compared to the more stable iron oxides as hematite Fe_2O_3 or goethite α-FeOOH, in an environment of organic molecules and a high supply of iron. Both of these factors are valid at the coating/electrolyte interface during deposition of the present Fe-C coating and the formation of metal hydroxides during electrodeposition of different coatings is well known [26]. Although the majority of the electrolyte consists of Fe-ions in their oxidation state Fe^{2+}, the presence of Fe^{3+} being required for the formation of ferrihydrite is likely due to the thermodynamically favored oxidation reaction of Fe^{2+} to Fe^{3+} in air. The hexagonal crystal structure of ferrihydrite would even explain some low intensity peaks causing an asymmetry for the 211 α-Fe peak, as previously reported from conventional laboratory XRD [6]. Ferrihydrite has strong adsorptive capacity and a large surface area that acts as a sink for organic matter [24], which makes the sorption of also carbon-containing species at the surface of ferrihydrite likely and explains that the evolution of all the co-deposited elements (hydrogen oxygen, carbon) is recorded during the third thermal event, thus, with the decomposition of the "nameless phase". The transformation of ferrihydrite into either magnetite or hematite, depends on the environment and access to oxygen [27]. A distinct exothermic peak maximum was reported [27] at about 360 °C as the thermal transformation of ferrihydrite into magnetite, and an additional transformation can occur at 505 °C [27], both fit well with the present data. The transformation of ferrihydrite is expected to be non-reversible and it is indeed not observed in the second heating cycle of the Fe-C coating. The corresponding introduction of a name for the yet "nameless phase" certainly is premature and its experimental verification as carbon-associated ferrihydrite is ongoing.

4.3 High temperature range – above 380 °C

After dehydrogenation of hydrogen from electrolysis (first thermal event) and the release of co-deposited carbon, oxygen and hydrogen by decomposition of both an organic phase (second thermal event) and the "nameless phase" (third thermal event), the ferrite phase is still present, while magnetite and cementite have formed additionally.

A transformation of Fe_3O_4 to FeO was consistently revealed by both diffraction and thermal analysis at a temperature of 570 °C, which fully agrees with thermodynamics. Diffraction analysis at room temperature of a previously annealed sample (not shown here) revealed that FeO still is present after cooling, which is promoted by a rapid cooling rate [28]. This explains the exothermic peak at 295 °C in the second heating cycle shown in Figure 3b as a transformation of still present FeO into Fe_3O_4, which then again transforms to FeO at higher temperature (interestingly, the second heating cycle, Figure 3b, indicates a temperature of 585 °C, compared to 570 °C in the first heating cycle, Figure 3a).

The austenitization temperature measured by DTA and EDD is in good agreement with the theoretical value of 727 °C for iron-carbon alloys in thermodynamic equilibrium. The diffraction analysis revealed an immediate transformation from α-Fe to γ-Fe without a measurable co-existence of both phases, which verifies that the actual carbon content of 0.88 wt% in the Fe-C coatings is close to the eutectoid concentration of 0.76 wt% for Fe-C alloys. The transformation of α-Fe into γ-Fe occurs at the same temperature in the second heating cycle to 1000 °C as measured by DTA (cf. Figure 3b).

5. Conclusion

The thermal evolution of electrodeposited Fe-C coatings was investigated systematically during isochronal annealing up to 800 °C by means of complementary methods of *in-situ* analysis. With *in-situ* energy-dispersive synchrotron diffraction, the crystalline phases in the as-deposited coating and the temperature-induced phase transformations were revealed with unique temperature resolution. With *in-situ* thermal analysis under the same isochronal annealing conditions, the evolution of co-deposited elements and associated mass changes were followed, and this supported the interpretation of the diffraction data and further allowed conclusions on non-crystalline phases. The complementary information from both *in-situ* methods essentially enhanced the understanding of both the as-deposited nature of the Fe-C coatings and their thermal stability.

As-deposited Fe-C coatings consist of i) ferrite, ii) a crystalline phase, possibly containing hydrogen, oxygen and iron (previously called the “nameless phase”), iii) a phase containing carbon and most likely also hydrogen and oxygen either being amorphous or constituting a low amount of a crystalline phase and iv) free hydrogen in atomic or molecular form. During annealing, already at low temperature (about 114 °C), the free hydrogen is released from the sample (first thermal event). At about 250 °C (second thermal event), again dehydrogenation occurs, but at the same time also oxygen and carbon redistribute and/or leave the sample, which indicates the decomposition of a phase containing all co-deposited light elements originating from the citric acid used as additive in the electrolyte. At this temperature, the crystalline “nameless” phase still remains unchanged, but decomposes at about 328 °C (third thermal event) with an associated release of hydrogen and carbon and oxygen from that phase, which subsequently form oxides and carbides at higher annealing temperatures.

The results highlight the essential role of the light elements carbon, oxygen and hydrogen, which are co-deposited together with iron. All these elements, thus, not only the intendedly co-deposited carbon, define the as-deposited state of the Fe-C coatings and rule their overall thermal evolution as well as the associated mechanical properties. The observed temperature-dependent changes provide a useful guide for dedicated post-deposition annealing treatments towards deliberate alterations of the internal structure and associated properties of electrodeposited Fe-C coatings.

Acknowledgments

The authors kindly acknowledge financial support by OCAS NV, ArcelorMittal Global R&D Gent (Belgium), a. h. nichro Haardchrom (Denmark) and Fast Track - Societal Partnership (Denmark), funded by the Innovation Fund Denmark (IFD).

M. Klaus, D. Apel, and C. Genzel from Helmholtz Zentrum für Materialien und Energie (HZME, Germany) are acknowledged for their valuable support during beamtime at the HZB-BESSY II Synchrotron Facility and during subsequent data analysis. Synchrotron diffraction measurements were financially supported by the project CALIPSOplus under the Grant Agreement 730872 from the EU Framework Programme for Research and Innovation HORIZON 2020, and by the Danish Natural Science Research Council via Danscatt.

Literature

[1] M. Izaki, H. Enomoto, T. Omi, Hardness and Carbon Content of Fe Electroplate from Sulfate Bath Containing l-Ascorbic Acid and Citric Acid, J. Surf. Fin. Soc. Jpn. 40 (1989) 1304–05.

[2] Y. Fujiwara, T. Nagayama, A. Nakae, M. Izaki, H. Enomoto, E. Yamauchi, Electrodeposition of Fe-C Alloys from Baths Containing Dicarboxylic Acids with a Linear Alkyl Chain, J. Electrochem. Soc. 143 (1996) 2584–2590.

[3] M. Panayotova, Deposition of Fe–C alloy on structural steel and cast iron for repair of worn machine parts, Surf. Coat. Technol. 124 (2000) 266–271.

[4] A.S.M.A. Haseeb, Y. Hayashi, M. Masuda, M. Arita, On the nature of the electrochemically synthesized hard Fe-0.96 mass pct C alloy film, Metall. Mater. Trans. B. 33B (2002) 921–927.

[5] T. Müller, J. Grimwood, A. Bachmaier, R. Pippan, Electrodeposition of Fe-C alloys from citrate baths: Structure, mechanical properties, and thermal stability, Metals. 8 (2018) 1–13.

[6] J.O. Nielsen, P. Møller, K. Pantleon, Electrodeposition of Iron with Co-deposition of Carbon: On the Nature of Nanocrystalline Fe-C Coatings, Metall. Mater. Trans. A. 50A (2019) 3785–3793.

[7] J.O. Nielsen, K. Pantleon, Evolution of hard Fe–C electrodeposits with temperature, Surf. Eng. (2019), in press. Published online in October 2019.

[8] M. Izaki, H. Enomoto, A. Nakae, S. Terada, Y. Eiko, T. Omi, Phase Transformations and Hardness Changes in Electrodeposited Alloy Films Iron-carbon alloy films., J. Surf- Fin. Soc. Jpn. 45 (1994) 1303–1309.

[9] A.S.M.A. Haseeb, M. Arita, Y. Hayashi, Thermal decomposition study of electrodeposited Fe-C and Fe-Ni-C alloys by differential scanning calorimetry, J. Mater. Sci. 6 (2001) 4739–4743.

[10] M. Schlesinger, M. Paunovic, Electrodeposition of Iron and Iron Alloys, in: Mod. Electroplat., 5th ed., Wiley, 2010: pp. 309–326.

[11] Y. Fujiwara, M. Izaki, H. Enomoto, A. Nakae, Effects of Hydroxycarboxylic Acids on the Electrodeposition of Fe-C Alloys, Denki Kagaku. 7 (1993) 840–842.

[12] A.S.M.A. Haseeb, M.Z. Huq, Electrodeposition of martensitic iron-carbon alloy coatings at room temperature, Met. Finish. 95 (1997) 30–34.

[13] N. Fukumuro, S. Kojima, M. Fujino, Y. Mizuta, T. Maruo, S. Yae, Y. Fukai, Hydrogen-Induced superabundant vacancies in electrodeposited Fe-C alloy films, J. Alloys Compd. 645 (2015) 404–407.

[14] Y. Fujiwara, M. Izaki, H. Enomoto, T. Nagayama, E. Yamauchi, A. Nakae, Optimization of bath composition for hard Fe-C alloy plating, J. Appl. Electrochem. 28 (1998) 855–862.

[15] M. Izaki, T. Omi, Structural characterization of martensitic iron-carbon alloy films electrodeposited from an iron(ll) sulfate solution, Metall. Mater. Trans. A. 27A (1996)

483–486.

[16] C. Genzel, I. A. Denks, J. Gibmeier, M. Klaus, G. Wagener, The materials science synchrotron beamline EDDI for energy-dispersive diffraction analysis, Nucl. Instruments Methods Phys. Res. A. 578 (2007) 23–33.

[17] E.J. Mittemeijer, Review Analysis of the kinetics of phase transformations, J. Mater. Sci. 27 (1992) 3977–3987.

[18] W.Y. Choo, J.Y. Lee, Thermal Analysis of Trapped Hydrogen in Pure Iron, Metall. Trans. A. 13A (1982) 135–140.

[19] L. Cheng, C.M. Brakman, B.M. Korevaar, E.J. Mittemeijer, The Tempering of Iron-Carbon Martensite; Dilatometric and Calorimetric Analysis, Metall. Trans. A. 19A (1988) 2415–2426.

[20] H.K.D.H. Bhadeshia, Carbide precipitation, in: Bainite Steels Theory Pract., 3rd ed., Maney Publishing, 2015: pp. 61–86.

[21] H.L. Yakel, Crystal structures of stable and metastable iron-containing carbides, Int. Met. Rev. 30 (1985) 17–40.

[22] U. Schwertmann, W.R. Fischer, Natural “amorphous” ferric hydroxide, Geoderma. 10 (1973) 237–247.

[23] E. Jansen, A. Kyek, W. Schäfer, U. Schwertmann, The structure of six-line ferrihydrite, Appl. Phys. A. 74 (2002) 1004–1006.

[24] S. Das, M.J. Hendry, J. Essilfie-Dughan, Transformation of two-line ferrihydrite to goethite and hematite as a function of pH and temperature, Environ. Sci. Technol. 45 (2011) 268–275.

[25] R.M. Cornell, U. Schewertmann, Soils, in: Iron Oxides Struct. Prop. React. Occur. Uses., 2nd ed., Wiley, 2003: pp. 433–468.

[26] M. Panunovic, M. Schlesinger, Fundamentals of Electrochemical Deposition, Wiley, 2006.

[27] A.S. Campbell, U. Schwertmann, P.A. Campbell, Formation of cubic phases on ferrihydrite heating, Clay Miner. 32 (1997) 615–622.

[28] X. Yu, Z. Jiang, J. Zhao, D. Wei, C. Zhou, Effect of cooling rate on oxidation behaviour of microalloyed steel, Appl. Mech. Mater. 395–396 (2013) 273–278.

7.2.2 Supplementary material for the in-situ annealing analysis

7.2.2.1 Chemical analysis for oxygen and hydrogen

The co-deposited hydrogen trapped at possible trapping sites (grain boundaries, dislocations, and microvoids) was quantified using the mass loss measured by TGA after isothermal annealing at low temperature in an inert atmosphere. The experiment was continued to estimate the amount of co-deposited oxygen using the TGA with a reducing H_2 atmosphere, high temperatures and a long duration.

Experimental setup

The following experimental setup was used: A substrate-free sample was used, which was obtained from the same deposition as described in Manuscript VI. The measurement was conducted using simultaneous TGA and DTA in a Netzsch STA 449F3 coupled with a Netzsch QMS 403 Aëolos quadrupole mass spectrometer.

A combination of in-situ isothermal and isochronal annealing was used for the chemical analysis using the stepwise procedure as described below: The sample was

1. hold for 2 hours at 40 °C to measure the precise weight of the sample, in Ar.
2. hold for 10 hours at 180 °C to dehydrogenate the sample, in Ar.
3. hold for 2 hours at 40 °C to measure the precise weight of the sample after dehydrogenation, in Ar.
4. hold for 1 hour at 400 °C for the phase transformation of the nameless phase to occur[12], in Ar.
5. hold for 2 hours at 40 °C to measure the precise weight after the transformation of the nameless phase, in Ar.
6. hold for 18 hours at 1080 °C to reduce carbon and oxygen, in H_2.
7. hold for 90 hours at 1000 °C to reduce carbon and oxygen, in H_2.
8. hold for 2 hours at 40 °C to measure the precise weight after reduction, in Ar.
9. isochronal annealed to 800 °C using a heating rate of 20 K/min to investigate if the phase transformation for magnetite to wüstite is measured at 580 °C, in Ar

Results

The results of the chemical analysis are shown in Table 12. The content of hydrogen originating from electrolysis of water was determined in step 2 to 0.14 wt%. The transformation of the "nameless phase" during step 4 resulted in a weight loss of 0.48 g from the desorption of hydrogen, carbon and oxygen. The calculated oxygen content of 3.9 wt% assumes that the carbon content of the sample is 0.88 wt% (Manuscript I) and does not include the weight loss during step 4. The phase transformation for magnetite to wüstite was measured during step 9 and revealed that not all the co-deposited oxygen has been removed from the sample during step 6 and 7.

---

[12] The thermal event is discussed in Manuscript V and VI

*Table 12: Results from the chemical analysis using TGA to estimate the content of hydrogen and oxygen in the Fe-C coating. Notes: *

Step	Total mass [g]	Mass loss [g]	Desorbed elements	Weight percentage [wt%]
1	268.18	0		
2	267.82	-0.36	Hydrogen	0.14
4	267.34	-0.48	Hydrogen, carbon, and oxygen	0.18[1]
6-7	254.52	-10.45	Oxygen	3.9[2]
		-2.36	Carbon	0.88[3]

Discussion and conclusion

The results show that the hydrogen content of 0.14 wt% and the oxygen content of 3.9 wt% in the as-deposited Fe-C coating are considerably higher compared to the values for the hydrogen content between 0.0015 to 0.014 wt% and oxygen content between 0.5 and 1.2 wt% that have been published in prior studies [17,24] and were discussed in Section 2.3.1.2. The operation conditions for the deposition of the Fe-C coatings were different and could results in different quantities for the co-deposited elements.

The large amount of hydrogen being co-deposited introduces a risk of hydrogen embrittlement during operation and can result in coating failure under mechanical loading. It is therefore recommend annealing the deposited sample at 100 °C for 24 hours after deposition to desorb the co-deposited hydrogen.

7.2.2.2 The change of sample height during annealing

The in-situ isochronal annealing EDD measurement as descirbed in Manuscript VI required repositioning of the sample during the measurement, which became obvious based on the recorded diffraction intensities. In general, there are some phenomena that could be associated with intensity changes, e.g. an increase in the intensity of the primary beam, evolution of crystallographic texture or a change in sample position. Changes of the beam intensity can be excluded, because the beam current is registered and remained stable throughout the experiment. Although texture may be affected by annealing, it cannot explain the present observation that all peaks of all phases increase in a similar manner before they return to their original intensity. Excluding all experimental influences and having reproduced that observation several times with various samples, the only explanation of the sudden intensity increase and later decrease is a change of the sample height. Although the sample was fixed by clamping, during annealing it must have move upwards, and that occured reproducible in the same temperature range, and subsequently, the sample moved back to its original position; both is associated with intensity changes because the sample moves out of focus.

Experimental setup

The change in sample height during in-situ isochronal annealing was measured with a heating rate of 8 K/min and a scattering angle of 2θ = 8°. The stage height (z) is cycled during the experiment from a relative position at 0 µm to 50 µm using a distance of 5 µm per step and an acquisition time of 1 second per step during the experiment. The relative stage height (z) is set in such a way that within each cycle the sample is moved into the beam and intensity is measured. The resolution of each loop amounts to 2.66 Kelvin per cycle. To adjust for background intensity, the sum of intensity for the first measured spectrum within a cycle is subtracted from the sum of intensity of each spectrum within a cycle. When the sample is below the beam and only background is measured the intensity will be close to zero and when the sample is moved into the beam a much higher intensity will be measured. The intensity is thereby directly related to the position of the samples surface.

Result and conclusion

The in-situ annealing experiment was performed to varify and quantify the change in sample height during annealing and the result is shown in Figure 55. Starting at around 390 °C, the sample increases in height by 20 µm and returns to its initial height when the temperature reached 520 °C. The higher initial and final temperatures compared to the values found Manuscript VI can be assigned to the higher heating rate of 8 K/min used for this experiment. The increase of 20 µm corresponds to an increase in sample height of 5.5%. The reproducibility of the event indicates that it is related to temperature-dependent changes in the coating being the transformation of the “nameless phase”. It is not fully understood how the transformation of the “nameless phase” can results in this change in sample height other than it is related to the release of hydrogen.

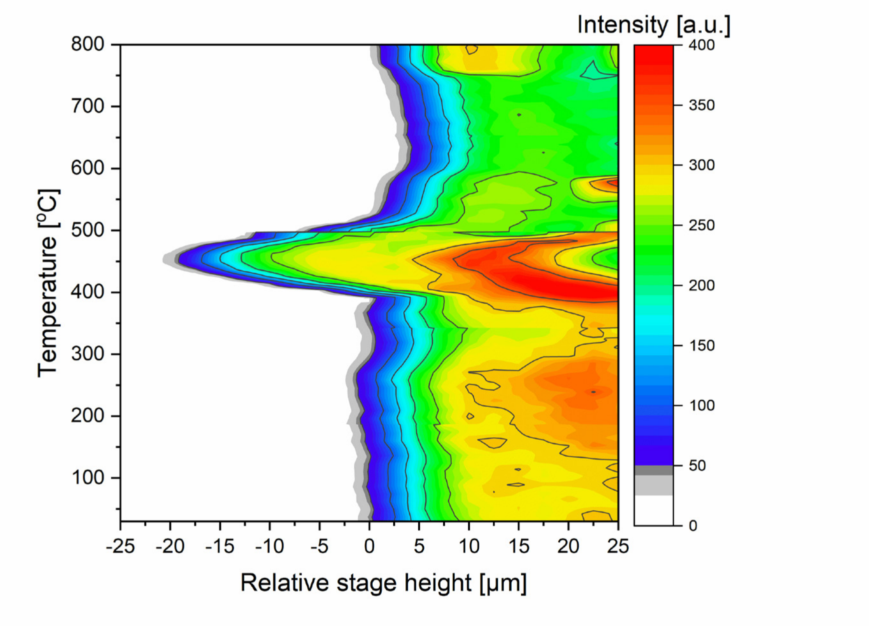

Figure 55: Integrated intensity of synchrotron diffraction of in-situ annealing of an as-deposited Fe-C coating measured at 8 °2Θ, looping around a relative stage height, using a heating rate of 8 K/min from 40 °C to 800 °C. In-situ isochronal annealing evaluation of the microstrain and crystallite size of ferrite

7.3 In-situ isochronal annealing evaluation of the microstrain and crystallite size of ferrite

7.3.1 Manuscript VII

Interpretation of the evolution of microstrain and crystallite size for ferrite during annealing of nanocrystalline electrodeposited Fe-C coatings[13]

Jacob Obitsø Nielsen, Flemming Bjerg Grumsen, Karen Pantleon

Technical University of Denmark, Department of Mechanical Engineering, Produktionstorvet, building 425, DK – 2800 Kongens Lyngby, Denmark

Abstract

The nanocrystalline Fe-C coatings were electrodeposited from an iron(II)sulfate electrolyte with citric acid used as carbon source. The thermal stability of the Fe-C coatings was investigated from room temperature to above the austenitization temperature with an in-situ energy-dispersive synchrotron diffraction analysis. The quantification of the internal structure of the ferrite phase, based on line profile analysis of the evolving diffraction peaks during isochronal annealing, revealed a correlation of the evolution of microstrain and crystallite size in ferrite with the evolution of other phases. The in-situ diffraction analysis was supplemented by transmission electron microscopy for selected samples, which confirmed not only the precipitation of cementite and magnetite during annealing, but also revealed that the ferrite grains remain of nanocrystalline size even after the phase transformations have occurred. The results support the understanding of the nature of the different phases in the as-deposited Fe-C coating and explain their thermal evolution, which also is associated with a substantial hardness increase.

1. Introduction

The iron-carbon (Fe-C) coatings electrodeposited from an iron-sulfate electrolyte with a carbon-containing additive have a huge potential as a wear resistant surface layer, because they can be deposited in thick layers with a hardness of around 800 HV [1-7]. The carbon-containing additive does not only serve as the carbon source that result in a carbon content of around 0.9 wt% in the as-deposited coating, but also causes the co-deposition of oxygen and hydrogen as by-products [2,4–9]. The as-deposited Fe-C coating appears to consist mainly of α-Fe (ferrite) with a strong <311> fiber texture and a strain-free lattice spacing matching carbon-free ferrite [6,7,9]. The thermal stability of Fe-C coatings was investigated by complementary in-situ and ex-situ annealing diffraction analysis and in-situ thermal analysis from room temperature to above the austenitization temperature and these were supplemented by hardness measurements of ex-situ annealed coatings [7,9]. The complementary methods of characterization have revealed that the co-deposited carbon and oxygen co-exist in two individual phases within the as-deposited Fe-C coating together with the major phase being carbon-free ferrite [6,7,9].

The first additional phase in the as-deposited Fe-C coating has been characterized solely by thermal analysis using simultaneous thermogravimetry (TGA) and differential thermal analysis (DTA) coupled with a mass spectrometer (MS) [7,9]. The phase has not been revealed by X-

---

[13] Manuscript in preparation for publication.

ray or electron diffraction, which indicates that it either is not crystalline or of too low volume fraction for measureable diffracted intensities [6,7,9]. However, the thermal analysis has shown that this phase consists of the light elements being carbon, oxygen, and hydrogen that were co-deposited from the applied additive during electrodeposition [7,9] and therefore the designation “organic compound” has been selected to represent this phase.

The second additional phase in the as-deposited Fe-C coating is a crystalline phase that has repeatedly been detected by X-ray diffraction as a single free-standing diffraction peak with a lattice spacing of 0.237 nm in the as-deposited coating [4–7,9]. The phase has previously been suggested as the ε/η-Fe_2C transition carbide [4,6], but recent results using complementary in-situ annealing diffraction analysis and in-situ thermal analysis have related transformation of that phase to an exothermic transformation that includes a mass loss and desorption of at least hydrogen, which excluded the ε/η-Fe_2C as a possible match [9]. The not yet identified single free-standing diffraction peak with a lattice spacing of 0.237 nm is reflected in the current terminology “nameless peak” referring to the “nameless phase” in the as-deposited Fe-C coatings.

The exothermic transformation of the “organic compound“ occurs at around 250 °C and the associated release of oxygen and carbon enables the precipitation of magnetite and cementite that are measured at higher temperatures by in-situ diffraction analysis [9]. The exothermic phase transformation of the “nameless phase” proceeds at around 330 °C, but the continuing progress of peaks associated to cementite and magnetite at this temperature hinders the analysis of the “nameless phase” transformation [9]. The increase in microhardness for ex-situ annealed Fe-C coatings can be cross-linked to the transformations of the “organic compound” and the “nameless phase” [7]. The Fe-C coatings increased their microhardness to around 950 HV by annealing at a temperature where the “organic compound” had transformed and the precipitation of magnetite and cementite have progressed, but the “nameless phase” was still intact. The microhardness of Fe-C coatings reached nearly 1300 HV when the annealing temperature was further increased such that the “nameless phase” also had transformed and grain coarsening was not yet started.

The present study is a continuation of the abovementioned previous in-situ annealing studies [7,9], which focused on the evolution of phases other than the ferrite matrix. The present work is addressed to the thermally induced changes of the ferrite phase, which will be cross-linked to the current understanding of the transformations of the “organic compound” and the “nameless phase” along with the precipitation of magnetite and cementite. The evolution of the microstrain and crystallite size of ferrite is revealed by in-situ diffraction analysis during isochronal annealing at different heating rates and is supplemented with ex-situ transmission electron microscopy of as-deposited and annealed coatings. The influence of the occurring phase transformations on the thermal evolution of ferrite is discussed.

2. Experimental

2.1 Electrochemical deposition

An iron-sulfate electrolyte was prepared from chemicals of analytical grade with a concentration of 0.143 mol/dm^3 iron (II) sulfate heptahydrate, 6.2 x 10^{-3} mol/dm^3 citric acid monohydrate, and deionized water. The electrolyte temperature amounted to 50 °C and the pH-value was maintained between 2.5-2.8 during deposition. Electrodeposition was carried out using a direct current with a current density of 3.0 A/dm^2 for a deposition time of 900 min. Further details about the operation conditions are described elsewhere [9].

2.2 Synchrotron diffraction

The EDDI beamline at the synchrotron facility BESSY II allowed the in-situ annealing energy-dispersive diffraction experiments. The energy-dispersive diffraction method requires a white X-ray beam with a continuous photon energy spectrum and diffraction occurs for crystallographic lattice planes with spacing d_{hkl} at a photon energy E_{hkl} according to [10].

$$E_{hkl} = \frac{h\,c}{2\sin\theta} \cdot \frac{1}{d_{hkl}}$$

where h is Planck's constant, c is the speed of light and θ is the diffraction angle.

A symmetric diffraction geometry was applied with a fixed diffraction angle of $2\theta = 8°$. The isochronal annealing was performed from 30 °C to 800 °C using heating rates of 2 and 8 K/min and an acquisition time of 30 seconds for recording each spectrum. A gold reference standard was used for calibration of the energy offset. A LaB_6 standard powder sample was used to correct for instrumental peak broadening. The diffraction lines of ferrite were fitted with a pseudo-Voigt profile function, which provided the following parameters for each fitted peak: (1) the position on the energy scale, (2) the integrated intensity, (3) the full-width-half-maximum (FWHM) and (4) the peak shape in terms of the Lorentz factor. The resulting physical peak broadening was calculated from the FWHM and the Lorentz factor, corrected by the instrumental effect and expressed as integral breadth (β_{pv}), which was separated into the individual contribution from the Gaussian (β_G) and the Lorentzian (β_L) peak profiles [11]. The β_L and β_G were used to calculate the crystallite size and microstrain, respectively, by applying the single line method for line profile analysis [12,13]. Further details about the experimental setup for synchrotron diffraction are described elsewhere [9].

2.3 Transmission electron microscopy

With transmission electron microscopy (TEM), both the as-deposited coating and a coating after isothermal annealing was investigated in plane view and in cross section view. The isothermal annealing of the Fe-C coating was performed at 400 °C for 1 hour in a Netzsch STA 449F3 and applying a constant argon flow of 30 mL/min to prevent oxidation. The electron transparent lamellae were prepared from the middle of the coating cross section by focused-ion beam (FIB) lift-out using a FEI Helios EBS3 dual beam microscope. A platinum layer was deposited on the region of interest, from which the TEM lamellae were produced, and the FIB thinning procedure was conducted using a low current to prevent damage or modifications of the coating. The TEM investigations were carried out at 300 kV using a Joel 3000F. The Fe-C coatings were characterized using true bright-field (BF) and dark-field (DF) imaging, and selected area electron diffraction (SAED) analysis.

3. Results

3.1 In-situ synchrotron diffraction

Following the evolution of the coating by diffraction analysis during in-situ annealing to above the austenization temperature with a heating rate of either 2 K/min or 8 K/min revealed several phase transformations. Selected diffraction spectra as snap shots from different temperatures during the in-situ annealing of an as-deposited Fe-C coating using a heating rate of 2 K/min are shown in Figure 1.

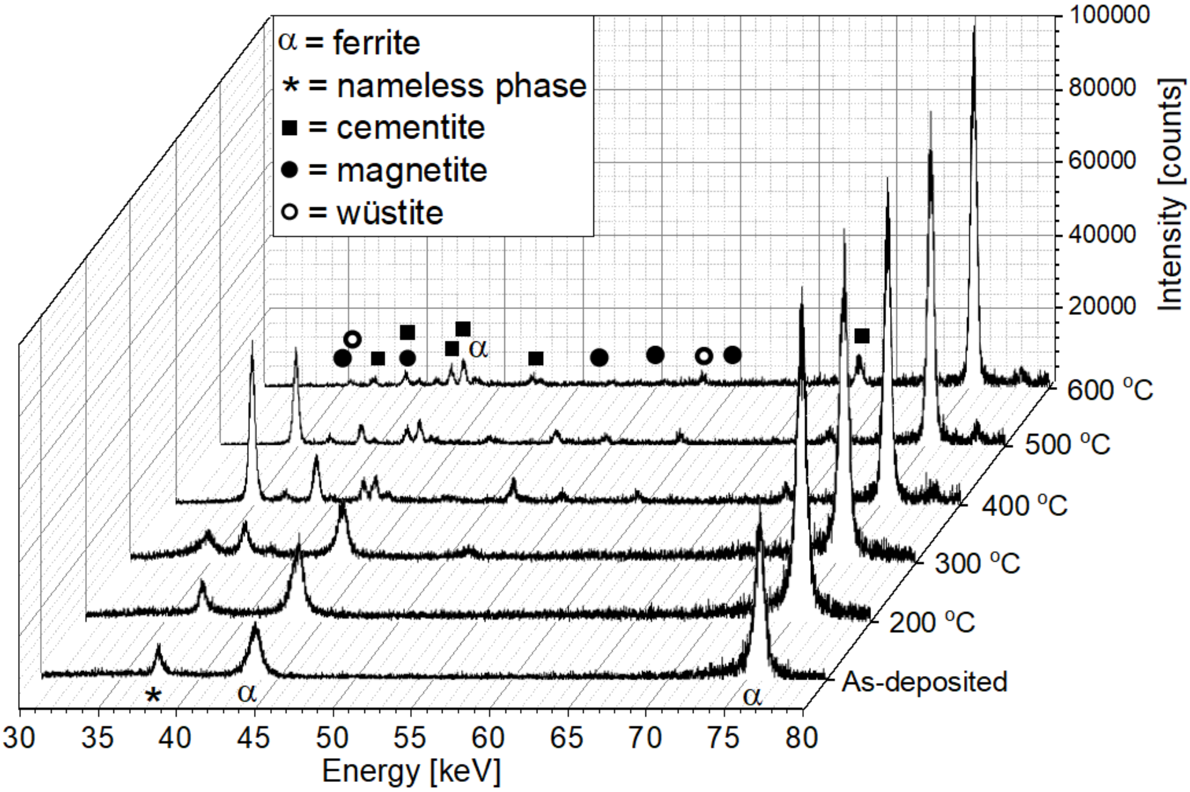

Figure 1: Snap-shots of synchrotron energy-dispersive diffraction spectra at selected temperatures during the in-situ isochronal annealing of an as-deposited Fe-C coating using a heating rate of 2 K/min. For the complete in-situ analysis with high temperature-resolution (1 spectrum per Kelvin) it is referred to [9].

The complete in-situ analysis of the sample can be found in a previous publication [9], which was addressed to the formation of new phases (oxides and carbides, related to the co-deposited light elements) during annealing, in contrast to the present study, which focuses on the evolution of the ferrite phase. Similar to the observations during heating with 2 K/min, the same phase transformations occur during heating at 8 K/min, but the heating rate affects the transformation temperatures: the faster heating shifts the transformations to higher temperatures. However, the increased heating rate will also increase the temperature difference between subsequently measured spectra as the acquisition time was kept constant, and the lower temperature resolution for the higher heating rate may be partly responsible for the observed shift of the transformation temperatures. The present work does not emphasize the absolute transformation temperatures, but rather the observation that the occurring phase transformations during annealing evolve in the same sequence independent of the heating rate and, for both heating rates, suggest a relation to the thermal stability of the ferrite phase.

The as-deposited coating consists of ferrite and (at least) one additional phase, recently called the "nameless phase", because diffraction analysis cannot unambiguously identify that phase (cf. [4–7,9]). During annealing, the first new phase, i.e. the precipitation of magnetite (Fe_3O_4), is detected at a temperature of 259 °C and 325 °C for a heating rate of 2 K/min and 8 K/min, respectively. The precipitation of cementite (Fe_3C) is measured at a temperature of 310 °C (2 K/min) and 338 °C (8 K/min), respectively. At these temperatures, the "nameless phase" is still present as it was in the as-deposited coating and its transformation is recorded only at temperatures of 328 °C and 358 °C for a heating rate of 2 K/min and 8 K/min, respectively. With continued annealing, magnetite transforms to wüstite (FeO) at 570 °C and ferrite transforms to austenite at 727 °C and both transformation temperatures fit exactly to the corresponding equilibrium temperatures as expected for the slow annealing with 2 K/min.

While the focus in previous publications [4,5,7,9,14,15] has been solely on the detection and understanding of the newly forming phases during annealing, the thermal evolution of the ferrite phase from its as-deposited state until it transforms to austenite has not been investigated previously. This requires thorough line profile analysis of the ferrite peaks, which are recorded with excellent temperature resolution of one spectrum per Kelvin during isochronal annealing (cf. Figure 1 and [9]). From the evolution of the determined integral breadth β_{pV} of the measured 211 reflection of α-Fe, which is shown in Figure 2, it is obvious that the ferrite phase changes during annealing, although the 211 reflection remains of highest intensity (cf. Figure 1).

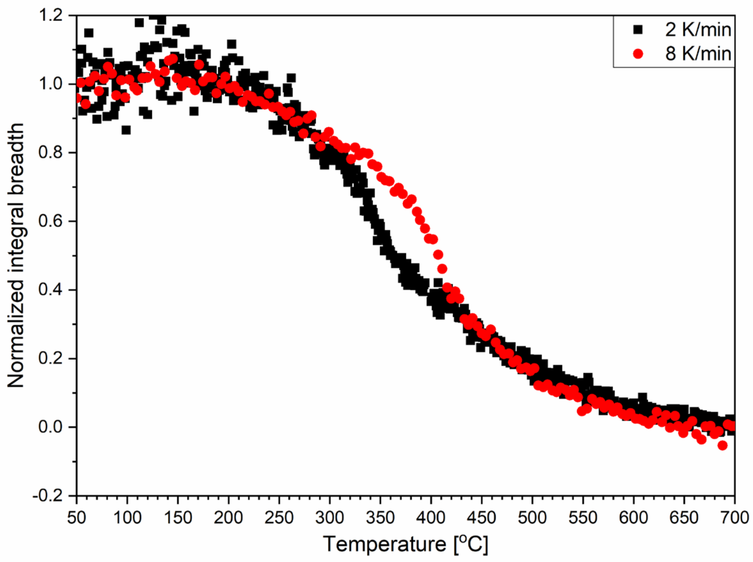

Figure 2: Evolution of the integral breadth β_{pV}, normalized to its initial value at room temperature, during in-situ isochronal annealing with a heating rate of 2 K/min (black squares) and 8 K/min (red circles), respectively.

The corresponding evolution of both the microstrain and the crystallite size was determined from the α-211 reflection, which represents the <211> oriented grains which only are about 10.7° away from the <311> orientation of the correspondingly measured <311> fiber texture for the Fe-C coatings [6]. It would be of interest to analyze the <311> oriented grains as they represent the majority of grains in the Fe-C coatings, but the 311 is a forbidden reflection for the bcc α-iron. The microstrain and crystallite size for the <211> oriented grains as a function of the temperature is shown in Figure 3 for the heating rates of 2 K/min and 8 K/min. The specific temperature for the transformation of the “nameless phase” is indicated in the Figure 3.

The as-deposited Fe-C coating is nanocrystalline with a crystallite size of the <211> oriented grains of around 50 nm and microstrain in these grains of about 8.4 x 10^{-3} rms. This as-deposited state remains unchanged over a wide temperature range, before the measured microstrain starts to decrease at around 250 °C independently of the applied heating rate. The microstrain decreases at fixed exponential rate with temperature until the decrease accelerates at the temperature where the transformation of the “nameless phase” was observed. The crystallite size increases first after the onset of microstrain changes and the growth continues towards micrometer large grains with continued annealing.

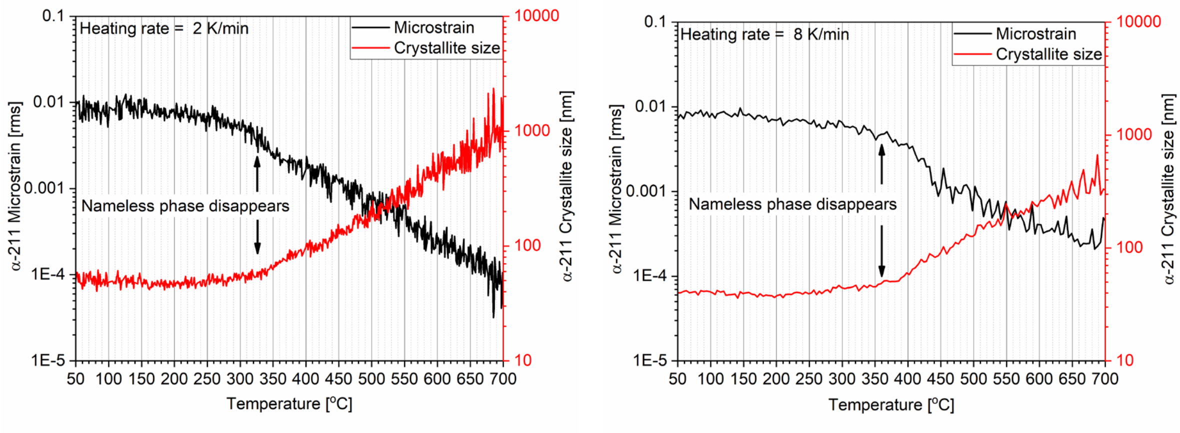

(a) (b)

Figure 3: Crystallite size (red) and microstrain (black) for <211> oriented grains as a function of temperature during in-situ isochronal annealing using a heating rate of 2 K/min (a) and 8 K/min (b). The temperature for the observed transformation of the "nameless phase" is indicated.

3.2 Microscopic analysis of Fe-C coatings

While the in-situ diffraction analysis revealed the evolution of the microstructure with temperature, TEM supplements with an ex-situ analysis for selected temperatures. The nanocrystalline nature of the as-deposited Fe-C coating is clearly shown in Figures 4 and 5a. The columnar ferrite grains are elongated along the growth direction as shown in Figure 5a. The morphology of the ferrite grains is determined using the dark field imaging of cross sections and a selection of the micrographs are shown in Figure 5d-f. The average width and length of the as-deposited grains are estimated to 16 and 48 nm, respectively. The SAED pattern and the radial brightness distribution are shown in Figure 5b-c and confirms that the as-deposited Fe-C coating mainly consist of ferrite. In addition, a diffuse uniform ring of low intensity is measured with a lattice spacing that could correspond to magnetite. Based on the knowledge of co-deposited light elements [6], the oxide may have formed during electrodeposition (although it is not detected by synchrotron diffraction), but it may also indicate the challenges of preventing oxidation of ferrite during preparation, handling or storage of the thin TEM lamella. The presence of a strong fiber texture in the as-deposited Fe-C coating shapes the diffraction rings into arcs, instead of circles of uniform intensity that would appear for a microstructure with a random crystallographic orientation [16]. This effect is clearly seen for the SAED pattern recorded from the cross section as the intensity from ferrite is only measured as individual segments.

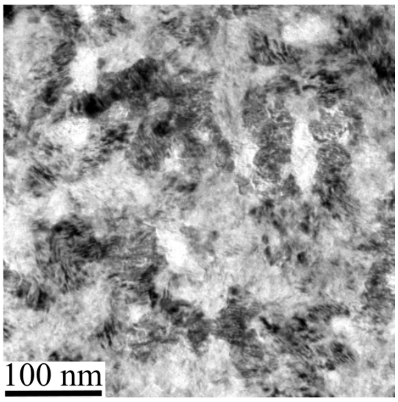

Figure 4: TEM bright-field micrograph of an as-deposited Fe-C coating in plane view.

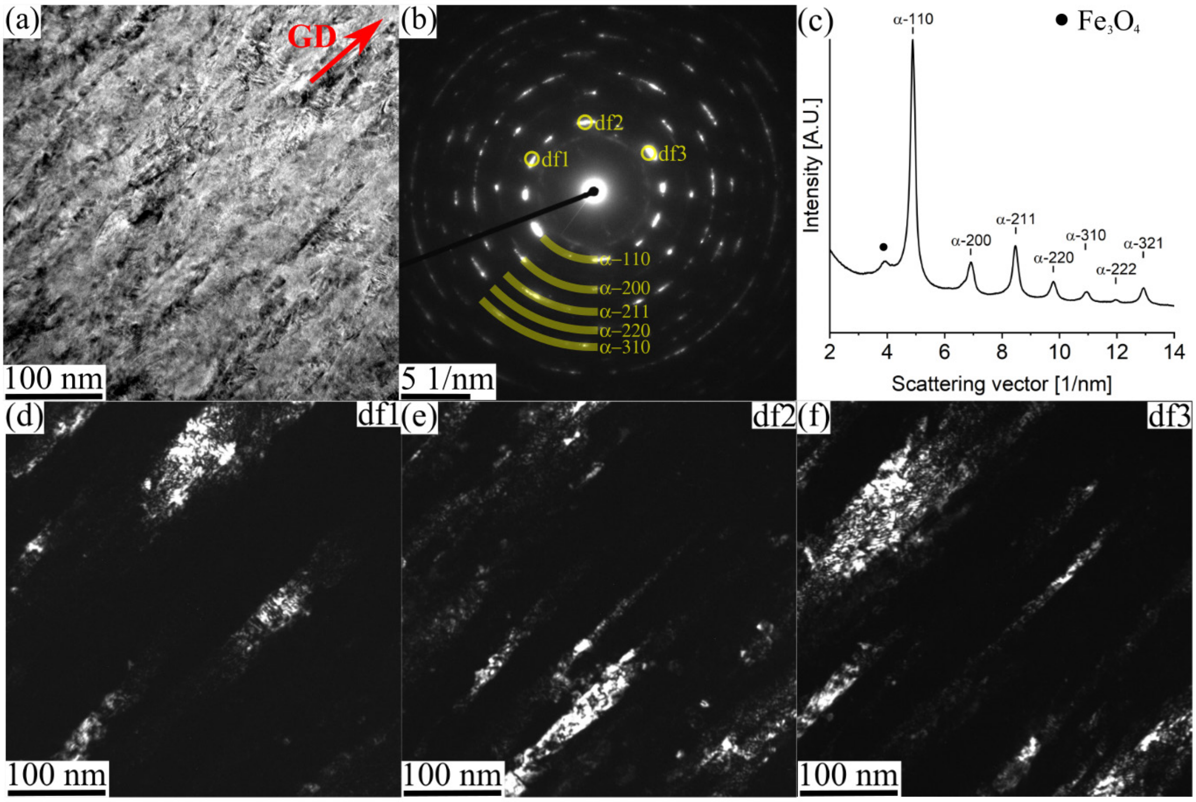

Figure 5: Microstructure of an as-deposited Fe-C coating in cross section with arrow indicating the growth direction; (a) true bright-field image (b) selected area electron diffraction pattern, (c) radial intensity distribution of (b), (d-f) dark field images of α-110 grains.

The Fe-C coating preserves its nanocrystalline microstructure after isothermal annealing at 400 °C for 1 hour as shown in Figures 6 and 7a. The morphology of the annealed ferrite grains was determined using the dark field imaging in cross section, as shown with selected micrographs in Figure 7d-e. The annealed ferrite grains have only slightly increased in size to an average width and length of about 23 nm and 55 nm, respectively. The SAED pattern and the radial brightness distribution are shown in 7b-c and confirm that the annealed Fe-C coating mainly consists of ferrite and the new diffraction spots match the d-spacings for both Fe_3C and Fe_3O_4. These precipitates are indeed localized in the microstructure, as shown in the dark field images for Fe_3O_4 in Figure 7f. The Fe_3O_4 oxides are uniformly distributed with nanoscale dimensions of 13 nm on average. The diffraction pattern for ferrite in the annealed Fe-C coating is similar to the diffraction pattern in the as-deposited coating with only individual segments of intensity at the respective d-spacings as a result of a strong fiber texture.

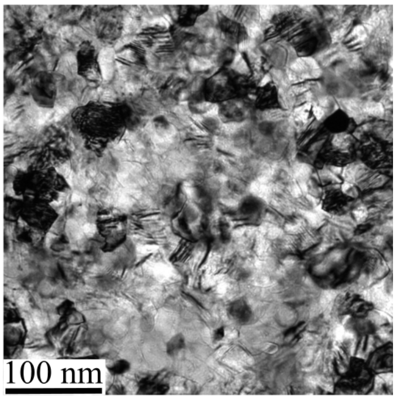

Figure 6: TEM bright-field micrograph of an annealed Fe-C coating at 400 °C for 1 hour in plane view.

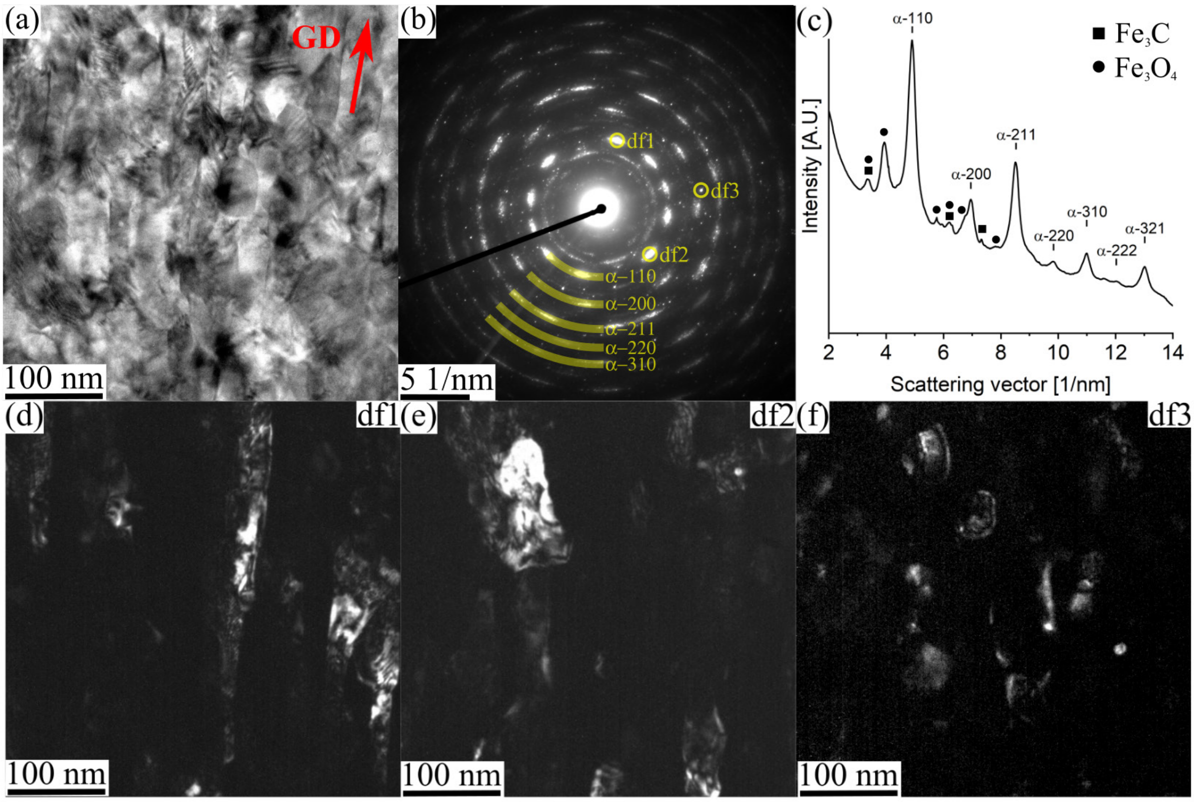

Figure 7: Microstructure of an annealed Fe-C coating at 400 °C for 1 hour in cross section with red arrow indicating the growth direction; (a) true bright-field image, (b) selected area electron diffraction pattern, (c) radial brightness distribution of (b), (d-e) dark field images of α-110 grains, (f) dark field image of Fe_3O_4 precipitates.

4. Discussion

The present in-situ diffraction analysis during isochronal heating essentially supports the interpretation of Fe-C coatings, regarding both their as-deposited state and their annealing behavior. It partly confirms and partly extends our previous analysis of in-situ and ex-situ synchrotron diffraction [7,9] and it further complements the diffraction results with transmission electron microscopy of selected samples. Although ferrite often appears to be the only phase in the as-deposited coatings [5,7–9], it certainly only is the major phase and easiest to detect experimentally. As indicated recently by in-situ thermal analysis and various diffraction measurements [4,5,7,9], additional phases certainly are present together with ferrite already in the as-deposited coatings, although they could not be identified unambiguously and are referred to the "organic compound" and the "nameless phase" [7,9]. The presence of these phases and their thermal evolution would likely affect the internal structure of the ferrite phase, which was investigated in the present study and the observed thermal evolution of ferrite is discussed below.

As widely accepted and frequently observed [2,5,7,8,17], from the cross section analysis, it is revealed that as-deposited Fe-C coatings consist of nanocrystalline ferrite grains, which are elongated in growth direction. The quantification of the column length by TEM in the present work might be affected slightly by the actual inclination of the grains with respect to the electron beam (an error of about 1.5 % is estimated for the applied experimental conditions). However, consistent results from microscopy and synchrotron diffraction (the latter only can reveal the size of crystallites in the direction of the diffraction vector, thus, normal to the surface) revealed less than 50 nm for the length of individual columnar grains and, based on microscopy, the widths of as-deposited ferrite grains is below 20 nm. These nanocrystalline grains consist of fairly high microstrain of about 0.01 rms and the often observed inverse relation between grain size and microstrain in nanocrystalline materials [18] seems to apply also for the Fe-C coatings. Typical other sources of microstrain like point defects can be rejected for the present coatings, because the co-deposited carbon, oxygen and hydrogen are not found to be in solid solution in the ferrite lattice [6,7,9], and neither a significant contribution from lattice dislocations is expected for the very small grains [19]. However, the additional phase(s) other than ferrite in the as-deposited Fe-C coatings will need to accommodate the associated misfit at their interface with ferrite and, depending on the type of interface (coherent or incoherent), this would cause microstrain in the ferrite grains and suggest an orientation relation between the phases in the as-deposited coating. The phase, which reproducibly has been detected by XRD with a lattice spacing of 0.237 nm (the "nameless phase" [7,9]) has previously been suggested to possess an orientation relation with ferrite, because the diffraction intensities of the measured single peak from the "nameless phase" and the 110 peak of ferrite appear to be coupled when tilting the sample around the azimuth angle until both peaks simultaneously disappear at a tilt angle of 12° [6]. The interrelation between both phases is further supported by an earlier observation of a correlated peak shift between ferrite and the "nameless phase" [6]. The "nameless phase" was not detected by electron microscopy in the present study, neither the plane view nor the cross section analysis of the as-deposited Fe-C coating revealed a diffraction spot corresponding to the lattice spacing of 0.237 nm and tilting the samples in the TEM sample holder did not reveal additional diffraction spots for the as-deposited Fe-C coating. Thus, the present analysis with TEM cannot conclude on the identity of the "nameless phase" or its location within the microstructure, although several attempts to reveal more understanding of that (still "nameless") phase have been carried out. However, an interesting observation shown in Figure 3 further supports its interrelation with ferrite and its importance for the thermal stability of Fe-C coatings.

Independent of the applied heating rate, the as-deposited Fe-C coatings remain thermally stable over a wide temperature range (cf. Figure 3), where neither new phases form nor the ferrite phase changes. Up to at least 250 °C during isochronal annealing, the as-deposited coating still consists mainly of ferrite with nanocrystalline columnar grains and fairly high microstrain. The initial decrease in microstrain measured at around 250 °C occurs at a slightly lower temperature than the precipitation of magnetite and cementite was detected, but can be linked to the decomposition of the "organic compound" that was characterized by thermal analysis [7,9]. This transformation of the "organic compound" enables the precipitation of cementite and magnetite and, thereby, causes an increase in the microhardness to around 950 HV [7]. Until it decomposes, the "organic compound" is suggested to be located in the numerous grain boundaries of the ferrite phase, where it formed from the segregated co-deposited elements. This causes localized strain fields in the adjacent regions and contributes to the high microstrains in the as-deposited ferrite grains, which start to relax when the "organic compound" decomposes.

An accelerated decrease of the microstrain in ferrite occurs during continued annealing at the same temperature, where the transformation of the "nameless phase" was observed and then the grain coarsening of the ferrite commences and continues simultaneously to the relaxation of microstrain; this occurs for both heating rates (cf. Figure 3a and 3b). The observed link between the occurring phase transformation and the evolution of the ferrite grains during isochronal annealing indicates that the growth of the ferrite grains is prevented by the presence of the “nameless phase”. The considerable microstrains in the electrodeposited Fe-C coatings further suggest that the “nameless phase” is formed as coherent or semi-coherent precipitate inside the ferrite grains and explains the suggested orientation relation with ferrite [6]. The “nameless phase” must be of even smaller size than the ferrite grains, in which it is precipitated, and finely dispersed in the microstructure to give an overall volume fraction for being detected by synchrotron diffraction. Such precipitates further explain both the high hardness of the as-deposited coatings with measured values of 800 HV [2–4,6,7,17] and the good thermal stability of these coatings. That the hardness further increases after the transformation of the “nameless phase” is caused by the magnetite and cementite precipitates, which continue to form and are expected to be fine dispersed in ferrite, which indeed was confirmed by the present TEM analysis. This is further consistent with the measurement of a hardness increase to nearly 1300 HV [7] after prolonged isothermal annealing of 24 h at 300 °C, where the majority of the “nameless phase” has transformed without a significant growth of the ferrite grains [7].

Apart from the detection of the “nameless phase”, the present TEM investigations confirm the synchrotron diffraction results and the previous interpretation of phase transformations based on thermal analysis [7,9]. The development of both cementite and magnetite during annealing (as detected by the in-situ diffraction analysis) was confirmed by TEM for the isothermally annealed sample investigated in cross section. It should be noted however, that magnetite was also revealed in the as-deposited TEM samples, which may indicate the challenges of preventing oxidation of ferrite during preparation, handling, or storage of the thin TEM lamella. However, for the annealed samples, in agreement to previous studies [7,9], the presence of magnetite indicates the transformation of the “nameless phase” as it is common for iron-hydroxides (including ferrihydrite) to transform into magnetite when the iron-hydroxides have access to air [20]. Such transformation could have happened also during the TEM sample preparation and explain the absence of the “nameless phase” in as-deposited TEM samples, where instead magnetite was found. Furthermore, the TEM analysis also confirms that the size of ferrite grains after isothermal annealing at 400 °C still is in the nanometer range, although a direct comparison with synchrotron diffraction results is not possible for the different annealing regimes of isochronal and isothermal annealing, respectively. In addition, the difference in the results could be related to the information depth of the diffraction analysis being closer to the surface compared to the TEM sample produced from the middle of the 360 μm thick Fe-C coating. However, both XRD and TEM confirm that the grains still are nanocrystalline, although the average crystallite size of around 100 nm (cf. Figure 3) determined by in-situ diffraction isochronal annealing for a temperature of 400 °C using a heating rate of 2 K/min is higher than the average length of the columnar grains measured by TEM for an isothermally annealed coating at 400 °C for 1 hour (cf. Figure 6). The size of grains at 400 °C in the present study is also significantly higher compared to nanocrystalline iron measured before and after isothermal annealing for 5 min at 400 °C, where the crystallite size was found to remain below 20 nm [21]. However, the present work consistently confirms that the ferrite grains still are nanocrystalline and no severe grain growth happens during (low temperature) annealing, which indicates a fairly good thermal stability of the electrodeposited Fe-C coatings.

5. Conclusion

Electrodeposited Fe-C coatings from an iron sulfate electrolyte with citric acid as an additive mainly consist of ferrite with nanocrystalline grains of columnar morphology and a strong crystallographic texture. An additional phase in the as-deposited Fe-C coating, which is repeatedly measured using synchrotron diffraction and also reported in literature, was not detected with TEM, neither by imaging nor diffraction analysis despite extensive experimental efforts. Accordingly, this phase still is called the "nameless phase", but its importance becomes obvious when following the evolution of the ferrite phase during annealing. The microstrain and crystallite size of ferrite were determined from in-situ isochronal annealing synchrotron diffraction analysis, which previously has been used to detect occurring phase changes other than comprising the ferrite phase [7,9]. The results show that the microstrain decreases with different rates at two separate temperatures, which indicates two influences on the microstrain in ferrite. The initial decrease in microstrain can be linked to the transformation of a co-deposited phase that solely has been detected by thermal analysis [7,9], thus, either is non-crystalline or of too low volume fraction for being detected by diffraction analysis, but initiates microstrain in ferrite with a corresponding relaxation at the temperature where this phase decomposes. The second and more pronounced decrease in microstrain occurred simultaneously with the transformation of the "nameless phase", which is known to be crystalline, but not possible to identify in its chemical nature. The presence of this phase in the as-deposited Fe-C coatings as coherent or semi-coherent precipitate inside the nanocrystalline ferrite grains with a specific orientation relation with ferrite, explains the high microstrain in the ferrite grains and the high hardness of the as-deposited coatings. It further is responsible for the good thermal stability of as-deposited coatings, which is ensured as long as the "nameless phase" is present. With its transformation at temperatures above 250 °C, the ferrite phase evolves with considerable reductions of microstrain and subsequent grain growth. The newly forming phases of carbides and oxides cause a considerable further hardness increase and their small dimensions appear to limit the growth of ferrite grains even at higher temperatures or longer holding times.

Acknowledgments

The authors kindly acknowledge financial support by OCAS NV, ArcelorMittal Global R&D Gent (Belgium), a. h. nichro Haardchrom (Denmark) and Fast Track - Societal Partnership (Denmark), funded by the Innovation Fund Denmark (IFD).

M. Klaus, D. Apel, and C. Genzel from Helmholtz Zentrum für Materialien und Energie (HZME, Germany) are acknowledged for their valuable support during beamtime at the HZB-BESSY II Synchrotron Facility and during subsequent data analysis. Synchrotron diffraction measurements were financially supported by the project CALIPSOplus under the Grant Agreement 730872 from the EU Framework Programme for Research and Innovation HORIZON 2020, and by the Danish Natural Science Research Council via Danscatt.

References

[1] M. Izaki, H. Enomoto, T. Omi, Hardness and Carbon Content of Fe Electroplate from Sulfate Bath Containing l-Ascorbic Acid and Citric Acid, J. Surf. Fin. Soc. Jpn. 40 (1989) 1304–05.

[2] Y. Fujiwara, T. Nagayama, A. Nakae, M. Izaki, H. Enomoto, E. Yamauchi, Electrodeposition of Fe-C Alloys from Baths Containing Dicarboxylic Acids with a Linear Alkyl Chain, J. Electrochem. Soc. 143 (1996) 2584–2590.

[3] M. Panayotova, Deposition of Fe–C alloy on structural steel and cast iron for repair of worn machine parts, Surf. Coat. Technol. 124 (2000) 266–271.

[4] A.S.M.A. Haseeb, Y. Hayashi, M. Masuda, M. Arita, On the nature of the electrochemically synthesized hard Fe-0.96 mass pct C alloy film, Metall. Mater. Trans. B. 33B (2002) 921–927.

[5] T. Müller, J. Grimwood, A. Bachmaier, R. Pippan, Electrodeposition of Fe-C alloys from citrate baths: Structure, mechanical properties, and thermal stability, Metals (Basel). 8 (2018) 1–13.

[6] J.O. Nielsen, P. Møller, K. Pantleon, Electrodeposition of Iron with Co-deposition of Carbon: On the Nature of Nanocrystalline Fe-C Coatings, Metall. Mater. Trans. A. 50A (2019) 3785–3793.

[7] J.O. Nielsen, K. Pantleon, Evolution of hard Fe–C electrodeposits with temperature, Surf. Eng. (2019) 1–6.

[8] N. Fukumuro, S. Kojima, M. Fujino, Y. Mizuta, T. Maruo, S. Yae, Y. Fukai, Hydrogen-induced superabundant vacancies in electrodeposited Fe-C alloy films, J. Alloys Compd. 645 (2015) 404–407.

[9] J.O. Nielsen, T.L. Christiansen, K. Pantleon, In-situ analysis of the thermal evolution of electrodeposited Fe-C coatings, (n.d.).

[10] C. Genzel, I.. A. Denks, J. Gibmeier, M. Klaus, G. Wagener, The materials science synchrotron beamline EDDI for energy-dispersive diffraction analysis, Nucl. Instruments Methods Phys. Res. A. 578 (2007) 23–33.

[11] R. Snyder, J. Fiala, H.J. Bunge, Defect and microstructure analysis by diffraction, 2000.

[12] J.I. Langford, A Rapid Method for Analysing the Breadths of Diffraction and Spectral Lines using the Voigt Function, J. Appl. Cryst. 11 (1978) 10–14.

[13] T.H. de Keijser, J.I. Langford, E.J. Mittemeijer, A.B.P. Vogels, Use of the Voigt function in a single-line method for the analysis of X-ray diffraction line broadening, J. Appl. Crystallogr. 15 (1982) 308–314.

[14] M. Izaki, H. Enomoto, A. Nakae, S. Terada, Y. Eiko, T. Omi, Phase Transformations and Hardness Changes in Electrodeposited Alloy Films Iron-carbon alloy films., J. Surf-Fin. Soc. Jpn. 45 (1994) 1303–1309.

[15] M. Izaki, H. Enomoto, T. Omi, Structure and Hardness of Fe-C alloy Film Electrodeposited from an Iron Sulfate Electrolyte, J. Japan Inst. Met. 56 (1992) 636–640.

[16] L. Tang, D.E. Laughlin, Electron Diffraction Patterns of Fibrous and Lamellar Textured Polycrystalline Thin Films. I. Theory, J. Appl. Crystallogr. 29 (1996) 411–418.

[17] M. Izaki, T. Omi, Structural characterization of martensitic iron-carbon alloy films electrodeposited from an iron(ll) sulfate solution, Metall. Mater. Trans. A. 27A (1996) 483–486.

[18] W. Qin, J.A. Szpunar, J.A. Szpunary, Philosophical Magazine Letters Origin of lattice strain in nanocrystalline materials Origin of lattice strain in nanocrystalline materials, Philos. Mag. Lett. 85 (2005) 649–656.

[19] A. Stukowski, J. Markmann, J. Weissmü Ller, K. Albe, Atomistic origin of microstrain broadening in diffraction data of nanocrystalline solids, Acta Mater. 57 (2009) 1648–1654.

[20] R.M. Cornell, U. Schwertmann, The iron oxides, Wiley, 2003.

[21] T.R. Malow, C.C. Koch, Grain growth in nanocrystalline iron prepared by mechanical attrition, Acta Mater. (1997).

7.3.2 Supplementary material related to isochronal to isothermal conversion

The in-situ isochronal annealing energy-dispersive synchrotron diffraction measurement that was analysed using the single line method showed that the grain coarsening of ferrite could be inhibited by the “nameless phase” as the microstrain decreased and the crystallite size of ferrite increased directly after the transformation of the “nameless phase”. A numerical integration method has been implemented by Wolfgang Pantleon to convert the isochronal annealing measurements using a constant heating rate into isothermal data at a fictive temperature as presented below. The method is still a work-in-progress.

The experimental setup for diffraction experiments and the line profile analysis are the same as described in Manuscript VI. The three heating rates applied for the in-situ measurements during isochronal annealing are 2, 4, and 8 K/min.

The calculated integral breadth of the α-211 has been normalized and is plotted as a function of the annealing temperature for the three heating rates as shown in Figure 56. The crystallite size and microstrain have been calculated from the integral breadth using the single line method and the results are shown in Figure 57. The interpretation of the results is described in Manuscript VII.

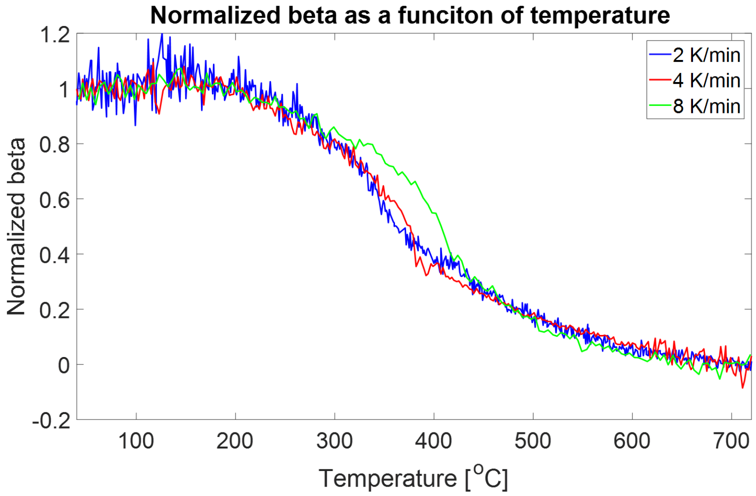

Figure 56: Normalized integral breadth β of α-211 as a function of the annealing temperature for the EDD isochronal annealing of the Fe-C coating at different heating rates.

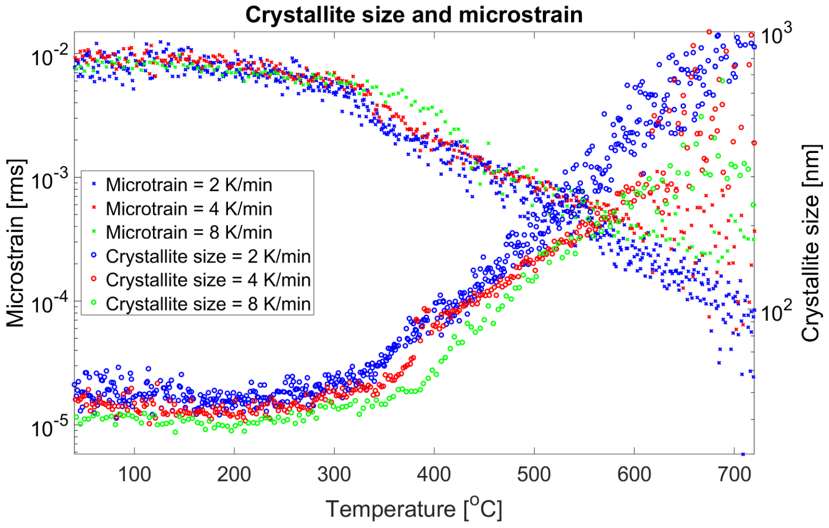

Figure 57: Microstrain and crystallite size as a function of temperature calculated by line profile analysis of the α-211 peak measured during EDD isochronal annealing using different heating rates.

Converting isochronal to fictive isothermal

The Arrhenius equation is adopted for isothermal annealing with a fixed rate constant and was shown in Equation (27) in Section 4.5.4. The Arrhenius equation for annealing with time dependent temperature can be written as shown in Equation (32).

$$\beta = \int_0^t k_0 \cdot e^{-\frac{E}{RT(t)}} \, \mathrm{dt} \tag{32}$$

The Arrhenius equation for isochronal annealing with fixed heating rate can be rewritten to a form as shown in Equation (33) that will allow the equation to be solved numerically.

$$\beta = \int_0^t k_0 \cdot e^{-\frac{E}{R(T_0+\Phi t)}} \, \mathrm{dt} \tag{33}$$

Numerical integration methods can generally be performed as a summation of the integrand at different time step in distance of dt to get an approximation to the integral. A function has been written by Wolfgang Pantleon for converting the isochronal annealing measurements using a constant heating rate into isothermal data at a fictive temperature as presented below,

```
E = ActivationEnergy * 1000; % J/mol
T0 = TempStart + 273; % K
Tref = fictivetemperature + 273; % K
K0 = 1; % Not taking into account
R = kB*NA; % 8.3104 J / (K*mol)
```

where T_0 is the initial temperature of the isochronal annealing and Tref is the fictive holding temperature for isothermal annealing. The activation energy for the transformation needs to be known in order to obtain a reliable result. The method for deriving the activation energy for both isothermal and isochronal annealing was shown in Section 4.5.4.

The integral shown in Equation (33) is evaluated as a finite set of points called integration points and a weighted sum of these values is used to approximate the integral. The function calculates a multiplicative correction factor, which has to be multiplied with the time during isochronal heating to determine the corresponding isothermal time (CorrectedTime) at fictive temperature,

```
Ntimes = numel(time);
Nsteps = 100000;
tt(:,:) = (0:Nsteps)'/Nsteps*time;
ttemp(:,:) = (0:Nsteps)'/Nsteps*(temp-T0+273);
f = exp( -E / R ./ (T0 + ttemp));
correctfactor = sum(f)*exp(E / R / Tref) / Nsteps;
CorrectedTime = time.*Correctfactor;
```

where Ntimes is the number of measurements for the isochronal annealing, Nsteps is the finite set of integration points, tt(:,:) is a matrix containing the integral values of time per measured spectrum, ttemp(:,:) is the matrix containing the integral values of temperature per measured spectrum, f is the matrix containing the evaluations of the integrand shown in Equation (33).

The isothermal analysis at a fictive holding temperature

The isochronal to isothermal conversions have been derived for different activation energies and a fictive temperature of 400 °C. The routine was tested with four activation energies, which were selected as follows: 40 kJ/mol is the activation energy where co-deposited hydrogen from electrolysis is desorbed as described in Manuscript VI, 98 kJ/mol is the activation energy for the decomposition of the "organic compound" as described in Manuscript VI, 151 kJ/mol is the activation energy for the transformation of the "nameless phase" as described in Manuscript VI and 275 kJ/mol is the value corresponding to the activation energy for lattice self diffusion in iron (251-282 kJ/mol) [59].

The integral breath

The turning points of the integral breadth curves plotted as a function of the corrected time are similar to the ones during isochronal annealing as shown in Figure 58 and the curves have been divided into four different sections: (1) A flat section where beta = 1, (2) A linear decreasing slope, (3) a convex decrease with a large slope, (4) A convex decrease with a smaller slope compared to section (3).

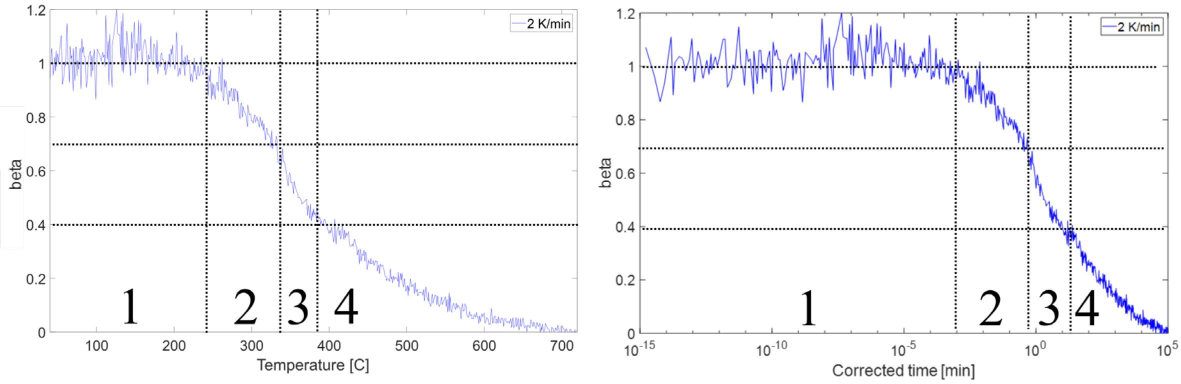

(a) (b)

Figure 58: (a) The integral breadth as a function of temperature using a heating rate of 2 K/min. (b) Integral breadth as a function of corrected time derived using a fictive temperature of 400 °C and an activation energy of 151 kJ/mol derived from the isochronal annealing with a heating rate of 2 K/min.

The normalized integral breadths of α-211 as a function of the corrected time at a fictive holding temperature of 400 °C derived using different activation energies are shown in Figure 59. Although the quantities are considerable different, the corrected time proceeds from a very small value towards a long holding time at the fictive temperature for all activation energies. The thermal activation that is introduced to the system below the fictive holding temperature corresponds to the same thermal activation that is introduced to the system in a very short time at the fictive holding temperature. Similarly, the thermal activation that is introduced to the system is much higher when the temperature is above the fictive holding temperature.

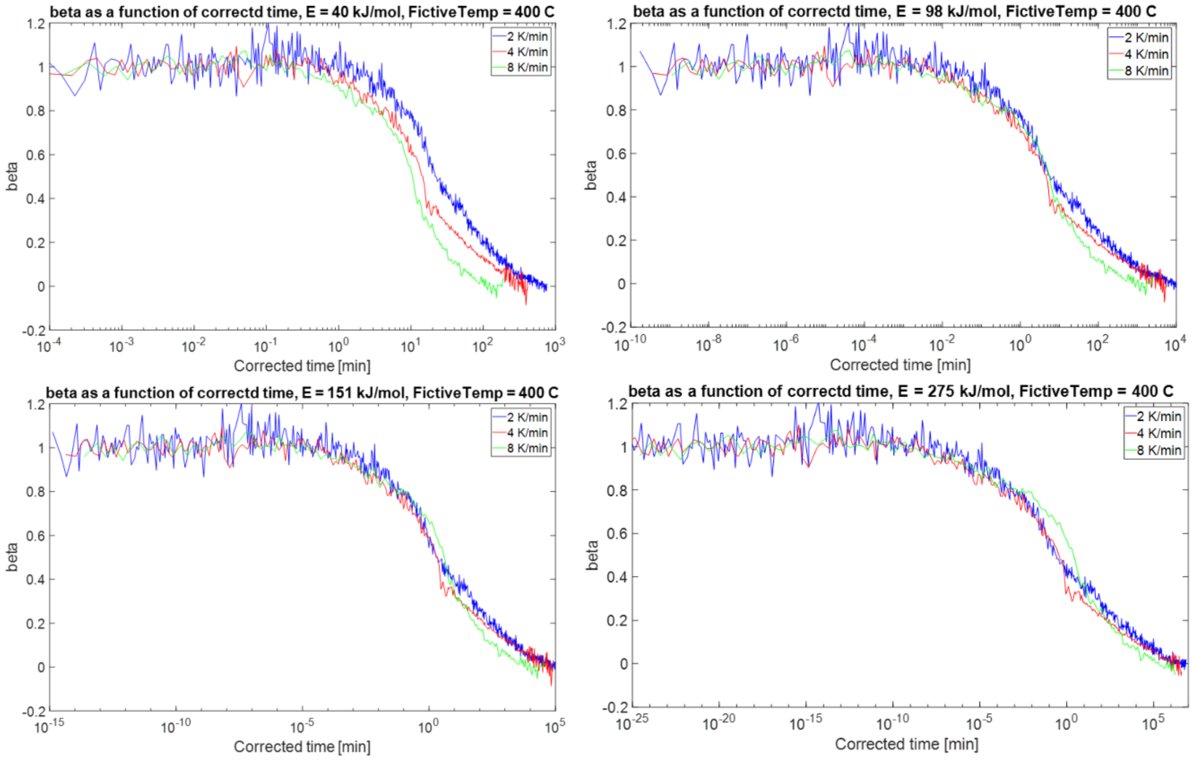

Figure 59: The integral breadth of α-211 measured using different heating rates as a function of corrected time at a fictive holding temperature of 400 °C calculated using different activation energies.

The proportion of the slope in the different sections dependent on the activation energy (cf. Figure 59). Therefore, they are only described in relatively terms at the moment and in more detail below. The influence of the activation energy on the corrected time for the different heating rates is clearly seen in the relative shift between the curves and values of corrected time. The conversion should result in three overlaying curves when the changes measured for the integral breadth of α-211 correspond to a single transformation and the corresponding activation energy is applied. However, the change measured for the integral breadth of α-211 is suggested to originate from more than one influence as described in Manuscript VII. Therefore, it cannot be expected that the conversion will result in complete overlaying curves for a single activation energy.

The initial section (1) where there are no changes measured for the integral breadth of α-211 (beta = 1) will not be discussed. The conversion using an activation energy of 40 kJ/mol does not produce an overlaying section for the different heating rates. The initial decreasing curve is the highest heating rate, which suggests that the applied activation energy is too low. The curves using different heating rates nearly overlap in the second and third sections when the calculation is performed using an activation energy of 98 and 151 kJ/mol, but the fourth section does not match. The curves nearly overlap in the fourth section when the activation energy is increased to 275 kJ/mol, but curves in the second and third sections do not overlap as well compared to the calculations using the lower activation energy.

Crystallite size and microstrain

The microstrain and crystallite size related to the α-211 have been calculated from the contribution of the Gaussian and Lorentz functions to the pseudo-Voigt function using Equation (17) and (18). The microstrain and crystallite size are plotted as a function of the corrected time for the different heating rates using a fictive temperature of 400 °C and an activation energy of 151 kJ/mol as shown in Figure 60. The interpretations for the decreases in microstrain are described in Manuscript VII and will not be discussed further.

The grain coarsening accelerates at the start of the third section (transformation of the "nameless phase") and the increase for the remaining duration represents a straight line independent of the heating rate in the log(crystallite size) vs log(time) plot. The three curves for grain growth overlap in section 1 and 2, whereas their turning point in section 3 is shifted slightly. The curves initially overlap again in section 4 but some scattering is seen for the higher heating rates in the final part.

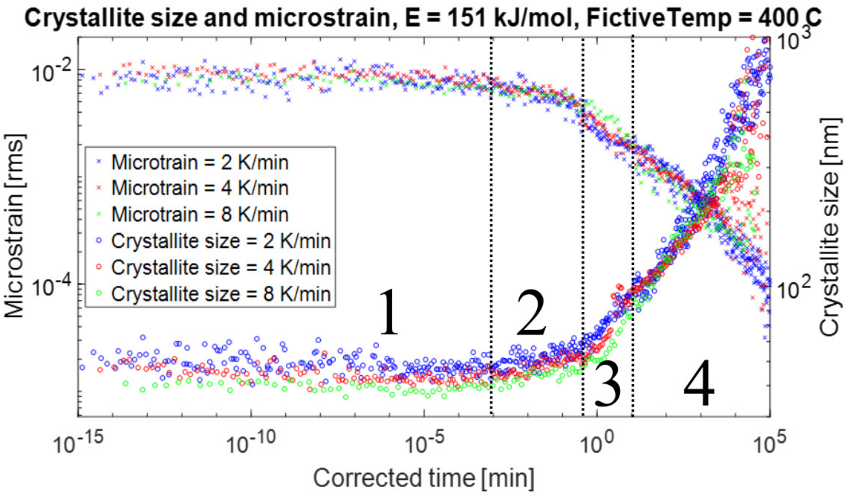

Figure 60: Microstrain and crystallite size of α-211 measured using different heating rates as a function of corrected time calculated using a fictive temperature of 400 °C and an activation energy of 151 kJ/mol.

Modelling the grain growth

The straight line in the log(crystallite size) vs log(time) is expected for the grain growth kinetics in single-phase metals is described in Equation (34) [60,61],

$$D^{1/n} - D_0^{1/n} = kt \tag{34}$$

where D is the grain size at a given time t, D_0 is the initial grain size, k is a proportionality constant, which increases with temperature, and n is an empirical constant. The value of n can be expected between 0.25 and 0.5 for iron, with n = 0.5 for a very pure metal and for high temperatures [62,63]. Equation (34) can be approximated to Equation (35) and (36).

$$D = D_0 + kt^n \tag{35}$$

$$D = kt^n \,, D_0 \cong 0, D \gg D_0 \tag{36}$$

The scattered measurement points in the final part of the measurement are not taken into account and n is fixed at 0.33. The solutions for the curve fitting of the crystallite size as a function of the corrected time for the heating rate of 2 K/min using a fictive temperature of 400 °C and an activation energy of 151 kJ/mol using Equation (35) and (36) are shown in Figure 61a and Figure 61b, respectively. The fitted solution using Equation (35) provides a good representation of the whole measurement, whereas the fitted solution using Equation (36) only provides a good representation of the values towards higher corrected time where grain coarsening is proceeding. However, only a small difference in the proportionality constant is determined with k = 19.6 nm/min$^{0.33}$ and k = 22.3 nm/min$^{0.33}$ for Equation (35) and (36), respectively.

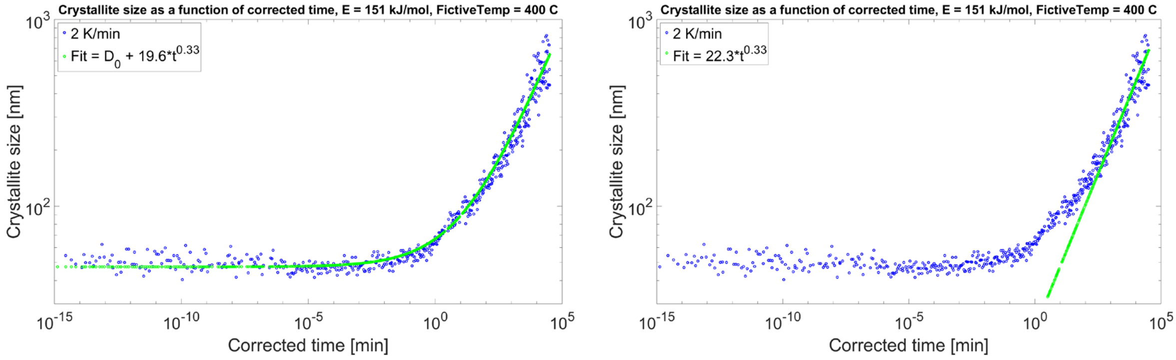

(a) (b)

Figure 61: Measured and fitted crystallite size of α-211 with Φ = 2 K/min as a function of the corrected time calculated using a fictive temperature of 400 °C and an activation energy of 151 kJ/mol. (a) fitted using $D = D_0 + kt^n$. (b) fitted using $D = kt^n$.

The solutions for the curve fitting of crystallite size as a function of the corrected time for the heating rate of 4 and 8 K/min using a fictive temperature of 400 °C and an activation energy of 151 kJ/mol using Equation (35) are shown in Figure 62. The fitted solution using Equation (35) provides a good representation of the measurement when Φ = 8 K/min, but a separation between the fitted solution and the measurement points is seen around a corrected time of 10^1 min for Φ = 4 K/min. The proportionality constants are determined as k = 14.9 nm/min$^{0.33}$ (4 K/min) and k = 16.0 nm/min$^{0.33}$ (8 K/min), which are only slightly below the value determined for a heating rate of 2 K/min.

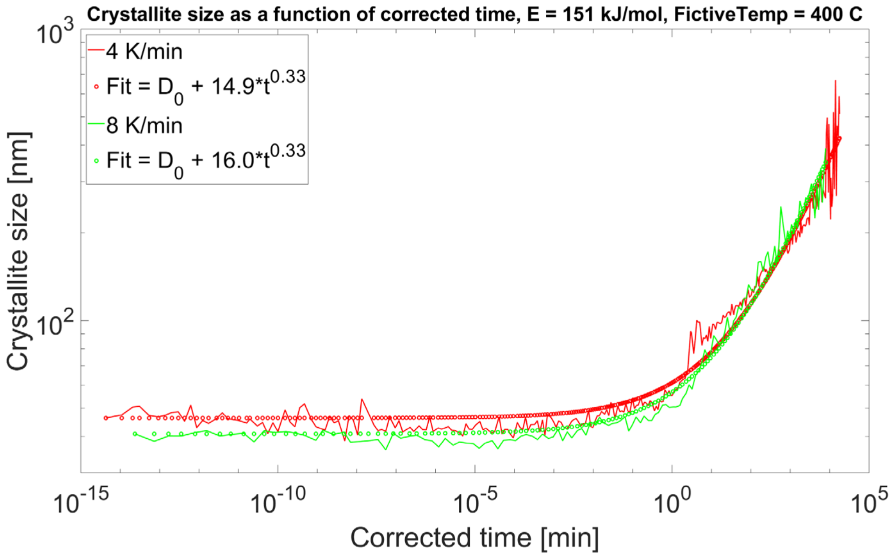

Figure 62: Measured and fitted crystallite size of α-211 with Φ = 4 and 8 K/min as a function of the corrected time calculated using a fictive temperature of 400 °C and an activation energy of 151 kJ/mol, fitted using $D = D_0 + kt^n$.

The solutions for the curve fitting of the crystallite size as a function of the corrected time for the heating rate of 2 K/min using fictive temperatures of 300 °C or 500 °C and an activation energy of 151 kJ/mol being fitted using Equation (35) are shown in Figure 63a and Figure 63b. The fitted solution using Equation (35) provides a good representation of the measurement and the proportionality constant decreases to 4 nm/min$^{0.33}$ when the fictive temperature is 300 °C and increases to 62 nm/min$^{0.33}$ when the fictive temperature is 500 °C.

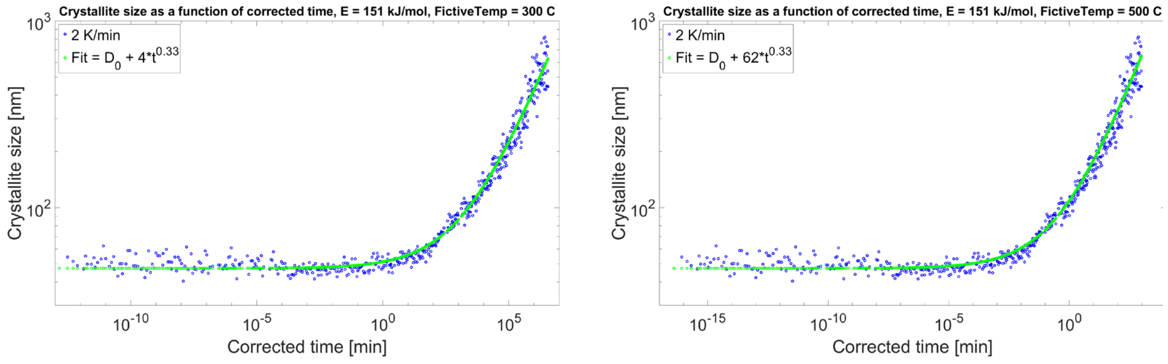

(a) (b)

Figure 63: Measured and fitted crystallite size of α-211 with Φ = 2 K/min as a function of the corrected time calculated using different fictive temperatures, an activation energy of 151 kJ/mol and fitted using $D = D_0 + kt^n$. (a) fictive temperature = 300 °C. (b) fictive temperature = 500 °C.

Prediction of grain size

The as-deposited length of the columnar ferrite grains (D_0) was calculated by line profile analysis to around 50 nm and matched the length determined from TEM dark field microscopy in Manuscript VII. The predicted grain size (column length) is between 105 nm (4 K/min) and 123 nm (2 K/min) for a sample that has been isothermally annealed at 400 °C for 1 hour when using Equation (35). The length of the ferrite grains determined by TEM in Manuscript VII for an isothermal annealing at 400 °C for 1 hour was 55 nm. As described in Manuscript VII, the difference between the grain size values from the line profile analysis and TEM could be related to the information depth of the diffraction analysis and the TEM sample produced from the middle of the Fe-C coating.

Summary

The described method to convert the isochronal measurement to isothermal annealing results at a fictive temperature that can be fitted to existing equations related to grain growth to evaluate the grain coarsening as a function of time at the fictive temperature of isothermal annealing. Ideally, the conversion could be a method to obtain the parameters required to predict grain coarsening and thereby estimate the decreasing hardness (solely based on changes of the ferrite phase) as a function of time.

The method is still a work-in-progress and the included material in this section is representative for the work that has been conducted within the period of the project.

8 Discussion

8.1 The phase constitution of the as-deposited Fe-C coating

The as-deposited Fe-C coating consists of four different phases as described in Manuscript VI being ferrite, hydrogen, an “organic compound” and the “nameless phase”. The phases ferrite, “organic compound” and “nameless phase” will be described individually below and put in relation to the prior understanding of the phase constitution of the as-deposited Fe-C as described in Section 2.3.1.

Ferrite

The strain free lattice spacings of ferrite, measured for multiple reflections by conventional XRD and EDD by tilting the sample in the strain-free direction, are identical with those for carbon-free ferrite and concluded that the phase is not martensite or tempered martensite as has been suggested [17–19,22,23]. The broadening of the ferrite peaks relates to their nanocrystalline grain size and the microstrain. The microstrain measured for ferrite was discussed in Manuscript VII as a result of the co-deposited elements, which cause the formation of phases in addition to ferrite, namely an “organic compound” and the “nameless phase”. The slight asymmetric peak profile that has been measured for the α-Fe cannot be caused by a chemical gradient, as this would require carbon or other elements to exist within the ferrite grains, which would have resulted in an increased strain-free lattice spacing. Instead, the peak asymmetry could be an effect of a stress gradient, but it has not been possible to confirm this or clarify its origin.

“Organic compound”

The “organic compound” was characterized solely by thermal analysis as described in Manuscript V and VI. The term “organic compound” was selected as this phase consists of the light elements that are being co-deposited from citric acid being carbon, oxygen, and hydrogen. The “organic compound” was found to exist up to a temperature of around 250 °C, hereafter it decomposes and releases hydrogen, carbon, and oxygen, and thereby enables the precipitation of magnetite and cementite. The “organic compound” likely is located in the grain boundaries of ferrite. The high carbon content within the as-deposited Fe-C coating could be part of this “organic compound” and explain the lack of diffraction peaks related to carbides in the as-deposited coating. The precipitation of magnetite and cementite, which form after the decomposition of the “organic compound”, increases the microhardness of the coating to around 950 HV0.025. The influence of the pH-value of the electrolyte on the carbon content of the Fe-C coatings was correlated to the equilibrium study of Fe^{2+} complexes with citric acid in an aqueous solution in Manuscript III. The Fe-C coatings carbon content was linked to the distribution of $FecitH_2^+$ complex as a function of the pH-value. Based on the present results, it can only be speculated that the $FecitH_2^+$ complex is co-deposited in the Fe-C coating and that the measured “organic compound” could be the ($citH_2^+$) part of the complex.

The XPS measurements that were described in Section 2.3.1.2 [17] supports the current interpretation that this phase is an organic one. The XPS measurement found that the phases related to the measured carbon signal were carboxyl groups, hydrocarbons, graphite, and a peak assigned to carbides. The measurement of hydrocarbons on the surface is due to contamination, but the surface contamination should be removed after sputtering for 25 min where the intensity from carboxyl groups is still measured. The presented XPS measurements in [17] does not allow the determination of the exact peak positions or peak intensities that would be required to search the databases related to specific phases and compounds being measured by XPS. Accordingly, the final identification of this “organic compound” is not possible at present.

“Nameless phase”

The “nameless phase” has been investigated using the complementary methods of materials characterization including diffraction analysis and thermal analysis and has been described in all manuscripts with the exception of Manuscript IV. The “nameless phase” is already present in the as-deposited coating, thus, it is caused by the deposition and has been observed for the deposition from both an iron(II)sulfate and an iron(II)chloride based electrolyte, thus, is does not include or require the elements sulfur or chlorine. The “nameless phase” is suggested as an iron hydroxide as hydrogen is part of the phase and its equilibrium transformation temperature was measured to be above 300 °C. The iron hydroxide has not been unambiguously identified, but the lattice spacing of the single free standing peak (“nameless peak”) measured by XRD along with the equilibrium transformation temperature measured by thermal analysis suggest ferrihydrite, as described in Manuscript VI. The measured intensity of the “nameless peak” changed as a result of the electrolytes pH-value, as described in Manuscript III, and the phase was not detected by XRD in the coatings deposited using the highest pH-value of the electrolyte. Instead, these specific coatings produced surface oxidation products that where visible by the naked-eye shortly after deposition. The information depth of conventional XRD is only a few micrometers and the lack of intensity from the “nameless peak” could be suggested as a result of the “nameless phase” being an iron hydroxide near the surface that transforms to an oxide in the presence of air. However, the reason why such transformation should only occur for the Fe-C coatings deposited at a high pH-value cannot be given yet. The location of the “nameless phase” within the Fe-C coating was discussed in Manuscript VII as a coherent or semi-coherent precipitate inside the ferrite grain. This would explain the origin of the high hardness of the as-deposited coatings in conjunction with the nanocrystalline grain size of ferrite. The transformation of the “nameless phase” increases the microhardness of the coating up to nearly 1300 HV0.025. The spike in hardness from the already high 950 HV0.025 (related to the precipitation of cementite and magnetite as a results of the decomposition of the “organic compound”) is suggested as a result of the location of the “nameless phase” being within the ferrite grains compared to the “organic compound” being in the grain boundaries. The in-situ diffraction analysis did not allow concluding on the transformation products from the “nameless phase”, but hydrogen, oxygen, and carbon were recorded during thermal analysis as described in Manuscript VI. It was also discussed in Manuscript VI that the ferrihydrite acts as a sink for organic matter and its transformation within the ferrite grains could therefore result in the precipitation of both magnetite and cementite inside the ferrite grains. Whereas, the decomposition of the “organic compound” would allow the precipitation of magnetite and cementite at the grain boundaries.

The presented material related to TEM analysis unfortunately does not reflect the amount of work that have been conducted in order to identify the “nameless phase” using SAED or high-resolution bright field. It has not been possible to measure a diffraction spot that matches the lattice spacing from the “nameless peak” measured by XRD or any additional spots not related to ferrite. This is independent of the sample preparation method being either electropolishing or FIB lift-out. The only additional intensity measured in the SAED patterns for the as-deposited Fe-C coatings have been a diffuse diffraction ring with a lattice spacing that matches magnetite. It was speculated in Manuscript V and VII that the measured intensity from magnetite might be a result of the easy transformation of the “nameless phase” or oxidation of the electron transparent samples during preparation and handling in air.

8.2 Effect of the operation conditions on the resulting Fe-C coating

The properties of the electrochemical deposited Fe-C coating is a result of the multiple operation conditions that intentionally can be adjusted prior to deposition. The parameters include the current density, chemical composition of the electrolyte, agitation, temperature, pH-value, additive, and substrate. The influence of some of the operation conditions have not been systematically investigated experimentally, like the temperature of the electrolyte and influence of agitation along with the additive, but are briefly discussed in relation to the present work.

Pre-treatment

The pre-treatment of a substrate prior to deposition was investigated in Manuscript IV. The results reveal that choosing a wrong method of pre-treatment leads to a low adhesion between the coating and substrate, which will result in failure during operation under load.

The pre-treatment that provided the highest mean value of work of adhesion between the Fe-C coating and hardened calmax steel was sulfuric acid, where the substrate acted as cathode during activation. However, the results pointed towards that it could be of interest to investigate the activation using dry acid as solution with the substrate acting as cathode, which was not included in the manuscript and has not been tested yet. It is suggested to do a risk-assessment before this specific method is tested as the partial reactions on the electrodes in a solution with fluoride acid could produce species of concern.

It has not been the intention of the presence work to find the ideal pre-treatment for any substrate that could be required for the deposition of the Fe-C coating. Instead, a method has been proposed in Manuscript IV that simply requires equipment for the metallographic preparation of a cross section and a Vickers microhardness instrument, both conditions are usually available, to test the adhesion of any combination of coating/substrate to benchmark the influence of different pre-treatments on the adhesion.

Substrate and thickness

It has been shown in Section 6.1 that the Fe-C coating can be deposited with the same material properties and having a hardness around 780 HV independent of the thickness of the coating and its substrate. These results are important for the industrial applications of the Fe-C coating, as it is not required to do initial tests related to the material properties of the coating before a new substrate material can be coated. However, specific substrates provides a low adhesion to the coating, which were advantages for the scientific purpose of thermal analysis and chemical analysis of the Fe-C coating, but would cause immediate failure during operation under load. However, a low adhesion is required for applications that require specific geometries that can be produced by electroforming, but this has not been an area of attention for the Fe-C coating yet. It is therefore recommend for the purpose of wear resistance or restoration of worn components, to estimate the adhesion between a new type of substrate and the Fe-C coating using the method described in Manuscript IV or another technique for the quantification of adhesion.

The pH-value of the electrolyte

The pH-value of the electrolyte is essential to maintain the between 2.5 and 3.0 in order to achieve the highest current efficiency and avoid the development of oxidation products on the surface of the coating after deposition, as described in Manuscript III. The carbon content of the as-deposited Fe-C coatings was influenced by the pH-value of the electrolyte, but the hardness of the coating was independent. The change in carbon content is of high scientific interest, but is not fully understood yet. For industrial applications, it is perhaps of higher interest that the hardness remains around 780 HV even when the pH-values is outside of the suggested operation condition.

Current density and iron concentration

The influences of the current density and the iron concentration are discussed together as the ratio between these two operation conditions is the determining criterion. This is shown in Manuscript II, where the same Fe-C coating could be deposited when the applied current density and the iron concentration were increased simultaneously. The experimental procedure in Manuscript II increased the current density by 0.5 A/dm^2 when the iron concentration was increased by 8 g/L (40 g/L $FeSO_4 \cdot 7H_2O$), compared to the operation conditions used in the Manuscripts I, V, VI, and VII. The deposition rate and current efficiency increased for the operation conditions using the highest iron concentration and current density. These operation conditions are therefore suggested for an industrial application, as they will save both time and energy.

Citric acid concentration

The influence of the citric acid concentration on the appearance of the coating was investigated in Section 6.2.2 and showed that is it not beneficial to increase the concentration above 1.2 g/L, independent of the iron concentration and the applied current density. An increase in citric acid will result in an inconsistent dull and brunt appearance. The citric acid will be consumed during deposition as described in Manuscript III and shall be replenished. The hardness of the coatings was found to be independent of the consumption of the citric acid up to the estimated amount of 12.5% that was tested.

Additive

The use of citric acid as additive was maintained during the present work, as the obtained hardness of the as-deposited Fe-C coating was reproducibly measured around 800 HV being among the highest presented hardness values in literature. The benefit of using citric acid is that the chemical is non-toxic, in-expensive and widely available along with its buffer properties in the electrolyte, which are beneficial for an industrial application. The use of citric acid as the only additive ensures the simplicity of the electrolyte with iron as the only counterpart that needs to be adjusted during long-term operation. The co-deposition of the additive is for some electrodeposited coatings viewed as an unwanted impurity, but could instead provide a different method of alloying using a specific additive that include a desired element. The CAS library of organic compounds includes millions of different organic structures with different radical groups and different elemental constitutions, which are currently registered. For example, the use for amino acids as additive should complex with Fe^{2+} and enable the co-deposition of nitrogen along with carbon, oxygen, and hydrogen.

Temperature of the electrolyte

The electrolyte temperature will influence the mobility of ions in the electrolyte and influences the diffusion and reaction overpotentials. Increasing the temperature should result in the deposition of larger grains on average and a higher evaporation of the electrolyte. The larger grains could decrease the hardness of the deposit and the higher evaporation will require more maintenance of the electrolyte. A lower electrolyte temperature could lead to a lower current efficiency as the diffusion of iron ions towards the cathode surface is reduced. With the currently applied electrolyte temperature of 50 °C an as-deposited Fe-C coating with a hardness of 800 HV can be deposited without evaporation being an issue.

Agitation

Testing the influence of the agitation is not straightforward as different methods of agitation can be applied. Further, the influence of the sample geometry and the quantification of agitation are complex. The agitation that has been applied in the present work has either been stirring of the electrolyte by a rotating magnet on the heating plate or rotation of the sample around the center axis of the cylinder workpieces. The purpose of the magnetic stirring was to ensure a uniform temperature in the electrolyte and the rotation of the workpiece was to ensure a uniform thickness of the coating. It has been proposed that a high stirring does not benefit the deposit [19] and the same impression was obtained during the present work. However, no systematic study has been performed.

8.3 Suggestions for an industrial electrochemical deposition setup

The small laboratory-scale operational setup that has been used to deposits the samples included in the present work has been described in details in Section 4.1.1 along with the partial reactions that proceed in the electrolyte during deposition and when no deposition is conducted. This lab-scale setup was not optimized for long-term industrial use as the deposition of samples was infrequent and the electrolyte was replaced for each new deposition.

The suggestions for large-scale long-term industrial use is described below and proposes methods to minimize the challenges that are related to iron deposition being oxidation of Fe^{2+} to Fe^{3+}, controlling the pH-value and ensuring a stable chemical composition.

One bath solution

The one bath solution having a large container and an electrolyte that needs to be operational for a long period of time is illustrated in Figure 64. The setup is similar to the small scale operation using sacrificial anodes with the modifications and additions of some components. The heating element is positioned in the electrolyte to maintain a stable operation temperature. The filtration system removes solid impurities from the electrolyte and acts as a container shielded from current field lines where the pH-value of the electrolyte can be measured in real-time. The plastic balls floating on the electrolyte will limit the electrolyte contact with air and reduce oxidation of Fe^{2+} to Fe^{3+}. There are commercial available solutions for automatic continuously pH-adjustments, as would be highly recommended during operation to avoid large pH-variations influences on the resulting deposits. The disadvantages of the small-scale setup shown in Figure 23 compared to the large-scale setup in Figure 64 is that the anode is consumed during operation and needs to be changed periodically. The iron concentration in the electrolyte will increase, as the cathodic current efficiency is below 100%, as shown in Manuscript I. It is therefore suggested for an industrial operation to electroplate using a fixed voltage compared to a fixed current as used during the present work. By using the fixed voltage on the power supply, the current will increase gradually as a result of the change in the chemical composition during deposition. The applied voltage will be different for samples having different sizes and geometries and also depend on the specific state of the electrolyte. The fixed voltage for a specific sample could be the same value as measured after the initial 5 min of deposition using a fixed current that would be required for the surface area of the sample and the current density based on the iron concentration of the electrolyte.

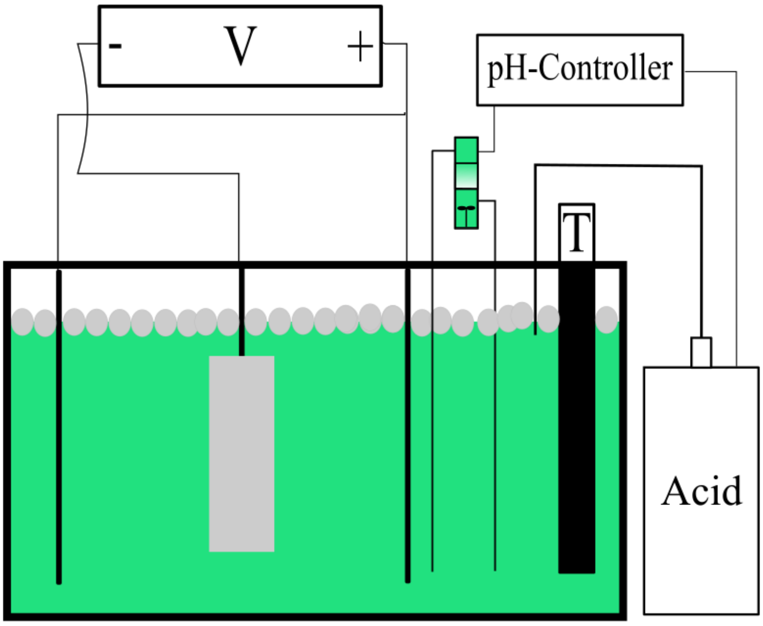

Figure 64: Operation conditions for a one bath Iron-Carbon deposition using sacrificial iron anodes and controlling the pH-value automatically using sulfuric acid.

Two baths solution

A more advanced setup is to apply an additional bath for controlling the pH-value and use an inert anode inserted in a nafion membrane for deposition of the requested workpiece, as illustrated in Figure 65. The inert anodes are used in the deposition bath to have a fixed geometry of the anode optimized for a specific workpiece. Sacrificial iron anodes are used in the adjustment bath with a cathode that does not have an application. The deposition bath using inert anodes will consume iron ions from the electrolyte and decrease the pH-value as described in Section 4.1.1.3. The adjustment bath using the sacrificial anodes will raise the iron concentration and the pH-value as the current efficiency of the process is below 100%. The electrolyte from the adjustments bath is pumped to the deposition bath through a filter that removes solid impurities and acts as a shielded container from the current field lines that allows the measurement of the pH-value. The deposition bath is placed slightly higher compared to the adjustments bath such that the electrolyte returns to the adjustments bath through a drain. This method ensures that the electrolytes surface in the deposition bath is maintained at the same level during deposition and, consequently, the evaporation will be limited to the adjustment bath. The pH-controller needs to be connected to the power supply adjusting the current in the adjustments bath and regulate the current density in real-time based on the pH-value to counter the effect of electrolysis from the inert anode lowering the pH-value. The iron concentration in this setup also needs to be monitored to avoid plating outside of the optimal operation condition. If a low amount of iron is measured, the missing concentration can be applied using iron-salts and the electrolyte can be diluted with water if the concentration of iron is too high. The two bath setup has been tested as a proof-of-concept with positive results [34].

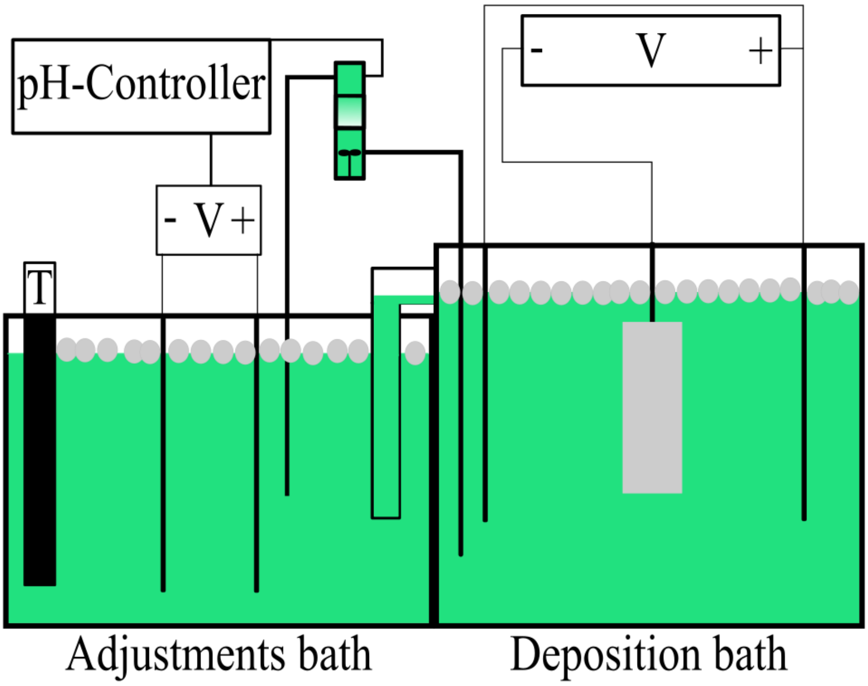

Figure 65: Operation conditions for a two baths Iron-Carbon deposition setup. Inert anodes with a nafion membrane is used in the bath where the workpiece is plated and sacrificial iron anodes is used in the controlling bath.

8.4 Fe-C coatings as an alternative to hard chrome

The present study has not included an investigation of the corrosion resistance of the Fe-C coatings as the coatings are currently indented for lubricated environments. The co-deposition of an additional element that could enhance the corrosion resistance capability of the coating was discussed in Section 4.1.2 along with the suggestion on how to proceed this development. The lack of corrosion resistance of the Fe-C coating limits the potential applications compared to the more versatile hard chrome.

However, the impact on the Danish hard chrome industry by the confirmed lowering of the threshold limit on chrome(VI) on 1/6-2020 and the prospect of a further reduction of the limit after four years is yet to be seen, but an investment for new staff protection equipment, shielding and/or new ventilation systems could become relevant. The Danish hard chrome industry needs to evaluate if such potential investments are meaningful to produce a hard chrome coating for a specific purpose with the risk that the current permissions provided by REACH are not renewed.

The wear resistance of the as-deposited Fe-C coating compared to hard chrome was tested in dry conditions using the Taber test (provided by a collaborator) and the results revealed a similar performance. The results have not been included in this present work due to confidentiality, but are shared between the project partners. The wear resistance of the as-deposited Fe-C coatings deposited on the cylinder samples shown in Figure 27 is currently being tested by OCAS NV, but the final results have not been obtained. The limited wear test results show the potential of the as-deposited Fe-C coatings as a wear resistant coating, but more tests are needed to conclude whether the Fe-C coatings perform similar to hard chrome in the multiple types of possible wear attacks. The post deposition thermal treatment can increase the hardness of the Fe-C coating, as the present results clearly reveal, but would be an additional cost and could influence the substrate condition. The ability for thermal treatments will also depend on the coating/substrate combination and precautions should be taken for a high difference in the coefficient of thermal expansion between coating and substrate to avoid the risk of delamination and/or cracks in the coating.

The next step is up-scaling the process for industrial large-scale deposition, which opens up for testing and implementation of the Fe-C coatings in industry. It is suggested that the Fe-C coating is initially employed as method to restore worn components with an additional coating added for corrosion resistance. This could be an attractive opportunity with the current political ambition of having a high focus on sustainability, circular economy, and environmental protection. This will provide experience on long-term operation and test the ability of the Fe-C coating in different applications. Alongside this operation, further research towards the wear resistance of the Fe-C coatings could continue along with the development of Fe-C-X coatings that could improve the corrosion

9 Summary

The layout of the doctoral thesis provides a detailed conclusion following the presented results in the individual sections. The summary of the significant conclusions from the manuscripts will be provided in bullet points sub-divided into the matters related to the operation conditions, the internal structure of the as-deposited Fe-C coating and the thermal stability of the Fe-C coating.

Operation conditions

- The citric acid concentration in the electrolyte should not exceed 1.2 g/L independent of the iron concentration and the applied current density.
- The same internal structure can be deposited when the iron concentration in the electrolyte and the applied current density are adjusted simultaneously to control the mass transfer rate.
- The pH-value of the electrolyte shall be maintained between 2.5 and 3.0 to avoid oxidation products being developed on the surface in dry conditions after deposition and to maximize the current efficiency of the process.

The internal structure of the as-deposited Fe-C coating

- The microstructure is nanocrystalline with column-like grains elongated in the growth direction.
- The coating contains around 0.9 wt% carbon and mainly consists of ferrite with a strong <311> fiber texture without the presence of carbides or oxides.
- The lattice spacings of ferrite in the strain-free directions are matching carbon-free ferrite.
- The “nameless phase” has not been identified unambiguously, but is suggested as an iron-hydroxide positioned as a coherent or semi-coherent precipitate inside the ferrite grains.
- The high amount of carbon is co-deposited as the “organic compound”.
- The residual stresses in the coating after deposition are in compression and below 200 MPa.
- The hardness of around 800 HV is independent of the carbon content, thickness of the coating and the substrate.

The thermal stability of the Fe-C coating

- The decomposition of the “organic compound” enables the precipitation of cementite and magnetite and will increase the hardness to around 950 HV.
- The transformation of the “nameless phase” will further increase the hardness, for example to around 1300 HV, when annealing at a temperature of 300 °C where grain coarsening is avoided.
- The thermal stability of the ferrite phase is affected by the transformation of the ”organic compound” and the “nameless phase”. At temperatures relevant for potential industrial applications of components deposited with Fe-C coatings, the coatings remain stable.

10 Outlook

The presented results establish the foundation for the next step of up-scaling the electrochemical deposition of Fe-C coatings for industrial application. The present work has explained in detail the recommendations for regulating the operation conditions to ensure a reproducible deposition with the same internal structure and mechanical properties. The suggestions to the work that would contribute to the present understanding of the internal structure and to improve the materials properties as well as being relevant for industrial applications are provided as follows

- The wear resistance capabilities of the Fe-C coatings should be investigated further using elevated temperatures and/or in lubricated environments to better understand the industrial applications, where the Fe-C coatings can be considered as an alternative to hard chrome.
- Change the citric acid to an amino acid to co-deposit nitrogen along with carbon and oxygen.
- The co-deposition of additional elements to increase the corrosion resistance by co-deposition of an element being less noble than iron or to increase the hardness by solid solution strengthening. The use of metallic salts or organometallics could provide different growth characteristics and grain refinement mechanisms.
- The identification of the "organic compound" has been attempted to investigate by nuclear magnetic resonance (NMR) spectroscopy using a free-standing Fe-C coating dissolved in sulfuric acid. The measurement was unsuccessful due to the complex capability between the "organic compound" and the dissolved iron ions. The free-standing Fe-C coating was also mashed into a powder for a solid-state NMR investigation, but the measurement was unsuccessful due to the magnetic field of iron and the low amount of carbon. It is recommended to use C^{13} marked citric acid, as the carbon signal will be increased by a factor of 100 for NMR. Two methods that could be conducted are: (1) the zero-field NMR would use the magnetic field of iron instead of an external magnetic field and (2) dissolve free-standing Fe-C in sulfuric acid, then increase the pH-value with NaOH for iron to settle as sediment, which will minimize complex formation disturbing the signal in NMR spectroscopy.
- The APT measurements using electric pulses resulted in multiple sample failures independent of the sample preparation method being FIB lift-outs or electropolishing by the microloop method. The APT method using laser pulses is recommended to investigate the distribution of carbon and oxygen in the as-deposited Fe-C coating. The APT measurement could also determine the position of the "organic compound" by measuring a sample ex-situ annealed at 250 °C for 24 hours where the "nameless phase" is still intact and the position of magnetite and cementite should be identical to the position of the decomposed "organic compound".
- Up-scaling from the laboratory setup to a long-term large-scale industrial production should start in collaboration with a customer that could risk of being affected by REACH not renewing the authorization to use chromium trioxide for protection of their specific products.

11 References

[1] M. Panunovic, M. Schlesinger, Fundamentals of Electrochemical Deposition, Wiley, 2006.

[2] R. Winand, Electrocrystallization - theory and applications, Hydrometallurgy. 29 (1992) 567–598.

[3] F.A. Lowenheim, J. Davis, Modern Electroplating, Wiley, 2010.

[4] G. Milazzo, S. Caroli, Tables of Standard Electrode Potentials, Wiley, 1978.

[5] P. Møller, L.P. Nielsen, Advanced Surface Technology, 2013.

[6] H. Fischer, Wirkungen der Inhibitoren bei der Elektrokristallisation, Electrochim. Acta. 2 (1960) 50–96.

[7] H.E. Cleaves, J.G. Thompson, Alloys of Iron Research, 1st ed., 1935.

[8] M. Schlesinger, M. Paunovic, Electrodeposition of Iron and Iron Alloys, in: Mod. Electroplat., 5th ed., Wiley, 2010: pp. 309–326.

[9] A.C. Becquerel, Considerations on electrocemical decomposition and on the reduction of iron oxide, zirconia and magnesia with the aid of low-voltage electic current, Ann. Chin. Phys. 48 (1831) 337–353.

[10] W.C. Roberts, On the electrodeposition of iron, Chem. News. 31 (1875) 137.

[11] W.C. Roberts-Austen, The electrodeposition of iron, J. Iron Steel Inst. 1 (1887) 71–74.

[12] A. Watt, Electrolysis of iron salts, Electrician. 55; 135; 1 (n.d.).

[13] G. Vie, Properties and preparation of electrolic iron, Ann. Chim. Anal. Chim. Appl. 1 (1919) 175–177.

[14] F. Foerster, V. Herold, O. Mustad, H. Lee, The Electrochemical Properties of Iron, Abhand. Deutch. Bunsen Hes. 2 (1909) 59–81.

[15] M. Izaki, H. Enomoto, T. Omi, Hardness and Carbon Content of Fe Electroplate from Sulfate Bath Containing l-Ascorbic Acid and Citric Acid, J. Surf. Fin. Soc. Jpn. 40 (1989) 1304–05.

[16] M. Izaki, H. Enomoto, A. Nakae, S. Terada, Y. Eiko, T. Omi, Phase Transformations and Hardness Changes in Electrodeposited Alloy Films Iron-carbon alloy films., J. Surf-Fin. Soc. Jpn. 45 (1994) 1303–1309.

[17] Y. Fujiwara, T. Nagayama, A. Nakae, M. Izaki, H. Enomoto, E. Yamauchi, Electrodeposition of Fe-C Alloys from Baths Containing Dicarboxylic Acids with a Linear Alkyl Chain, J. Electrochem. Soc. 143 (1996) 2584–2590.

[18] M. Izaki, T. Omi, Structural characterization of martensitic iron-carbon alloy films electrodeposited from an iron(ll) sulfate solution, Metall. Mater. Trans. A. 27A (1996) 483–486.

[19] Y. Fujiwara, M. Izaki, H. Enomoto, A. Nakae, Effects of Hydroxycarboxylic Acids on the Electrodeposition of Fe-C Alloys, Denki Kagaku. 7 (1993) 840–842.

[20] M. Izaki, H. Enomoto, T. Omi, Structure and Hardness of Fe-C alloy Film Electrodeposited from an Iron Sulfate Electrolyte, J. Japan Inst. Met. 56 (1992) 636–640.

[21] Y. Fujiwara, M. Izaki, H. Enomoto, T. Nagayama, E. Yamauchi, A. Nakae, Optimization of bath composition for hard Fe-C alloy plating, J. Appl. Electrochem. 28 (1998) 855–862.

[22] A.S.M.A. Haseeb, M.Z. Huq, Electrodeposition of martensitic iron-carbon alloy coatings at room temperature, Met. Finish. 95 (1997) 30–34.

[23] M. Panayotova, Deposition of Fe–C alloy on structural steel and cast iron for repair of worn machine parts, Surf. Coat. Technol. 124 (2000) 266–271.

[24] N. Fukumuro, S. Kojima, M. Fujino, Y. Mizuta, T. Maruo, S. Yae, Y. Fukai, Hydrogen-induced superabundant vacancies in electrodeposited Fe-C alloy films, J. Alloys Compd. 645 (2015) 404–407.

[25] T. Müller, J. Grimwood, A. Bachmaier, R. Pippan, Electrodeposition of Fe-C alloys from citrate baths: Structure, mechanical properties, and thermal stability, Metals. 8 (2018) 1–13.

[26] A.S.M.A. Haseeb, Y. Hayashi, M. Masuda, M. Arita, On the nature of the electrochemically synthesized hard Fe-0.96 mass pct C alloy film, Metall. Mater. Trans. B. 33B (2002) 921–927.

[27] W.Y. Choo, J.Y. Lee, Thermal Analysis of Trapped Hydrogen in Pure Iron, Metall. Trans. A. 13A (1982) 135–140.

[28] A.S.M.A. Haseeb, T. Nishida, M. Masuda, Y. Hayashi, Mössbauer investigation on electrodeposited Fe-C and Fe-Ni-C alloys, Scr. Mater. 44 (2001) 519–523.

[29] A.S.M.A. Haseeb, M. Arita, Y. Hayashi, Thermal decomposition study of electrodeposited Fe-C and Fe-Ni-C alloys by differential scanning calorimetry, J. Mater. Sci. 6 (2001) 4739–4743.

[30] L.I.U. Cheng, A. Böttger, T.H. de Keijser, E.J. Mittemeijer, Lattice parameters of iron-carbon and iron-nitrogen martensites and austenites, Scr. Metall. Mater. 24 (1990) 509–514.

[31] M.J. Van Genderen, A. Böttger, R.J. Gernik, E.J. Mittemeijer, Early Stages of Decomposition in Iron-Carbon and Iron-Nitrogen Martensites: Diffraction Analysis Using Synchrotron Radiation, Metall. Trans. A. 24A (1993) 1965–1973.

[32] M.J. Genderen, M. Isac, a. Böttger, E.J. Mittemeijer, Aging and tempering behavior of iron-nickel-carbon and iron-carbon martensite, Metall. Mater. Trans. A. 28 (1997) 545–561.

[33] H.L. Yakel, Crystal structures of stable and metastable iron-containing carbides, Int. Met. Rev. 30 (1985) 17–40.

[34] C.R. Jørgensen, K. Løkkegaard, J.O. Nielsen, Udvikling af hårdkrom erstatning Elektrokemiske jernbelægninger, 2017.

[35] H. Okamoto, M.E. Schlesinger, E.M. Mueller, ASM Handbook, Volume 3, Alloy Phase Diagrams, 2016.

[36] M. Pourbaix, Atlas of electrochemical equilibria in aqueous solutions, 1974.

[37] V. Hauk, Structural and Residual Stress Analysis by Nondestructive Methods, Elsevier, 1997.

[38] G.K. Williamson, W.H. Hall, X-ray line broadening from filed aluminium and wolfram,

Acta Metall. 1 (1953) 22–31.

[39] T.H. de Keijser, J.I. Langford, E.J. Mittemeijer, A.B.P. Vogels, Use of the Voigt function in a single-line method for the analysis of X-ray diffraction line broadening, J. Appl. Crystallogr. 15 (1982) 308–314.

[40] E.J. Mittemeijer, U. Welzel, C. Genzel, I.. A. Denks, M. Klaus, Modern Diffraction Methods, Wiley, 2013.

[41] E. Macherauch, P. Müller, Das sin2psi-Verfahren der röntgenographischen Spannungsmessung, Zeitschrift Für Angew. Phys. 13 (1961) 305–312.

[42] U. Welzel, E.J. Mittemeijer, Applicability of the crystallite group method to fibre textured specimens, Mater. Sci. Forum. 443–444 (2004) 131–136.

[43] C. Genzel, I.. A. Denks, J. Gibmeier, M. Klaus, G. Wagener, The materials science synchrotron beamline EDDI for energy-dispersive diffraction analysis, Nucl. Instruments Methods Phys. Res. A. 578 (2007) 23–33.

[44] D. Apel, M. Klaus, C. Genzel, D. Balzar, Rietveld refinement of energy-dispersive synchrotron measurements, Zeitschrift Fur Krist. 226 (2011) 934–943.

[45] A.C. Thompson, X-ray data booklet, 2009.

[46] R. Snyder, J. Fiala, H.J. Bunge, Defect and microstructure analysis by diffraction, 2000.

[47] C. Esling, E. Bechler-Ferry, H.J. Bunge, Numerical calculation of the odd part of the texture function, J. Phys. Lettres. 42 (1981) 141–144.

[48] Y. Leng, Materials Characterization, Second edi, Wiley, 2013.

[49] F. Niessen, A. Burrows, A.B. da S. Fanta, A systematic comparison of on-axis and off-axis transmission Kikuchi diffraction, Ultramicroscopy. 186 (2018) 158–170.

[50] F. Archie, M.Z. Mughal, M. Sebastiani, E. Bemporad, S. Zaefferer, Anisotropic distribution of the micro residual stresses in lath martensite revealed by FIB ring-core milling technique, Acta Mater. 150 (2018) 327–338.

[51] A.M. Korsunsky, M. Sebastiani, E. Bemporad, Residual stress evaluation at the micrometer scale: Analysis of thin coatings by FIB milling and digital image correlation, Surf. Coatings Technol. 205 (2010) 2393–2403.

[52] D.B. Williams, C.B. Carter, Transmission Electron Microscopy, 2009.

[53] L. Tang, D.E. Laughlin, Electron Diffraction Patterns of Fibrous and Lamellar Textured Polycrystalline Thin Films. I. Theory, J. Appl. Crystallogr. 29 (1996) 411–418.

[54] R.F. Egerton, Electron Energy Loss Sepctroscopy in the electron microscope, 1986.

[55] W. Lefebvre-Ulrikson, F. Vurpillot, X. Sauvage, Atom Probe Tomography, 2016.

[56] L. Cheng, C.M. Brakman, B.M. Korevaar, E.J. Mittemeijer, The Tempering of Iron-Carbon Martensite; Dilatometric and Calorimetric Analysis, Metall. Trans. A. 19A (1988) 2415–2426.

[57] E.J. Mittemeijer, Review Analysis of the kinetics of phase transformations, J. Mater. Sci. 27 (1992) 3977–3987.

[58] H.E. Kissinger, Reaction Kinetics in Differential Thermal Analysis, Anal. Chem. 29 (1957) 1702–1706.

[59] Smithells Metal Reference Book, 7th ed., Butterworth-Heineman, London, 1992.

[60] P.A. Beck, J.C. Kremer, L.J. Demer, M.L. Holzworth, Grain Growth in High-Purity Aluminium and in an Aluminiummagnesium Alloy, Trans. Am. Inst. Min. Metall. Eng. 175 (1948) 372–400.

[61] J.E. Burke, Some Factors Affecting the Rate of Grain Growth in Metals, Trans. Am. Inst. Min. Metall. Eng. 180 (1949) 73–91.

[62] R.A. Vandermeer, H. Hu, On the Grain Growth Exponent of Pure Iron, 1994.

[63] T.R. Malow, C.C. Koch, Grain growth in nanocrystalline iron prepared by mechanical attrition, Acta Mater. (1997).

[64] J.T. Sebastian, O.C. Hellman, D.N. Seidman, New method for the calibration of three-dimensional atom-probe mass spectra, Rev. Sci. Instrum. 72 (2001) 2984–2988.

[65] M.K. Miller, Atom Probe Tomography and the Local Electrode Atom Probe, 2000.

[66] L. Yang, Materials Characterization, 2013.

[67] N. Wollschläger, L. Palasse, I. Häusler, K. Dirscherl, F. Oswald, S. Narbey, E. Ortel, V.D. Hodoroaba, Characterization of the inner structure of porous TiO2 nanoparticle films in dye sensitive solar cells (DSSC) by focused ion beam (FIB) tomography and transmission Kikuchi diffraction (TKD) in the scanning electron microscope (SEM), Mater. Charact. 131 (2017) 39–48.

12 Appendix

12.1 Atom probe tomography

Introduction

The atom probe tomography (APT) uses a field evaporation of atoms to build a 3-dimensional reconstruction of the evaporated volume by analysis of the time of flight and the impact of the individual ions on a 2D detector [55]. The field evaporation from the needle-shaped sample was controlled by imposing a high voltage field by a local electrode. The specimens were needles of a sharp angle (less than 20°) with a radius of curvature in the range of 20-100 nm at its apex to enable field evaporation. The nature of individual ions can be determined by converting the time of flight to a mass to charge ratio. The main purpose of the APT measurement was to investigate the distribution of carbon and oxygen in the as-deposited coating. Three to five similar measurements would be necessary to conclude whether the carbon has either segregated at grain boundaries or other lattice defects or exists in significant supersaturation within the ferrite lattice.

The instrument and software

All investigations were carried out at CNRS, Normandie University in Rouen, France on a CAMECA LEAP 4000 HR atom probe. The mass of the individual ions is measured between 0 to 200 u.

The commercial software IVAS 3.8.0 was used for data analysis. The reconstruction, bowl and voltage corrections was kindly provided by the instrument responsible Frederic Danoix using well known iron-based samples, and the mass spectrum was calibrated on a couple of known peaks [64].

The identification of an element based on the mass to charge ratio can be complex as both the isotope state and ion charge state needs to be taken into account. For example, iron $^{56}Fe^{3+}$, $^{56}Fe^{2+}$or $^{56}Fe^{+}$ will be measured at 18.645, 27.967 and 55.935 u. The elements can also combine in the vacuum during their flight from the sample tip to the detector and be measured as for example $^{56}Fe^{16}O^{+}$ at 71.93 u. The mass-to-charge for the individual isotopes and ions charge state was found in [65].

Sample preparation

The lift-out technique was used to prepare samples for the atom probe tomography (APT) investigation as described in Section 4.3.3.2. The APT samples was prepared such that the grain boundaries within the needle were either perpendicular or rotated by 45° compared to the direction of the needle (cf. Figure 32).

An APT coupon having 36 pillars for positioning a sample was used as sample holder for the FIB prepared APT samples. The initial steps 2-8 of the lift-out to produce an APT sample are similar to that of a lift-out to produce an electron transparent lamella for TEM as illustrated in Figure 33. The initial deposition of the protective platinum layer on top of the ROI is not used, as it would be a contamination of the tip of the needle.

The FIB lift-out sample attached to the Omniprobe was positioned on the top of a pillar on the APT coupon and welded onto the pillar by platinum deposition using the ion beam (30 kV, 26 pA). The part of the sample attached to the pillar was milled from the sample attached to the

Omniprobe using the ion beam (30 kV, 0.44 pA). Each lift-out from the deposit was separated into five samples and welded to a pillar each. The samples on top of the pillars were further welded by platinum deposition using the ion beam (30 kV, 26 pA) on the opposite side of the first weld on the pillar. The samples on the pillars were thinned stepwise using an initial ion beam (30 kV, 90 pA) and annular milling until a diameter around 100 nm was achieved using the final beam (30 kV, 26 pA). The samples were cleaned from the top using a low voltage cleaning step from the ion beam (5 kV, 26 pA).

A free-standing as-deposited coating with a thickness of 360 µm was cut into a 360 x 360 µm match having a length of 1.5 cm. The match was sharpened by the responsible person at the APT-instrument using the microloop method as shown in Figure 66. The setup is composed of a direct current power supply, an optical microscope to magnify the ROI, a specimen stage, and a platinum microloop of 5 mm diameter. A drop of a low concentrated electrolyte solution is put in the microloop. The specimen and the microloop are connected to the power supply with the microloop acting as cathode. The specimen is electropolished when it penetrates the electrolyte solution in the microloop and current is applied. The electropolishing is done in several steps until the needle had the requested geometry. The needle was rinsed in ethanol and dried following the electropolishing to prevent oxidation.

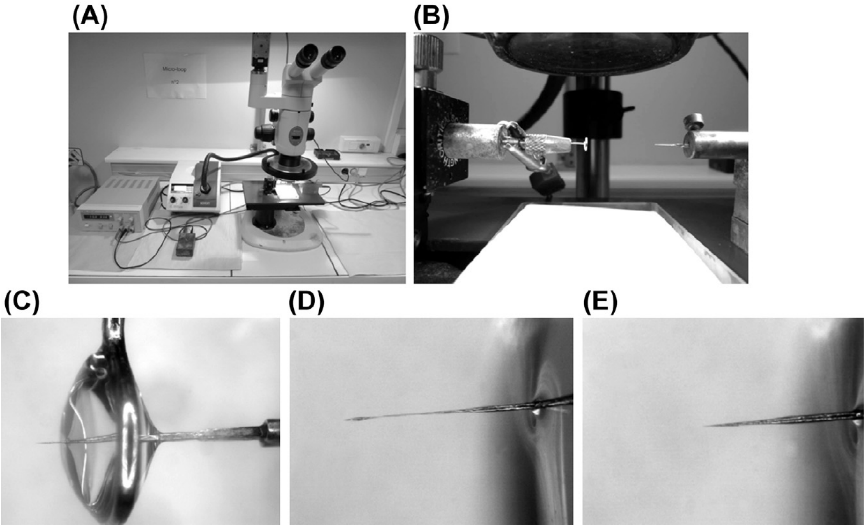

Figure 66: Specimen preparation using the microloop method. (A) Overview of the assembly composed of a direct current voltage power supply, an optical microscope, a specimen stage, and a platinum microloop. (B) Closer view of the specimen facing the microloop. (C) A drop of low concentrated solution is put in the microloop and the specimen is penetrating the electrolyte (D) Image of a sharped needle (E) The needle is removed from the neck with short applications of voltage. Figure from [55].

Results

The APT measurement caused the majority of the FIB and electropolished prepared samples to break prematurely during the measurement. The only one measurement with a FIB prepared sample having its grain boundary with a 45° angle compared to the direction of the APT needle proceeded for a longer period of time and the result is shown as the 3-dimensional reconstruction of the elements iron, carbon, oxygen, and hydrogen in Figure 67. The measurement contained a significant amount of gallium ions from the sample preparation process, which impedes the analysis. The 3-dimensional reconstruction (cf. Figure 67) has a length of 90 nm and a width of 50 nm. The elemental concentration of iron is uniform in the measured volume. The carbon map shows there is a uniform concentration of carbon measured by the time of flight detector as single atoms and a thin region with a 45° tilt compared to the direction of the needle with a higher quantity of carbon measured as combined carbon atoms (C_3). The thin region with a 45° compared to the direction of the needle corresponds to a grain boundary separating two ferrite grains. The oxygen map shows that the amount of oxygen in the grain below the grain boundary is higher compared to the grain above the grain boundary. The highest oxygen content is measured within the grain boundary. The hydrogen map shows a higher content in the grain below the grain boundary compared to the grain above.

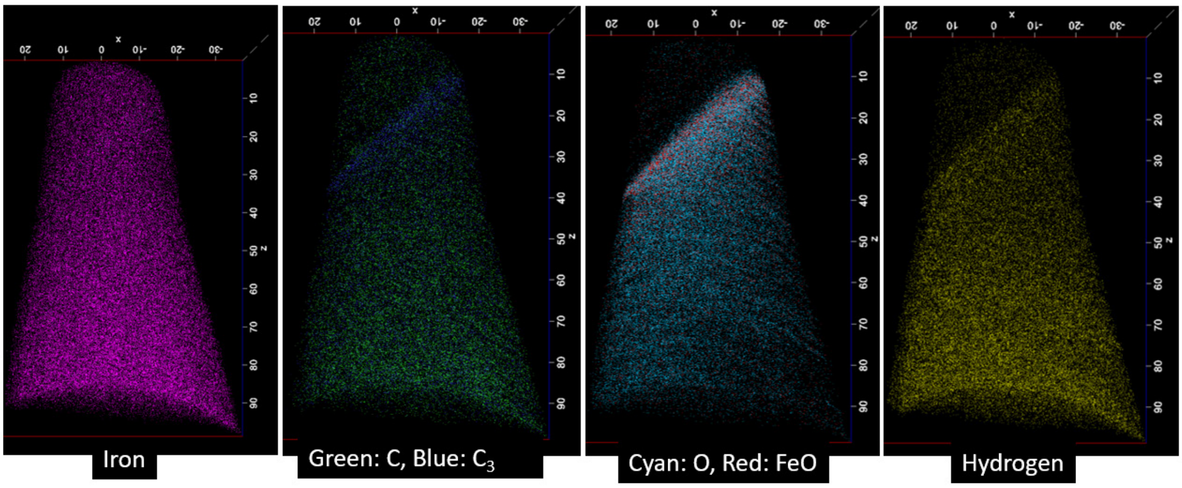

Figure 67: APT atom maps of iron, carbon, oxygen, and hydrogen.

The measured quantity of the light elements are plotted as a contour region within the measured volume with the highlighted region having an atomic content above the value described below the map as shown in Figure 68. The atomic maps shows that the highest contents of carbon and oxygen are within the grain boundary. The highlighted regions of carbon also show multiple small volumes uniformly spread in both grains with an increased content of carbon.

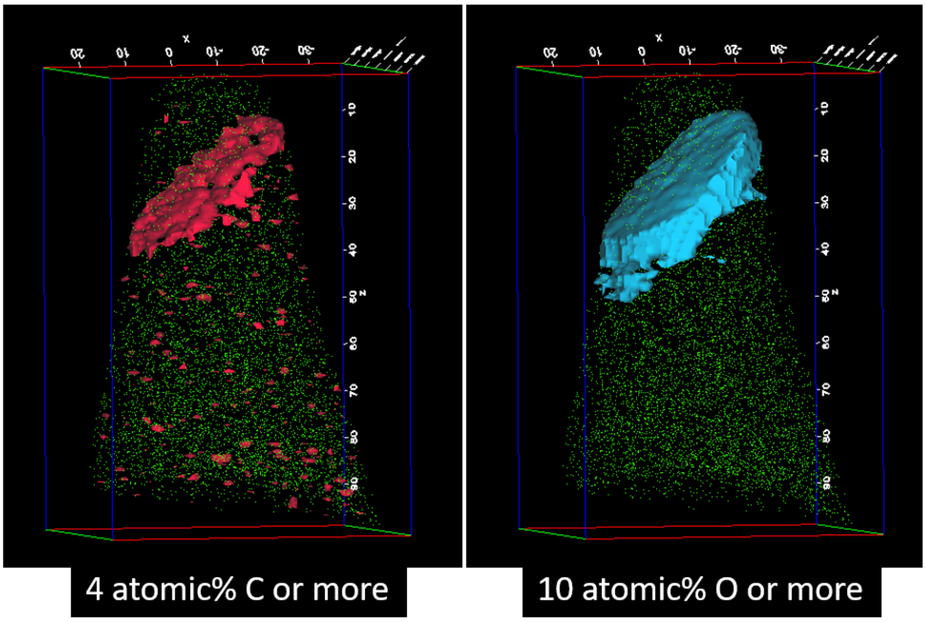

Figure 68: APT atom maps of carbon and oxygen. The highlighted region has an atomic content above the value described below the map.

Summary

The measurement indicate that the majority of carbon and oxygen is within the grain boundary, but the amount of gallium ions from the sample preparation process hinders a trustworthy analysis and no final conclusion can be drawn.

12.2 Transmission Kikuchi diffraction

Introduction

Electron backscatter diffraction (EBSD) is a technique to determine the crystallographic orientation of individual grains within a polycrystalline specimen and to identify separate crystalline phases [66]. The technique bases on the interaction of the electron beam with a sample tilted toward an EBSD-detector to capture the backscattered diffracted electrons. The captured diffraction patterns are Kikuchi-patterns, which arise from Bragg-diffraction of incoherently scattered electrons. The specimen for EBSD is normally a bulk metallic sample that has been electropolished to have a smooth oxide-free surface, free from residual stress or strain. The formation of Kikuchi patterns by transmission through an electron transparent specimen in the SEM is a technique that improves the spatial resolution compared to EBSD and a spatial resolution around 15 nm can be obtained [49]. The difference between the experimental setup of EBSD and TKD is illustrated in Figure 69. The Kikuchi diffraction patterns and the applied hardware for TKD is similar to that used in EBSD.

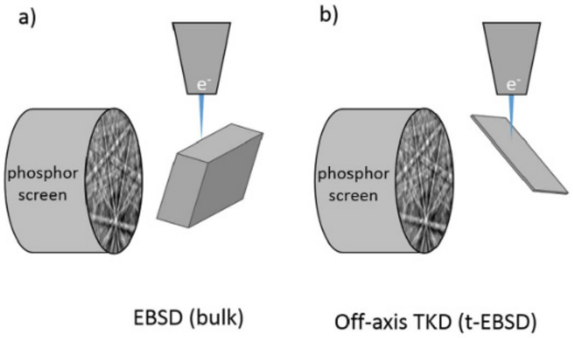

Figure 69: Illustration of the difference in experimental setup in SEM between (a) EBSD and (b) TKD. Figure from [67]

Experimental setup

The TKD measurements were intended to provide information of the growth mechanism of the Fe-C coating during nucleation on the substrate and its evolution in the first few micrometers. Thin electron transparent lamellae that included the substrate and Fe-C coating were prepared from a sample where the Fe-C coating had been deposited on a steel substrate. The electron transparent lamella of Fe-C coatings was prepared by the FIB-lift out technique as described in Section 4.3.3.2 for an off-axis transmission Kikuchi diffraction investigation of the cross section [49]. The thin lamella is shown as a BF TEM micrograph in Figure 70.

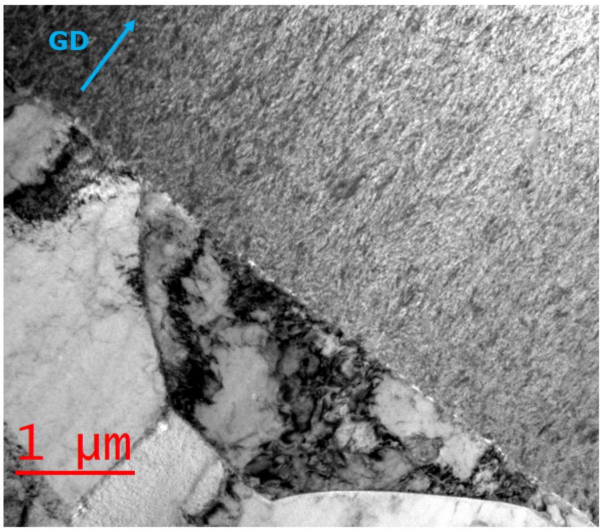

Figure 70: TEM bright field micrograph of as-deposited Fe-C coating on steel substrate in cross section.

Summary

The TKD measurements was intended to provide information of the growth mechanism of the Fe-C coating during nucleation on the substrate and its evolution in the first few micrometers. The investigation, however, was unsuccessful as only a few of the Kikuchi patterns obtained during an area scan could be matched.

12.3 Electron energy-loss spectroscopy

Introduction

The position of the light elements carbon and oxygen in the microstructure of the as-deposited Fe-C coating was investigated in a TEM by EELS using a converged electron beam for a line profile scan over several grain boundaries.

Experimental setup and results

An as-deposited Fe-C coating deposited using the operation conditions described in Manuscript I was prepared in plan-view by the FIB lift-out technique as described in Section 4.3.3.2. The Titan Analytical 80-300ST (300 keV) was used for the measurement. The converged electron beam was used to obtain a nanometer spatial resolution for the line profile scan over the grain boundaries and the high-angle annular dark-field detector (HAADF) was used to acquire the micrograph. The HAADF detector only measures the diffracted electrons and the grain boundaries will appear as black region as no electron diffraction occurs.

The HAADF micrograph with the EELS line profile scan and the measured signal from iron, carbon and oxygen are shown in Figure 71a and Figure 71b, respectively. The line profile scan over the four grains separated by three grain boundaries measured a decrease of the intensity for iron at three specific positions, where an increase for the signal of oxygen is measured. The position of the changes in chemical composition match the position of the grain boundaries in the line profile scan. This indicate that a higher concentration of oxygen is present in the grain boundaries, which is similar to the result of the single APT measurement, described in Appendix 12.1. However, the result is error-prone as the electron transparent iron samples are shown to develop magnetite shortly after preparation as shown in Manuscript V and VII, which hinders a clear conclusion. The measured signal for carbon increases in the initial part of the line profile scan and remains at the same intensity for the rest of the measurement. The intensity profile of carbon suggests a carbon contamination on the sample due to the strong intensity of the converged high energy electron beam.

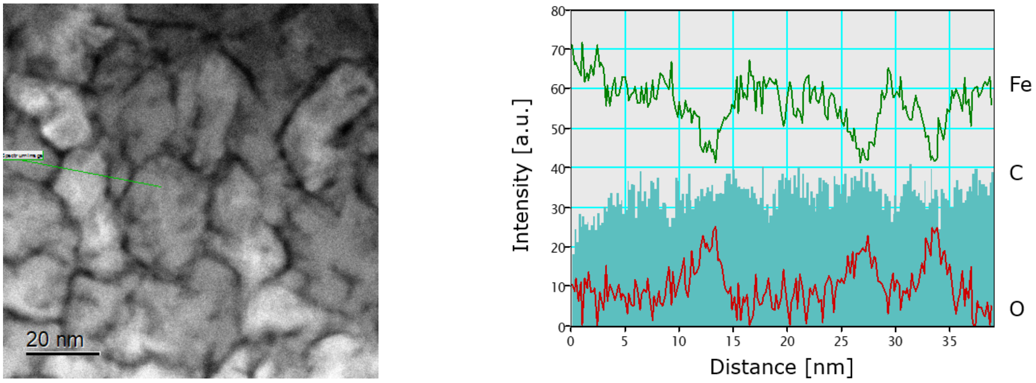

(a) (b)

Figure 71: (a) HAADF micrograph with a green line showing the EELS line profile scan across grain boundaries on an electron transparent thin lamella of an as-deposited Fe-C coating prepared in plane-view and (b) the measured signal from iron, carbon, and oxygen during the EELS line profile scan.

12.4 Ring-core milling

Introduction

The residual stresses were investigated on the surface of the Fe-C coating using the FIB ring-core milling technique [50,51]. Ring-core milling uses image correlation to measure variations in distance between characteristic features on a surface that will change when material is stepwise sputtered away around the investigated area as illustrated in Figure 72.

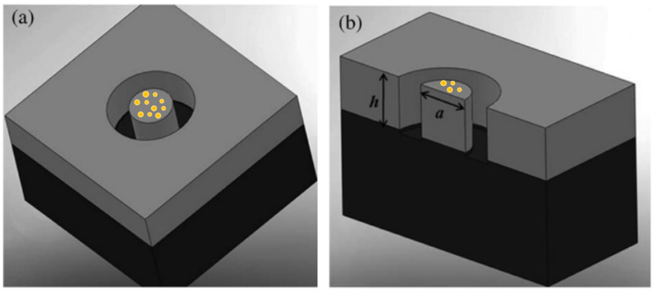

Figure 72: Illustration of the ring-core milling technique where material was sputtered away around a core having a characteristic pattern. Figure modified from [51].

The distance that the feature moves towards or away from its initial position is converted to the release of residual stresses using Hooke's law. The expressions for the stress state with bi-axial rotational symmetry in the surface (σ_1 and σ_2) are then obtained by using the general form of the Hooke's law as shown in Equation (37) and (38),

$$\sigma_1 = -\frac{E}{(1-v^2)}[\Delta\varepsilon_\infty^1 + v\Delta\varepsilon_\infty^2] \tag{37}$$

$$\sigma_2 = -\frac{E}{(1-v^2)}[\Delta\varepsilon_\infty^2 + v\Delta\varepsilon_\infty^1] \tag{38}$$

where $\Delta\varepsilon^1_\infty$ and $\Delta\varepsilon^2_\infty$ are the principal strains, E is the Young's modulus and v is the Poisson's ratio. The assumption is made that stresses perpendicular to the surface are negligible in the specimen, thus ensuring that the plane-stress version of Hooke's law can be used.

Experimental setup and results

The SEM micrographs in Figure 73 shows the platinum mask that is deposited prior to the milling and acts as the characteristic feature used for image correlation. The initial FIB ring-core milling step is also shown in Figure 73 where the material has been sputtered away around the circle with the characteristic pattern along with different steps of the milling process and finally the measured height of the core.

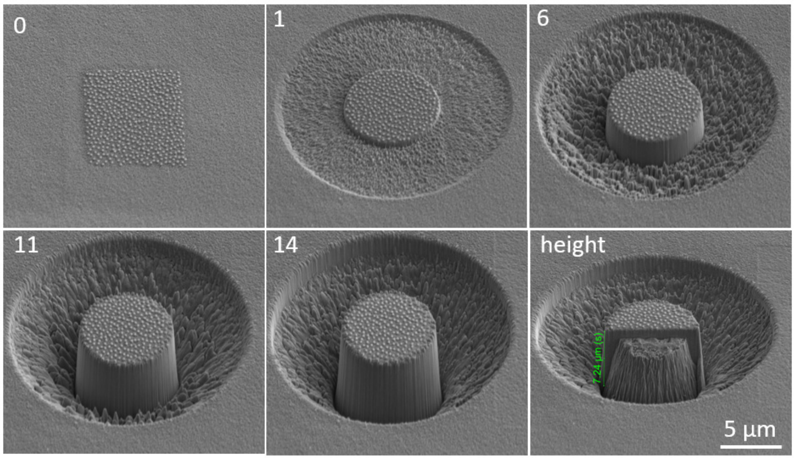

Figure 73: SEM micrograph of the different ring core milling steps of a Fe-C sample. (0) The characteristic Pt pattern has been applied, (1) first milling step has been conducted, (6) six milling step has been conducted, (11) eleven milling steps has been conducted, (14) fourteen milling step has been conducted, and (height) the height of the pillar is measured.

The image correlation software GOM correlate 2019 was applied for the estimation of the residual stresses. The SEM micrograph of the undisturbed characteristic pattern and micrograph acquired after each milling step is loaded into GOM correlate and the final pattern is used to apply a surface component for image correlation as shown in Figure 74b. The final step is used for the surface component as the FIB milling can alter the edges of the core slightly in each step. This can happens in case of a slight drift in the sample position or if the sample is being slightly charged between each milling step.

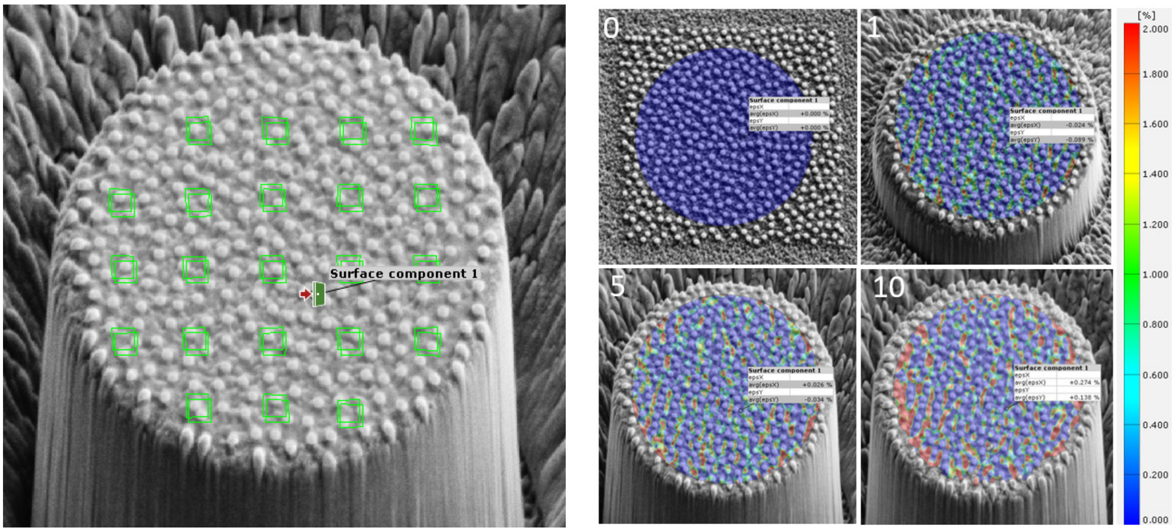

(a) (b)

Figure 74: (a) Image from the software GOM correlate 2019, where the facet point for the surface component is show on the SEM micrograph of the final ring-core milling step. (b) The surface component shown as a contour plot representing the displacement of features.

The initial pattern prior to the FIB milling is used as the starting point and the displacement of the characteristic features is measured on each micrograph representing each milling step as shown in Figure 74b.

Summary

The ring-core-milling investigation of the residual stresses relies on a stable microscope with no sample drift during the milling process. This was not achieved using the FEI Helios EBS3 dual beam scanning electron microscope at the time of investigation and the investigation was halted after a few unsuccessful attempts.

DTU Mechanical Engineering
Section of Materials and Surface Engineering
Technical University of Denmark

Produktionstorvet, Bld. 425
DK-2800 Kgs. Lyngby
Denmark

Tlf.: +45 4525 2205
Fax: +45 4525 1961

www.mek.dtu.dk

April 2020

ISBN: 978-87-7475-590-6